

Self-Assembled Arrays of Magnetic Nanostructures on Morphologically Patterned Semiconductor Substrates

by

Brendan O'Dowd

A thesis submitted to the University of Dublin in partial fulfilment for the degree of Doctor of Philosophy

School of Physics
Trinity College Dublin
University of Dublin
Dublin 2
Ireland

April 2014

Declaration of Authorship

This thesis is submitted by the undersigned for examination for the degree of Doctor of Philosophy at the University of Dublin. It has not been submitted as an exercise for a degree at any other University.

With the exception of the assistance noted in the acknowledgements, this thesis is entirely my own work.

I agree that the library of the University of Dublin may lend or copy this thesis freely upon request.

Signed: _____

Date: _____

Summary

This thesis deals with the formation of morphological patterns on single-crystal semiconductor surfaces via self-assembly processes, followed by the subsequent fabrication of magnetic nanostructures whose dimensions are defined by the underlying template. Stepped surfaces on Si (111) were achieved by high temperature DC annealing of vicinal Si templates which causes the atomic steps to form step-bunches and/or facets. In particular, for templates annealed with the current directed in the ascending step direction it was shown that the cooling rate from the annealing temperature can be used as a precise control of step periodicity. A shallow angle deposition technique was used to create ordered rows of magnetic nanowires on the step-bunched Si templates, whose dimensions are determined by the size of the underlying steps as well as the duration and angle of deposition. It is shown that wire width can be well defined down to as low as 30 nm and that the technique is applicable to a range of magnetic materials. Ordered arrays of nanodots can also be grown via shallow angle deposition onto faceted vicinal alumina templates, and it is shown that the substrate temperature during deposition influences the ellipticity and separation of the nanodots produced.

Magnetic measurements reveal that the nanowires have in-plane magnetic shape anisotropy, while measurements of coercivity as a function of temperature allow the investigation of parameters relating to the energy barriers of magnetisation reversal. Henkel analysis was used to probe the extent of interwire interactions, and it was shown that reducing interwire separation led to dipolar coupling, as had been shown in previous studies of vertical wire arrays. The samples were also investigated using FMR, with measurements being taken as the sample was rotated about each of its principal axes. The results of this study indicated that the use of MgO as a capping layer leads to the formation of an oxide layer which may reduce the effective thickness of the nanowires, and over time gives rise to an additional unidirectional exchange anisotropy. Some preliminary results obtained through the analysis of first order reversal curves (FORCs) are also presented. This method of analysis has the potential to identify the influence of one-dimensional structures as well as superparamagnetic nanoparticles on the magnetisation of the system as a whole, and it is likely to be a very useful tool for future investigations into the properties of such magnetic nanostructure arrays.

Random arrays of vertical GaAs nanowires are commonly grown via the VLS (vapour-liquid-solid) mechanism. The wires grown using this technique have an inherent distribution in dimensions due to the non-uniformity of diameter and separation of the seed particles. This creates a large uncertainty in any statistical analysis that seeks to relate the shape and size of the wires with the growth process. In this study, arrays of seed

particles (gold nanodots) are defined using EBL, resulting in far greater wire uniformity and thereby facilitating comparisons between different growth conditions. For example, the effects of shadowing as a function of separation between neighbours in the array can be quantitatively measured, and a simple model is presented which closely matches the experimental data. The study of GaAs nanowire growth from pre-patterned seed particles is also important from an applications point of view, since most proposed applications require the precise placement of nanowires rather than arbitrary locations. Growth in As-limited conditions was investigated, a regime which is usually ignored in studies of nanowire growth that uses catalyst particles. Many features of previous studies were replicated, but at a significantly lower growth temperature allowed through the use of Au catalyst particles. Growth under As_2 flux was compared to As_4. There were prominent differences in shape, volume and facets making up the wire sidewalls. These findings were related to the different reactivities and diffusion properties of the two molecules on the nanowire sidewalls.

The control of shadowing allowed substantial radial growth to occur uniformly along the wire sidewalls. This effect resulted in wires which were much wider than the seed particles (for example wires with diameter of $\approx 300\,\mathrm{nm}$ width having droplet diameters of only 20 nm was common). In all instances, the radial growth occurred epitaxially, with no defect planes in the axial direction seen in any sample. Some samples had a certain density of wurtzite to zincblende defects or zincblende twinning planes. These defects traversed the wire width in each case. Moreover, the appearance of these defects was closely associated with instances where the contact angle between the nanowire sidewalls and the alloy droplet atop the wire was significantly greater or less than $90\,^\circ$. This phenomenon is described in detail in relation to the crystal structure at the growth interface.

Finally, in a similar manner to the deposition of Fe onto the step-bunched Si templates, Fe was also deposited onto the sidewalls of the GaAs nanowire arrays, resulting in core-shell GaAs-Fe structures, with an additional coating of Au for protective capping. The degree to which this aim was successful was investigated using STEM. It was found that the procedure was moderately successful, with some areas uniformly coated in Au while in other areas the Au seemed to form droplets on the wire sidewalls. A sample having an array of GaAs nanowires which had an angle of approximately $35\,^\circ$ to the substrate normal and were coated with Fe-Au was investigated using FMR. It was found that the behaviour of magnitude of the resonance field as a function of the angle of the applied field with respect to the sample corresponded accurately to the wire axis, indicating that the Fe-coated nanowires have an easy axis of magnetisation parallel to their length, which is likely due to the shape anisotropy of the cylindrical Fe structure.

Acknowledgements

Throughout the past four years I have had the great fortune of meeting and working with some wonderful people. I would like to thank all those who were so generous with their time. They really have been an inspiration for me.

I would like to thank my supervisor Prof. Igor Shvets for all of his support and guidance. In all my dealings with Igor I have always found him to be very easy to work with. He has always been a good listener and very thoughtful in his approach.

I would like to thank everyone in the Applied Physics Research Group for their support, advice and good humour. Their attitude has made coming to work every day for the last four years a very positive experience, and I have always appreciated the lengths that they have all gone to whenever I needed help. Ruggero has been a great friend and a valuable source of advice. Cormac has been very helpful with his guidance, particularly in practical lab matters. Sunil contributed to planning and trained me on range of equipment. Karsten has been very generous, regularly putting aside his work to help me for as long as was needed. Ciarán has been a great help with administrative issues and has saved me countless headaches. In the run-up to submission, Barry and Ellen were both invaluable sources of support and advice.

I have greatly enjoyed working at CRANN and in the School of Physics. In both institutions there is a wealth of experience and advice. I'd like to thank all the staff and researchers here who contribute to the wonderful working environment.

I'd like to thank Prof. Jacek Furdyna for welcoming me into his group. He has a passion for research that is contagious and a very warm personality that made working with him a pleasure. I'd like to thank the other professors in the group; Xinyu Liu, Malgorzata Dobrowolska, and Tomasz Wojtowicz. Prof. Liu and Prof. Wojtowicz put in a great deal of work in the fabrication of samples for my analysis. I'd like to thank Brendan Benapfl, Joe Hagmann, Jon Leiner and Rich Pimpinella for making sure that I now have great memories as well as some good data from my time at Notre Dame. I had a great time getting to know each of them. I worked closely with Dr. Sergei Rouvimov who took some excellent TEM images. I'd like to thank Sergei for his kind attitude and acknowledge his talent and hard work. In general I had a great time at Notre Dame. There was a very positive and calm atmosphere and it was a great place to work. I'd like to thank all the other Ph.D. students there as well as the staff at the Department of Physics, especially Susan and Shari who were very welcoming and helpful.

I would also like to acknowledge the input of all of our collaborators. Pardeep Thakur and Nicholas Brookes conducted XMCD measurements for us at the European Synchrotron

Radiation Facility. Sarnjeet Dhesi carried out some XMCD measurements at the Diamond Light Source in Oxfordshire, England. Some TEM images of our nanowire arrays were taken by the Atomic Manipulation Spectroscopy Group at the Catalan Institute of Nanotechnology. Kritsanu Tivakornsasithorn and Richard Pimpinella participated in the FMR and SEM investigations of the Fe-coated GaAs nanowires. FMR measurements and analysis were carried out by the group of Oleksandr Tovstolytkin at the Institute of Magnetism in the National Academy of Science of Ukraine, in Kiev, Ukraine. EBL for the patterned arrays of Au nanodots which formed the seed particles for the GaAs nanowire arrays was carried out by the Growth and Physics of Low Dimensional Crystals group under Prof. Wojtowicz at the Institute of Physics, Polish Academy of Sciences, Warsaw, Poland. I should also mention here that some software was used which was free to download, namely Gwyddion which was used for AFM analysis and generating FFTs in post-production, and FORCinel for Igor Pro, which which was used to process the FORC data.

I would like to thank Zara for her love and support throughout my studies. She has been great in every way and is always there for me through all the ups and downs. Thanks to all my close friends over the past few years. Thanks to my teachers and lecturers through the years. Thanks to my brothers Ciarán, Enda and Patrick, and a huge thanks to my parents for all the sacrifices they made for my education.

Finally I'd like to offer my sincere thanks to the Naughton family, particularly Martin, Carmel and Fergal Naughton, and everyone involved with the Naughton Foundation for the organisation and funding of the scholarship that made the last four years possible. It has been a wonderful experience, in terms of the work that I've been able to do, the places I've had the opportunity to visit and the people that I've met along the way.

Contents

Declaration of Authorship iii

Summary v

Acknowledgements vii

List of Figures xiii

List of Tables xvii

Abbreviations xix

Publications xxi

1 Introduction and Motivation 1
- 1.1 Manipulation of Semiconductor Surfaces . . . 1
- 1.2 Magnetic Nanostructures . . . 3
- 1.3 Thesis Outline . . . 6

2 Experimental Methods 9
- 2.1 Sample Fabrication . . . 9
  - 2.1.1 Vacuum System for Si Annealing and Glancing Angle Depositions . . . 9
  - 2.1.2 GaAs Nanowire Growth Chamber . . . 12
  - 2.1.3 Tube Furnace . . . 13
- 2.2 Characterisation of Sample Morphology . . . 13
  - 2.2.1 Atomic Force Microscopy (AFM) . . . 13
  - 2.2.2 Scanning Electron Microscopy (SEM) . . . 14
    - 2.2.2.1 Additional SEM capabilities . . . 17
  - 2.2.3 Transmission Electron Microscopy (TEM) . . . 18
  - 2.2.4 Scanning Transmission Electron Microscopy (TEM) . . . 19
  - 2.2.5 Statistical Analysis of Nanoparticle Dimensions . . . 19
- 2.3 Magnetic Characterisation . . . 20
  - 2.3.1 Vibrating Sample Magnetometer (VSM) . . . 20

2.3.2 Alternating Gradient Field Magnetometer 21
2.3.2.1 Addition AGFM Measurements 21
2.3.3 Ferromagnetic Resonance (FMR) 23

3 Template Preparation and Glancing Angle Deposition 27
3.1 Background 27
3.2 Si Template Preparation 30
3.2.1 Si (111) 30
3.2.2 Step Bunching on Si (111) 33
3.2.2.1 BCF and Stoyanov Theory 36
3.2.2.2 Faceting in Regime I 38
3.2.3 Si Annealing Procedure 39
3.2.4 Results 41
3.3 Sapphire Template Preparation 45
3.3.1 Sapphire 45
3.3.2 Faceting Mechanism on Sapphire 45
3.3.3 Annealing Procedure 48
3.3.4 Results 48
3.4 Glancing Angle Deposition Technique 49
3.4.1 Nanowires Grown on Large-Step Samples 51
3.4.2 Nanowires Grown on Small-Step Samples 51
3.4.2.1 Downhill Depositions on Si 51
3.4.2.2 Uphill Depositions on Si 57
3.4.2.3 Uphill Depositions on Sapphire 59
3.5 Conclusions 61

4 Magnetic Characterisation of Nanowire Arrays 63
4.1 Magnetic Phenomena in Nanowire Arrays 63
4.1.1 Magnetic Anisotropy 64
4.1.1.1 FMR as a probe of magnetic anisotropy 68
4.1.2 Important Length Scales in Magnetism 69
4.1.3 Reversal Mechanisms 71
4.1.4 Interwire Interactions 73
4.2 Results 75
4.2.1 Shape Anisotropy 75
4.2.2 Reversal Mechanism 79
4.2.3 Interwire Interactions 82
4.2.4 FMR 84
4.3 Conclusions and Further Work 91

5 GaAs Nanowires 99
5.1 GaAs 99
5.2 Motivation for Ordered Arrays of GaAs nanowires 99
5.3 VLS Method 100
5.4 Crystal Structure of GaAs Nanowires Grown in [111] Direction 106
5.5 GaAs Nanowire Fabrication Procedure 112
5.6 Results 114

5.6.1 Ordered Arrays of Nanowires . . . 114
5.6.2 Pencil-Shaped Nanowires . . . 117
5.6.3 Examination of Effect of Shadowing for Pencil-Shaped Nanowires . 120
5.6.4 Critical Dot Diameter for Nanowire Growth . . . 123
5.6.5 Growth in As-limited Regime . . . 126
5.6.6 Nanowire Growth using As Dimers . . . 136
5.7 Conclusions and Further Work . . . 144

6 GaAs Nanowires Coated with Fe **147**
6.1 Introduction . . . 147
6.2 Experimental Procedure . . . 149
6.3 Results . . . 150
6.3.1 SEM . . . 150
6.3.2 STEM and EDX . . . 151
6.3.3 FMR . . . 153
6.4 Conclusions and Further Work . . . 155

7 Conclusions and Outlook **157**

A Derivation of Magnetic Resonance Expression **163**

B Effect of Shadowing on Nanowire Volume **169**

Bibliography **177**

List of Figures

1.1 Typical FED design incorporating nanowire array . . . 3
1.2 HDD units from 1956 and 2008 . . . 4

2.1 Chamber for glancing angle deposition and Si annealing . . . 10
2.2 Glancing angle deposition schematic . . . 11
2.3 VLS Chamber . . . 12
2.4 SEM Schematic . . . 15
2.5 SEM Interaction Volume . . . 16
2.6 Statistical Analysis using AutoCAD . . . 20
2.7 Schematic for finding $M_R(H)$ and $M_D(H)$. . . . 22
2.8 Schematic for finding FORCs. . . . 23
2.9 FMR Setup Schematic . . . 24

3.1 Unit cell of Si. . . . 30
3.2 Atomic steps on Si(001) . . . 31
3.3 The (111) surface of Si . . . 31
3.4 Single atomic steps on Si (111) . . . 32
3.5 Si 7×7 reconstructed surface unit cell . . . 33
3.6 Cubic model of atom locations . . . 35
3.7 Schematic of adatom gradient effect on terrace of atomic step . . . 37
3.8 Two Si (111) terraces separated by a (331) facet . . . 39
3.9 Samples annealed with step-up current in Regime I with different cooling rates . . . 41
3.10 Dependence of periodicity on cooling rate for step-up current in Regime I 42
3.11 Height and angle profile of a step-bunched sample . . . 43
3.12 Step bunches in Regime I and II . . . 44
3.13 Crystal structure of Al_2O_3 . . . 46
3.14 Side profile and C-plane of Al_2O_3 . . . 46
3.15 Dependence of periodicity of annealed Al_2O_3 substrates on temperature . 47
3.16 AFM of faceted Al_2O_3 . . . 49
3.17 Glancing Angle Deposition Schematic . . . 50
3.18 Glancing angle deposition results on large-step samples . . . 52
3.19 Single nanowire produced on a large-step sample . . . 52
3.20 Fe nanowires with varying deposition angle . . . 53
3.21 Height profiles across nanowires with varying deposition angle and thickness 54
3.22 TEM of Fe nanowires . . . 55
3.23 TEM of Co nanowires . . . 56
3.24 AFM data from Ni nanowire arrays with varying thickness . . . 57

3.25 AFM data from arrays of nanowires composed of Co, Fe and Ni deposited in the uphill direction 58
3.26 Co nanowires and nanoparticles on faceted Al_2O_3 substrates 59
3.27 Important dimensions of Co nanoparticles 60

4.1 Labels and axes of wire array parameters. 68
4.2 Schematic images of the effect of dipolar coupling with nanowire arrays. . 74
4.3 Shape Anisotropy of Fe nanowire arrays of varying thickness. 76
4.4 Dependency of wire structure on deposition thickness. 77
4.5 Shape Anisotropy of Co nanowire arrays of varying thickness. 78
4.6 Dependency of coercivity of Fe nanowire arrays as a function of temperature 80
4.7 SEM images of samples for Henkel analysis. 82
4.8 $M - H$ loops for samples in Henkel analysis. 83
4.9 Henkel plots for varying separation. 84
4.10 Axis and angle labels for FMR. 85
4.11 In-plane FMR spectra for Fe nanowire array. 86
4.12 Out of plane FMR spectra for Fe nanowire array. 87
4.13 Sample of FMR spectra. 88
4.14 Resonance Field as a function of angle. 89
4.15 Resonance Field as a function of angle for sample with ageing effects. . . . 90
4.16 Signatures of magnetic features on a FORC distribution plot. 94
4.17 FORC plot for Fe nanowire array. 95
4.18 FORC distribution plots for different nanowire and nanodot arrays. 96

5.1 Routes of Ga to growth interface 103
5.2 Unit cell of zincblende GaAs. 107
5.3 Different Hexagonal Facet Groups for Zincblende and Wurtzite Structures. 109
5.4 Schematic of contact angle and angle of inclination of sidewalls. 110
5.5 Schematic of competing facet groups during growth. 111
5.6 Two possible facets of wurtzite GaAs nanowire sidewalls. 112
5.7 Liquid-solid phase boundaries for AuGa and PdGa alloys. 113
5.8 Ordered and Random Array of GaAs Nanowires. 114
5.9 Height Distributions for Ordered and Random Nanowire Arrays. 115
5.10 TEM analysis of wires in patterned array. 116
5.11 SEM images of pencil-shaped nanowire array. 117
5.12 TEM images of pencil-shaped nanowire. 119
5.13 Dependency of Nanowire Volume with Separation. 121
5.14 Dependency of nanowire volume distribution with separation. 122
5.15 Nanowire volume vs. separation with numerical model 123
5.16 Probability of Nanodot initiating Wire Growth vs. Radius of Nanodot. . . 125
5.17 Nanowires grown in As-limited regime 127
5.18 Histogram of heights of nanowires grown in As-limited regime 127
5.19 Nanowires grown from patterned arrays in As-limited regime 129
5.20 STEM of Nanowires grown in As-limited regime 130
5.21 EDX examination of Nanowires grown in As-limited regime 131
5.22 High resolution TEM images with crystal structure overlay. 132

5.23 High resolution TEM images taken of a nanowire grown in As-limited conditions. . . . 133
5.24 Schematic of nanowire with microfacets . . . 134
5.25 As-limited growth of shorter duration . . . 134
5.26 Nanowires grown using As_2 . . . 137
5.27 Volume of cone-shaped nanowires as a function of separation . . . 138
5.28 2D density plot of wire heights and angles . . . 139
5.29 2D density plots of wire heights and angles for wires with varying droplet diameter . . . 140
5.30 TEM analysis of wire with small droplet grown in As_2. . . . 141
5.31 TEM analysis of wire with large droplet grown in As_2. . . . 142
5.32 Contact angles for wires with varying droplet size . . . 143

6.1 Growth directions of GaAs nanowires on various GaAs substrates . . . 149
6.2 GaAs Nanowire arrays coated in Fe and Au . . . 150
6.3 STEM and EDX linescans of Fe/Au coated GaAs nanowires . . . 151
6.4 STEM and EDX linescans of particular features on Fe/Au coated GaAs nanowires . . . 153
6.5 FMR of Fe-coated GaAs nanowires . . . 154

A.1 Spherical co-ordinate system used in FMR . . . 163
A.2 Labels and axes of wire array parameters. . . . 166

B.1 Schematic of shadowing considerations . . . 170
B.2 Effect of varying values for the diffusion length (D) . . . 172
B.3 Effect of varying the initial nanowire diameter . . . 173
B.4 Numerical model with experimental data . . . 174

List of Tables

3.1 Si (111) Step-Bunching Temperature Regimes 34
3.2 Average dimensions of nanoparticles grown at two different substrate deposition temperatures 60

4.1 Demagnetising Factors for Common Shapes 67
4.2 Useful parameters for common ferromagnetic materials 71
4.3 Fitting parameters of temperature dependence of coercivity 80
4.4 Summary of Fe nanowire array samples analysed with FMR. 87
4.5 Parameters determined from fitting to samples with unidirectional anisotropy. 91

Abbreviations

AAO	**A**nodized **A**luminium **O**xide
AFM	**A**tomic **F**orce **M**icroscope
AGFM	**A**lternating **G**radient **F**ield **M**agnetometer
ATLAS	**A**tomic **T**errace **L**ow **A**ngle **S**hadowing
BSE	**B**ack-**S**cattered **E**lectrons
CBE	**C**hemical **B**eam **E**pitaxy
DMA	**D**ifferential **M**obility **A**nalyser
EBL	**E**lectron **B**eam **L**ithography
EDX	**E**nergy **D**ispersive **X**-ray Spectroscopy
(Sometimes also referred to as EDS or XEDS)	
FED	**F**ield **E**mission **D**isplay
FMR	**F**erro**m**agnetic **R**esonance
GMR	**G**iant **M**agneto**r**esistance
FFT	**F**ast **F**ourier **T**ransform
HAADF	**H**igh-**A**ngle **A**nnular **D**ark **F**ield (Imaging)
HDD	**H**ard **D**isk **D**rive
LCG	**L**aser-Assisted **C**atalytic **G**rowth
LED	**L**ight **E**mitting **D**iode
MBE	**M**olecular **B**eam **E**pitaxy
MCD	**M**agnetic **C**ircular **D**ichroism
MFM	**M**agnetic **F**orce **M**icroscopy
MOVPE	**M**etal **O**rganic **V**apour **P**hase **E**pitaxy
OAG	**O**xide **A**ssisted **G**rowth
PE	**P**rimary **E**lectrons
PEM	**P**hoto **E**lastic **M**odulator

PPMS	**P**hysical **P**roperties **M**easurement **S**ystem
SAED	**S**elective **A**rea **E**lectron **D**iffraction
SAG	**S**elective **A**rea **G**rowth
SE	**S**econdary **E**lectrons
SEM	**S**canning **E**lectron **M**icroscope
(**S**)**MOKE**	(**S**urface) **M**agneto **O**ptic **K**err **E**ffect
STEM	**S**canning **T**ransmisison **E**lectron **M**icroscope
STM	**S**canning **T**unnelling **M**icroscope
TEM	**S**canning **E**lectron **M**icroscope
UHV	**U**ltra **H**igh **V**acuum
VLS	**V**apour **L**iquid **S**olid
VSM	**V**ibrating **S**ample **M**agnetometer
XAS	**X**-ray **A**bsorption **S**pectroscopy
XMCD	**X**-ray **M**agnetic **C**ircular **D**ichroism
XPS	**X**-ray **P**hotoelectron **S**pectroscopy

Publications

Arora, S. K., ODowd, B. J., McElligot, P. C., Shvets, I. V., Thakur, P., and Brookes, N. B. (2011). Magnetic properties of planar arrays of Fe-nanowires grown on oxidized vicinal silicon (111) templates. Journal of Applied Physics, 109(7), 07B106. doi:10.1063/1.3554264

Arora, S. K., ODowd, B. J., Ballesteros, B., Gambardella, P., and Shvets, I. V. (2012). Magnetic properties of planar nanowire arrays of Co fabricated on oxidized step-bunched silicon templates. Nanotechnology, 23(23), 235702. doi:10.1088/0957-4484/23/23/235702

Fox, D., Verre, R., ODowd, B. J., Arora, S. K., Faulkner, C. C., Shvets, I. V., and Zhang, H. (2012). Investigation of coupled cobaltsilver nanoparticle system by plan view TEM. Progress in Natural Science: Materials International, 22(3), 186192. doi:10.1016/j.pnsc.2012.04.001

Arora, S. K., ODowd, B. J., Nistor, C., Balashov, T., Ballesteros, B., Lodi Rizzini, a., Shvets, I. V. (2012). Structural and magnetic properties of planar nanowire arrays of Co grown on oxidized vicinal silicon (111) templates. Journal of Applied Physics, 111(7), 07E342. doi:10.1063/1.3679033

Pimpinella, R. E., Zhang, D., McCartney, M. R., Smith, D. J., Krycka, K. L., Kirby, B. J., Furdyna, J. K. (2013). Magnetic properties of GaAs/Fe core/shell nanowires. Journal of Applied Physics, 113(17), 17B520. doi:10.1063/1.4799252

Arora, S. K., ODowd, B. J., Polishchuk, D. M., Tovstolytkin, A. I., Thakur, P., Brookes, N. B., Shvets, I. V. (2013). Observation of out-of-plane unidirectional anisotropy in MgO-capped planar nanowire arrays of Fe. Journal of Applied Physics, 114(13), 1339031339037. doi:10.1063/1.4823514

For Zara and my parents

Chapter 1

Introduction and Motivation

This thesis deals with ordered arrays of magnetic nanowires and nanoparticles that have been deposited onto specially prepared crystalline substrates, namely the semiconductors Si and GaAs as well as the insulator Al_2O_3. The nanowires/nanoparticles take their shape from the texture of the substrate. As such, the two central themes of this thesis are the manipulation of semiconductor surfaces to produce ordered morphologies, and the subsequent fabrication and analysis of magnetic nanostructures.

1.1 Manipulation of Semiconductor Surfaces

The control and preparation of highly uniform single crystal structures such as Si has been a key enabler of many of the advancements that underpin the technological revolution of the past 50 years. While the first solid-state transistors were made using germanium, today Si is the most commonly used material for the integrated circuits which today are found in almost all electronic equipment, such as computers, radios, calculators and many more besides. Si also has important applications in the solar cell industry and a wide variety of sensing apparatus. Silicon's popularity is also related to its abundance, being the second most common element making up the earth's crust (after oxygen) [1]. GaAs, while not as ubiquitous as Si, has important niche applications where it out-performs Si. For example, its higher electron mobility makes it a suitable candidate for the manufacture of high-frequency transistors in communications electronics.

Central to the realisation of proposed devices, and the improvement of existing ones, has been our growing awareness and ability to manipulate behaviour at the atomic level. For this reason, a huge volume of research continues to be conducted to enhance our

fundamental understanding of these materials. In this work, separate investigations are carried out into particular nanoscale growth processes of Si and GaAs, which are utilised here for the subsequent fabrication of magnetic nanostructures, but are interesting in their own right as they further our understanding of the properties of these two important materials. With regard to Si, an investigation into the migration of surface atoms leading to the bunching of atomic steps is carried out as described in the first half of chapter 3. The desire to investigate and control the behaviour of atomic steps on single crystal structures is a natural outcome of the inevitability of their appearance, since, in spite of the enormous advances in crystal preparation, for device-sized pieces of Si ($> \mu$m) it is practically impossible to produce atomically flat surfaces. The long-term goals of such experiments are to learn about how these surface defects can be managed in such a way as to prevent them from influencing the proper functioning of devices, or perhaps even to open up new possibilities for functions based on the controlled use of such defects. The formation of nanowires and nanoparticles on step-bunched substrates which is described in the second half of chapter 3 can be considered a very primitive example of the latter.

With regard to GaAs, an investigation is carried out into a very interesting growth process known as the Vapour-Liquid-Solid (VLS) mechanism. The full details are given in chapter 5. Studies of this sort provide important contributions to our fundamental understanding of the properties of the material itself, such as surface energies, growth modes, stability of facets and diffusion lengths of adatoms on those facets. Moreover, the nanowires grown using this mechanism may have direct application uses. Due to their sharpness and high aspect ratio the use of crystalline nanopillars has been proposed for Atomic Force Microscopy (AFM) tips. Examples of commercialisation initiatives include the Trinity College startup company Adama Innovations. The advantages of a nanowire or nanopillar in this application is that the high aspect ratio of the tip will allow the imaging of surfaces with deep indentations such as pore arrays and right-angled trenches. Conventional cone or pyramid shaped tips would not be able to reach to the bottom of such features and would underestimate the slope of very steep steps. An additional benefit is that, provided the radius of the nanowire/pillar is uniform, wearing of the tip due to use should not affect its resolution. Another proposed application is in the area of solar cells, where the use of core-shell nanowires promise greater surface area than flat designs, as well as incorporation into a transparent, flexible polymer [2, 3]. Other applications for these structures include a wide range of optoelectronic and nanoelectronic applications [4–6], including field emission displays (FED) [7]. A diagram of a potential FED device including a vertical nanowire array is shown in figure 1.1. The design is based on an amalgamation of features commonly seen in proposed devices [8–10].

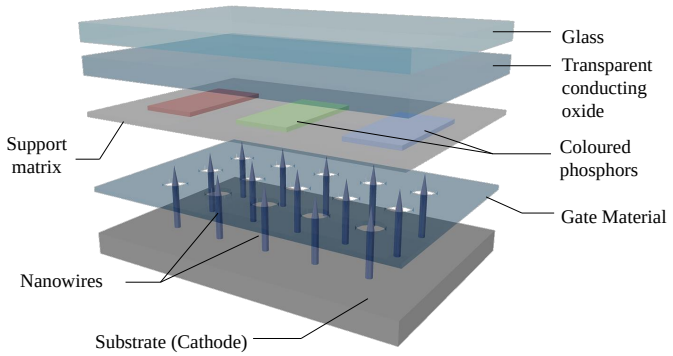


FIGURE 1.1: Typical FED design incorporating nanowire array

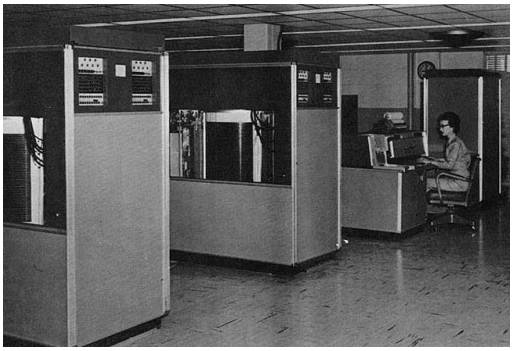
Possible FED (Field Emission Display) device based on an ordered array of nanowires. This design consists of an amalgamation of features typically seen in proposed FED devices [8–10].

The challenges associated with the implementation of these applications include our understanding and control of the growth process. Specifically, we would like to be able to minimise defects in the crystal structure, and specify the overall shape of the nanowire. Many proposed applications also require precise placement of the nanowires, rather than simply a disordered array. The experiments in chapter 5 regularly refer to these obstacles.

1.2 Magnetic Nanostructures

The study and understanding of magnetic nanostructures is crucial for a number of applications and their continued development, in particular for the manufacture of magnetic data storage devices. Despite a recent slump in the hard disk drive (HDD) market due to the popularity of smartphones and tablet computers (which use flash memory), over 550 million hard disk drive (HDD) units are expected to be sold in 2013, with global sales of of approximately $33 billion [11]. The growing trend of online or 'cloud' storage is expected to strengthen HDD sales in the coming years.

The rate of improvement in HDD memory density, cost and weight has been extraordinary. While the progress of transistor minimisation is well known, with the 'Moore's Law' prediction of a doubling of component density on integrated circuits every two years holding true since 1965 [12], the pace of minimisation in the field of magnetic storage devices has been even more dramatic, with a 50-million-fold increase in bit density since 1956 [13]. As a brief example, two hard drives are shown in figure 1.2. The first image in figure 1.2(a) is the IBM 305 RAMAC, which was the first commercial HDD, released in 1956. Due to the high cost of computers at the time, devices such as this were typically rented rather than bought. The 305 RAMAC cost $3,200 a month to rent,

a) 

b) 

Model:	IBM 305 RAMAC	Western Digital Blue - 500GB Portable SATA
Year:	1956	2008
Capacity:	4.4 MB	500 GB
Mass:	>1000 kg	82g
Cost	$3,200 per month,1957 (≈ $26,500, 2013)	≈$80

FIGURE 1.2: HDD units from 1956 and 2008

a) Two IBM 305 RAMAC HDDs (foreground) with operator, processing unit and console in the background. This photo is in the public domain and was taken by the U.S. Army Red River Arsenal.
b) Modern 2.5" laptop hard drive, produced by Western Digital. The photo is in the public domain. It was obtained from Wikimedia where it was uploaded by user 'Evan-Amos' as a part of Vanamo Media.

approximately equivalent to $26,500 in 2013 after adjusting for inflation [1][14]. It could store only 4.4-5 MB of data. Figure 1.2(b) shows a modern 2.5" laptop hard drive, which stores 500 GB and weighs less than 100 g. In terms of cost per MB, these two examples represent a decrease of over 8 orders of magnitude. The continued improvement in HDD performance and memory density are some of the main motivations behind many of the hot topics in magnetism research today. Two examples of areas of particular interest are Heat-Assisted Magnetic Recording (HAMR), which uses a laser or other localised heat source to temporarily lower the magnetisation reversal barrier of the bit being written, and Bit-Patterned Media (BPM), which uses distinct, patterned bit entities [15]. BPM has the potential for greater bit density than current designs employing granular films, though implementation of BPM will require a high throughput nanoscale writing technique that is also low in cost [16, 17]. One example of a technique hoped to allow the definition of theses individual bits is nano-imprint lithography, though further improvements in efficiency and reproducibility are still required [18, 19]. The research in this thesis is fundamental in nature, and is not specific to any particular device design.

Another potential application for magnetic nanowires is domain wall logic [20, 21]. In such devices, Boolean logic functions such as AND, OR, NAND, XOR etc. can be carried

[1]For effect of inflation, the online Consumer Price Index Inflation Calculator produced by the United States Bureau of Labour Statistics was used. (`http://www.bls.gov/data/inflation_calculator.htm`)

out by propagating a domain wall through a specially designed circuit of magnetic nanowires, which are usually composed of permalloy ($Ni_{80}Fe_{20}$). The magnetisation will preferentially lie along one or other direction of the wires involved, corresponding to a logical 1 or 0. The initial magnetic 'inputs' and the propagation of domain walls are governed via the application of external fields, and the logical outcome at the output wire is determined by the manner in which the 'input' magnetisations interact with the circuit and each other. Prior to fabrication and testing in the lab, circuit designs are usually rigorously tested using a micromagnetic simulation software package such as OOMMF (Object Oriented MicroMagnetic Framework, ITL/NIST).

Other varied uses for magnetic nanowires include the growing area of spin transfer and spintronics [22], high frequency devices [23], magnetic sensing [24] and cell manipulation in biological systems [25].

Prior to implementation in proposed applications, a comprehensive understanding of the fundamental behaviour of the magnetisation within the wires will be required. The sensitivities of conventional magnetometers coupled with the tiny volumes of magnetic material in these structures is such that it is far more convenient to measure many thousands or millions of wires at once in order to gain an understanding of the behaviour of a single entity. Thus it is desirable to quickly produce large arrays of well-aligned nanowires with minimum distribution of their dimensions. A background to some of the existing strategies for fabrication of such arrays is given in section 3.1, but here it is mentioned that one of the most popular methods results in a vertical array of nanowires perpendicular to the substrate surface. Far less attention has been paid to planar arrays, which may hold important lessons for industry since most mechanized patterning procedures are tailored towards planar features. In chapter 3, a simple procedure for the fabrication of large (order of mm^2) arrays of highly regular nanowire arrays is presented. It is shown that the thickness, width and separation can be specified by appropriate choice of template and growth parameters, and moreover that the technique is applicable to a wide range of magnetic materials.

With regard to the magnetic phenomena and their relevance to the challenge of device minimisation and overall improvement, the central themes explored in the present study include magnetic shape anisotropy, magnetisation reversal mechanisms and inter-wire interactions. Each of these effects are important considerations for the design of many of the proposed applications mentioned above. Magnetic anisotropy is the cause of stabilisation of magnetic direction in any structure, and hence the non-volatility of data storage. At dimensions approaching the nanoscale magnetic anisotropy becomes increasingly important, as thermal effects rival the magnetic reversal barrier in magnetic nanostructures. Studies of reversal mechanisms can reveal the expected form of domain

walls (if any) during reversal, as well as the energy or applied field required to reverse the direction of magnetisation. The effect of interwire interactions is an important consideration for the design of devices containing magnetic nanowires, since the dominance of this phenomenon will determine the maximum density that can be safely achieved before neighbouring particles impede the proper functionality of constituent components. Finally, as is described in chapter 6, Fe was deposited onto the sidewalls of the vertical GaAs nanowires to form hollow nanowires or nanotubes of Fe. Although only shape anisotropy is exhibited in these structures, it may be the case that the magnetisation may prefer the arrangement of closed loops which would theoretically have a very low stray field. Closed magnetic loops in nanostructures have been the basis for investigations into simple spin-valve devices [26], although due to the low stray field and zero net magnetisation, these closed loops may be difficult to detect experimentally.

1.3 Thesis Outline

The following chapter will give an outline of the various experimental apparatus used throughout the study. It is roughly divided into sections relating to the fabrication of the samples themselves, the analysis of the structural properties of the samples, and finally the tools for magnetic characterisation.

In chapter 3 it will be shown that highly regular arrays of bunches of atomic steps can be produced on vicinal Si and Al_2O_3 substrates. It is shown that the dimensions of these steps including height and separation can be determined by appropriate choice of the annealing parameters. In the latter half of this chapter the technique for producing nanowire arrays via glancing angle deposition is described. It is shown that the dimensions of these wire are controlled either by the ordered morphology of the template or by choice of deposition angle and thickness. It is also shown that the technique is applicable to a variety of magnetic materials.

Chapter 4 concentrates on the magnetic analysis of the nanowire arrays through a range of different experimental methods. Particular phenomena that are investigated include the shape anisotropy arising from the high aspect ratio of the nanowires, the effect of temperature on coercivity and its implications for the modes and energy barriers of magnetisation reversal, the effect of interwire separation on interactions between the wires, the effect of ageing on the wire arrays and the resulting appearance of a unidirectional magnetic anisotropy.

In chapter 5 the VLS method for growth of vertical GaAs nanowires is described and a summary is given into what is known about how the various parameters affect the

shape and crystal structure of the wires. Each study in this chapter includes the results of wires grown from ordered arrays of Au droplets produced using EBL as well as a random array of droplets produced by annealing a thin Au film. The ordered arrays of nanowires are discussed and the effect of shadowing by neighbouring wires is examined. The use of ordered arrays of Au nanodots allows for an investigation into the percentage of nanodots which successfully promote wire growth, which is an area that receives very little attention. Other studies include wire growth in As-limited conditions and under As_2 rather than As_4, and the differing shapes achieved are discussed in relation to atomistic processes. A common observation is the effect on the density of defects of the contact angle, which is the angle between the sides of the droplet atop the wire and the solid-liquid interface. It is shown that small droplet diameters are associated with smaller contact angles, and consequently with lower defect densities. High resolution TEM images show that excellent regularity of crystal structure can be achieved in certain conditions.

Chapter 6 deals with random arrays of GaAs nanowires that have been coated in an outer layer of Fe (as well as a subsequent protective capping layer of Au). A detailed investigation using STEM and EDX is described, which illustrates the abilities and limitations of the Fe-coating process. Finally, some preliminary FMR results are shown which indicate an easy axis whose direction corresponds to that of the wire direction.

Chapter 2

Experimental Methods

This chapter will describe the equipment and processes used throughout the entire thesis. The principles of operation will be presented, as well as particular features, capabilities and limitations of the equipment in relation to the experiments. Theory which is specific to the experiment, such as the intricacies of the growth processes, will be found in later chapters. Also excluded from this chapter are precise experimental procedures which vary from one sample to another. These will be found in the chapter corresponding to the experiment. The chapter is divided according to the usual experimental procedure, which is to first fabricate the sample, then check its physical structure and finally carry out magnetic analysis. Accordingly, the following sections each deal with fabrication apparatus, structural characterisation and finally magnetic characterisation.

2.1 Sample Fabrication

The procedures used for sample preparation in the studies that follow are typical thin film fabrication procedures. The first two sections deal with MBE growth of planar magnetic nanowire arrays and vertical growth of GaAs nanowires. The final section simply deals with high temperature annealing of samples which was necessary for certain step-bunching and oxidation procedures.

2.1.1 Vacuum System for Si Annealing and Glancing Angle Depositions

This section refers to the hardware used for the DC annealing of Si samples in order to produce step-bunched templates and for the deposition of materials onto those templates at a shallow angle ($\leq 6\,^{\circ}$). The exact experimental procedures for Si annealing and

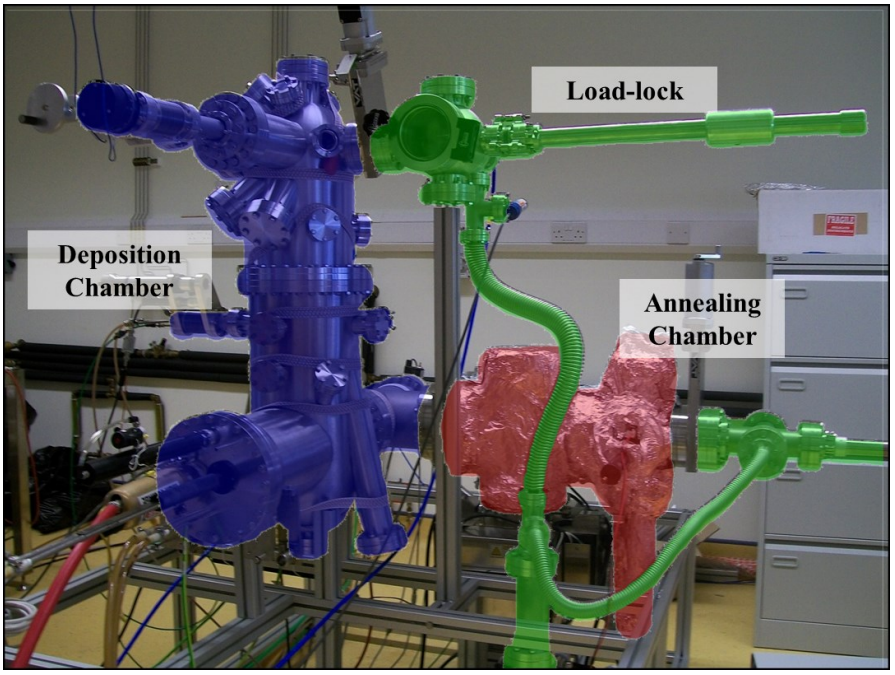


FIGURE 2.1: Chamber for glancing angle deposition and Si annealing

Photograph of vacuum system with false colour added to indicate uses of the different chamber regions. The blue region is used for shallow angle deposition, the red region is the annealing chamber for step bunching of Si templates, and the green region is the load-lock for sample transfer from the laboratory environment.

glancing angle deposition are best discussed following an introduction to the materials involved, motivation, etc. For this reason the experimental procedures are described in later sections (annealing Si samples in section 3.2.3 and the glancing angle deposition in section 3.4) while in the following, the chamber itself itself is described, as well as some details on the use of hardware specific to this setup.

A photograph of the vacuum system used for growth of nanowires and nanoparticles via the glancing angle deposition technique is shown in Figure 2.1 with colour overlaid to indicate the use of the different regions. The main chamber is a custom-designed, electro-mechanically polished, internally welded stainless steel chamber. It is evacuated by means of an ion pump and turbo-molecular pump which also has a rotary backing pump, while the load-lock for sample insertion is evacuated by a smaller turbo-molecular pump with a diaphragm backing pump. The diaphragm backing pump is ideal since it is oil-free and easily serviced. The chamber is divided into regions for annealing and deposition by a pneumatic gate valve. Each of the two regions houses a sample stage with electrical connections to pass current through the sample. Samples are delivered from the load-lock by one of the two magnetically coupled linear drives. As well as several viewports to aid sample manipulation, there is a dedicated strain-free window

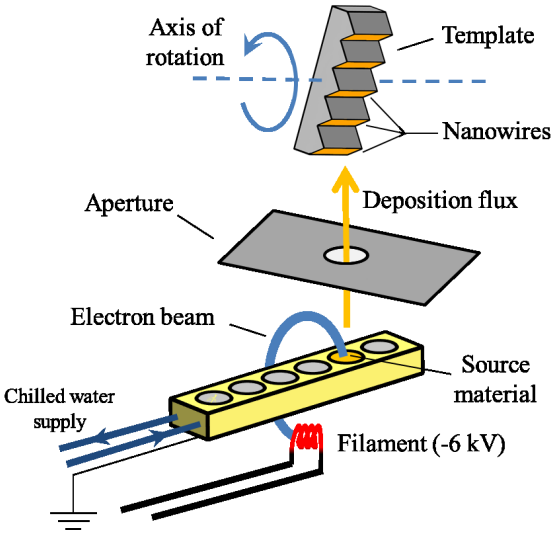


FIGURE 2.2: Glancing angle deposition schematic

Schematic of deposition setup (not to scale). Material is evaporated from a crucible by means of an electron beam. The deposition flux then passes through an aperture before landing on the template. The sample stage can be rotated about an axis as shown, which varies the angle of incidence of the flux.

next to the sample stage for *in situ* optical measurements. Following any exposition to atmosphere, the chamber is baked out at 200 °C for 24 hours to remove moisture and contamination from the chamber walls. Samples are not loaded in the chamber during bake-out to prevent surface contamination.

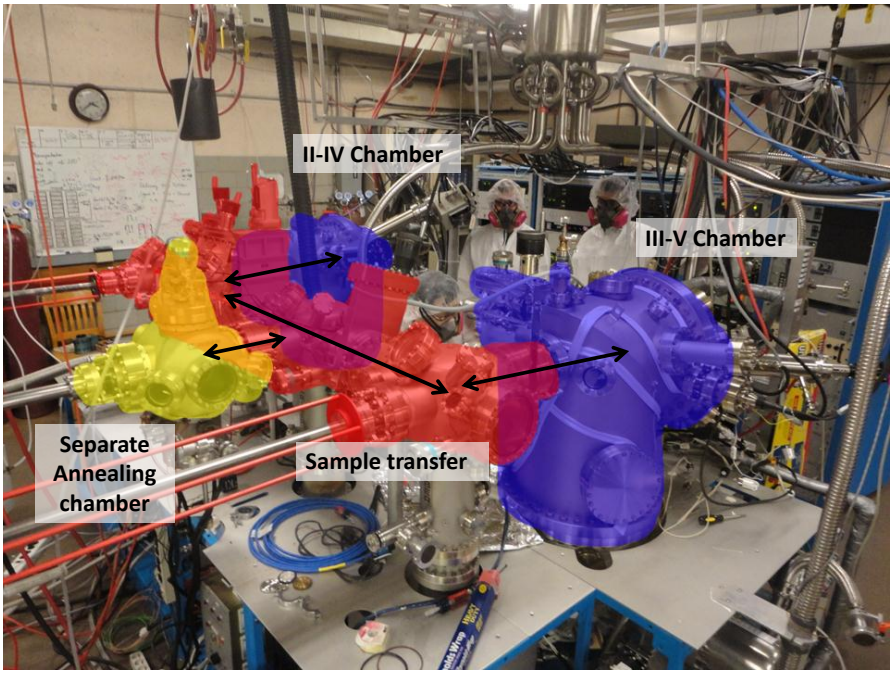
A schematic for the deposition system is shown in figure 2.2. Material for deposition onto the substrate surface is evaporated by means of a 6 pocket e-beam evaporator (Telemark). This consists of a water-cooled copper hearth with a row of 6 crucibles which are filled with the materials for evaporation. Nearby is a tungsten filament which is heated up to produce electrons. A high voltage (6-10 kV) and permanent magnets are used to direct the electrons from the tungsten filament to the material for evaporation. Sweep coils are also used to fine-tune the heating spot and to define a heating pattern. The thickness of material deposited is monitored using a quartz crystal microbalance (Inficon). The sample stage can be rotated to vary the angle of the incident flux with respect to the sample surface with precision of 0.1 °. The source to sample distance is approximately 40 cm, which ensures a low distribution in the angle of the flux with respect to the surface along its length (20 mm).

Prior to sample insertion for glancing angle deposition, step-bunched templates were cleaned using isopropanol in an ultrasonic bath. Once loaded onto the sample stage, the samples were heated for not less than 3 hours at approximately 300 °C to outgas contamination from the surface.

2.1.2 GaAs Nanowire Growth Chamber

A photo of the chamber used for growth of GaAs nanowires via the Vapour-Liquid-Solid mechanism (see chapter 5) with colour overlaid indicating the purpose of the different regions is shown in Figure 2.3(a), and a schematic of this chamber is shown in Figure 2.3(b). This setup consists of two separate Riber 32 MBE (Molecular Beam Epitaxy) chambers connected by a sample transfer chamber some 2 metres in length. The chambers are separately dedicated to the fabrication of II-VI and III-V semiconductor samples. They

(a)



(b)

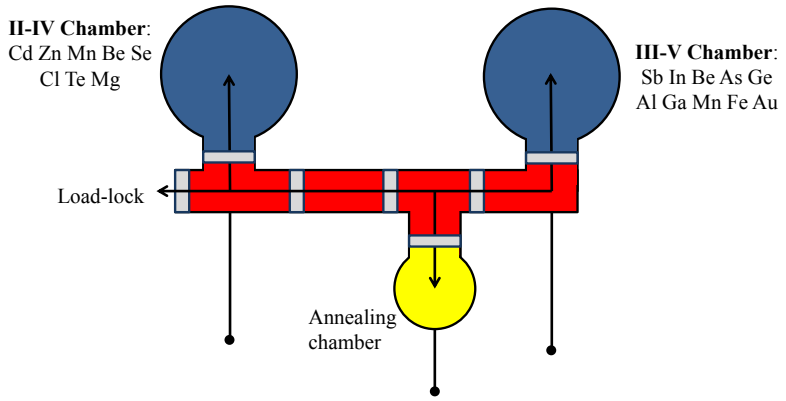


FIGURE 2.3: VLS Chamber

(a) Photograph of UHV chamber for MBE growth with false colour added to indicate the different regions. The blue areas are two Riber 32 MBE chambers for growth of II-VI and III-V materials. They are connected by the sample transfer corridor in red, and in yellow is shown an additional annealing chamber.
(b) Schematic plan-view of the UHV system with materials available for deposition indicated.

are evacuated by a combination of ion, cryogenic and titanium sublimation pumps. In addition, there is a an inner wall around the sample space (but not obstructing deposition flux and sample manipulation) through which liquid nitrogen is circulated. This is designed to trap residual molecules and minimise pressure in the vicinity of the sample. Samples are attached to a molybdenum block using a small quantity of melted indium. When attached to the sample stage the molybdenum blocks can be rotated and heated during deposition. Most of the sources are evaporated by means of Knudsen Cells or K-Cells. These are ceramic pockets that are resistively heated to evaporate the material within them. Fe and Au could also be deposited by means of an e-beam evaporator. Arsenic is introduced into the chamber using an Arsenic Cracker source, which first sublimates solid As and then passes the gas through a heating system whose temperature determines the species of As molecule that will eventually make its way into the deposition chamber. As_4 and As_2 were produced by using a cracker temperature of 600 °C and 1000 °C respectively.

2.1.3 Tube Furnace

Two tube furnaces were used for different purposes during the studies below. A Pyrotherm tube furnace with quartz tube was used for oxidising Si samples prior to their use as a substrate for nanowire deposition. Samples were heated to 830 ° C for 15 hours in the presence of high purity O_2 at atmospheric pressure. This is carried out to form an oxide layer approximately 100 nm thick at the surface of the sample. AFM is used to confirm that this procedure does not affect surface morphology.

A second tube furnace (MTI GSL1600 XL) was used for annealing sapphire substrates. Annealing was carried out at atmospheric pressure and at a temperature between 1000 °C and 1550 °C. Temperature was regulated and calibrated using both S-type and B-type thermocouples. The tube and crucible were both of high-purity alumina to prevent contamination of the sample surface. Cylindrical alumina bricks were used to close the tube openings to further reduce contamination and to allow a more homogeneous temperature profile.

2.2 Characterisation of Sample Morphology

2.2.1 Atomic Force Microscopy (AFM)

An Atomic Force Microscope (AFM) is a device used to precisely examine surface morphology. By conducting a rastered height profile, it provides a 3-dimensional description

of the surface. Two AFM devices are available to the group; a Solver Pro, NT MDT and an Asylum Research MFP-3D. In AFM, a very sharp tip (radius 20 nm or less) at the end of a silicon cantilever is lowered to the surface of the sample to be investigated. The tip experiences van der Waals forces due to its proximity to the surface, and the cantilever is bent slightly downwards as a result. A laser beam in the visible range is directed at the cantilever whose top surface is highly reflective. The reflected laser light is measured using a photodiode, thus measuring the deflection of the cantilever. The tip is rastered across the surface using piezoelectrics to measure the height of the surface at each point. All the AFM imaging in this study was conducted in semi-contact or "tapping" mode. In this mode, the cantilever is made to oscillate by applying an alternating electric field, with an amplitude of approximately 100-200 nm. This amplitude is reduced when the tip is in the vicinity of the sample surface due to van der Waals forces, dipole-dipole coupling and electrostatic interactions. Operating an AFM in semi-contact mode allows concurrent phase imaging. This procedure measures the phase difference of the oscillating tip to the driving signal which is material dependent.

2.2.2 Scanning Electron Microscopy (SEM)

Scanning Electron Microscopy is a very common tool in the area of nanoscience research. It provides a quick and relatively easy method for morphological analysis with some degree of elemental contrast incorporated. It is adaptable to encompass a range of other functions such as quantitative chemical analysis and electron beam lithography (EBL). Standard SEMs such as those used throughout this work (Zeiss Ultra Plus, Zeiss Supra 40, FEI-Magellan 400 FESEM) are able to resolve details as small as 3 nm. A schematic illustrating the design of an SEM is shown in Figure 2.4. An SEM consists of an evacuated chamber in which the sample is mounted, an electron source, a series of lenses and scanning coils to focus the electron flux into a collimated beam and electron detection apparatus. The electrons are produced via Schottky Field Emission at a heated source (usually a tungsten filament) near the top of the electron column. The Wehnelt cap is a cylinder surrounding the electron source at a voltage, known at the extraction voltage, which can be varied to control the emission current. The total voltage can be as high as 30 kV, as determined by the voltage at the anode. The electron beam is focussed using a series of electromagnetic lenses, while the position where it strikes the surface is controlled by electrostatic scanning coils.

The detection system of an SEM is based on the collection of electrons, and in certain modes of imaging also the x-rays, that are emitted from the sample. The resolution of the SEM will depend on the volume of the sample from which these electrons and x-rays will be emitted. This will in turn depend on the total volume of the sample which is

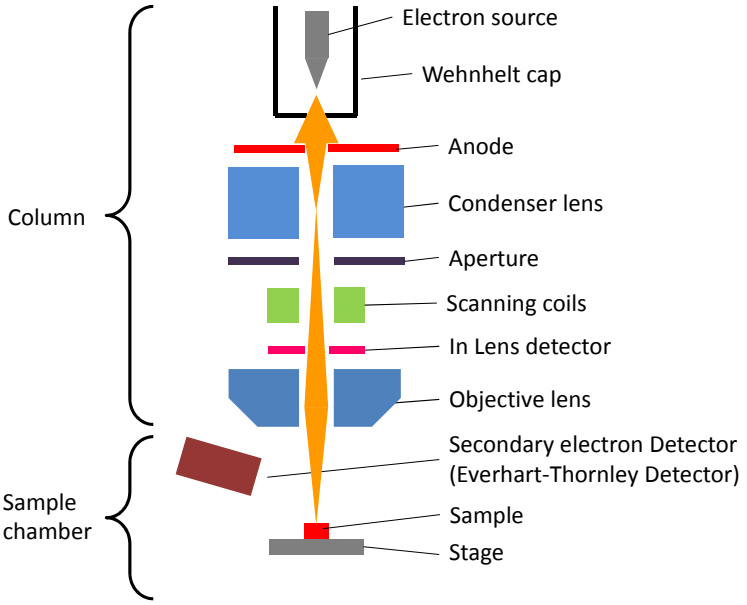


FIGURE 2.4: SEM Schematic

Schematic of a Scanning Electron Microscope showing the various components.

excited by the incident beam, called the "interaction volume", as well as the variety of electrons or x-rays that are being measured. The radius of the effective interaction volume (R_{IV}) will depend strongly on the energy of the incident electrons (E), the density of the material under investigation (ρ), the relative atomic mass (A) and atomic number (Z). the following equation for the radius of the interaction volume was derived by Kanaya and Okayama and is used here as a guide [27]:

$$R_{IV} = \frac{0.0276\, A\, E^{1.67}}{\rho\, Z^{0.89}} (\mu m) \tag{2.1}$$

As can be seen, increasing the voltage will increase the interaction volume resulting in poorer resolution, but in practice a more intense signal is achieved due to the greater number of backscattered and secondary electrons (see below) that can be measured. The signal intensity can also be improved by increasing current, but the drawbacks may include damaging the sample surface either through heating or build-up or electric charge (a common phenomenon especially for poorly conducting samples known as "charging"). These are important concepts to understand when using an SEM and analysing data, because the region being probed may be orders of magnitude greater in diameter than the beam spot size. In the following, the different types of electrons produced and the main detection methods associated with them shall be discussed.

When the incident electrons or primary electrons (PE) (orange beam in figure 2.5) hit the

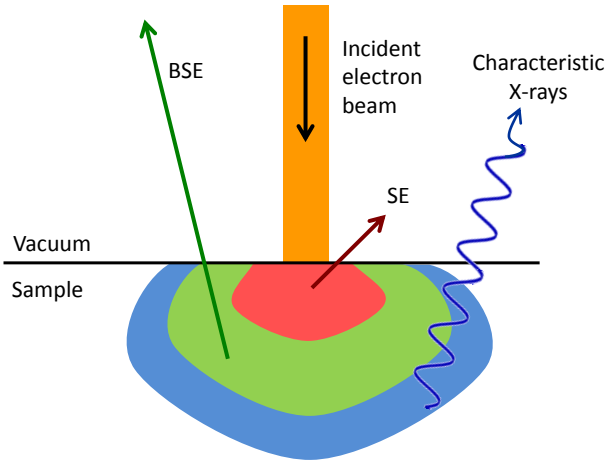


FIGURE 2.5: SEM Interaction Volume

The relative sizes (not to scale) of the interaction volume for different types of electron and x-ray measurement that may be carried out using an SEM. Red indicates the interaction volume for secondary electron, green indicates back-scattered electrons and blue indicates characteristic x-rays.

sample surface a large number of secondary electrons (SE) are produced in a cascade-like fashion due to inelastic collisions of the PE. Their energy is low (typically $< 50\,\text{eV}$) and thus their mean-free path and depth from which they can escape is small (red region in figure 2.5). The spatial resolution is therefore very good. The Everhart-Thornley detector is the most common method of detection for SE. This consists of a metal grid at a positive voltage to attract the low energy SE. The SE are accelerated by the grid towards a solid-state detector. Since the Everhart-Thornley detector is positioned to one side of the sample chamber it draws a larger signal for surfaces that are tilted towards it than those tilted away from it. Thus this imaging mode has an intrinsic slope-dependent contrast which allows good imaging of topographical features.

Some PE hit the sample surface and collide elastically retaining much of their incident energy. These are known as backscattered electrons (BSE). Since they have a high energy they have a high mean-free path, and so the resolution associated with BSE is poorer than for SE (green region in figure 2.5). Since the angle through which BSE are scattered is small they form the bulk of the electrons measured by the "In Lens" detector, which is situated inside the pole-piece of the electron column. The proportion of PE which are backscattered will depend on the atomic mass of the material under inspection, so in many circumstances In Lens detection offers a useful intrinsic elemental contrast.

X-rays are also produced whose energies are characteristic of the elements under investigation. Their measurement is discussed in section 2.2.2.1, but here it is worth mentioning

that the resolution associated with x-ray analysis is relatively poor (blue region in figure 2.5) due to the high energies required to generate the x-rays and the relative ease with which x-rays can escape from deep within the sample.

2.2.2.1 Additional SEM capabilities

- **Electron Beam Lithography (EBL)**

  Electron Beam Lithography is a technique used to "draw" patterns of metal onto substrates with very small dimensions; as low as 20 nm using the latest equipment. Often the patterns are designed to form a circuit enabling nanoscale conductivity measurements, but may also be used to design a grid of similar shapes such as the nanoparticle arrays discussed in chapter 5. EBL begins with spin-coating a thin layer (≈ 10 nm) of "resist" (polymer liquid) onto the sample surface, which is then set by baking the sample at 180 °C. The key feature of the resist (Polymethyl methacrylate, PMMA) is that it will degrade (the polymer chains are broken down) when exposed to the electron beam. The SEM is used to expose regions of the surface to the electron flux in an automated manner according to a pattern designed by the user. The degraded regions are then removed by rinsing the sample in a solvent known in this procedure as the "developer" (Methyl isobutyl ketone, MIBK). A resist which is removed in regions exposed to the beam, such as PMMA, is known as a 'positive' resist. 'Negative' resists also exist, wherein the only regions that remain post-development are those that are exposed to the beam during exposure. Following development, a layer of the desired film is then deposited over the entire sample surface, including regions covered and uncovered by the remaining resist. The rest of the resist is removed using acetone, leaving the deposited layer attached only in regions where the resist had been etched away.

- **Energy Dispersive X-Ray Spectroscopy (EDX)**

  In this technique a high voltage electron beam either rasters the surface or just scans a single line or point according to the user. At the same time an x-ray detector in the sample chamber records x-ray spectra specific to each point as it is being scanned. The electron beam ejects inner electrons from the atoms under investigation and outer electrons will subsequently drop down to fill the hole that has been created. An x-ray photon having an energy equal to the difference of the two shells is emitted and measured by the detector. The software is able to characterise the proportion of elements present according to the relative intensities of the characteristic x-ray peaks measured. Due to the fact that many elements will have overlapping peaks and to reduce computation time, the user is usually

required to specify which elements they expect to see in their sample. The PE must have sufficient energy, greater than the "critical excitation energy" needed to eject the inner electrons, in order to make each characteristic peak accessible. In practice the acceleration voltage of the PE is as large as possible, often some 20 or 30 kV in order to maximise the intensity of each peak. This in turn means that the interaction volume is several times greater in diameter than the beam spot size, meaning that resolution is negatively affected.

2.2.3 Transmission Electron Microscopy (TEM)

TEM, like SEM, is a ubiquitous tool in the area of nanoscience research. It can be used to provide images with sub-nanometre resolution and can resolve the crystal structure of crystalline solids. Since it relies on electron transmission, this technique is applicable only to samples that are sufficiently thin for a perceptible proportion of the incident electrons to pass through. The sample may be cut into a narrow wedge using a FIB (Focussed Ion Beam) or if the sample under investigation consists of a collection of nanoparticles then these may be dispersed onto a special grid which is almost transparent to the incident electrons. The TEM is operated at high voltages (≈ 300 kV) to maximise electron transmission and resolution. Like the SEM, the TEM consists of an electron source, a column with lenses and focussing apparatus and sample stage. However, the voltages involved are much larger and since transmitted electrons are measured, the detection equipment lies beneath the sample holder. Another key difference, as mentioned above, is that the electron beam hits the sample surface not as a finely focussed point but as a column that illuminates the entire region being imaged at once. The most common imaging mode is Bright-Field imaging, wherein electrons that have a very small angle of scattering are detected. In this mode empty space appears bright (hence the name) while thicker regions appear darker.

One of the key abilities of TEM is diffraction analysis. In this mode, the magnetic lenses are adjusted such that the back focal plane of the beam lies on the detection apparatus rather than the imaging plane. This allows the user to view the diffraction pattern from the sample, which contains important information such as the symmetry of the system and the separation between planes of atoms in the different directions. Typically diffraction analysis is used in tandem with bright-field imaging so that images can be taken along directions of high symmetry. For samples greater than a few monolayers it is only along such directions that one can identify atomic-scale structure such as individual planes.

2.2.4 Scanning Transmission Electron Microscopy (TEM)

Both SEM and TEM microscopes may offer STEM mode. As the name suggests, this tool deals with electrons that pass through the sample rather than those that are scattered backwards from the surface. Since this procedure is very similar to the conventional Transmission Electron Microscope (TEM) which is discussed above, here just the main difference distinguishing the two will be outlined, namely that while the TEM illuminates the entire region being imaged with a column of electrons, in STEM the surface is rastered by a point-like beam of electrons. STEM mode on a SEM is useful since it can be used to provide some information on the structure of the sample below the surface. On a TEM, the resolution is usually worse when switching to STEM mode, but doing so allows the user to carry out high resolution EDX linescans.

2.2.5 Statistical Analysis of Nanoparticle Dimensions

When nanoparticle arrays were grown with slightly different growth parameters resulting in variations in their shape and separation, it was necessary to quantify the findings by means of an accurate, statistical analysis of specific dimensions of the nanoparticles. Likewise, for the GaAs NW arrays, a quantitative analysis was needed to study the effect of growth conditions on the size and shape of the resulting NWs. The conventional approach to this task would be to convert an image to a binary black and white format based on some threshold parameter and then use software to automatically identify shapes and distances. However, this is not well-suited to more complicated images where human judgement is required to identify features and where only a proportion of features are unobscured and suitable for measurement. In order to carry out these surveys, AutoCAD software was used (AutoCAD 2013, Autodesk). While this software is primarily intended for product design and construction planning, its huge array of tools makes it suitable for image analysis. Images taken using the SEM were opened in AutoCAD and scaled to size so that measurements could easily be read off. Then lines, circles or ellipses are drawn over the features of interest until a statistically significant quantity were included. Figure 2.6 shows a screenshot of the program being used to measure the lengths of cone-shaped GaAs NWs, as well as the diameter of their tips and the angle near the top of the cone.

The *Extract Data* tool was then used to isolate specific dimensions of the objects drawn and convert these to a data file. Separate code was written in C++ to perform tasks such as generating distributions of the measurements, calculating inter-particle separations and finding the density of wires or dots per unit area.

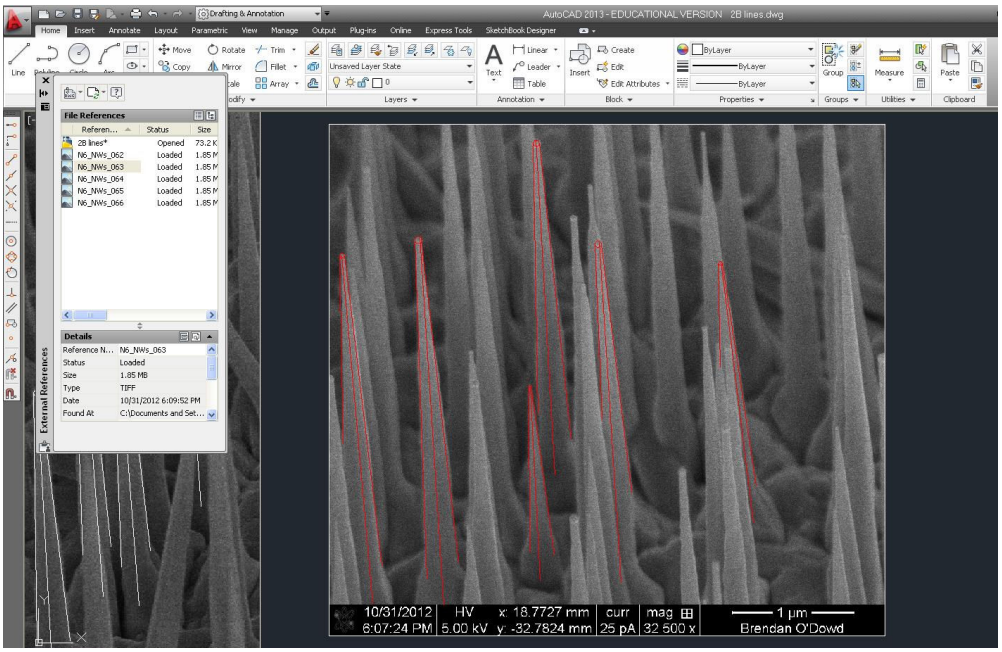


FIGURE 2.6: Statistical Analysis using AutoCAD

Screenshot of AutoCAD software being used to specify multiple features in an SEM image of an array of GaAs NWs. The dimensions of the features may be extracted to a data file using the software for quantitative analysis, which can also correct for shortening caused by the viewing angle as in the case above.

2.3 Magnetic Characterisation

2.3.1 Vibrating Sample Magnetometer (VSM)

A vibrating sample magnetometer (PPMS, Quantum Design) was used for magnetic analysis of samples at temperatures ranging from 300 K to 4 K. The device consists of a non-magnetic sample holder vertically inserted into the centre of a superconducting magnet which can produce a vertical magnetic field of up to 14 T. A motor at the top of the PPMS vibrates the sample causing it to induce a voltage in two pick-up coils which is proportional to its magnetic moment. In this way the magnetometer can measure magnetic moment as a function of temperature and applied field. While the use of a superconducting magnet is advantageous in its ability to produce very large fields, a disadvantage associated with it is that it takes up to a minute to reach and stabilise at the desired field value. This renders it unsuitable for certain types of procedures such as sample demagnetisation and remanence measurements where rapid changing of the magnetic field is required.

2.3.2 Alternating Gradient Field Magnetometer

In short, while a VSM causes the sample to oscillate and measures the induced field, the AGFM applies an oscillating gradient field and measures the resultant vibration of the sample. Again a magnet applies a fixed field on the sample (fixed in the timeframe of the individual measurement), although in this case an electromagnet with maximum field of 1 T is used rather than a superconducting magnet. The alternating gradient field is produced by smaller coils positioned at the pole pieces of the electromagnet. This exerts a force $\mathbf{f}$ on the sample according to $\mathbf{f} = \nabla(\mathbf{m} \cdot \mathbf{B}_0)$ where $\mathbf{m}$ is the magnetic moment and $\mathbf{B}_0$ is the applied magnetic field. The frequency of the oscillating gradient field is chosen to be equal to the mechanical oscillating resonance frequency of the sample together with its non-magnetic holder.

The disadvantages of this system are that it is limited to room temperature measurements and that the maximum field is only 1 T. However, since the applied field can be changed rapidly there are several advantages to the AGFM. The first is that samples can be demagnetised by alternating the direction of the applied field, starting from a value large enough to saturate the sample and finishing at zero applied field with as many intervening steps as practically possible [28]. This process is known as AC demagnetisation. In effect, this process divides all of the domains into two groups with magnetisation pointing in opposite directions according to the magnitude of their switching field. By making the increments of the decreasing field magnitude small enough the end result is a practically random orientation of all the domains.

Another advantage is the potential to carry out additional modes of measurements, two of which are outlined below.

2.3.2.1 Addition AGFM Measurements

- **Remanence Measurements**

  There are two types of remanence measurement which are both necessary for the study of interwire interactions. In order to measure the first type, Isothermal Remanence Magnetisation, the sample must first undergo AC demagnetisation as described above. A field H is applied and removed shortly (≈ 1 second) afterwards. The remanence measured is then the Isothermal Remanence Magnetisation $M_R(H)$. This is carried out as a function of increasing H. The sample does not need to be demagnetised between increasing measurements of H since domains with switching field greater than previous values of H are unaffected. The second type of remanence measurement is DC Demagnetisation Remanence. First the

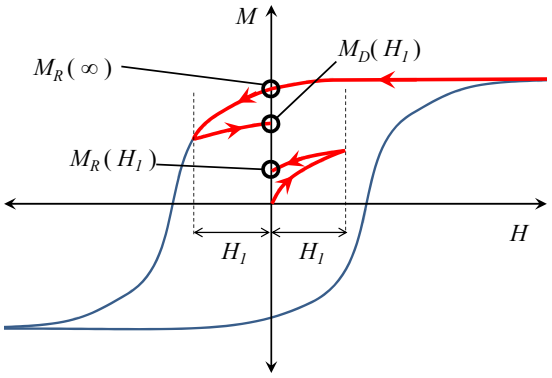


FIGURE 2.7: Schematic for finding $M_R(H)$ and $M_D(H)$.

Here a hysteresis loop for a hypothetical system is shown in blue. Also shown are curves in red which illustrate how M_R and M_D are experimentally found for an applied field H_1.

sample is saturated in (say) the $+x$ direction. Then a field H is applied in the $-x$ direction and removed, whereupon the DC demagnetisation remanence, $M_D(H)$ is measured. Figure 2.7 illustrates how M_R and M_D are found on an $M-H$ graph for a hypothetical ferromagnetic system.

Also shown in this figure is the remanence for infinite applied field (or in practice a field high enough to saturate the sample). This is labelled '$M_R(\infty)$' and is in actuality just what is normally understood as the remanence, and is, of course, equal to $M_D(\infty)$. Normalised versions of M_R and M_D are defined as follows:

$$\begin{aligned} m_R(H) &= \frac{M_R(H)}{M_R(\infty)} \\ m_D(H) &= \frac{M_D(H)}{M_R(\infty)} \end{aligned} \tag{2.2}$$

- **First Order Reversal Curves (FORCs)**

  To measure a first order reversal curve the sample is first saturated in, say, the $+x$ direction. Then the applied field is reduced to a value H_a known as the "reversal field". The magnetisation is then recorded as the applied field, now labelled H_b is increased from H_a back up to saturation. This is repeated for values of H_a usually ranging from close to positive and negative saturating fields. A schematic illustrating how a single FORC measurement is made for a hypothetical magnetic system is shown in figure 2.8.

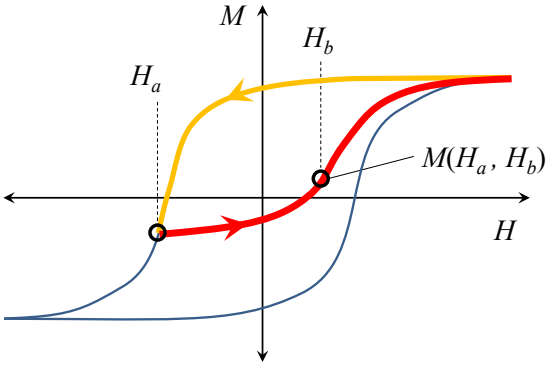


FIGURE 2.8: Schematic for finding FORCs.

A hysteresis loop for a hypothetical system is shown in blue. The orange curve illustrates the applied field being reduced from a saturating field to the reversal field H_a. While this curve is part of the procedure, it is not part of the measurement, and recording this curve is not necessary. The red curve shows a single first order reversal curve (FORC), which measures the magnetisation $M(H_a,H_b)$ as the applied field H_b is increased from H_a back up to saturation.

2.3.3 Ferromagnetic Resonance (FMR)

Room temperature FMR measurements of Fe nanowire arrays and Fe-coated GaAs nanowires were carried out using FMR (Bruker EMX, operated at 9.47 GHz) at the University of Notre Dame, Indiana, USA. Further analysis of the Fe nanowire arrays was conducted at the Institute of Magnetism at the National Academy of Sciences in Kiev, Ukraine. These measurements were also carried out at room temperature using an X-band (9.44 GHz operating frequency) ELEXSYS E500 spectrometer, which includes an automatic goniometer for sample rotation.

The mathematical background for the role of the FMR as a probe of magnetic anisotropy is given in section 4.1.1.1. Here is given a qualitative discussion of its operation for use as a probe of magnetic anisotropy and a description of the hardware involved. A schematic of the experimental setup is shown in figure 2.9. The sample is loaded into a quartz tube, preferably oriented with one of its principal axes parallel to the tube axis so that the resonance field can be probed as the sample is rotated about a known axis. The tube is filled with He gas, sealed and inserted into its holder between the poles of the electromagnet. The magnet applies a static field H_0, where 'static' implies that it is fixed for the duration of the measurement of a single data point (< 1 second). The magnetic moment of magnetic particles in the sample will precess with a frequency called the Larmor Frequency, which is proportional to the applied field. The applied field is increased from 0 to 1.2 T. For some value of applied field the Larmor frequency will be equal to the frequency of the incoming microwave radiation, and the absorption will increase dramatically. Of course the net field experienced by the magnetic moments is

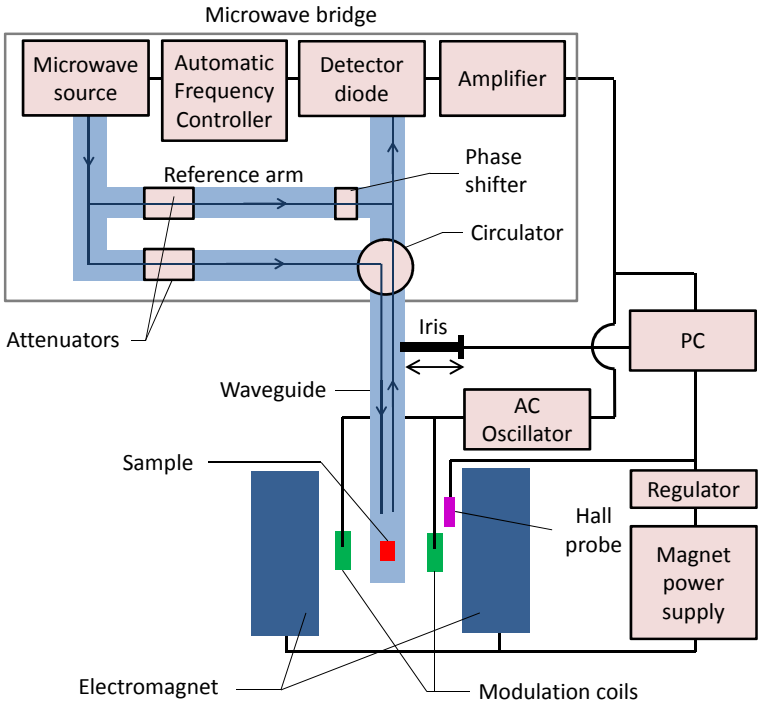


FIGURE 2.9: FMR Setup Schematic

not just the applied field but also included a contribution from the internal demagnetising field, H_d. The magnitude of the demagnetising field depends on the demagnetising factors of the sample, and thus the resonance frequency will depend on the magnetic anisotropy of the system. In addition to the 'static' magnetic field, there is a time-varying field of lower amplitude produced by modulating coils so that the reflected microwave amplitude is modulated at the same frequency. The frequency of this modulating field is usually 100 kHz. The signal to noise ratio is improved by reading the diode current with an amplifier locked in to the AC oscillator. In addition, this causes the output signal to be the derivative of the actual absorbance spectrum. While it can be easily integrated, it is often easier to accurately extract data such as absorption peak width, from the differentiated signal provided.

The microwaves are guided from the klystron source to the sample in the FMR cavity via a waveguide. A certain proportion is reflected and makes its way back to a detector diode. A microwave signal is also sent to the detector diode along a "reference arm" within the microwave bridge. This is done to provide sufficient power to the diode so that it is operating in its linear regime (at low power levels the diode operates as a square law detector, which is not optimal). Attenuators along the main waveguide and the reference arm control the relative power along each path, while a phase shifter ensures that both signals are in phase when they arrive at the detector. An "iris" is a screw which controls the opening from the waveguide to the cavity, thereby adjusting the impedance so that

the cavity is critically coupled with the waveguide. Critical coupling means that the power transfer between the microwave source and the sample cavity is maximised.

Chapter 3

Template Preparation and Glancing Angle Deposition

This chapter covers the fabrication procedure for ordered arrays of nanowires and nanoparticle arrays, which consisted of two key procedures. The first is the preparation of a step-bunched substrate, which was achieved by annealing vicinal silicon or sapphire (α-Al_2O_3). These procedures are outlined in sections 3.2 and 3.3 respectively. In the case of the preparation of sapphire templates, the procedure and apparatus are almost identical to that used in a study by Verre *et al.* [29] and so some representative results will be shown rather than an in-depth study into the dependencies of the various parameters.

The second key procedure is the deposition at glancing angle onto the step-bunched templates, which is described in section 3.4. As shall be shown, the advantages of this approach include its ability to define a well-ordered nanowire array with good control over the width, separation and thickness of the wires, and its applicability to a range of choices for nanowire material as well as substrate material.

3.1 Background

The fabrication and study of nanowires is a very wide and active area of research, with a myriad of proposed applications. As mentioned in chapter 1, the study of magnetic nanoparticles is important for the hard disk dive (HDD) industry since it provides a means for examining and overcoming the obstacles associated with device minimisation, as well as exploring the range of exciting effects at the atomic level that can be employed in future designs. Other areas with application potential include domain wall logic devices [20, 21], magnetic sensing [24], devices for high-frequency signal processing [23],

spin-polarised electronics [22] and devices employing giant magnetoresistance (GMR) [30].

The ubiquity of Si for production of electronic devices makes it attractive for use as a template for growth of nanowires for two reasons. Firstly, because of the existing knowledge and experience within the scientific community of working with and understanding this material, and secondly due to the potential for bridging the gap between prototype and device by using the existing substrate of choice of the electronics industry. While similar templates may be produced using oxides or metals, these specific advantages make Si attractive for use as the underlying material for our arrays.

There is much interest in producing magnetic nanowires that have a width on the order of a few nanometres, but they should also be sufficiently thick in order to overcome superparamagnetism at room temperature if they are to be of use in practical applications. Superparamagnetism is when a ferromagnetic particle is small enough for thermal effects to cause its magnetisation to randomly flip [1][31, 32]. This will be discussed in more detail in section 4.1.3, but for now it suffices to say that the wire thickness will typically need to be on the order of nm in order to exhibit ferromagnetic behaviour at room temperature, and this is a significant challenge for various methods of nanowire fabrication.

Production of arrays of nanowires can be done using bottom-up or top-down approaches. A typical top-down approach is Electron Beam Lithography (EBL). Feature size using EBL is limited by beam spot size, around 20 nm diameter for most up-to-date devices. EBL is also a relatively slow and expensive process.

Bottom-up approaches, with the possibility of smaller feature size and greater throughput, are an attractive option. A fast and cheap self-assembly method for generating nanowire arrays would potentially allow for an exploration of the key dimensions and how they affect the behaviour of the overall system. Findings from such experiments are of academic importance since it provides an avenue for exploration of nano-scale magnetic processes, and from an industrial perspective it is also useful since it presents a 'playground' in which to quickly and easily probe certain dependencies. Magnetic nanowire arrays of varying wire/stripe width ranging from single atom (1-D atomic chains) to several hundred nm are reported on a variety of templates. Vertical pillars of Fe, Ni and Co have been formed in porous alumina [33–38]. In this approach, alumina is anodized in an acid electrolyte which results in highly regular vertical cavities throughout the alumina layer. A similar array of vertical pores can be produced by exposing polycarbonate films to a beam of particles which leave tracks in the film. These tracks

[1]Strictly speaking, the definition of superparamagnetic depends on the measurement time. For magnetic recording applications the average flipping time should be on the order of decades.

can be widened to create cylindrical pores by etching the film. These films are known as 'track-etched membranes' [39–43]. Both anodized aluminium oxide (AAO) nanopore arrays and track-etched porous membranes are commercially available [2][41]. The pores of the arrays are filled via electro-deposition using aqueous salt solutions of the wire material. Perpendicular magnetic anisotropy (out-of-plane) has been demonstrated using this approach. For in-plane anisotropy, fabrication of planar arrays of nanowires is required.

Glancing angle depositions have been used in the past to create nanowires inclined at an angle to the substrate. Combined with a rotating substrate, this technique can be used to produce vertical spirals with interesting optical properties [44–46]. However, unless ordered arrays of nuclei are produced (e.g. by EBL), the locations of the resulting nanowires will be random.

With regard to the fabrication of planar arrays of nanowires, deposition onto vicinal substrates has been a very attractive method in the past. Many of the procedures rely on the preferential attachment of deposited material to the groove of the step, which is at a lower energy due to reduced surface area. Depending on the materials used for the substrate and adsorbate, elevated temperatures may be needed to acquire the necessary diffusion to allow the adsorbate to travel to the step edge; otherwise islands of adsorbate on the terraces occurs. The material gathered at the edge can be the nanowires themselves, or it can form a template for subsequent nanowire deposition. Using this technique, Gambardella *et al.* succeeded in producing arrays of monatomic Co nanowires on a vicinal Pt substrate [47]. Their magnetic properties were investigated at 10 K using XMCD. Using vicinal W(110) substrates, Elmers *et al.* also grew monatomic nanowires of Fe [48]. These wires were found to have an easy axis of magnetisation in-plane, perpendicular to the wire direction, but again, these were not ferromagnetic at room temperature. Cheng *et al.* went further, depositing Fe nanowires that were as thick as four monolayers [49]. The ferromagnetism of these wire arrays was studied *in situ* using surface magneto-optical Kerr effect (SMOKE) at 35 K. They were found to have an easy axis which pointed out of plane for thin wires but with greater thickness (> 2 monolayers) the easy axis switched to a direction in-plane and parallel to the wires' axis. Fruchart *et al.* deposited Fe on vicinal Al_2O_3 (with an intermediate layer of Mo or W) and then annealed the sample, resulting in magnetic nanowire arrays that were ferromagnetic at room temperature [31]. However, the fluctuation of wire width is large (20-200% of average wire width). Glancing angle deposition of Fe and Nb onto faceted

[2] AAO templates are available from companies such as Enable IPC, SmartMembranes GmbH, and SPI Supplies ('Anopore'). Track-etched membranes are available from Whatman, part of GE Healthcare, under the trade name Nuclepore, and also from Maine Manufacturing and Poretics.

Al_2O_3 was carried out by Huth *et al.*, though the magnetic properties of the nanowires were not investigated [50].

A more elaborate technique described by Lin *et al.* involves epitaxial deposition of CaF_2 onto vicinal Si (111) [51]. The CaF_2 self-organises on the Si (111) leading to periodic arrays of narrow rectangular trenches at the step edge. Iron is then deposited into the trenches to produce nanowires as narrow as 3nm with 15nm spacing.

3.2 Si Template Preparation

3.2.1 Si (111)

Bulk crystalline Si has a diamond cubic crystal structure with a lattice spacing of 5.431 Å and a bond-length of 2.352 Å. The two most common surfaces of Si produced for application purposes are the (001) and (111) planes. Because of the stringent demands of the semiconductor industry, these planes are commonly made to a very high standard in terms of the level of control over orientation and density of defects. The unit cell of Si is shown in figure 3.1. The (001) and (111) planes are indicated by the pink square and light grey triangle respectively.

No matter how careful the preparation procedure, no surface will be a perfectly uniform plane on a macroscopic scale and there will always be some atomic steps. It is therefore attractive to work with high symmetry planes such as (001) and (111) which have an intentional miscut at a small angle in some direction. This, in principle, will yield rows of atomic steps which we seek to manipulate. For Si (001) miscut in the ⟨110⟩ directions

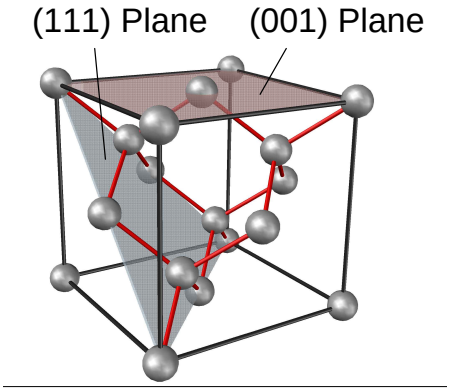


FIGURE 3.1: Unit cell of Si.

The unit cell of Si, with the (111) plane and (001) planes indicated by the light grey triangle and the pink square respectively.

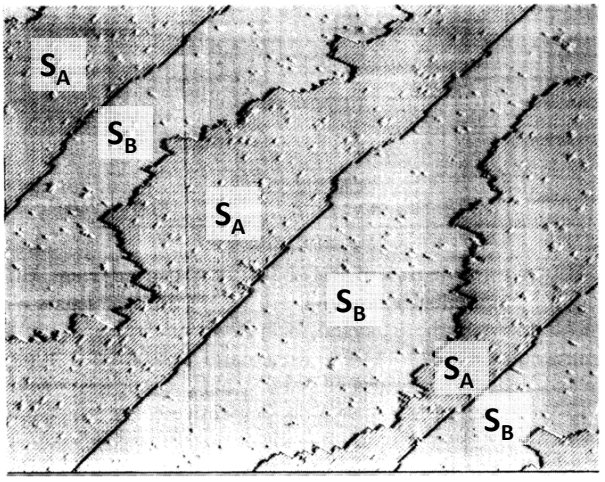


FIGURE 3.2: Atomic steps on Si(001)

STM image of atomic steps on Si(001) miscut in the [110] direction taken from Swartzentruber *et al.* [52]. The surface steps down from top left to bottom right. Labels have been added to indicate the species of the dimers present on the surface. As can be seen the S_A dimer regions have straight step edges while the S_B dimers end in rough step edges.

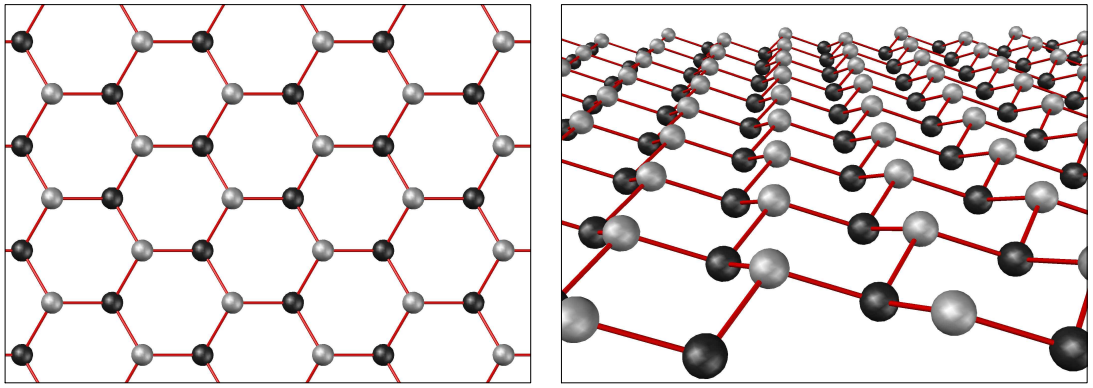


FIGURE 3.3: The (111) surface of Si

Two views of the (111) surface of Si. On the left is a top-down view and on the right is a perspective view at an angle between the $[\overline{1}11]$ and $[1\overline{1}0]$ directions. In both images the $[11\overline{2}]$ direction is to the left. The darker dots are slightly below the (111) surface and have no dangling bonds, while the paler dots are slightly raised from the (111) and have one dangling bond each.

this results in 2 subsets of 2×2 dimer reconstructions oriented either parallel (so-called S_A dimers) or perpendicular (S_B dimers) to the miscut direction [52]. Unfortunately, the S_B subset produces rough step edges as shown in figure 3.2 (which is taken from Swartzentruber *et al.* [52]). This makes the (001) surface unattractive for use as a step-bunched template.

A schematic of the atomic (111) surface is shown in figure 3.3. This surface is composed

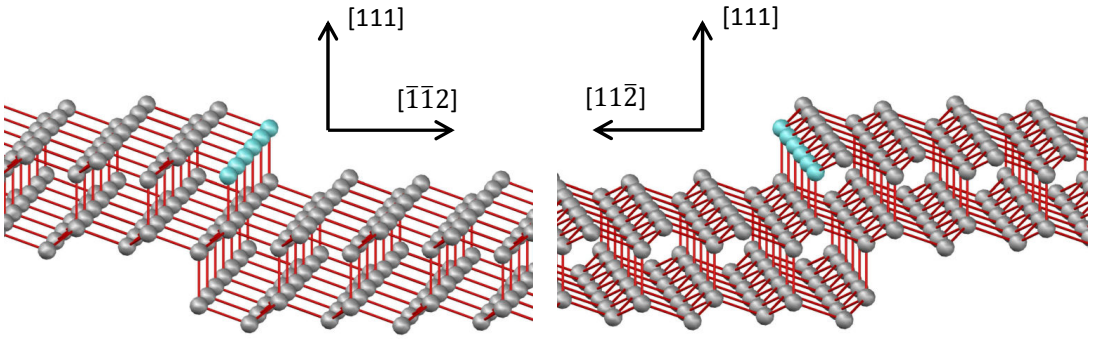


FIGURE 3.4: Single atomic steps on Si (111)

The (111) surface of Si with a single (un-reconstructed) atomic step caused by a miscut of the crystal in the [11$\bar{2}$] (left) and [$\bar{1}\bar{1}$2] (right) directions. The step-edge atoms (coloured in blue) have a different termination and number of dangling bonds in each case.

of two subsets of atoms which make up two planes at slightly different distances along the [111] direction. The paler dots are higher and have one dangling bond each, while the darker dots are slightly lower and have no dangling bonds. This is important since it implies that the symmetry of the surface is not six-fold as it appears from directly above but three-fold.

Figure 3.4 shows two single atomic steps caused by a miscut in the [11$\bar{2}$] (left) and [$\bar{1}\bar{1}$2] (right) directions. It is important to note that these miscut directions are not equivalent. We see that the chemical bond configuration is different for the step edge atoms (highlighted in blue) in each case. The sample miscut in the [11$\bar{2}$] direction has one dangling bond per step edge atom while there are two dangling bonds per edge atom in the [$\bar{1}\bar{1}$2] case.

The bulk truncated (111) face reconstructs in a 2×1 dimer pattern. Above 670 °C however, it will adopt the 7×7 Takayanagi reconstruction, sometimes known as the Dimer-Adatom-Stacking-Fault (DAS) model, as shown in figure 3.5 [53]. Since Si is commonly deoxidised at 800 °C or above, this is often the reconstruction that is dealt with experimentally. It is composed of two triangles with holes at the corners and divided by dimer rows. The triangle on the right hand side of figure 3.5 has a stacking fault (faulted half) while the triangle on the left does not (unfaulted half). Step edges running through the middle of the 7×7 unit cell (along the dimer rows shown in blue in figure 3.5) are strongly stabilized by the reconstructed surface pattern. These step edges correspond to the [1$\bar{1}$0] direction, and can be exposed by choosing a small miscut in the [11$\bar{2}$] or [$\bar{1}\bar{1}$2] directions. These step edges will be terminated, respectively, by the unfaulted and faulted halves of the 7×7 unit cell, and as a result the behaviour of the surface depends on the choice of miscut direction.

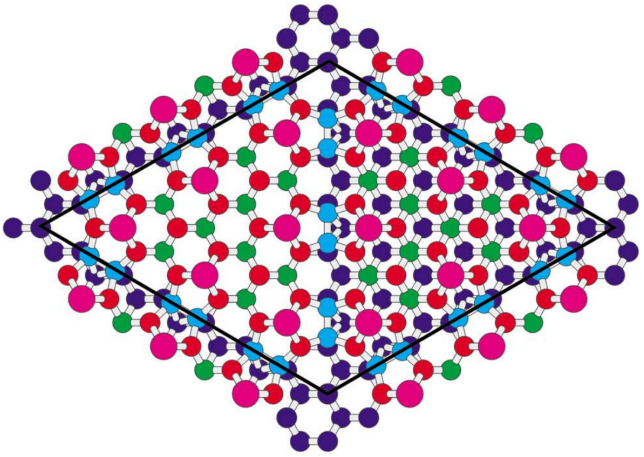


FIGURE 3.5: Si 7×7 reconstructed surface unit cell

The unit cell of the 7×7 reconstructed surface of Si (111). The left hand side is the unfaulted half while the right hand side has a stacking fault (faulted half). The $[11\bar{2}]$ direction is to the right. This image is taken from a publication by D.P. Woodruff in the journal *Surface Science*, 2002 [54].

Atomic steps caused by a miscut in both the $[11\bar{2}]$ and $[\bar{1}\bar{1}2]$ directions can be induced to group together in so called "step bunches" by heating to temperatures above 850 °C. Above this temperature the 7×7 reconstructed (111) surface becomes a 1×1 disordered phase [55–57]. In the case of miscuts towards the $[\bar{1}\bar{1}2]$ direction, however, triple steps are more favourable for miscut angles greater than 1.5 ° [58], and so for controlled step bunched vicinal surfaces with miscuts in excess of 1.5 ° the $[11\bar{2}]$ miscut direction is the more favourable option.

3.2.2 Step Bunching on Si (111)

The first study to observe and identify step-bunching on vicinal Si (111) was carried out by Latyshev *et al.* in 1989 [59]. In a STM study of miscut Si (111), they noticed that the atomic steps could be caused to bunch together by passing a DC current through the sample. They identified some of the temperature dependencies which would be examined in further detail in the following years [60, 61]. They noted that in Regime I, bunches containing a greater number of steps moved more slowly, and that monatomic step velocity is proportional to the distance between the steps.

The fact that studies are still regularly being published about fundamental aspects of step bunching on Si is testament to the complexity of the problem. There is a rich variety of different regimes strongly dependent on temperature, electric field, miscut angle and current direction. It is this zoo of regimes that has made it very difficult to

TABLE 3.1: Si (111) Step-Bunching Temperature Regimes

Occurrences of step bunching on Si (111) miscut in the $[11\overline{2}]$ direction for 4 different temperature regimes. "SB" indicates that step bunching occurs for the specified current direction and temperature, while "R" stands for a Regular array of atomic steps. This table is adapted from Yagi [61] who compiled it from experiments carried out to that point.

Regime	I	II	III	IV
Temperature (°C)	850 - 950	1040-1190	1200-1300	>1300
Current in step-up direction	*R*	SB	*R*	SB
Current in step-down direction	SB	*R*	SB	*R*

formulate an all-encompassing theory, and so despite significant interest and examination, no conclusive model has been found which satisfies all the observed phenomena. In this work we concern ourselves solely with step-bunching effects on Si (111) miscut in the $[11\overline{2}]$ direction with current passing perpendicularly to the step-edges. We call the two current directions "step-up" and "step-down" referring to current in the $[\overline{1}\overline{1}2]$ and $[11\overline{2}]$ directions respectively. In these cases there are four temperature regimes as follows: Regime I from 850 - 950 °C, Regime II from 1040 - 1190 °C, Regime III from 1200 - 1300 °C and Regime IV from 1300 °C upwards. These regimes are summarised in table 3.1. Step-bunching can occur with a step-up current in Regime II and IV and with a step-down current in Regimes I and III. When the current is applied in the opposite direction to that described here for a specific regime and the miscut angle is less than 1 °, we get a regular array of single atomic steps.

In all regimes it is assumed that the energy of an atom will depend on the number of its bonds which are saturated. A simple cubic model is introduced in figure 3.6 to describe this idea. A single atom in the system is represented by the red cube. The images (i)-(vi) are arranged in order of increasing number of exposed sides, which corresponds to an increasing number of dangling bonds and therefore increasing free energy. In figure 3.6(i) the atom is encapsulated within the solid and is at its lowest possible energy state. In figure 3.6(ii) the atom forms part of the surface of the crystal and in 3.6(iii) it forms part of a step edge which is running across the crystal surface. In 3.6(iv) the atom is located at a kink in the step edge, while in 3.6(v) it is attached to a step edge but exposed on 4 sides. Finally a solitary atom on the surface of the crystal is shown in 3.6(vi). By supplying energy to the atom, typically in the form of heat, it may move between these 6 states, with a preference for moving to a lower energy state as described by figure 3.6. The supply of heat will also cause the desorption of atoms from the surface, which may be considered a 7^{th} state having the greatest energy.

Since there is an electric field, the surface atoms will experience a force depending on their "effective charge" $Z_{\text{eff}}\, e$ and the electric field E:

$$F = Z_{\text{eff}}\, e\, E. \tag{3.1}$$

The velocity of the adatoms is called the drift velocity, v_{d}, and is related to the force via a surface diffusion coefficient D_{S} as follows:

$$v_{\text{d}} = \frac{D_{\text{S}} F}{k_B T} \tag{3.2}$$

The effective charge can be thought of as the sum of two terms, one due to electrostatic interactions, Z_{el}, and the other due to the "wind force" applied to the atom by the flow of charge carriers, Z_{w}. The competition between these two components will determine the net sign of Z_{eff} and the direction of travel of the adatoms. One might imagine that it is this effective charge that is changing values at the regime temperature boundaries that gives rise to the appearance and absence of step-bunching, and this has been examined theoretically by Kandel *et al.* [62]. An experimental study was carried out by Degawa *et al.* [63] who etched a trench into the vicinal (111) surface and examined its profile following DC current anneal. They found that the drift direction was parallel to the current direction in regimes I, II and III, suggesting that while Z_{eff} might change in magnitude, it does not change in sign as a function of temperature in the regimes studied.

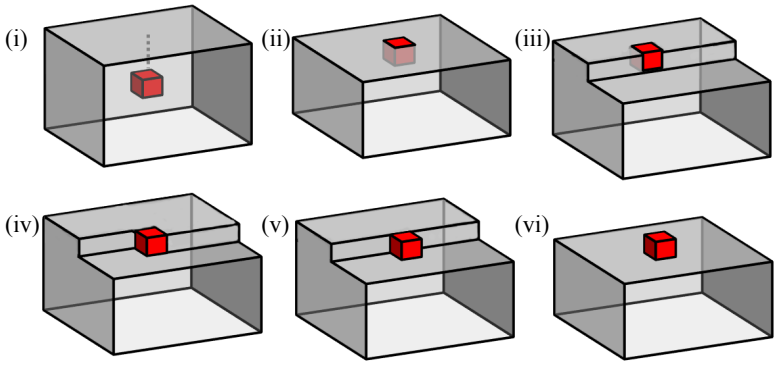


FIGURE 3.6: Cubic model of atom locations

This schematic illustrates a simple cubic model of an atom (red cube) on or in a crystal. The images (i)-(vi) are arranged in order of increasing number of exposed sides of the atom and thus increasing energy.

3.2.2.1 BCF and Stoyanov Theory

Burton, Cabrera and Frank [64] laid some of the groundwork for our understanding of the processes occurring at step edges on the surface of single crystals. They considered the advancement of a row of equally spaced steps as the crystal grows via the arrival of adatoms from the vapour, and showed that this depends on the initial separation of the steps. However, the potential for this effect to lead to an array of step-bunches was not addressed in their work. When reporting the discovery of step-bunches, Latyshev suggested that the role of the effective charge of the adatoms was central. Stoyanov undertook a detailed inspection involving the distribution of adatoms on the terraces of the steps and its effect on the motion of the step edges. The origin of the adatom gradient is discussed in reference to figure 3.7(a) which shows two atomic step edges on a vicinal substrate. This figure is adapted from an image in a publication from 1991 by Stoyanov *et al.* [65]. In this figure the adatoms (blue circles) can diffuse/desorb in the direction of the arrows. They experience a force F due to the electric field. The separation between step edges along the x direction is l. Central to the explanation for the origin of step-bunches is the concept that the rates of release and arrival of adatoms at step edges are both finite. When an atom leaves A its replacement by the step edge will not be immediate, and likewise when an adatom arrives at the top of step edge B it will not be accepted immediately. Thus a gradient with increasing adatom concentration along x appears naturally, and is illustrated in figure 3.7(b). This gives rise to a back-diffusion of adatoms that marginally counteracts the flux in the $+x$ direction. The gradient is less prevalent as l increases, and so the flux is reduced to a lesser extent by back-diffusion for greater terrace sizes. Thus, taking only the effect of back-diffusion and the force F into consideration, we have described a regime where wider steps will grow wider at the expense of narrower steps, giving rise to step-bunching. If the force is reversed, then the net flux including back-diffusion from B to A will be an increasing function of l, and the surface will be stable against step-bunching. This mechanism may therefore be sufficient to describe the effects seen in Regime I.

The effect of desorption due to the heating can have a pronounced effect on the mechanism of step bunching. If desorption is great enough then the adatom concentration n_s will be less than the equilibrium value, n_s^e, across the entire terrace, as illustrated in figure 3.7(c). In this circumstance back-diffusion will be negligible. Since atoms being lost by desorption and are not being replaced, the average step velocity $\bar{v}$ will be in the $-x$ direction. We are interested in whether individual step velocities are greater or less than $\bar{v}$ and how this depends on their individual terrace size l. This will depend on the net number of atoms leaving a step edge per unit time. In figure 3.7(a), since A is supplying atoms to B it is retarding B's velocity v_B. The supply is greater when l is smaller since

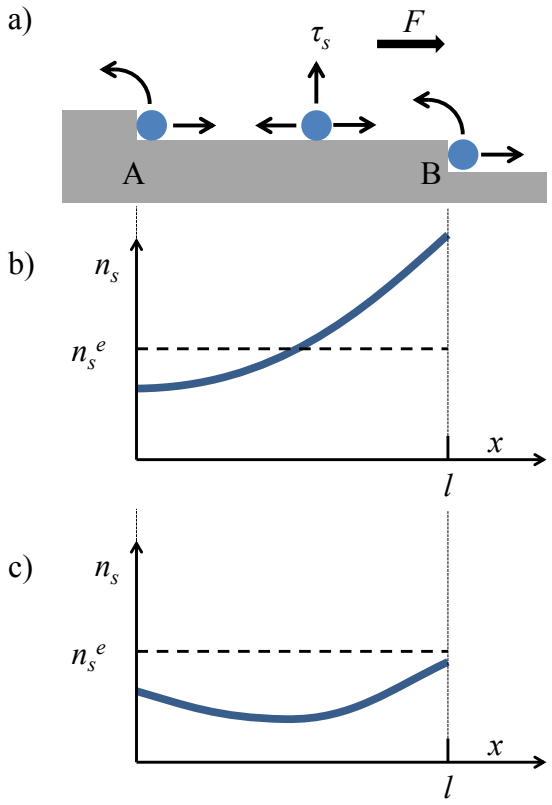


FIGURE 3.7: Schematic of adatom gradient effect on terrace of atomic step

a) Schematic cross-section of the Si (111) surface with two atomic steps, A and B. The arrows indicate that the potential directions of diffusion/desorption. The label τ_s indicates the average time for desorption of an adatom on the flat terrace.
b) Illustration of the gradient of adatom surface density n_s along the terrace of the step which has length l. The dashed line indicates the equilibrium value for adatom concentration n_s^e whereon the net flux of adatoms is zero. The concentration increases along x causing a back-diffusion of adatoms that marginally counteracts the flux toward $+x$.
c) Adatom concentration along x again but significantly reduced due to heating desorption. The concentration is below n_s^e along the entire terrace and back-diffusion can be ignored.

fewer atoms are lost to desorption en-route to B. Thus narrower terraces are more likely to grow and wider terraces will shrink, so for a step down force the surface as a whole is stable against step-bunching. When the force is in the step-up direction, however, A receives a greater supply of atoms from B the smaller l is, and thus smaller terrace are likely to be reduced (though not to a width of exactly zero) at the expense of terraces with a larger initial size. Hence we have described a desorption dependent mechanism that may be responsible for one of the regime changes.

For a full mathematical description of step-bunching, one may follow Stoyanov with the following expression for the adatom density n_s along the x-axis as a starting point [66]:

$$D_{\mathrm{S}}\frac{d^2 n_s}{dx^2} - \frac{D_s F}{k_B T}\frac{d\, n_s}{dx} - \frac{n_s}{\tau_s} = 0 \tag{3.3}$$

where D_S is the coefficient of surface diffusion and the other terms are as previously described. The first term describes a diffusion of adatoms due to the curvature of adatom concentration. The second term describes the effect of the force F due to the presence of the electric field, and the third term is related to the desorption of adatoms due to heating. Further pursuit of the mathematical model will require the description of step edges along x and the boundary conditions for adatoms at these step edges, but this is a considerable task in itself and is not the focus of the present study. In fact, the step-bunched templates used for the majority of samples described in this thesis are formed in Regime I with a step-up current. As described in table 3.1, one would expect a regular array of atomic-height steps, and yet step-bunched templates are obtained. The theory behind these step bunches is different to that for 'conventional' step bunch arrays (which have periodicity on the order of μm), as shall be described in the following section.

3.2.2.2 Faceting in Regime I

As mentioned above, when annealing in Regime I with a step-up current one expects to get an array of atomic height steps. One study with experimental evidence of this was conducted by by Yang, Fu and Williams [67], who annealed samples with a step-up current at 945 °C and used a very fast cooling rate of approximately 100 °C/s in order to "preserve the step structure at the annealing temperature". It has also been shown, however, that by carefully cooling through the 1×1 to 7×7 transition which is at around 870 °C, small step bunches can be formed on these samples [55, 68–70]. In many of these studies, the heat is applied either by purely resistive heating or by DC heating with the current parallel to the step-edge direction, suggesting that the role of electromigration is not central to the process. Thus a rapid quenching as used by Yang *et al.* seems to be a requirement for atomic-height steps.

The importance of the cooling rate is mentioned in passing in a number of studies dealing with step-bunching. Homma *et al.* mention that the cooling rate is one of the main influences on the facet structure for their step-bunched templates, and mention that their terrace width is associated with a particular cooling rate, but do not give details on the dependency [60]. Lin *et al.* mention that the cooling rate is "particularly important" and describe how a cooling rate through the transition temperature of 0.5 °C/s or less is needed for ordered step bunches. They report that faster cooling rates prevent many steps from joining bunches, and rapid quenching preserves single step heights [55]. Petrovykh mentioned that the establishment of the (7×7) reconstruction relies on slow cooling [71], and so it would appear that increasing the cooling rate limits the extent of the reconstruction which is necessary to stabilise the step bunches.

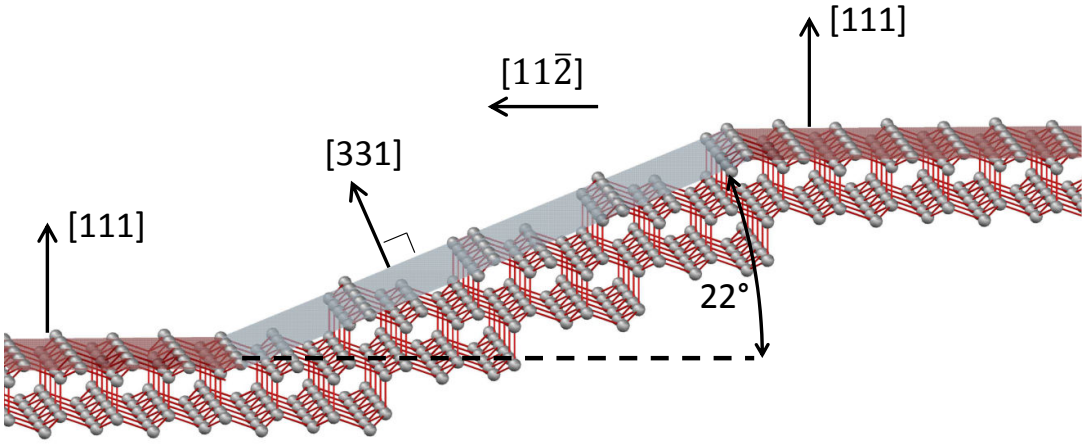


FIGURE 3.8: Two Si (111) terraces separated by a (331) facet

Two Si (111) terraces separated by a (331) facet. Portions of the (111) and (331) surfaces are shaded red and blue respectively. The (331) facet may assume an ordering other than the unreconstructed arrangement as shown, but this is beyond the scope of our aims.

To summarise these various studies, it seems that step-bunching in any regime is stabilised by the 7×7 reconstruction that comes about as the Si is cooled through 870 °C. In the case of a downhill directed current in Regime I this reconstruction has the effect of preserving the steps that are brought about by bunching during the anneal, but with step-up current it is the reconstruction itself that brings about the steps. The 1×1→7×7 transition acts as a quasi-equilibrium state during which the 7×7 reconstructed areas can form, grow and produce ordered steps. In some studies these step bunches, which are on the order of nanometres or a few tens of nanometres, have been identified as (331) facets [68, 72, 73], while in other studies [55, 70] the stepped surface more closely resembles what one would call a bunching of atomic steps, with visible roughness within the bunch and an angle to the (111) surface of significantly less than that of the (331) facet, which is exactly 22 °. A 3D image of an unreconstructed (331) facet between two (111) terraces is shown in figure 3.8. Ordered arrays of these facets have not been studied nearly as extensively as the large-sized (orders of microns) step bunches produced by using a step-down current in Regime I or step-up current in Regime II. Since the cooling rate seems to play a pivotal role, it is interesting to study its effects on the outcome of the step-bunch pattern.

3.2.3 Si Annealing Procedure

Samples were taken from n-type doped 0.525 mm thick Si (111) wafers (*Siltronix*, resistivity ≈ 1 Ω cm) with miscut angles of between 1.5 ° and 4 ° in the [11$\bar{2}$] direction. The wafers were cut into rectangular samples using an automated wafer dicing tool (Disco

DAD 3220 wafer dicer) measuring 20 mm in length and 2.5 mm in width, with the long side of the sample parallel to the miscut direction. The accuracy of the dicing tool is 5 µm or less, ensuring reproducible results. Following dicing, the samples underwent 3 ultrasonic cleaning cycles of 15 minutes each in acetone, methanol and isopropanol. They were blown dry with nitrogen and clamped to the sample stage for loading into the vacuum chamber. Once loaded in the annealing stage, current was passed through the sample and surface temperature was monitored using an infra-red pyrometer (Ircon Multimax UX20P). No other source of heating apart from DC-annealing is applied.

The sample first underwent a pre-anneal at 650 °C for 12 hours. The purpose of the pre-anneal is to deoxidise the sample surface and remove defects which can act as pinning sites during step motion. The samples are then flash-annealed 30 times to 1250 °C. The flashes are 10 seconds in duration with pauses of 30 seconds between. Flash-annealing is a common technique to de-oxidise the surface and drive residual carbon into the bulk [69, 74]. Detailed discussions on this procedure are available elsewhere [75, 76]. The brief time spent at the raised temperature ensures that step-bunching does not commence. For an anneal in Regime I, the sample is heated to 920 °C and kept at this temperature for 6 hours. For Regime II the anneal temperature used is 1120 °C. After the primary anneal, the sample is cooled at a specific rate (0.2 °C/second - 100 °C/second). The cooling rate is chosen to fine-tune the periodicity of the templates, with a faster cooling rate giving smaller periodicity. In the case of samples annealed in Regime II the cool-down is fast (10 seconds) in order to prevent de-bunching while passing through Regime I. The sample then undergoes a post-anneal at 650 °C for 6 hours. The purpose of the post-anneal is to smooth out step edges and allow the (7×7) domains to grow as large as possible in order to stabilise the step edges [55]. The sample was then brought to room temperature and removed via the load lock for AFM analysis.

Following AFM imaging, the step-bunched silicon sample was oxidised by placing it in a tube furnace at 830 °C for 15 hours in the presence of high purity O_2 at atmospheric pressure. This creates a SiO layer around 100nm thick. The oxide thickness was later confirmed using TEM. However, the precise thickness of the oxide layer is not important; its purpose is simply to prevent the formation of silicide compounds at the interface between the wires and the substrate. A visual inspection was sufficient to confirm the formation of the SiO layer, since as it increases in thickness, the sample changes colour due to optical interference from silver to tan, to brown, to violet, to blue [77]. The sample was again examined using AFM following the oxidation to ensure that the procedure had no effect on the morphology.

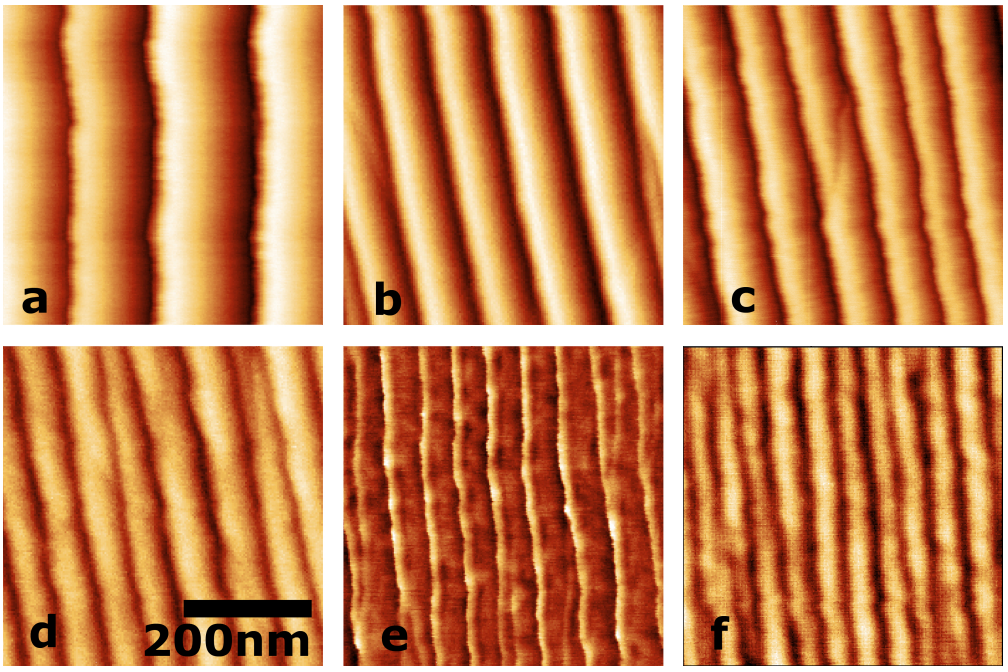


FIGURE 3.9: Samples annealed with step-up current in Regime I with different cooling rates

A series of topographical AFM images of Si samples with a miscut of 3.5 °annealed with a step up current in Regime I and a variety of cooling rates. From a) to f) the cooling rates were 0.43 °C/s, 2.1 °C/s, 4.3 °C/s, 8.5 °C/s, 21.3 °C/s and 43 °C/s. The step-up direction is to the right in each case. The scale bar is 200 nm and all images are to the same scale.

3.2.4 Results

A large number of step-bunched templates were produced with a diversity of annealing parameters. As mentioned previously, one of the key investigations that was planned was a variation of cooling rate for samples annealed with a step-up current in Regime I. Several samples were taken from a wafer with a 3.5 ° miscut in the $11\overline{2}$ direction and annealed as described in section 3.2.3 with a step-up current in Regime I, but with the cooling rate varied from 0.43 °C/s to 43 °C/s. Topographical AFM results are shown in figure 3.9. First we notice that ordered rows of step-bunches have been grown with a reasonably low distribution in step-edge to step-edge distance. We also see that there is a continuous decrease in the average step-edge to step-edge distance (or the "periodicity") as the cooling rate is increased. Using AutoCAD software, AFM images from these samples were scaled and the step-edge to step-edge distance for hundreds of steps were measured. The average value gives the periodicity of each sample. The black and red data points in figure 3.10 show the dependence of periodicity on cooling rate on a semi-log plot for samples with 3.5 ° and 2.5 ° miscuts respectively. The shape of the plot suggests that there is a power law dependency on cooling rate. One also

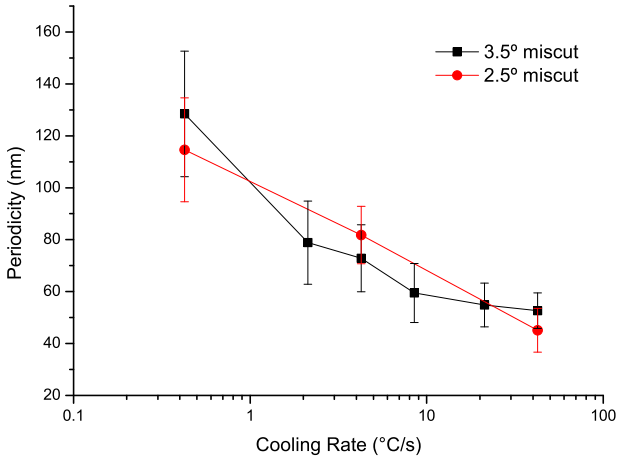


FIGURE 3.10: Dependence of periodicity on cooling rate for step-up current in Regime I

Periodicity of step-bunched Si templates plotted as a function of the cooling rate used for samples annealed in Regime I with a step-up current. The error bars represent the standard deviation of the step size data. The miscut angle of the samples in these images was 3.5 °.

immediately notices that there appears to be no dependency of the periodicity on the miscut angle in this range. This periodicity independence has been noted previously by a number of studies for samples which were resistively annealed or annealed with the current perpendicular to the step-edges [55, 70, 71], but not for the case of step-up current.

One notices that the cooling rate has to be altered quite significantly in order to change the periodicity by a noticeable amount. For example, in order to halve the periodicity, the cooling rate needs to be increased by two orders of magnitude. This makes it an attractive parameter for fine-tuning of the periodicity. This result also shows the importance of recording the cooling rate when carrying out an analysis on a step-bunching mechanism, since it may play an important role in the outcome. As far as we are aware this is the first such study on the dependence of cooling rate on periodicity of a step-bunched Si template.

The fact that the periodicity increases with slower cooling rate supports the suggestion that the mechanism for step-bunching in this manner is brought about by prolonging the quasi-equilibrium state around the 1×1 to 7×7 transition. By moving more slowly through this temperature region, we allow the 7×7 reconstruction to expand and stabilise the step-bunch pattern.

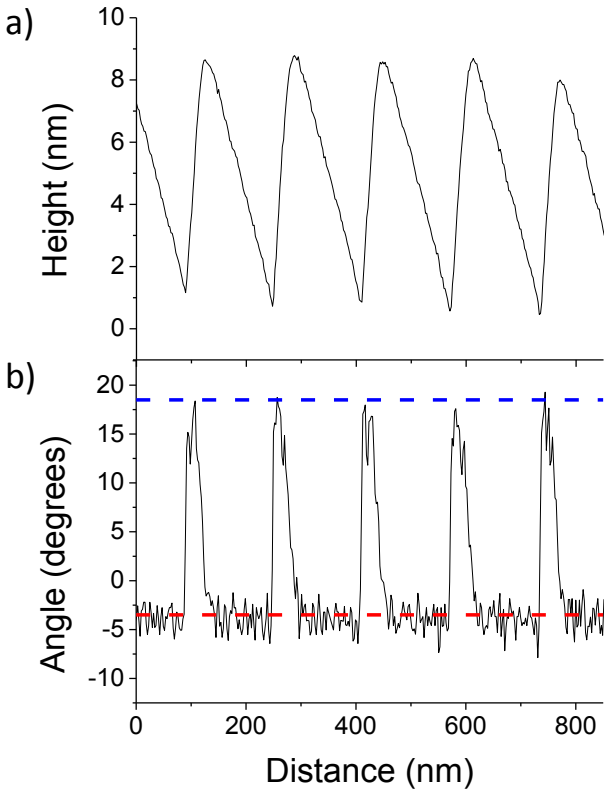


FIGURE 3.11: Height and angle profile of a step-bunched sample

Height and associated angle profile of a 3.5 ° miscut step-bunched sample as a function of distance in the direction perpendicular to the step edges. The sample was annealed in Regime I with a step-up current. Superimposed on the angle profile is the -3.5 ° (red) and 18.5 ° (blue) angles. The -3.5 ° angle should correspond to the (111) terraces, since the miscut angle of the sample is 3.5 °. The 18.5 ° angle is highlighted since it is inclined at 22 ° to the (111) plane, and this is the angle one would expect to find a (331) facet.

Shown in figure 3.11 are height and angle profiles across one of the samples used in the cooling rate study with a 3.5 ° miscut. The angle profile is produced by simply taking the first derivative of the height profile. Two angles are superimposed in the angle profile. In red is -3.5 ° which corresponds to the angle of the (111) plane, since the miscut of this sample is 3.5 °. In blue is 18.5 °, which is at 22 ° to the (111) plane, and equal to the angle that one would expect to find a (331) plane, as shown in figure 3.8. As can be seen, the dashed red line at -3.5 ° matches up well with the terraces between the step-bunches, confirming that they are indeed (111) facets. The angle of the step-bunches, meanwhile, is quite close to the angle expected for (331) facets. Previous studies using techniques including STM, LEED and RHEED have confirmed that the (331) surface may come about for vicinal Si annealed in this way, although in some studies the (331) surface was found to be slightly rough [55, 56, 68, 72]. Thus we could plausibly state that the step-bunches produced in Regime I with a step-up current are actually facets. However,

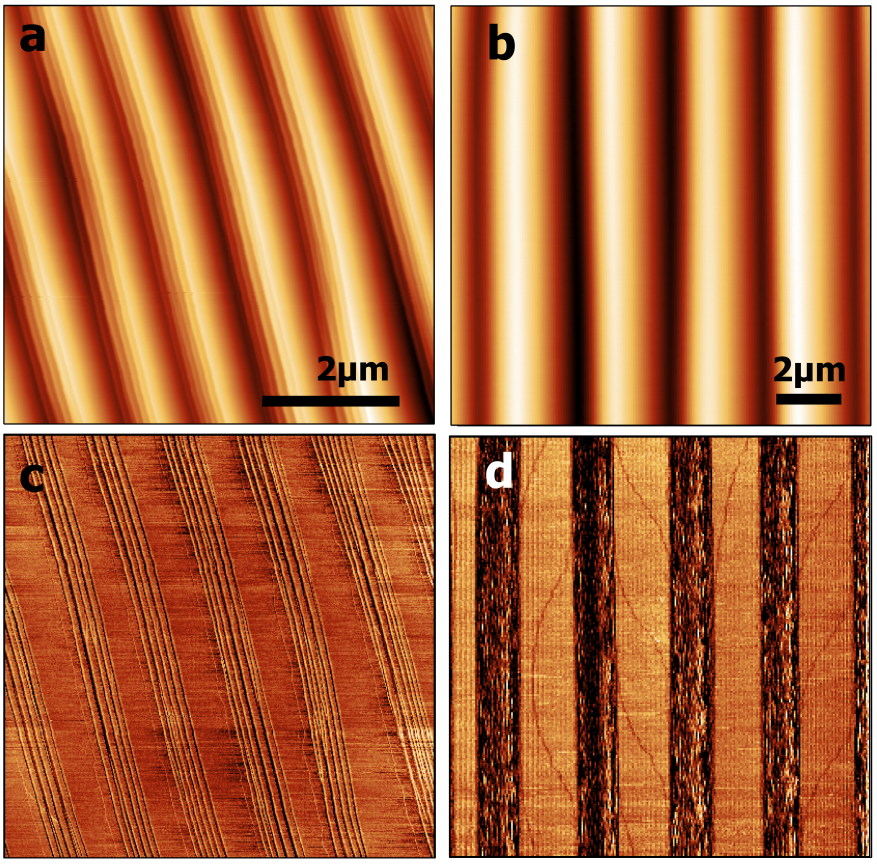


FIGURE 3.12: Step bunches in Regime I and II

(a) and (b): Topographical AFM images of samples annealed in Regimes I and II respectively. The (111) templates have a miscut of 3.5 ° in the $[11\bar{2}]$ direction.
(c) and (d): Phase images corresponding to the images directly above.

for smaller periodicities the angle cannot be measured precisely since the tip of the AFM is comparable in size to the step-bunch. We also have no way of determining the atomic roughness of these surfaces or whether the (331) surface undergoes any reconstruction. For these reasons we shall refer to these surfaces as step-bunches and suggest that further experiments would be necessary to determine their exact nature.

As mentioned above, samples were also annealed in Regime I with step-down current and Regime II with step-up current to produce the sort of step-bunched arrays most commonly seen in the scientific literature. These have periodicity on the order of microns. Examples are shown in figure 3.12. In (a) and (c) are height and phase images respectively of a sample annealed in Regime I (at 920 °C) with a step-down current, producing large step bunches with a periodicity on the order of approximately 1.1 μm, while (b) and (c) show height and phase images respectively of a sample annealed in Regime II (at 1120 °C) with a step-up current. These steps have a periodicity of approximately 2.9 μm. As can be seen from the phase images, the step bunches are visibly rough, and

may well be formed of bunches within the bunch itself. The roughness of the bunch has been noted by previous studies of steps of this size [55, 70]. Also visible in (d) are monatomic steps which cross the terraces called 'crossing steps'. Their behaviour has been linked to the formation of 'antibands' and critical electromigration fields [78, 79], but these are not the focus of this study.

3.3 Sapphire Template Preparation

3.3.1 Sapphire

Sapphire or α-Al_2O_3 has many qualities that makes it an attractive material for use as a substrate in a large number of materials science applications. It is chemically stable and is an electrical insulator but has good thermal conductivity. It has high mechanical strength and a high melting point ($\approx 2070\,^{\circ}\mathrm{C}$) and is transparent across the visible range. The crystal structure is hexagonal with a rhombohedral primitive cell as shown in figure 3.13(a). The lattice vectors of the basal plane, $\vec{a_1}$, $\vec{a_2}$ and $\vec{a_3}$, are indicated, and have a length of 4.578 Å, while the vertical lattice vector $\vec{c}$ has a length of 12.992Å. The O^{2-} anions form a distorted hexagonal close-packed lattice, with the Al^{3+} filling two thirds of the octahedral hollows. The strong oxygen bonding lends the material its hardness and insulating properties. Figure 3.13(b) shows the most commonly used planes of sapphire (reconstructions neglected). We deal with C-plane sapphire due to the ability to form ordered steps on its surface.

Figure 3.14(a) shows the side profile of the unit cell. We can see the 6 oxygen layers and the aluminium bilayers that separate them. The dotted lines show the three different surface terminations that are possible, each exposing a different surface crystal structure. We may have an oxygen layer (A, in figure 3.14(c)), a double aluminium layer (B) or a single aluminium layer (C), which turns out to be the most energetically favourable option [80], and therefore the most commonly used in research. The crystal structure of the surface corresponding to termination C is shown in figure 3.14(b).

3.3.2 Faceting Mechanism on Sapphire

The behaviour of vicinal sapphire when annealed is a fairly well understood process compared to the complex nature of step-bunching on vicinal silicon. Mechanically polished C-plane samples can be ordered from manufacturers with a well-defined miscut angle in the $[1\bar{2}10]$ direction, producing single steps with height $c/6$, i.e. one-sixth the unit cell height. Heating the sapphire increases the energy of the surface atoms, allowing the

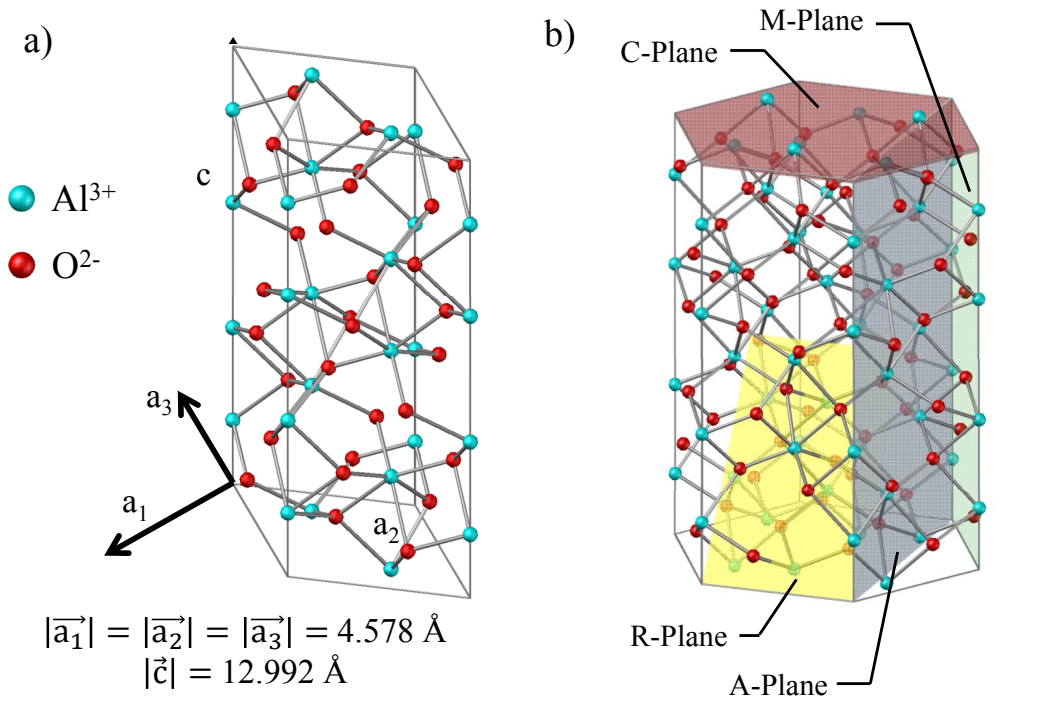


FIGURE 3.13: Crystal structure of Al_2O_3

a) Rhombohedral primitive cell of α-Al_2O_3. Lattice vectors of the basal plane ($\vec{a_1}$, $\vec{a_2}$ and $\vec{a_3}$ are indicated, as is the vertical lattice vector $\vec{c}$).
b) Unit cell of α-Al_2O_3 with four most commonly used planes indicated as follows. Red: C-plane (0001), green: M-plane ($1\bar{1}00$), blue: A-plane ($11\bar{2}0$), yellow: R-plane ($1\bar{1}02$).

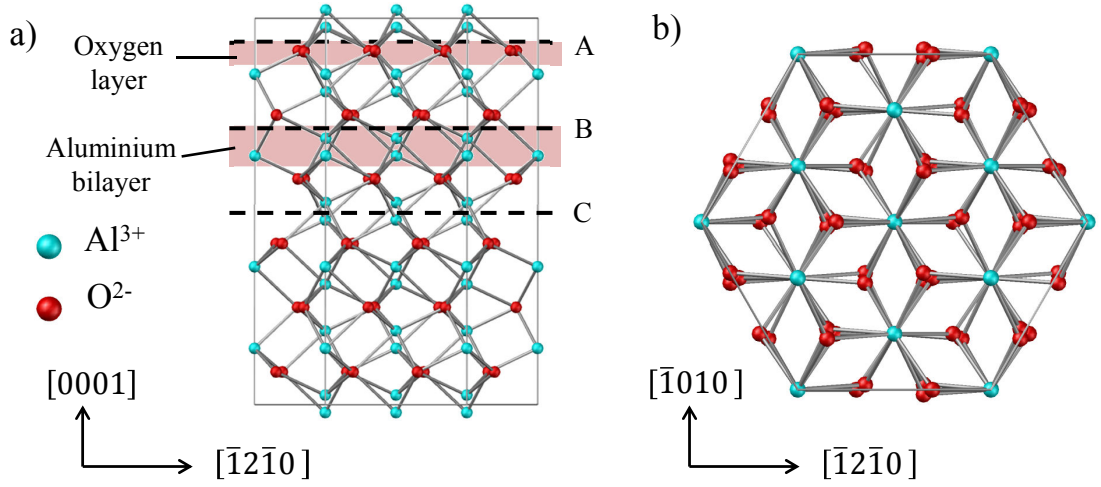


FIGURE 3.14: Side profile and C-plane of Al_2O_3

a) Side profile of Al_2O_3 unit cell. The 6 oxygen layers separated by aluminium bilayers can be clearly seen. The dotted lines A, B and C indicate the three possible terminations of the crystal surface, each of which will result in a slightly different surface crystal structure.
b) C-plane surface of Al_2O_3 when terminated between the aluminium layers as indicated by the dotted line C in (a).

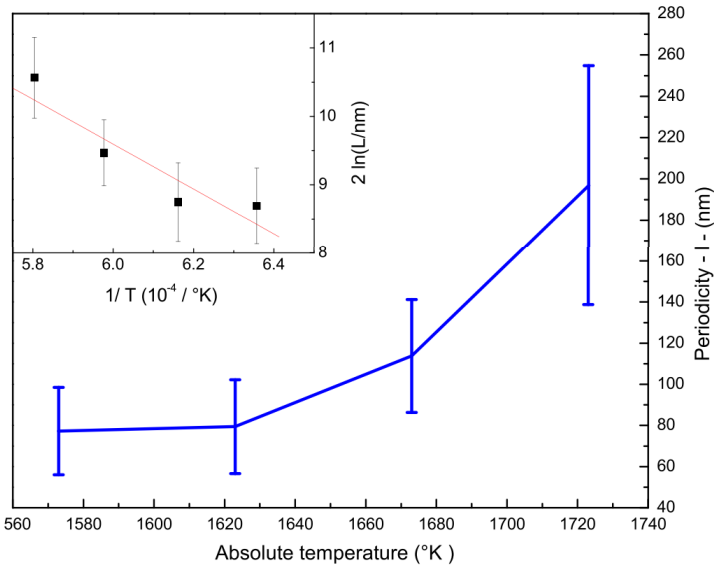


FIGURE 3.15: Dependence of periodicity of annealed Al_2O_3 substrates on temperature

Temperature dependency of the periodicity for 6 ° miscut Al_2O_3 samples. There is an exponential increase in periodicity with temperature. Following equation 3.4 an Arrhenius plot is used (see inset) to calculate the activation energy for surface atom diffusion. This plot is taken from Verre *et al.* which used the same experimental setup for preparation of Al_2O_3 samples as the current study [29].

surface to reach a thermodynamic equilibrium state composed of lower energy facets. There are conflicting reports about intermediate states where the atomic steps may join to form double-steps of height $2c/6$ [81], with another study going further to state that step heights continue to prefer to be an even multiple of $c/6$ [82]. Another report suggests that the intermediate phase consists of roughly shaped islands on the terraces of height $c/6$. Since this study is concerned only with the production of these stepped-surfaces for use as a deposition template, the intricacies of the faceting mechanism are unimportant.

Various reports have been carried out investigating the effect of temperature [29, 82–85] and time [81, 83, 85, 86] on the periodicity of the step arrays formed. With a small number of contradictions, the trend is towards greater periodicity with higher temperature (the references cited here include temperatures in the range of 1100 °C to 1550 °C). Figure 3.15 is taken from a study by Verre *et al.* [29] and shows the dependence of periodicity on temperature for Al_2O_3 substrates with a 6 ° miscut. As can be seen from the graph, there is an exponential increase in periodicity with temperature. It is suggested that the faceting mechanism is a thermally activated diffusion process in which the periodicity is assumed to be equivalent to the average displacement of the adatoms. The periodicity is therefore proportional to an effective diffusion constant D

which can be given by

$$D = D_0\, exp(-E_{ac}/k_B T) \tag{3.4}$$

where E_{ac} is the activation energy, k_B is the Boltzmann constant and T is the temperature. According to this equation, plotting the natural log of the periodicity against the inverse of the temperature should give a straight line graph whose slope is equal to $-E_{ac}/k_B$. This graph, which is an example of an Arrhenius plot, is shown in the inset of figure 3.15. From the fit the activation energy was found to be 2.8 eV ±0.8eV, which is close to the 2.0 eV reported for nominally flat sapphire [82].

Most studies agree that periodicity increases with the annealing time up to a point, beyond which additional annealing has little affect on the outcome [85]. While the periodicity might not increase much beyond a certain point, Cuccureddu *et al.* found that prolonged annealing did have the effect of narrowing the terrace-width distribution [86]. In an isolated finding, one study found a decrease in periodicity for very long anneal times at their highest anneal temperature [83]. Other studies have looked at the effect on faceting by atmosphere [84] and pressure [87].

3.3.3 Annealing Procedure

Single crystal C-plane α-Al_2O_3 substrates (*MTI* USA) with a 6 ° miscut (± 0.1 °) in the $[1\bar{2}10]$ direction were cleaned using a similar procedure to that used for Si samples (see section 3.2.3). The samples, 10 mm×10 mm in size, were slowly loaded into the tube furnace which was already at a temperature of 700 °C. The sample was then heated to the desired annealing temperature at a rate of 5 °C/minute, and was also cooled at this rate at the end of the annealing period to bring the sample back to 700 °C. After removal from the furnace the samples were analysed using AFM in tapping mode.

3.3.4 Results

Figure 3.16(a) shows a typical AFM image taken of a (0001) Al_2O_3 sample which has a miscut of 6 ° in the $[1\bar{2}10]$ direction following a 15 hour anneal at 1400 °C. This rather straightforward procedure (compared to the Si annealing procedure) has resulted in a well-ordered array of terraces and step-bunches/facets. A line profile taken across the image in (a) is shown in figure 3.16(b). In this case, the periodicity is approximately 120 nm, which is in good agreement with the previous study by Verre *et al.* (see graph in figure 3.15) [29]. From a differentiation of this plot (not shown) it can be seen that the terraces correspond to the 6 ° miscut as expected, but the angle of the step-bunched facet is not reliably found from AFM. The facet angle is known from TEM to be 42 °,

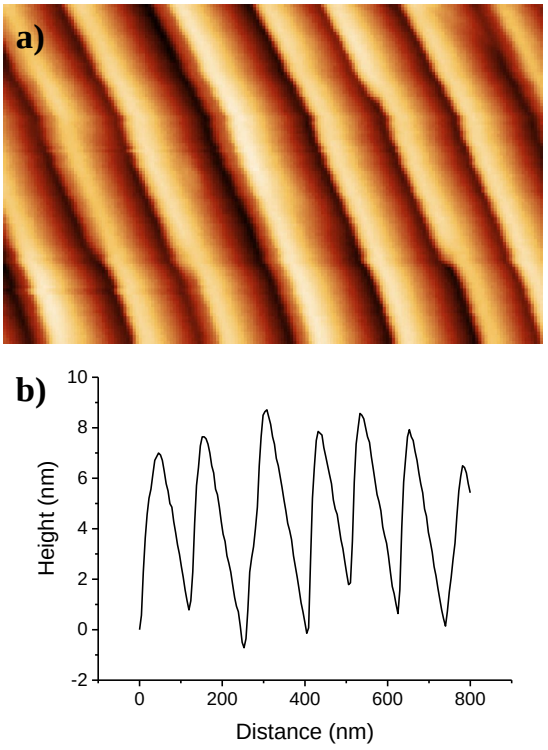


FIGURE 3.16: AFM of faceted Al_2O_3

a) Typical AFM image of faceted vicinal Al_2O_3 template following an annealing process. The area of the image is 800 nm×500 nm.
b) Height profile across the image in (a). The average periodicity for this sample is approximately 120 nm.

corresponding to the $(1\bar{2}16)$ facet [29]. Therefore it is not surprising that such a steep slope which is also quite narrow ($\approx$ 20 nm) is not reflected in an examination by AFM with a tip diameter of only 20 nm.

3.4 Glancing Angle Deposition Technique

With our templates of step-bunched Si and faceted Al_2O_3, a number of different options were available to us to with regard to glancing angle deposition. As mentioned in section 3.2.3, steps with a periodicity of approximately 1 μm or larger can be grown by annealing with a step-down current in Regime I or a step-up current in Regime II, while steps with a periodicity of 50-150 nm can be grown using a step-up current in Regime I. Hereafter these two groups shall be referred to as 'large-step' and 'small-step' samples respectively.

The formation of nanowire or nanoparticle arrays on these templates can be performed by depositing at a glancing angle in either the uphill or downhill direction, as shown in figure 3.17. In this figure the deposition flux is given by the black arrow and the

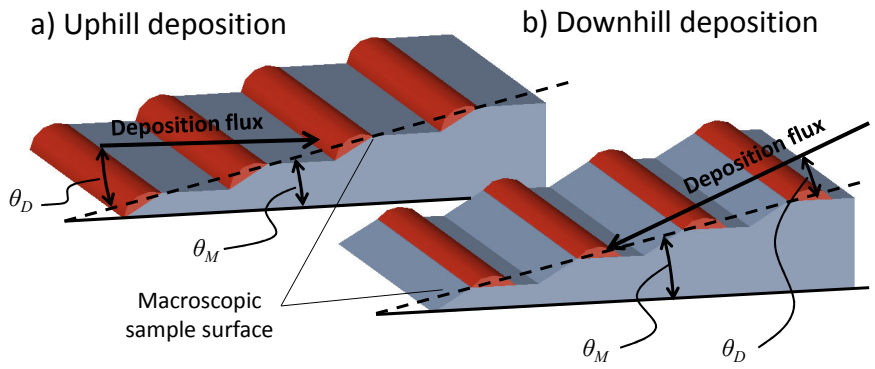


FIGURE 3.17: Glancing Angle Deposition Schematic

Schematic images of an uphill (a) and downhill (b) deposition. Here the dashed lines indicate the macroscopic sample surface. θ_D is the deposition angle and θ_M is the miscut angle.

macroscopic sample surface is shown as a dashed black line, and the deposition angle θ_D is the angle between these two. Uphill depositions were never carried on large-step samples due to the roughness of the step-bunches, as can be seen in figure 3.12, but we regularly carried out uphill depositions on small step-samples and on faceted Al_2O_3 samples. Since in these cases the step bunch was on the order of a few tens of nanometres in width, the entire step-bunch was covered with the deposited material. For uphill depositions it was found that it was best to deposit with a deposition angle equal to the miscut angle θ_M. Depositing at a greater angle than θ_M results in deposition on the terraces, while using a smaller angle than θ_M results in a distribution of wire widths which is even greater than the distribution of step-bunch widths due to self-shadowing.

Downhill depositions were carried out on both large- and small-step samples. As shown in figure 3.17(b), the deposition angle θ_M can be chosen to expose only a certain proportion of the terrace width, thereby allowing us to specify the wire width for a given sample.

In most circumstances involving thin film deposition, the thickness T is determined simply by the deposition flux incident on a flat substrate, f, in units of nm/minute for example, multiplied by the duration of the deposition (in minutes for this example). Since we are dealing with partial coverage and a deposition flux which is directed at a very shallow angle, some adjustments are required to calculate the resultant wire height, but it is helpful to consider the thickness T that would be deposited onto a flat substrate located at the same position in the chamber as our step-bunched template. Wire height h can be expressed in relation to T via

$$h = \frac{T \times \sin(\theta_D)}{\Omega} \tag{3.5}$$

where Ω is the proportion of the terraces which is covered. For example, if the periodicity is 130 nm and the deposition flux is only incident on the step-bunches which have a width of 30 nm, then $\Omega = 30/130 \approx 0.23$.

Samples for magnetic analysis were covered in a capping layer of MgO or Ag which was deposited at normal incidence. This was done without removing the sample from the vacuum to prevent oxidation of the nanowire material.

3.4.1 Nanowires Grown on Large-Step Samples

Figure 3.18 shows two examples of nanowire arrays produced by using glancing angle deposition onto step-bunched Si substrates. These are both AFM phase images carried out in tapping mode. The template in figure 3.18(a) was achieved by annealing with a step-down current in Regime I to produce a large-step array with a periodicity of approximately 840 nm, while the template in 3.18(b) was created by annealing with a step-up current in Regime II to attain a periodicity of approximately 2.7 µm. Both templates were oxidised as described in section 3.2.3, and subsequently examined using AFM to ensure that the oxidation procedure had no adverse effect on the step morphology. Fe was deposited in the downhill direction at room temperature at an angle of 1.5 ° with respect to the macroscopic sample surface. The results show successful implementation of the glancing angle deposition technique, producing ordered rows of wires with widths on the order of hundreds of nanometres, and thicknesses which can be specified by choosing an appropriate duration of deposition. From the phase images above, it appears that the wires are quite rough. Figure 3.19, which shows a height profile of a single Fe nanowire from this sample, gives a clearer indication of the roughness of the nanowires produced using this method. We can see that it is composed of an aggregation of Fe grains. It is understandable that the growth is not epitaxial, given that the Si surface is oxidised and most likely amorphous as a result. The finding also suggests that the crystalline axes of the nanowire material are randomly oriented, and so the role of magnetocrystalline anisotropy of the system can safely be neglected.

3.4.2 Nanowires Grown on Small-Step Samples

3.4.2.1 Downhill Depositions on Si

Four identical templates were prepared for downhill depositions by annealing Si substrates with a miscut of 2.5 ° in the $[11\bar{2}]$ direction in Regime I with a step-up current. This produced step-bunched templates with a periodicity of approximately 140 nm, similar to that seen in figure 3.9(a).

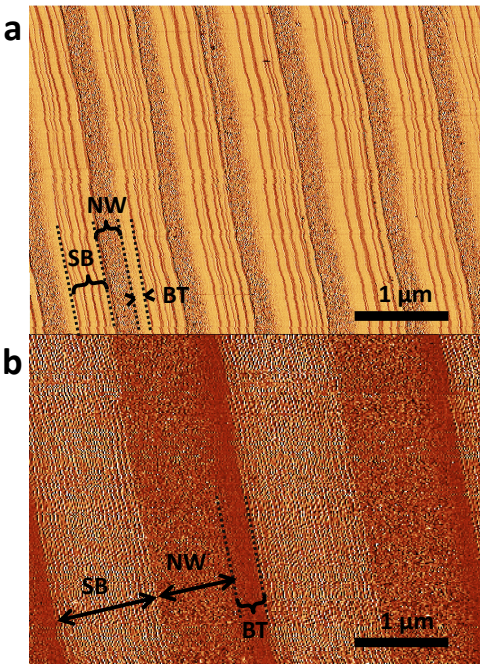


FIGURE 3.18: Glancing angle deposition results on large-step samples

AFM phase images of large-step Si step-bunched templates with nanowire arrays produced via glancing angle deposition. The regions are labelled "SB", for step-bunches, "NW" for nanowires and "BT" for Bare Terrace, which are the regions of the terraces that have been shadowed by the preceding step.
(a) Sample annealed in Regime I with periodicity of approximately 850 nm. Fe has been deposited at 1.5 ° resulting in coverage of approximately 70% of the terrace surface, yielding wires of 260 nm width.
(b) Sample annealed in Regime II with periodicity of approximately 2.7 µm. Fe has been deposited at 1.5 ° resulting in coverage of approximately 80% of the terrace surface, yielding wires of 900 nm width.

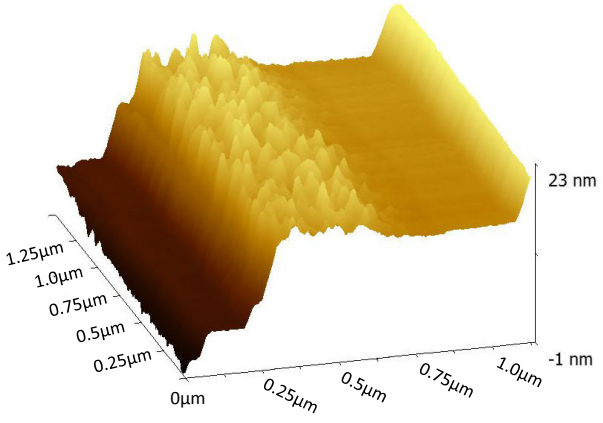


FIGURE 3.19: Single nanowire produced on a large-step sample

Height profile of a single nanowire deposited on a large-step sample whose periodicity is 850 nm. The surface of the nanowire surface appears rough, suggesting that it is composed of an agglomeration of grains. The slopes to the left and right do not represent the entirety of the neighbouring step-bunches.

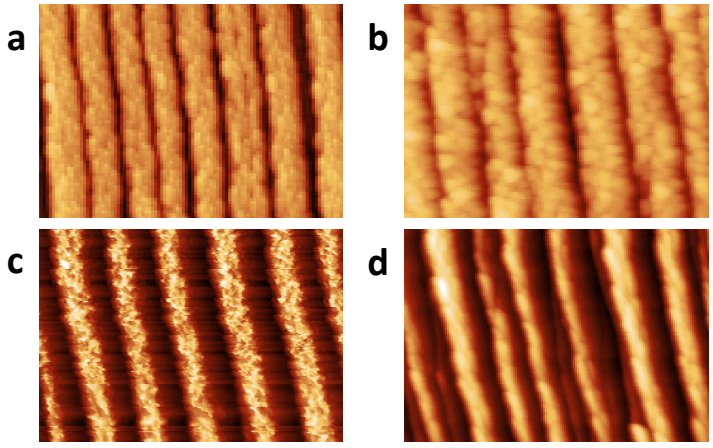


FIGURE 3.20: Fe nanowires with varying deposition angle

Topographical AFM images of Fe nanowire arrays produced by depositing in the downhill direction on four samples. The deposition angle used for each sample was (a) 2.5 °, (b) 1.5 °, (c) 1.0 ° and (d) 0.5 °. Each image is 1000×700 nm.

Fe was deposited in the downhill direction on the four samples, a, b, c and d, using a deposition angle θ_D, of 2.5 °, 1.5 °, 1.0 ° and 0.5 ° respectively. AFM results are shown in figure 3.20. As can be seen, the technique successfully resulted in ordered rows of Fe-nanowires with good regularity of direction and size. For (a) and (b) where θ_D is at least 1.5 °, it is apparent that the entire terrace is covered in Fe, with only small gaps between the wires at the step-bunches. In (c) we can see a reduction in terrace coverage with regions of bare terrace visible. In (d), the proportion of the terrace which is covered in Fe has been further reduced. It is also evident that the wires seem to be formed of grains of Fe, similar to the case of wires deposited on large-step samples (e.g. figure 3.19).

A selection of individual height profiles from three of the four samples are shown in figure 3.21(a). In these three height profiles, the nanowires are labelled 'NW', the step-bunches are labelled 'SB' and the regions of bare terrace, if present, are labelled 'BT'. It is evident that the region of the terrace covered by nanowire material decreases with deposition angle. Thus, using this technique we are able to specify the wire width of an array through appropriate choice of deposition angle.

In addition, we can alter the deposition time to control the thickness of the wires within the array. For this study, three step-bunched templates were produced having a periodicity of approximately 90 nm. Downhill Fe depositions were carried out with θ_D equal to 0.5 °. The thickness deposited onto the three samples was equivalent to a normal deposition thickness (i.e. T, in equation 3.5) of 75, 100 and 150 nm. Figure 3.21(b) shows height profile scans across nanowires from each of the three samples. The height

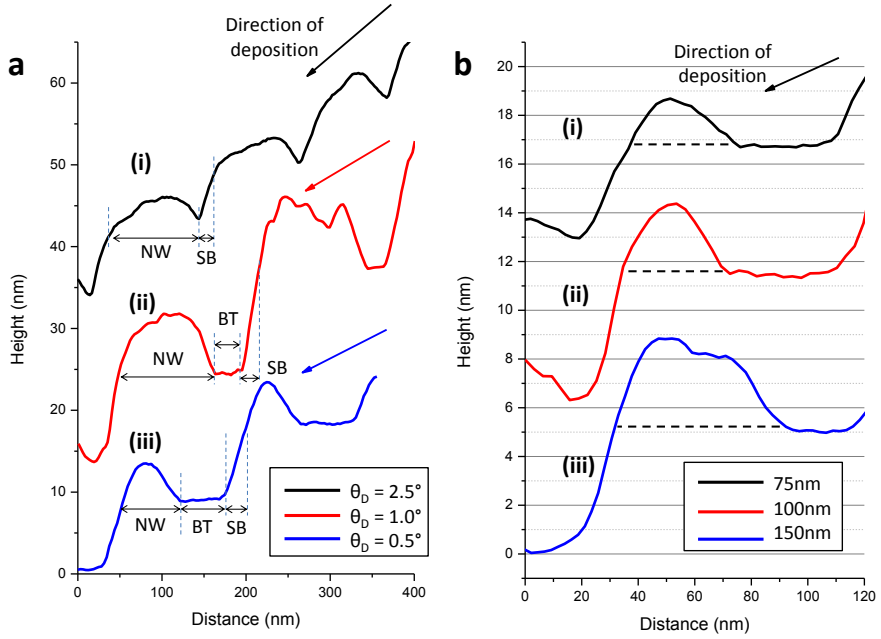


FIGURE 3.21: Height profiles across nanowires with varying deposition angle and thickness

a) Height profiles from three Fe nanowire array samples with different deposition angles used. The angle of deposition for each sample is indicated by the black, red and blue arrows. As the deposition angle is reduced, the portion of the terrace covered by nanowire material (labelled 'NW') is reduced, and the bare regions of the terraces (labelled 'BT') increases. Also labelled are the step-bunches, 'SB'.
b) Height profiles of Fe nanowires taken from three nanowire arrays with periodicities of 90 nm and varying deposition time. The deposited thickness given is equivalent to that which would be measured on a a substrate aligned normally to the deposition flux. The region between the dotted line and the height profile represents the cross-section of the wire in each case. The arrow indicates the angle of the deposition flux for all three samples.

profiles illustrate how the wire thickness increases with deposition time. In addition, for the thickest sample (figure 3.21(b)(iii)) we see that the width of the wire is slightly increased. This is understandable, considering that the flux is directed at only 3 ° from the plane of the terrace.

Fe nanowire arrays were also examined using High Resolution Transmission Electron Microscopy (HRTEM, FEI Tecnai F30 operated at 300 kV). Prior to TEM examination, the samples were prepared using a Focussed Ion Beam (FIB) on a Helios Nanolab microscope. The preparation involves first coating the sample surface with a layer of Au and Pt, which protect the sample details and provide contrast while imaging. Then the FIB is used to cut a thin electron-transparent lamella from the sample whose long edge is perpendicular to the step-edges. The results of the TEM study are shown in figure 3.22. In figure 3.22(a) we see the cross section of about 5 wires from the sample. The wires appear as granular stripes close to the surface. Figure 3.22(b) shows a single Fe

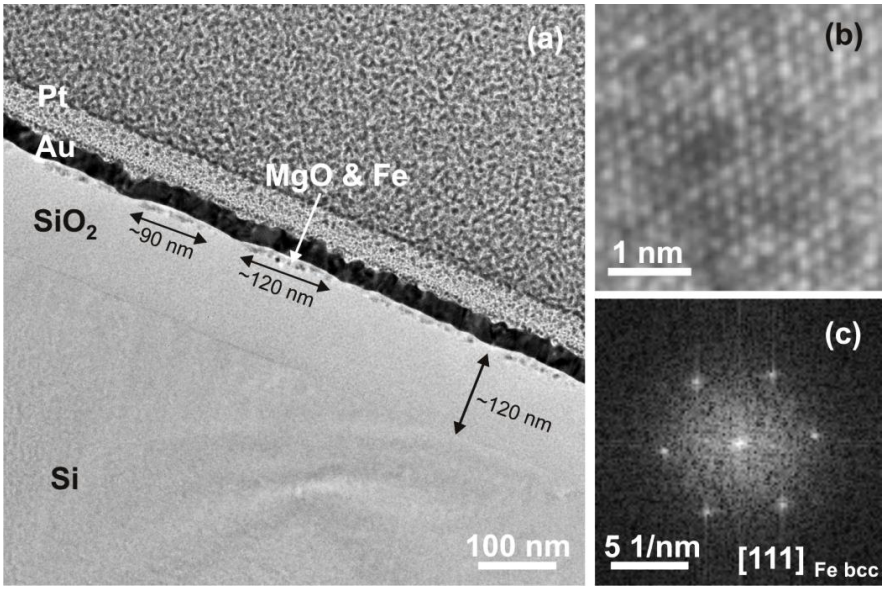


FIGURE 3.22: TEM of Fe nanowires

a) TEM cross-section of several Fe nanowires in a nanowire array.
b) Close-up image of a single grain from one of the wires shown in (a).
c) FFT of the Fe grain shown in (b). The pattern indicates that the grain is bcc and that we are viewing along the [111] axis.

grain approximately 4 nm in diameter, and the FFT of this region is shown in 3.22(c). From the FFT we can tell that the grain in (b) is body-centred cubic (bcc) in structure, and that the direction along which we are viewing is the [111] axis.

Apart from Fe, other materials for the nanowire arrays were also investigated. Figure 3.23 shows some typical images from a TEM examination of a Co nanowire array. In figure 3.23(a) we see the Co nanowire as a dark stripe which covers almost the entire step terrace. The widths of the nanowires vary from 50 to 70 nm due to statistical fluctuations in the periodicity of the Si template. We can also see that the SiO_2 layer which was caused by annealing the template in O_2-rich atmosphere is approximately 110 nm in thickness. Figure 3.23(b) shows a close-up of one of these nanowires. We can see that it is composed of small regions (≈ 5 nm) of continuous crystallinity. This reinforces our earlier suspicion that the wires were polycrystalline, as suggested by the grainy structures seen in figure 3.20, for example. Figure 3.23(c) shows a close-up of one of these grains, and its Fast Fourier Transform (FFT) is shown in 3.23(d). From the FFT we can identify the crystal structure as hcp (hexagonal close-packed) and the direction along which we are viewing as the [112] axis. A few regions exhibited fcc (face-centred cubic) structure, as determined from selected area diffraction analysis, while other areas were fcc CoO, where oxidation was most likely due to the interface with the MgO capping layer or SiO_2 substrate.

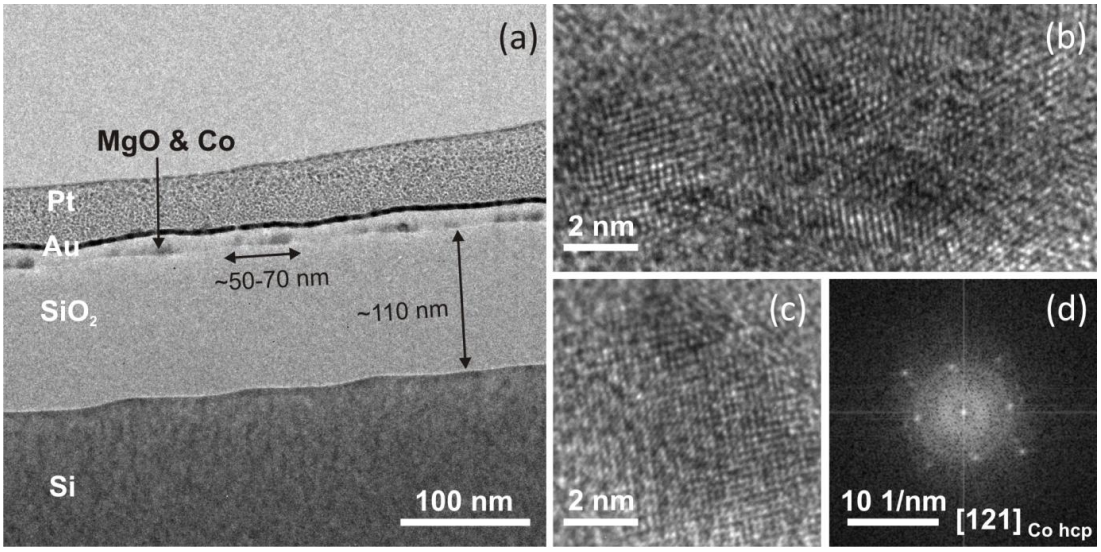


FIGURE 3.23: TEM of Co nanowires

a) TEM cross-section of nanowire array showing several nanowires grown by depositing Co onto a step-bunched Si template in the downhill direction.
b) Close-up image of some of the Co grains comprising the nanowire. We can see that the crystallinity is continuous only over short ranges ($\approx 5\,\text{nm}$) indicating that the nanowires are polycrystalline.
c) Close-up of a single Co grain.
d) FFT of the Co grain shown in (c). The pattern tells us that we are viewing the Co grain along the [121] axis.

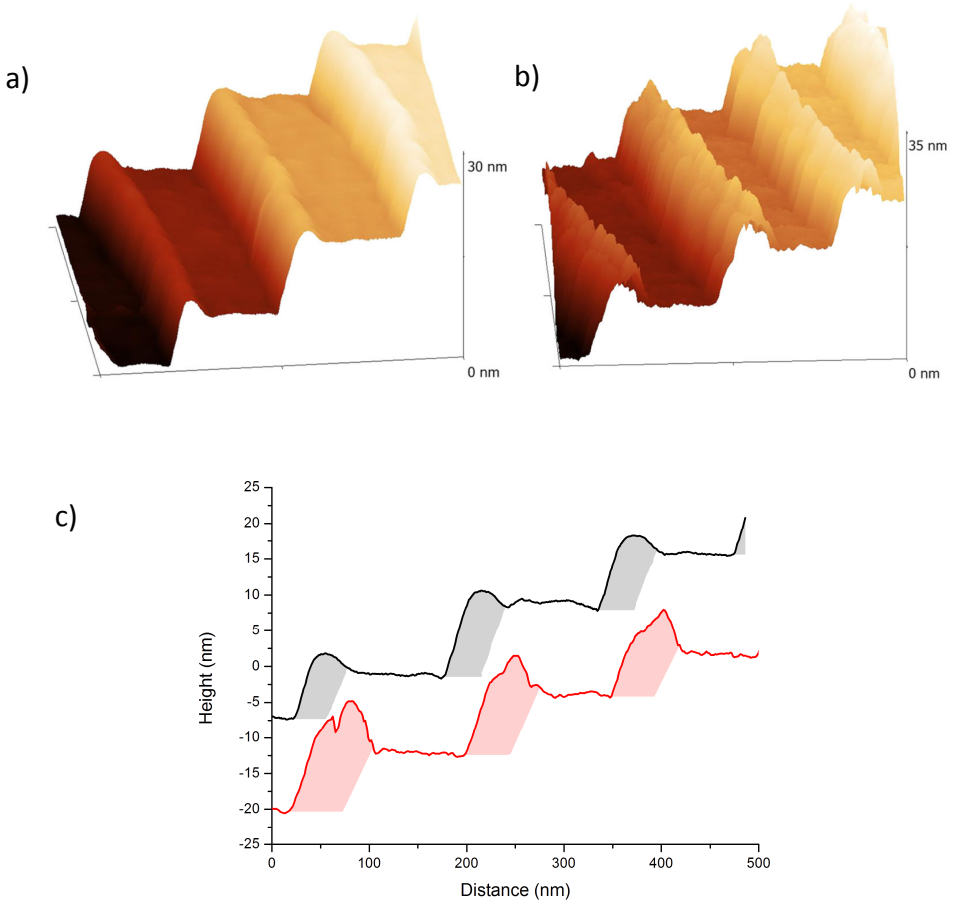


FIGURE 3.24: AFM data from Ni nanowire arrays with varying thickness

a) and b): 3D AFM images of Ni nanowire arrays produced by using a effective normal incidence thickness of 125 and 250 nm respectively. The areas are 500×500 nm in size, and the z-axis is to the same scale for both images. The Ni is deposited on identical Si step-bunched templates with a periodicity of approximately 140 nm. We can see that the nanowires are very straight, regular and well-separated.
c) Height profiles across each of the two samples in (a) and (b) are shown in black and red respectively. The grey and pink shaded regions in the two profiles correspond to the cross sections of the Ni nanowires.

3.4.2.2 Uphill Depositions on Si

A number of experiments were carried out to explore the variety of nanowire arrays that could be produced by depositing in the uphill direction. The effect of deposition time was examined by carrying out two Ni depositions in the uphill direction, with deposition thicknesses at normal incidence of 125 and 250 nm. 3D AFM images of the resulting nanowire arrays are shown in figure 3.24(a) and (b). As can be seen from these images, the method results in ordered rows of Ni nanowires which are very straight and well separated. From these images we can see an increase in width and thickness of the Ni nanowires which is more evident in figure 3.24(c), which shows height profiles

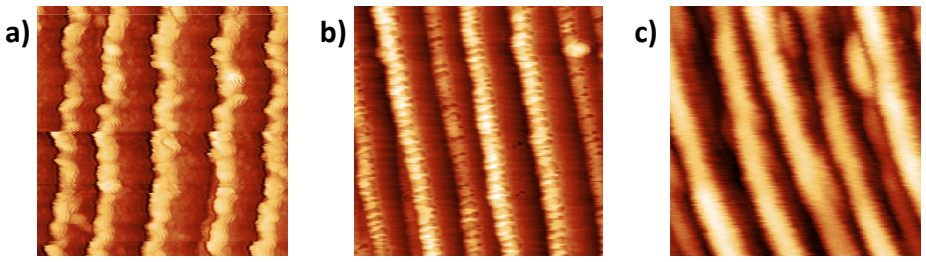


FIGURE 3.25: AFM data from arrays of nanowires composed of Co, Fe and Ni deposited in the uphill direction

Arrays of nanowires composed of Co, Fe and Ni are shown in a), b) and c) respectively. The material is deposited in the uphill direction onto samples with similar periodicity and deposition time. The areas shown are 500×500 nm in size.

across these two samples. In these profiles, the miscut angle of the Si substrate has been subtracted, and the regions corresponding to the wire cross-sections have been shaded in. We can analyse the shaded regions in this image and show that the grey areas are 57% the area of the pink regions, which is close to the 50% that we expected, although local variations in wire and step dimensions are expected. Here it is assumed that the beginning of the wire is the point where the height increases above that of the flat terrace. From separate TEM inspections of samples produced using this system, this assumption is reasonable [88]. The wires do not seem to be affected by shadowing arising from the portion of the leading wire that is slightly above the terrace height.

In order to show the applicability of the glancing angle technique to various wire materials, uphill depositions were carried out on similar step-bunched templates by evaporating Fe, Co and Ni. Typical AFM images of the resulting arrays are shown in figure 3.25. As can be seen, ordered rows were successfully grown of these three materials. Wires of non-magnetic materials can also be grown with similar results. This demonstrates the versatility of the method and show that there is a broad potential for this simple technique in terms of the range of systems that can be investigated.

3.4.2.3 Uphill Depositions on Sapphire

Glancing angle depositions on faceted Al_2O_3 templates has previously been shown to produce ordered arrays of nanoparticles of a variety of materials, including Cu, Ag and Au [89]. The focus of previous work on these nanoparticles has been the analysis of their optical properties. Hence, Al_2O_3 is the material chosen for the substrate rather than Si, since it is transparent in the visible range and does ont contribute to the reflectance anisotropy of the system. In this work we focus solely on nanoparticle arrays of magnetic materials. To demonstrate the applicability of the technique for fabrication of ordered rows of nanoparticles, and to examine one of the key parameters, we carried out three Co uphill depositions, each differing only by substrate temperature, on faceted Al_2O_3 templates which have a periodicity of approximately 70 nm. The deposition angle in each case was equal to the miscut angle (6 °). Sample A was at room temperature during the deposition, sample B at 260 °C, and sample C at 400 °C. SEM images from the 3 samples are shown in figure 3.26. One can see that the depositions have resulted in ordered rows of nanowires in the case of sample A, and nanoparticles for samples B and C. The locations of the wires and particles are confined by the dimensions of the step-edge facet, with very little material on the (0001) terraces. From the close-up image 3.26A(ii), it can be seen that the wires are composed of grains ($\approx$ 5 nm or less in diameter), and figures 3.26B(ii) and C(ii) show that the droplets are slightly elliptical in shape with their long axis parallel to the step-edges. It seems that the diffusion length

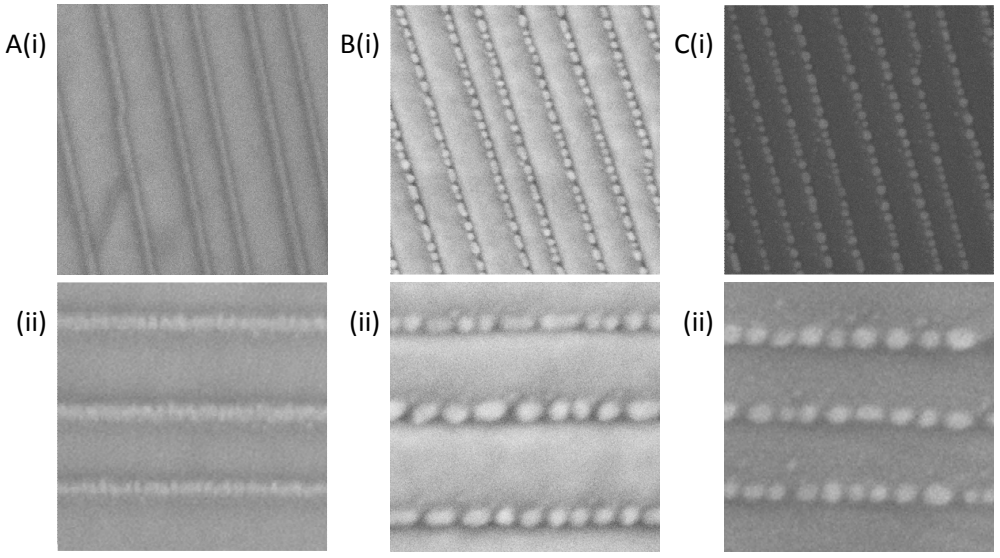


FIGURE 3.26: Co nanowires and nanoparticles on faceted Al_2O_3 substrates

Arrays of nanowires (A) and nanoparticles (B and C) produced by depositing Co in the uphill direction on faceted Al_2O_3 templates. Part (i) images are 500×500 nm and part (ii) images are 200×200nm.

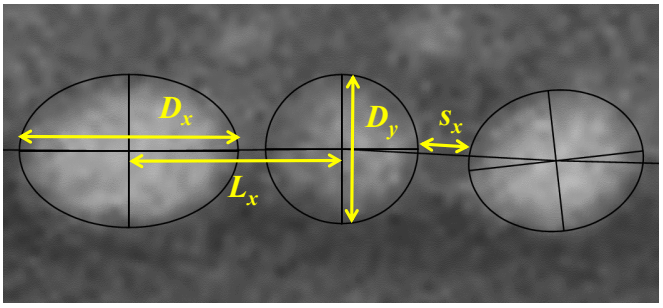


FIGURE 3.27: Important dimensions of Co nanoparticles

Dimensions of nanoparticles which will be referred to throughout the present text. D_x and D_y are the lengths of the major and minor axes respectively. L_x is the centre-to-centre separation of neighbouring nanoparticles along the step-edge direction, and s_x is the interparticle separation.

of the Co atoms has increased with temperature, allowing them to form droplets which lowers the surface energy of the system. As the temperature is increased further, one would expect the droplets to become slightly rounder, and comparing 3.26B(ii) and C(ii) this seems to be the case. To state this with certainty, it was decided to carry out a full analysis on the dimensions of the ellipses. Figure 3.27 shows the relevant dimensions superimposed on an SEM image of three Co nanoparticles. In this figure, D_x and D_y are the lengths of the major and minor axes respectively. L_x is the centre-to-centre separation of neighbouring nanoparticles along the step-edge direction, and s_x is the interparticle separation. Over 400 nanoparticles from each of the two samples were examined using AutoCAD software. The average values for the major and minor axes $\langle D_x \rangle$ and $\langle D_y \rangle$, as well as their standard deviations (σ), average interparticle separation $\langle s_x \rangle$ and average eccentricity, $\langle e \rangle$, (calculated by equation 3.6) are shown in table 3.2.

$$e = \sqrt{1 - \left(\frac{D_y}{D_x}\right)^2} \tag{3.6}$$

The data for D_x and D_y show that the average nanoparticle size has increased. This can be explained by the increasing temperature causing some of the nanoparticles to coalesce.

TABLE 3.2: Average dimensions of nanoparticles grown at two different substrate deposition temperatures

Average major and minor axis values for elliptical nanoparticles grown at 260 °C and 400 °C. Also shown for each sample is the average interparticle separation s and eccentricity, e.

Temperature	$\langle D_x \rangle$ - nm (σ)	$\langle D_y \rangle$ - nm (σ)	$\langle s_x \rangle$ - nm	$\langle e \rangle$
260 °C	18.2 (4.6)	13.6 (1.8)	3.1	0.60
400 °C	18.5 (3.7)	15.5 (2.4)	4.5	0.49

Furthermore there is a decrease in eccentricity. This is caused by the increased mobility of the Co atoms, which allows the nanoparticles to assume a rounder shape which has lower surface energy. The interparticle separation increases with temperature, which is linked to the previously mentioned findings as the total Co volume remains constant. These results are important, since the shape and separation of these nanostructures will determine their magnetic behaviour, as shown in section 4.3, as well as their optical response, as has been demonstrated in separate studies [89, 90].

3.5 Conclusions

The main findings of this chapter relate to the preparation of step-bunched Si templates and the formation of ordered arrays of nanowires and nanodots. With regard to the former, it was shown that highly ordered rows of step-bunches could be formed on templates with a miscut in the $\left[11\bar{2}\right]$ direction by annealing with a current in the step-up or step-down directions. Step bunches with a periodicity of 50-150 nm were achieved with a step-up current in Regime I (as defined in table 3.1). Larger step-bunches having a periodicity of 1.1 μm were attained by annealing with a step-down current in Regime I, and still larger bunches with a periodicity of 2.9 μm were achieved with step-up current by annealing in Regime II.

Previous studies have focused on the effect of temperature and annealing time on the resulting morphology. Here, it was shown how the cooling rate from the annealing temperature to a lower resting temperature below the 1×1→7×7 transition temperature can affect the periodicity of the resulting step array. Specifically, it was found that the periodicity was smaller for faster cooling rates. Assuming that quenching the sample preserves its higher temperature morphology, this indicates that the surface at the annealing temperature is a uniform array of single atomic height steps, and that the bunching is a process that occurs during cooling across the 1×1→7×7 transition. Slower cooling rates prolong the time spent at this quasi-equilibrium state, allowing the 7×7 facets to expand, thereby giving rise to greater periodicity. By analysing the slope across the sample, it was noted that the difference between the angles of the bunches and the terraces was approximately 22 °. This suggests that the bunches witnessed may in fact be (331) facets, and that the bunching procedure may be a period of co-stabilisation of the two facet groups. Other studies of Si samples prepared in a very similar manner have demonstrated the formation of (331) facets [68].

The use of cooling rate as a functional parameter for periodicity control is attractive due to the small change of periodicity as a function of the control, i.e. varying the cooling rate by an order of magnitude changes the periodicity by a relatively small

amount. This makes it useful for fine-tuning of the periodicity, and furthermore makes it a useful parameter for obtaining reproducible results across several annealing systems, where exact definition of other parameters such as temperature may be problematic. Additionally, the finding highlights that it is important that the cooling rate is considered and reported in any experiment where Si (111) is annealed at high temperatures and subsequently cooled. While no variation in periodicity was noticed as a function of angle, the range investigated was very narrow and further experiments will need to be carried out to check for dependency.

In relation to the formation of wire arrays, it was shown that well ordered rows of nanowires of a variety of materials could be grown. It was also shown how wire width and thickness could be controlled by choice of deposition angle and duration respectively. TEM images of Fe and Co nanowire arrays revealed that the wires are polycrystalline as suspected from the AFM images.

The ability to grow ordered arrays of nanoparticles on faceted Al_2O_3 templates was demonstrated. It was shown that carrying out the deposition at higher temperatures resulted in rounder nanoparticles due to the increased mobility of the adatoms on the surface of the template. This is expected to alter the absorption resonance frequency of the nanoparticles. The heating also results in an increased average inter-particle separation, which will affect the level of dipolar coupling between nanoparticles. This is expected to have consequences both for the resonant frequency of the nanoparticles as well as the magnetic shape anisotropy of the array as a whole, which may act as a system of disconnected particles whose magnetic shape anisotropy is primarily due to inter-particle interactions [91].

Chapter 4

Magnetic Characterisation of Nanowire Arrays

Minimisation of feature size in electronic devices is attractive for reasons of both convenience of smaller device volume and due to the exciting phenomena that emerge at the nanoscale which we seek to control and manipulate [13]. The study of magnetism, which has important applications in existing technologies such as memory storage, and emerging fields such as spintronics, is no different this respect [92]. A challenge associated with minimisation is that as dimensions are reduced, thermal energy rivals the magnetostatic energies that stabilise magnetisation. Nanowires of magnetic materials are attractive in this area since their shape anisotropy can stabilise the direction of magnetisation more effectively than isotropic structures. Since the magnetisation will typically be aligned in specific directions, they are naturally attractive for use in logic or storage devices which require binary expression (although ternary and quaternary magnetic storage devices have also been proposed [93–96]). This chapter begins with a discussion of the origin of shape-induced magnetic anisotropy and two important effects relating to magnetic nanowires, namely reversal mechanisms and interwire interactions. In the second half of this chapter experimental data from measurements of the nanowire arrays whose fabrication was described in the previous chapter will be shown relating to each of these topics.

4.1 Magnetic Phenomena in Nanowire Arrays

This section will look at some of the aspects of magnetisation which are expected to arise in studies of magnetic nanowire arrays. Much of the more general details can be found in good books on magnetism such as *Introduction to the Theory of Ferromagnetism* by

Amikam Aharoni, *Physics of Ferromagnetism* by Soshin Chikazumi and *Magnetism and Magnetic Materials* by J.M.D. Coey [97–99]. Other references are given for more specific details.

4.1.1 Magnetic Anisotropy

Magnetic anisotropy is the energy dependence of the direction of magnetisation, $\mathbf{e}_M$, with respect to certain axes. The directions which are energetically favourable and unfavourable for the magnetisation to point towards are called 'easy axes' and 'hard axes' respectively. The anisotropy energy density, E_a, is related to the angle θ between the magnetisation and the easy axis via the anisotropy coefficient K, which has unit $\mathrm{J\,m^{-3}}$. Magnetic anisotropy is key to the stabilisation of the direction of magnetisation, $\mathbf{e}_M$, in a particular direction. Without some source of anisotropy, $\mathbf{e}_M$ would fluctuate randomly, as the switching field and energy of reversal would both be zero. There are several different sources of magnetic anisotropy, which are outlined in the following. More than one source of anisotropy may be present for a given system.

- **Shape Anisotropy**

  Shape anisotropy is due to the energy of a sample in its own demagnetising field H_d, which is brought about by dipole-dipole interactions between spins. The demagnetising field is lowest when the magnetisation is aligned with the longest dimension of the magnetic particle, and hence this is the lowest energy configuration. This form of anisotropy is the main focus of the experiments on magnetic nanowires described in this chapter. Further discussion, including the expressions for self-energy as a function of the demagnetising field will be given later. The coefficient for shape anisotropy is denoted K_{SH}.

- **Magnetocrystalline Anisotropy**

  Magnetocrystalline anisotropy is the dependence of the energy on the direction of $\mathbf{e}_M$ with respect to the principal axes of the crystal structure. It is due to the interaction of the crystal field with the electronic orbitals, and therefore with the spin, via spin-orbit coupling. In the case of crystal structures with uniaxial anisotropy, such as hexagonal crystals, interatomic dipole-dipole interactions also contribute. Magnetocrystalline anisotropy is an intrinsic property of a material, and the anisotropy coefficient is denoted K_{MA}.

- **Induced Anisotropy**

  These are anisotropies that are brought about during the growth of the magnetic material. Induced anisotropy may be due to stress brought about by epitaxial

growth on a slightly mismatched substrate. This is also called strain-induced anisotropy and is an example of a magnetoelastic effect. Anisotropy can also be induced through texturing or by annealing certain films in the presence of large magnetic fields.

- **Surface Anisotropy**

  For thin films and nanoparticles, surface anisotropy must also be considered, which is caused by the broken symmetry of the crystal at surfaces. In this case the energy density term, K_{SA}, has units of $\mathrm{J\,m^{-2}}$, and the surface anisotropy energy is

$$\varepsilon_{SA} = \int K_{SA} \left[1 - (\mathbf{e}_M \cdot \mathbf{e}_n)^2\right] \, d^2r \tag{4.1}$$

  where $\mathbf{e}_n$ is the unit vector pointing normal to the surface. For positive K_{SA}, this is minimised by having the magnetisation pointing normally to the surface, whereas parallel alignment is preferred for $K_{SA} < 0$. Positive K_{SA} is the norm for most ferromagnetic materials [100, 101], but this is commonly overwhelmed for very thin films and at certain interfaces due to magnetoelastic strain [32, 102, 103].

- **Exchange Anisotropy**

  Exchange anisotropy is brought about due to exchange interactions at an interface between ferromagnetic and antiferromagnetic materials. Unlike other sources of anisotropy it is unidirectional, with the easy direction being defined by the direction of the spins of the antiferromagnetic layer at the interface. It may also arise at a hard/soft magnetic interface, in which case the easy direction is defined by the direction of magnetisation in the hard layer. If θ is the angle between the easy direction and $\mathbf{e}_M$, then the exchange anisotropy energy is

$$\varepsilon_{EA} = -\int K_{EA} cos\,\theta \, d^2r \tag{4.2}$$

  where K_{EA} is the anisotropy energy coefficient. In the case of a ferromagnetic/antiferromagnetic interface, the direction of the antiferromagnetic spins at the interface is 'set' by cooling the system across its Néel temperature in the presence of a magnetic field. This antiferromagnetic interface will then 'pin' the ferromagnetic layer via exchange coupling, causing a shift of its hysteresis loop in the $+H$ or $-H$ direction, depending on the direction of the applied field during cooling. An important application of exchange pinning is the 'spin valve', a device whose resistance depends on the relative directions of magnetisation between a ferromagnetic 'pinned layer' whose direction is exchange coupled by an antiferromagnetic layer, and another ferromagnetic 'free layer' which is separated from the pinned layer by a metallic or insulating thin spacer layer [92, 104].

For hard/soft magnetic interfaces, for example a bilayer interface, the system is first saturated in a particular direction, and thereafter the hard magnetic region will influence an exchange anisotropy on the soft magnetic layer, provided the applied field does not exceed the switching field of the hard layer.

This formalism can be used to describe any unidirectional anisotropy which may come about for a variety of reasons.

Since the wires in the present study, which are grown on oxidised, step-bunched Si templates, are composed of randomly oriented crystalline grains with no long-range order (as evidenced by results in the previous chapter such as figures 3.20 and 3.23), the possibility of a 'net' easy axis arising from from magnetocrystalline anisotropy is discounted. However, the distribution of easy axis direction at the scale of the individual grains may impinge on the effect of shape anisotropy, for example by reducing remanence due to a localised preference for magnetisation direction which may be different from the wire axis. Typical sources of stress or strain such as epitaxial growth on a slightly mismatched substrate are absent, ruling out the potential for induced anisotropy. Therefore in the following analysis, the main source of anisotropy is assumed to be shape anisotropy, although due to the small thicknesses involved and the presence of oxide interfaces, there may also be an influence from surface and exchange anisotropies.

As mentioned above, magnetic shape anisotropy is due to the energy of a sample in its own demagnetising field H_d. The magnetostatic energy due to shape anisotropy can be given by

$$\varepsilon_m = \tfrac{1}{2}\mu_0 \int_V \mathbf{H}_d \cdot \mathbf{M}\, \mathrm{d}^3 r \tag{4.3}$$

where $\mathbf{H}_d$ is the demagnetising field, $\mathbf{M}$ is the magnetisation and the integral is over the entire volume of the ferromagnet, V. The demagnetising field is the field created by the magnetisation of the object itself. It is also called the stray field. Usually the terms 'demagnetising field' and 'stray field' are used in relation to the field inside and outside the magnet respectively. The demagnetising field (inside the magnet) can be given by

$$H_{di} = -\mathcal{N}_{ij} M_j \qquad i, j = x, y, z \tag{4.4}$$

where $\mathcal{N}_{ij}$ is the demagnetising tensor. For an ellipsoidal ferromagnetic particle, $\mathbf{H}_d$ and $\mathbf{M}$ are uniform throughout the entire volume, and $\mathcal{N}$ is diagonal with entries, $\mathcal{N}_x$, $\mathcal{N}_y$, $\mathcal{N}_z$, known as demagnetising factors. The trace of $\mathcal{N}$ is 1, and so by symmetry, a sphere has $\mathcal{N}_x = \mathcal{N}_y = \mathcal{N}_z = 1/3$. The demagnetising factors for some other simple shapes are shown in table 4.1. Long axes of ferromagnetic shapes, such as the long axis of a rod or wire, or a planar axis of a thin film, have correspondingly low demagnetisation factors,

TABLE 4.1: Demagnetising Factors for Common Shapes

Demagnetising factors for some common shapes. The z axis is chosen to be perpendicular to the plane of the film and parallel to the long axis of the rod. The oblate/prolate spheroid has x, y and z semi-axes of length a, b and c with $a = b$ and $c \neq a$.

Shape	$\mathcal{N}_x$	$\mathcal{N}_y$	$\mathcal{N}_z$
Sphere	$1/3$	$1/3$	$1/3$
Thin Film	0	0	1
Narrow Rod	$1/2$	$1/2$	0
Oblate/Prolate Spheroid	$\mathcal{N}_a$	$\mathcal{N}_a$	$\mathcal{N}_c = 1 - 2\mathcal{N}_a$

and vice versa. Axes with low and high demagnetisation factors are said to be 'easy' and 'hard' axes respectively.

For an ellipsoidal particle, the general form for the demagnetising field energy is

$$\varepsilon_m = \tfrac{1}{2}\mu_0 V M^2 \left(\mathcal{N}_x m_x^2 + \mathcal{N}_y m_y^2 + \mathcal{N}_z m_z^2\right) \tag{4.5}$$

where the m_i ($i = x,y,z$) are the projections of the unit vector of the magnetisation ($\hat{\mathbf{m}}$) along the x, y and z axes. If we assume a particular axis with the demagnetising factor given simply by $\mathcal{N}$, we have

$$\varepsilon_m = \tfrac{1}{2}\mu_0 V \mathcal{N} M^2 \tag{4.6}$$

where $\mathcal{N}$ is for the shared axis of M and H_d. The difference in energy between alignment of magnetisation along an easy and a hard axis may now be calculated for this case. Let us suppose that the demagnetisation factor along an easy axis is $\mathcal{N}$, and along two equivalent hard axes it is $\mathcal{N}' = 1/2\,(1 - \mathcal{N})$. Then the difference in magnetostatic energy between the cases where the magnetisation is aligned along the hard and easy axes, $\Delta\varepsilon_m$, is given by

$$\Delta\varepsilon_m = \tfrac{1}{4}\mu_0 V M^2 \,(1 - 3\mathcal{N})\,. \tag{4.7}$$

Dividing this value by V gives the magnetostatic energy density E_a, which can be described in relation to the angle between the magnetisation $\mathbf{M}$ and the easy-axis:

$$E_a = K_{SH} \sin^2(\theta) \tag{4.8}$$

where K_{SH} is the anisotropy constant in units of $\mathrm{J\,m^{-3}}$ and is equal to

$$K_{SH} = \tfrac{1}{4}\mu_0 M^2 \,(1 - 3\mathcal{N})\,. \tag{4.9}$$

The preference for magnetisation to lie along the long axes of ferromagnetic shapes can also be understood by considering the phenomenon of 'charge avoidance'. The magnetic surface charge can be given by $\mathbf{M} \cdot \mathbf{e}_n$ where $\mathbf{e}_n$ is the surface normal vector. The energy

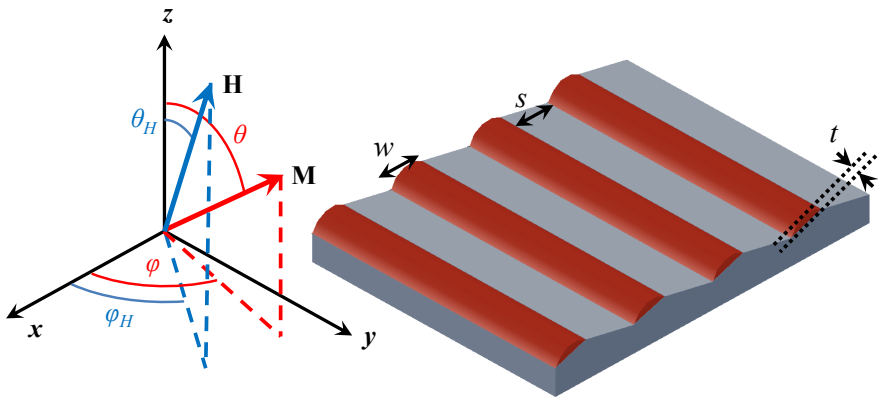


FIGURE 4.1: Labels and axes of wire array parameters.

cost is associated with the stray field H_d, which can be used to give an alternative, yet equivalent expression for ε_m:

$$\varepsilon_m = \tfrac{1}{2}\mu_0 \int H_d^2 \, d^3r \tag{4.10}$$

where the integral is over the all space. Thus a ferromagnetic particle will seek to avoid surface charge by preferentially aligning its magnetisation parallel to its sides. Minimising surface charge will mean aligning magnetisation parallel to its longest sides, which gives a qualitative explanation for the observed behaviour.

4.1.1.1 FMR as a probe of magnetic anisotropy

The resonance condition of a ferromagnetic system can be described using the Smit-Beljers formalism. The full derivation of this is given in Appendix A. Here, only the definition of the co-ordinate system and the final result are given. The co-ordinates and their relation to the sample axes are as shown in figure 4.1. As can be seen the sample surface is described by the $x-y$ plane, with the wires being parallel to the $y-$axis. Also included in this images are the labels for the wire width, separation and thickness, which are denoted w, s and t respectively.

For the case of elongated nanowires, the demagnetising factor corresponding to the direction parallel to the axis of the nanowires, $\mathcal{N}_y$, is assumed to be zero, meaning that the other demagnetising factors are related by $\mathcal{N}_x = 1 - \mathcal{N}_z$. The model was fitted to experimental data taken when the applied field was directed in the xz plane,

meaning that $\varphi_H = 0$. Given these conditions, the final expressions using the Smit-Beljers formalism are:

$$H_R \sin(\theta_H - \theta) - \tfrac{1}{2}(1 - 2\mathcal{N}_z) M \sin(2\theta) = 0$$

$$\left(\frac{\omega}{\gamma}\right)^2 = \left[H_R \cos(\theta - \theta_H) + (1 - 2\mathcal{N}_z) M \cos(2\theta)\right] \times \left[H_R \frac{\sin\theta_H}{\sin\theta} - M(1 - \mathcal{N}_z)\right], \tag{4.11}$$

where H_R is the value of the applied field at which resonance occurs, ω is the resonance frequency and M is the magnitude of the magnetisation.

4.1.2 Important Length Scales in Magnetism

This section contains a brief review of length scales that are relevant for magnetic nanostructures. These will be referred to in later discussion and analysis. The following closely follows *Magnetism and Magnetic Materials* by J. M. D. Coey [32] and a review paper by C. H. Marrows [105].

A useful starting point for length scales is the 'exchange length', l_{ex}, which characterises the relative competition between the exchange energy and the dipolar energy. On a length scale of l_{ex} within a material the exchange dominates the direction of magnetisation $\mathbf{e}_M$. It is given by

$$l_{\mathrm{ex}} = \sqrt{\frac{A}{\mu_0 M_s^2}}. \tag{4.12}$$

Here, A is the exchange stiffness, which is proportional to both the Curie temperature T_C and the exchange constant $\mathcal{J}$. Two evaluations for A are $k_B T_C / 2\, a_0$, where a_0 is the lattice parameter of the unit cell, and $\mathcal{J} S^2 Z_c / a_0$, where $\mathcal{J}$ is the exchange constant, S is the spin quantum number and Z_c is the number of atoms per unit cell.

As mentioned in section 4.1.1, without magnetic anisotropy the magnetisation would not have a preferred direction and its direction would fluctuate randomly due to thermal effects. Thus anisotropy is intrinsically linked with stability of the direction of magnetisation. Even with some anisotropy, there will be a certain size below which the thermal effects will overcome the magnetostatic energy and will cause the the magnetisation to flip randomly. Such a particle is said to be superparamagnetic, since it no longer exhibits typical ferromagnetic traits such as hysteresis and remanence. The superparamagnetic blocking radius, R_b, is the radius below which a particle will undergo the spontaneous

fluctuations of $\mathbf{e}_M$ and it is given by

$$R_b = \left(\frac{6\, k_B\, T}{K_1} \right)^{1/3} \tag{4.13}$$

where K_1 is the anisotropy constant.

Since domain walls are regions where the magnetisation turns between two preferred directions, the anisotropy constant also has a role to play in their width. Here a Bloch wall is considered, which is the most common variety of domain wall. In a Bloch wall, the magnetisation rotates in the plane of the wall. The beauty of the Bloch wall is that even though the direction of magnetisation ($\mathbf{e}_M$) rotates, we still have $\nabla \cdot \mathbf{M} = 0$ everywhere, and so there is no magnetostatic energy cost associated with the wall apart from the exchange energy cost. In the strictest sense, a domain wall has infinite width since the rotation asymptotically approaches the anti-symmetric directions on either side of the wall. However, useful values for domain wall width can be calculated by weighing the exchange energy cost versus the anisotropy energy cost for a number of planes in the domain wall [105]. The result is a domain wall width δ_w given by

$$\delta_w = \pi \sqrt{\frac{A}{K_1}}. \tag{4.14}$$

As it happens, the exchange stiffness A does not vary a great deal from one material to another, while K may vary over several orders of magnitude, and is therefore the key parameter for determining the width of a domain wall.

The 'hardness parameter' κ is a useful parameter which gives the ratio of anisotropy to dipole energy. It is equal to

$$\kappa = \sqrt{\frac{K_1}{\mu_0\, M_s^2}}. \tag{4.15}$$

The hardness parameter is directly related to the 'quality factor', Q, which is equal to $2\kappa^2$. This parameter gives us a convenient way of expressing the maximum radius for a particle that may be single-domain in equilibrium, R_{sd}. Particles which are in equilibrium and have diameter greater than this value always reduce their total energy by inclusion of at least one domain wall, with the increase in exchange energy offset by the reduction of magnetostatic energy associated with the stray field. R_{sd} is given by

$$R_{sd} = 34\, \kappa\, l_{\mathrm{ex}} \tag{4.16}$$

If a particle is sufficiently small, then its direction of magnetisation may be changed uniformly within the entire body of the nanoparticle, i.e. the direction of magnetisation $\mathbf{e}_M$ does not depend on location within the nanoparticle. This is known as coherent

TABLE 4.2: Useful parameters for common ferromagnetic materials

Values for saturation magnetisation M_s, exchange length l_{ex},exchange stiffness A, hardness parameter κ, maximum radius for coherent rotation R_{coh},maximum radius for a single domain particle at equilibrium R_{sd}, width of Bloch domain wall δ_w and Curie temperature T_C.

Material	M_s	l_{ex}	A	κ	R_b	R_{coh}	R_{sd}	δ_w	T_C
Unit	MA m^{-1}	nm	pJ m^{-1}		nm	nm	nm	nm	°C
Fe	1.71	2.4	21	0.12	8	12	10	64	771
Co	1.44	3.4	31	0.45	4	17	56	24	1117
Ni	0.485	5.1	8	0.13	17	25	24	125	358
$Ni_{80}Fe_{20}$	0.84	3.4	10	0.01	55	17	1.6	800	450

rotation, and the maximum radius for a particle whose magnetisation may rotate coherently is known as the coherent radius, R_{coh}, and is related to the exchange length as follows:

$$R_{coh} = \sqrt{24}\, l_{\mathrm{ex}}. \tag{4.17}$$

Values for M_s, l_{ex}, A, κ, R_{coh}, R_{sd} and δ_w are given in table 4.2. Also included for convenience in the table is the Curie temperature, T_C.

4.1.3 Reversal Mechanisms

Understanding the reversal mechanism of magnetic nanowires is important, since this will influence the switching time as well as the stability of the magnetisation, which are both important considerations for application purposes. As mentioned above, ferromagnetic particles with radii below R_{coh} may rotate coherently and without the need for a domain wall. For larger particles where magnetostatic self-energy becomes more important, reversal may take place 'incoherently', whereby the magnetisation may rotate at different rates throughout the material. For still larger particles or nanowires, a domain may nucleate at one end of the particle and propagate along the length of the body until the magnetisation is completely reversed. This form of reversal is known as 'nucleation-propagation' reversal. Identifying whether coherent or nucleation-propagation mode reversal in nanowires is of interest to researchers and is commonly investigated by examining the temperature dependence of coercivity. In principle the coercivity can be found by first finding the shape anisotropy for an infinite wire using equation 4.9. Letting $\mathcal{N} = 0$ in this equation gives us

$$K_{SH} = \tfrac{1}{4}\,\mu_0\, M_s^2. \tag{4.18}$$

Following Brown [106], for a uniformly magnetised ellipsoid the coercivity is given by

$$\begin{aligned} H_c &\geq \frac{2\,K}{\mu_0\,M_s} - \mathcal{N}\,M_s \\ \Rightarrow H_c &= \frac{2\,K_{SH}}{\mu_0\,M_s} \\ \Rightarrow H_c &= \frac{M_s}{2}. \end{aligned} \tag{4.19}$$

In reality, coercivities never reach such values, a phenomenon known as Brown's Paradox [33, 100, 107]. This is due to a range of reasons, including shapes being inhomogeneous, deviations from ideal ellipsoidal shapes, the need to first nucleate a domain and local variations in anisotropy. Thermal effects also play a role in reducing coercivity from theoretical values, yet fortunately this behaviour is relatively more predictable and can yield useful insights as shall be illustrated.

Following Néel, the energy barrier for magnetisation reversal E_B can expressed as a power law

$$E_B = E_0 \left(1 - \frac{H}{H_0}\right)^m \tag{4.20}$$

where H_0 is the switching field at T= 0K and E_0 is the energy barrier when the applied field is zero [108, 109]. The factor m is equal to 2 in the case of aligned Stoner-Wolfarth particles undergoing coherent reversal provided that the applied field is directed parallel to the easy axis. Howver, for reversal via nucleation of a domain wall which propagates along the length of the particle (nucleation-propagation reversal) m is reduced to $3/2$ [110]. Assuming an attempt frequency f_0 for crossing the energy barrier, then there is an associated relaxation time τ, given by

$$\frac{1}{\tau} = f_0 \exp\left(\frac{-E_B}{k_B T}\right). \tag{4.21}$$

Using typical values for f_0 and assuming a measurement time on the order of 100 s, this can be re-arranged to get

$$E_B \approx 25\,k_B T. \tag{4.22}$$

Substituting this value back into 4.20 gives

$$H_c(T) = H_0(T)\left(1 - \left(\frac{25\,k_B T}{E_0(T)}\right)^{1/m}\right). \tag{4.23}$$

The temperature dependencies of H_0 and E_0 can be related to that of M_s, which is more user-friendly, by assuming that H_0 is proportional to M_s and E_0 is proportional to M_s^2. Setting $H_0(T) = H_c(0)M_s(T)/M_{s0}$ and $E_0(T) = E_{00}M_s^2/M_{s0}^2$ (where H_{c0}, M_{s0} and E_{00} are the 0 K values of coercivity, saturation magnetisation and energy barrier height in

zero applied field, respectively), the following expression for $H_c(T)$ is obtained.

$$H_c(T) = H_{c0}\frac{M_s(T)}{M_{s0}}\left[1 - \left(\frac{25\,k_B T\,M_{s0}^2}{E_{00}M_s^2}\right)^{1/m}\right] \tag{4.24}$$

By fitting coercivity to this equation we have a means of finding m and thus we have a means of identifying the reversal mechanism, which is a central to our understanding of magnetic behaviour at a fundamental level. This approach has been used is the past by studies investigating polycrystalline magnetic nanowires grown via electrodeposition into porous Anodized Aluminium Oxide (AAO) templates [37, 110–112].

4.1.4 Interwire Interactions

Most of us are aware that when two bar magnets are brought close together, that the opposite poles will attract, and if they are allowed to move freely then they will align with their magnetisation pointing in opposite directions. This is an effort by the system to reduce its magnetostatic dipolar energy. On the nanoscale where positions of magnetic nanowires are fixed, they may still attempt to reduce the dipolar energy by opting for anti-symmetric alignment of magnetisation in neighbouring nanowires. This effect is expected to increase as a function of decreasing distance between the nanowires. As such, the study of interwire interactions is hugely important for application purposes since reducing bit density means decreasing the separation between magnetic components. While a number of studies have been carried out on coupling between wires in vertical nanowire arrays [34, 113–117], there has been very little examination of coupling in planar arrays of magnetic nanowires, which for some application purposes may more accurately represent the end-product. A series of studies by Elmers, Hauschild *et al.* found a transition from superparamagnetic to ferromagnetic behaviour in their thin (2 monolayers or less) nanowires of Fe on W(110), which they say is due to dipolar coupling between wires [118–121]. However, there is little direct evidence provided for dipolar coupling at room temperature.

The effect of dipolar coupling in nanowire arrays is illustrated schematically in figure 4.2. In this figure, the arrows represent the direction of magnetisation in neighbouring nanowires within an array. The blue wires (4.2a(i) and 4.2a(ii)) have a large separation between them so that they are effectively isolated or non-interacting, whereas the green wires (4.2b(i) and 4.2b(ii)) are close together and are interacting. For the non-interacting case, both the parallel and anti-parallel alignments of magnetisation have a similar magnetostatic energy E (see points a(i) and a(ii) in the energy graph on the right-hand panel of figure 4.2). Since the wires have an easy axis parallel to their length, there is an energy barrier associated with the transition between parallel and anti-parallel

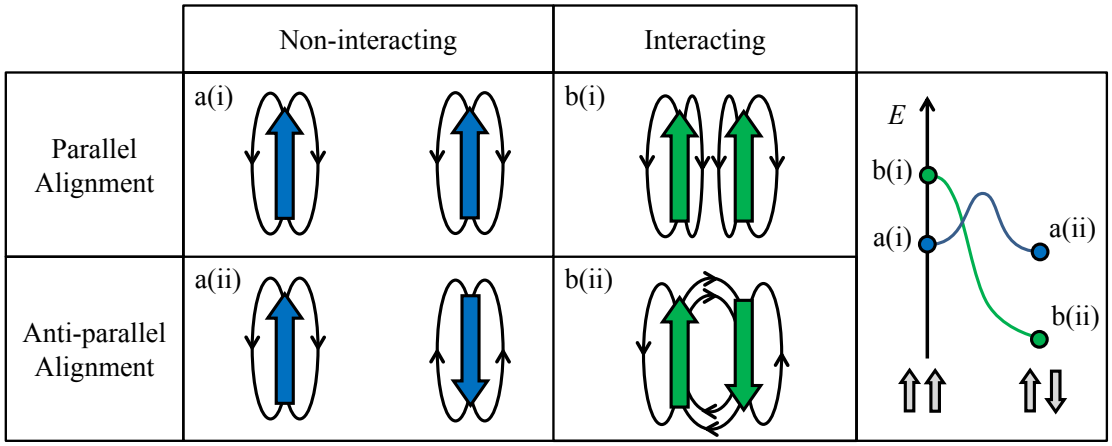


FIGURE 4.2: Schematic images of the effect of dipolar coupling with nanowire arrays.

Schematic images showing the stray fields of nanowires in planar arrays. The arrows correspond to the direction of the magnetisation of the nanowires. The blue wires (a(i) and a(ii)) represent wires which are sufficiently separated so that they are effectively isolated, while the green wires (a(i) and a(ii)) have a small separation and are influenced by the stray field of their neighbours (black arrows). There is little difference between the energy levels of both configurations of the non-interacting wires (blue dots in panel on right), while the anti-parallel alignment is energetically preferred over the parallel alignment in the case of interacting wires (green dots in panel on right).

alignments and so both arrangements are energetically stable. For the interacting case (green wires), however, the anti-parallel alignment more energetically favourable than the parallel alignment. depending on the specific dimensions and conditions, there might not be an energy barrier between the two states (right-hand panel, green curve) and the system may freely adopt an anti-parallel configuration from an initial parallel one. Note that these curves and the positioning of the coloured dots on the right-hand panel of figure 4.2 are for illustration purposes only.

Thus, if an external field is applied in the plane of the array parallel to the axis of the wires (the y-axis according to figure 4.1) and subsequently removed, then the magnetisation of the wires will remain in a parallel alignment in the case of non-interacting wires, but for wires which are closer together and are interacting there will be a greater probability that neighbouring wires will adopt the anti-parallel configuration. This will result in lower remanence and coercivity for wires with smaller separation. Adeyeye *et al.* showed that this effect becomes noticeable in stripe-like wire (such as those described here) for $s/w < 1$ [122].

However, when the external field is directed in the direction in-plane perpendicular to the axis of the wires (the x-axis in figure 4.1) the case may be different. This was shown by Zighem *et al.* who conducted a series of simulations investigating the effects of dipolar coupling in arrays of ferromagnetic nanowires [114]. They found that in the

case of applied field being applied along x, that coercivity and remanence increased for reduced separation compared to the isolated case. They explained the finding by showing that the stray fields favour alignment, and that in the limit $s \to 0$ the array becomes a continuous film and x is an easy axis like y. Some of these predictions have been confirmed experimentally [35] though most studies of interwire interactions which are carried out in AAO templates vary wire width in order to vary separation, so the wire volume for each case is different, which somewhat complicates the analysis.

The study of interwire interactions using Henkel analysis is based on a manipulation of the two different remanence measurements described in section 2.3.2.1, i.e. the isothermal remanent magnetisation $m_R(H)$ and DC demagnetisation remanence $m_D(H)$. The lowercase 'm' here indicates that both values are normalised with respect to the remanence for infinite applied field, $M_R(\infty)$.

Henkel showed that the quantity δm given by

$$\delta m(H) = m_D(H) - (1 - 2m_R(H)) \tag{4.25}$$

should be equal to zero for all H [123]. Deviations from zero are usually considered evidence of dipolar or exchange interactions between particles in the system, and plots of δm versus H, known as 'Henkel Plots' are widely used to investigate interwire interactions [34, 116, 117, 124–127]. Strictly speaking, deviations may also be caused by non-uniaxial anisotropy and deviations from the single domain state, so care must be taken when making comparisons. Positive and negative peaks in the Henkel plot point to 'cooperative-' and 'non-cooperative reversal' respectively [125]. In cooperative reversal the dominant interaction is exchange interaction and particles prefer to be aligned throughout the reversal whereas in non-cooperative mode the dipolar interaction is dominant and particles prefer to by aligned anti-symmetrically. The distinction depends on the alignment for the lowest energy state at zero applied field. The position of the peak along the H axis should theoretically be at $H = H_c$ [33, 128] and this has also been shown experimentally for vertical arrays [117].

4.2 Results

4.2.1 Shape Anisotropy

In order to investigate the existence of shape anisotropy in our nanowire arrays, it was decided to produce five samples while varying only one deposition parameter, namely the deposited thickness of Fe [129]. Identical Si templates were cut from a wafer with a 3.5 °

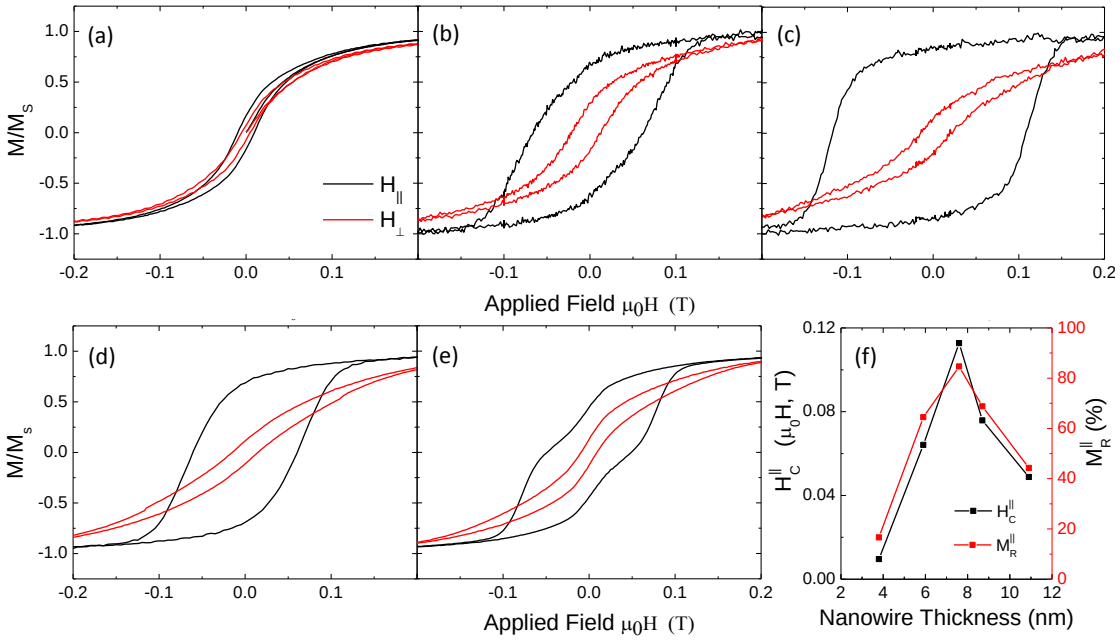


FIGURE 4.3: Shape Anisotropy of Fe nanowire arrays of varying thickness.

Here (a)-(e) show hysteresis loops taken at 300 K for Fe nanowire arrays measured with the magnetisation aligned in-plane parallel (black) and perpendicular (red) to the direction of the wires. Thickness increases gradually from 4.0 nm (a) to 12.1 nm (e), while wire width and separation are kept fixed at 30 nm and 100 nm respectively.
The graph in (f) shows the behaviour of coercivity as a function of the deposited thickness.

miscut in the $[11\overline{2}]$ direction. These were individually annealed with a step-up current as described in section 3.2.3, resulting in regular step-bunches with a periodicity of 128 nm ($\pm 24\,nm$). Following oxidation, deposition was carried out in the uphill direction at an angle equal to the wafer miscut, producing Fe nanowires with a thickness equal to the step-bunch width ($\approx$30 nm). The deposition time was adjusted for samples A, B, C, D and E in order to produce wires with a vertical thickness of 4.0, 6.3, 8.0, 9 and 12.1 nm respectively. Samples were subsequently capped with a 10 nm protective layer of either Ag or MgO. Smaller pieces measuring 3×2.5 mm of each of the samples were cut from the larger sample for magnetic analysis. Hysteresis loops were measured at 300 K using the magnetometer described in section 2.3. Measurements were taken with the magnetic field applied in-plane, both parallel and perpendicular to the wire direction. The results for the five samples are shown in figure 4.3. The coercivity in the parallel and perpendicular directions shall be denoted $H_C^{\parallel}$ and $H_C^{\perp}$ respectively, and similarly the remanence in both directions are denoted by $M_R^{\parallel}$ and $M_R^{\perp}$. As can be seen, for all samples the parallel direction to the wires (black curves) is the easy axis, with greater coercivity and remanence compared to the in-plane perpendicular direction (red curves). One can see that $H_C^{\parallel}$ and $H_C^{\perp}$ initially increase with deposited thickness (figures a-c) but as thickness is increased further, both coercivity and remanence decrease. The behaviours

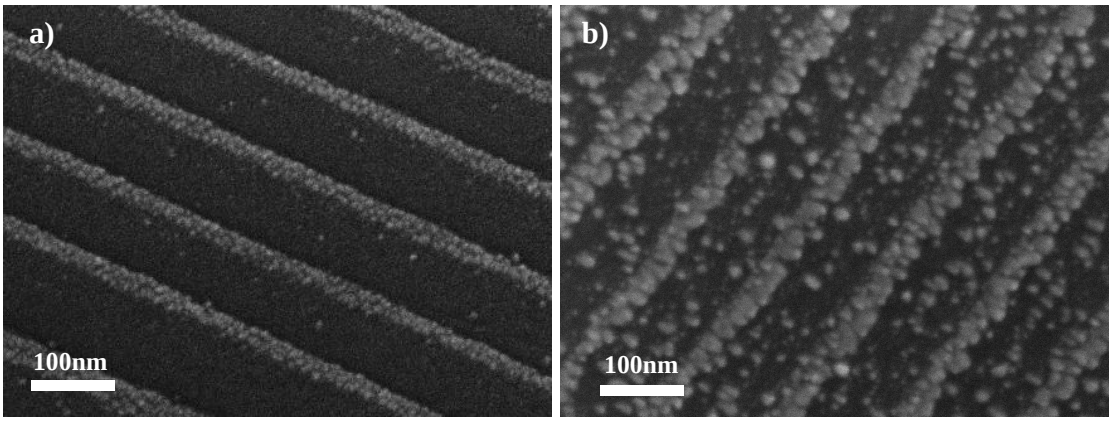


FIGURE 4.4: Dependency of wire structure on deposition thickness.

SEM images of nanowire arrays with wire thicknesses of (a) 2.7 nm and (b) 10 nm.

of $H_C^{\parallel}$ and $M_R^{\parallel}$ as functions of nanowire thickness are shown in figure 4.3(f). The decrease in $H_C^{\parallel}$ and $M_R^{\parallel}$ at low thicknesses is most likely due to a proportion of the grains within the wire behaving superparamagnetically. As thickness increases the grains grow in size and coalesce, resulting in wires composed of strongly interacting grains. This causes $H_C^{\parallel}$ and $M_R^{\parallel}$ to increase as shape anisotropy becomes more influential.

Most unusually, for the greatest thickness, the hysteresis loop seems to be constricted or 'pinched' in the centre (figure 4.3(e)). Some studies have found shifted hysteresis loops due to the behaviour of domain walls at junctions between nanowires [130, 131]. For the present system however, the geometry of the nanowire junctions is not tightly controlled. Other studies have observed pinched loops in cases where magnetocrystalline anisotropy was present, sometimes brought about by carrying out an epitaxial deposition onto a lattice-matched substrate [132–135]. However in the present case, there is no evidence nor any reason to suspect that the grains of which the nanowires are composed have long-range order of their crystal axes. In order to investigate the cause of the pinched loop obsevered for the thickest sample in figure 4.3(e), SEM was carried out on two uncapped samples grown on similar step-bunched templates with deposition times yielding wire thicknesses of 2.7 nm and 10.9 nm. The results are shown in figures 4.4(a) and 4.4(b) respectively. As can be seen from these images, there is a large increase in the number of nanoparticles situated on the terraces as deposition thickness is increased. While just a few small particles can be seen on the terrace for the thinner sample, in figure 4.4(b) we can see that the material on the terraces comprises a sizeable proportion of the total magnetic material. Hence the "pinched" hysteresis loop seen in figure 4.3(e) is likely to be a superposition of hysteresis loops belonging to the nanowires which are well aligned with the step-bunches and the magnetic nanoparticles which decorate the terraces. These particles would also have the effect of reducing the coercivity of the

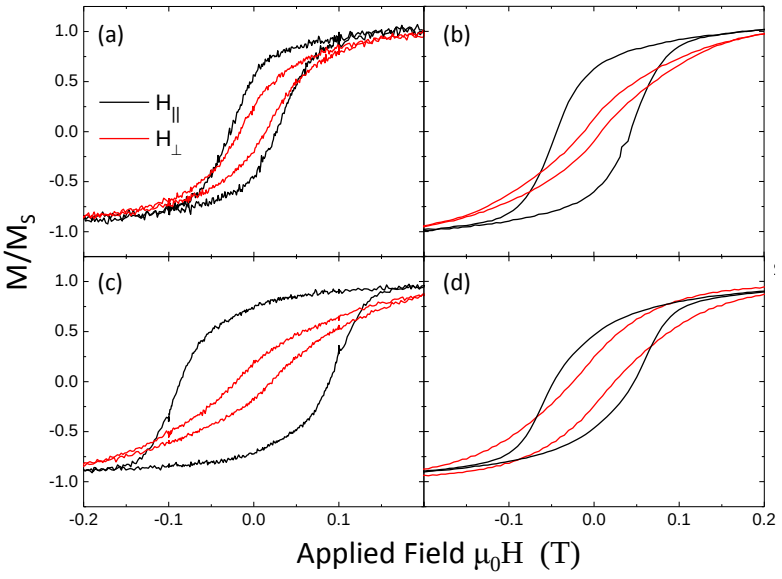


FIGURE 4.5: Shape Anisotropy of Co nanowire arrays of varying thickness.

Shown here are hysteresis loops for four samples A, B, C and D with wire thicknesses of 4, 6, 9 and 13 nm respectively. Black and red curves correspond to magnetisation measured with the applied field directed parallel and perpendicular (respectively) to the axis of the wires.

wires themselves by promoting interwire interaction and reducing shape anisotropy due to localised variations in wire width. Their presence may explain the reduced coercivity and remanence of sample D compared to sample C. In fact, hysteresis loops with very similar shape were noted in a study by Tauxe *et al.* with the reason given being the presence of superparamagnetic particles alongside single-domain particles [136]. Neglecting nanoparticles on the terraces, the increased wire thickness may also have reduced coercivity and remanence via dipolar coupling between the wires [114]. Most likely, the behaviour observed is due to a combination of these effects.

A similar experiment was carried out with arrays of Co nanowires [137]. Four step-bunched Si templates with periodicity of approximately 130 nm were produced in the same manner as those used for the Fe nanowire experiments described above. Following oxidation of the templates, Co was deposited in the uphill direction with deposition times chosen to produce wire thicknesses of 4 nm, 6 nm, 9 nm and 13 nm for samples which shall be referred to as A, B, C and D respectively. Each sample was also covered in a 10 nm protective capping layer. Magnetisation measurements were conducted in the same manner as before, i.e. at 300 K with the field applied in-plane both parallel and perpendicular to the wire direction. The results for the four samples are shown in figure 4.5. The behaviour is very similar to that seen in the case of Fe nanowire arrays. The easy axis corresponds to the direction parallel to the axis of the nanowires. Initially the curves for parallel and perpendicular directions are quite similar, but as thickness

increases the shape anisotropy becomes more prevalent, and the surface anisotropy effect becomes less important as the surface to volume ratio decreases. This causes the large increase of $H_C^{\parallel}$ and $M_R^{\parallel}$ in figure 4.5(b) and (c). As thickness is further increased both $H_C^{\parallel}$ and $M_R^{\parallel}$ decrease (see figure 4.5(d)). The 'pinching' of the hysteresis loop which was very clear in the case of the Fe nanowire array in figure 4.3(e) is very slight in this case, visible only as a slight dip in the curve near the y-axis. Again this is likely to be due to the growing number and size of particles on the terraces, as well as the effect of dipolar coupling between wires. The fact that the pinching is less noticeable in the case of Co may be associated with the fact that the crystal structure is fcc rather than bcc as is the case of Fe. Since the crystal structure is different, so too is the magnetocrystalline anisotropy which will influence behaviour at the scale of the individual grains.

4.2.2 Reversal Mechanism

The reversal mechanism of Fe nanowire arrays was investigated by measuring $H_C^{\parallel}$ as a function of temperature as described in section 4.1.3. This was carried out for four of the five nanowire samples described in the study above, on the effect of thickness on magnetisation at 300 K, namely the samples A, B, C and E. The results of this study are shown in figure 4.6. As can be seen, the effect of increasing temperature causes a monotonic reduction in $H_C^{\parallel}$ for each sample. The decrease becomes less dramatic for thicker samples, indicating that the thermal effects have a greater influence on thinner samples, as would be expected.

As mentioned in section 4.1.3, equation 4.24 can be used to predict the reversal mechanism of nanowire arrays based on the temperature dependence of $H_C^{\parallel}$, with the parameter m equal to 1.5 and 2 for nucleation-propagation mode and coherent mode reversal mechanisms respectively. To determine the reversal mechanism, this equation was fitted with the value of m fixed for each of the two mechanisms. The results of the fitting for m equal to 1.5 and 2 are shown by the red and blue curves (respectively) in figure 4.6. As can be seen, there appears to be little difference between the two plots. The results for the fittings are shown in table 4.3. The χ^2 values for the curves with $m = 2$ and $m = 1.5$ are denoted $\chi^2_{m=2}$ and $\chi^2_{m=1.5}$ respectively, and the ratio between the two ($\chi^2_{m=2}/\chi^2_{m=1.5}$) is given in the third column of table 4.3. As can be seen this value is between 0.7 and 0.48 for the four samples, indicating that the coherent reversal mode is the better fit for the data for each of the four samples. The value of E_{00} initially increases with increasing wire thickness, in agreement with the findings of Zeng *et al.*[111], but is lower for the final sample. The breakdown of this trend is due to the abundance of nanoparticles on the terraces as shown in figure 4.4. It is expected that these nanoparticles, due to their

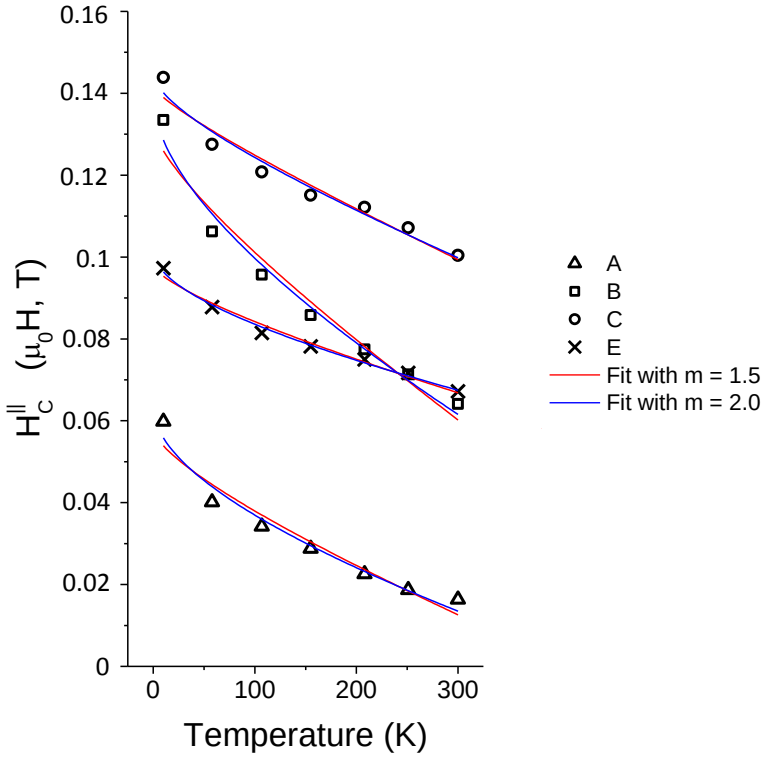


FIGURE 4.6: Dependency of coercivity of Fe nanowire arrays as a function of temperature

Data points for $H_C^{\parallel}$ as a function of temperature for four of the five Fe nanowire array samples described in section 4.2.1. The four samples are prepared in an identical manner except for the deposited thickness of the nanowires, t. The functions fitted correspond to equation 4.24 with the parameter m fixed with a value of 1.5 (red line) and 2 (blue line).

TABLE 4.3: Fitting parameters of temperature dependence of coercivity

Fitting parameters of curves shown in figure 4.6, which were fitted according to equation 4.24. The columns refer to nanowire thickness in the out-of-plane direction, the ratio of the χ^2 values for the two models ($\chi^2_{m=2}/\chi^2_{m=1.5}$), the coercivity at 0 K (H_{C0}), the energy barrier for magnetisation reversal at 0 K in zero applied field (E_{00}), the effective volume of magnetisation reversal V_{eff}, and finally V_{eff} divided by the product of wire thickness and width. The last four columns give values for the model of coherent reversal ($m = 2$)

Sample	**Wire Thickness (nm)**	$\boldsymbol{\chi^2_{m=2}/\chi^2_{m=1.5}}$	$\boldsymbol{H_{C0}\ (m=2)}$ $\boldsymbol{(\mu_0 H, T)}$	$\boldsymbol{E_{00}(m=2)}$ **(eV)**	$\boldsymbol{V_{eff}(m=2)}$ **(nm³)**	$\boldsymbol{V_{eff}/(t\times w)}$ **(nm³)**
A	4.0	0.53	0.064	1.58	2350	19.6
B	6.3	0.48	0.140	3.85	2600	13.7
C	8.0	0.69	0.145	24.46	15870	66.1
E	12.1	0.42	0.102	9.18	8520	23.5

round shape and small size, would have a low barrier for magnetisation reversal, and hence the value of E_{00} for the sample as a whole is reduced.

Following Zeng *et al.* and Wernsdorfer *et al.* [111, 138], the 'effective volume' for magnetisation reversal at 0 K, V_{eff} may be calculated via

$$V_{eff} = \frac{E_{00}}{\mu_0 \, H_{C0} \, M_S}. \tag{4.26}$$

The calculated values for V_{eff} are shown in the 6^{th} column of table 4.3. In line with the findings of Zeng *et al.*, this increases with wire thickness for the first three samples, suggesting that the volume of material which reverses coherently increases with greater wire thickness, as would be expected due to the increasing size of grains of which the wires are comprised. This value falls for the thickest sample, which again is due to the influence of the small, isolated particles on the terraces, both in terms of their superparamagnetic behaviour and their potential to affect the magnetostatic interactions between the wires. The final column shows the wire length associated with the effective volume, which was found by dividing V_{eff} by the product of the nanowire width and thickness for each sample. This value would be expected to behave like E_{00} and V_{eff}, and increase with thickness for samples A to C but decrease for sample E. This trend is not realised exactly, however, perhaps due to the uncertainties accumulated in the calculation of this value.

In summary, this technique was not successful in conclusively proving which reversal mechanism was dominant for each sample. More data points between 0 K and 100 K would provide the means to state more decisively which model was a closer fit to the data. It was noticed that for all four samples the 10 K measurement for $H_C^{\parallel}$ was consistently higher than the fitted curve. It is possible, therefore, that there is some systematic error in the measurement process. For example, it may be necessary to conduct careful temperature calibration of the apparatus. Another possibility is that there is a significant proportion of particles or parts of the nanowires which are superparamagnetic, and contribute to the coercivity only at low temperatures. In spite of this, the fittings did yield meaningful parameters relating to the energy barrier and effective volume of magnetisation reversal at 0 K. Both of these increased with wire thickness as expected an in accordance with previous findings, except for the last sample, whose values of E_{00} and V_{eff} are reduced. This break in trend can be explained as being due to the influence of the nanoparticles on the substrate terraces which have small volume and low energy barrier for magnetisation reversal compared to the nanowires making up the array.

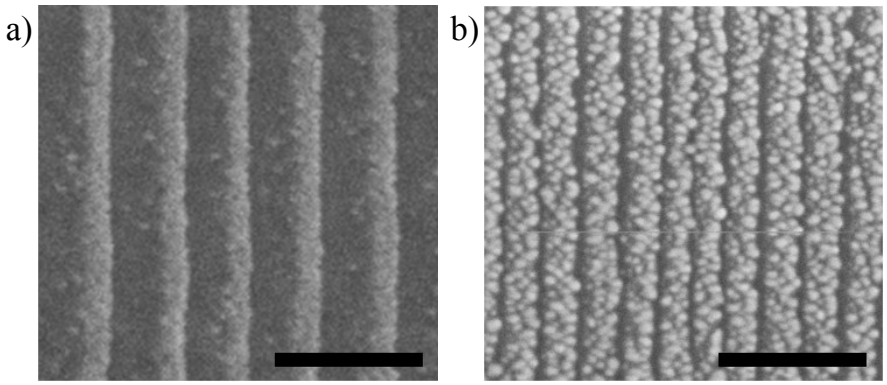


FIGURE 4.7: SEM images of samples for Henkel analysis.

SEM images of two samples which were uncapped but otherwise identically prepared to samples used for a Henkel analysis investigation of dipolar coupling between nanowires. Both samples have a wire width of 30 nm. Sample A has a separation of 60 nm while sample B has a separation of 15 nm. The scale bar in each case is 200 nm.

4.2.3 Interwire Interactions

To investigate the effect of dipolar coupling between nanowires in an array, two samples were created having equal wire width but two different separations. For sample A, Fe was deposited in the uphill direction onto a step-bunched vicinal template with 90 nm periodicity. This resulted in wires having 30 nm width and 60 nm separation. For sample B, Fe was deposited in the downhill direction template with a periodicity of 45 nm. Again this yielded 30 nm width but a separation of only 15 nm. As mentioned in section 4.1.4, Adeyeye *et al.* found a change in behaviour when separation was reduced below the wire width [122], so the two samples here should correspond to interacting and isolated regimes. Deposition time was chosen to achieve identical wire thickness for the two samples (4.4 nm). Prior to growth of the capped samples for magnetic analysis, uncapped samples were produced for SEM analysis to confirm the growth process. The SEM results are shown in figure 4.7. While is appears from the SEM images of the two samples that sample B is more granular or rough than sample A, this is related to the the fact that the resolution of the SEM is limited in this case by the percentage coverage of the surface in metallic material. Since the substrates are oxidised Si, these samples are very prone to charging when imaging using SEM, and so the greater the coverage the more this effect is reduced and the better imaging becomes.

All magnetic measurements were carried out on the AGFM described in section 2.3.2. Prior to the remanence measurements, hysteresis loops were first recorded to examine the effects of dipolar coupling. The $M-H$ loops for the in-plane directions both parallel and perpendicular to the long wire axes are shown in figure 4.8. As can be seen in the $M-H$ loops for sample A, there is clear shape anisotropy with $H_C^{\parallel}$ noticeably greater

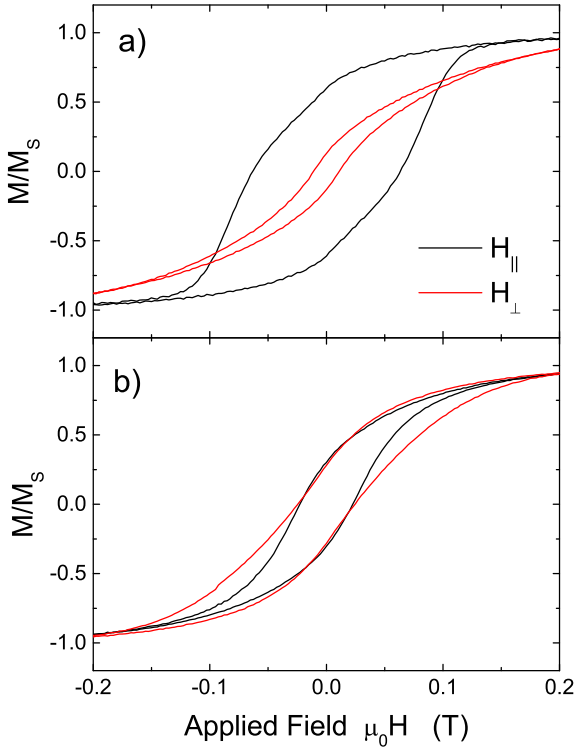


FIGURE 4.8: $M - H$ loops for samples in Henkel analysis.

Hysteresis loops for two Fe nanowire arrays samples. Samples A and B have an interwire separation of 60 nm and 15 nm respectively. Both samples exhibit an easy axis parallel to the wire direction, but for small separation (sample B) the $H_C^{\parallel}$ is reduced and $H_C^{\perp}$ is increased compared to wider separation (sample A).

than $H_C^{\perp}$ ($\mu_0 H_C = 63.3$ and 11.1 mT respectively) as well as a marked difference in remanence (60.5% vs. 13%). The difference in magnetic behaviour between parallel and perpendicular directions is much more subtle in the case of sample B which has smaller interwire separation. Comparing sample A to sample B, one notices a decrease in $H_C^{\parallel}$ and $M_R^{\parallel}$, with $\mu_0 H_C^{\parallel}$ reducing from 63.3 to 22.6 mT, and $M_R^{\parallel}$ reducing from 60.5% to 30%. Meanwhile in the perpendicular direction there is an increase in coercivity from sample A to sample B, where $\mu_0 H_C^{\perp} = 11.1$ to 24.5 mT) as well as $M_R^{\perp}$ (13% to 28%). This has been predicted theoretically as was mentioned in section 4.1.4.

The plots for m_R, m_D (as defined by 2.2) and δm (as defined by 4.25) are shown in figure 4.9. As can be seen from this image, the plot for δm for sample A is a flat line with no clear peak, as expected for the case of isolated nanowires, while with sample B, there is a noticeable negative peak centred around $H/H_c = 1$, as expected for a peak originating from dipolar coupling. In a similar Henkel analysis study by Fodor *et al.* cylindrical wires having width of 35 nm and separation of 20 nm, the δm plot had a

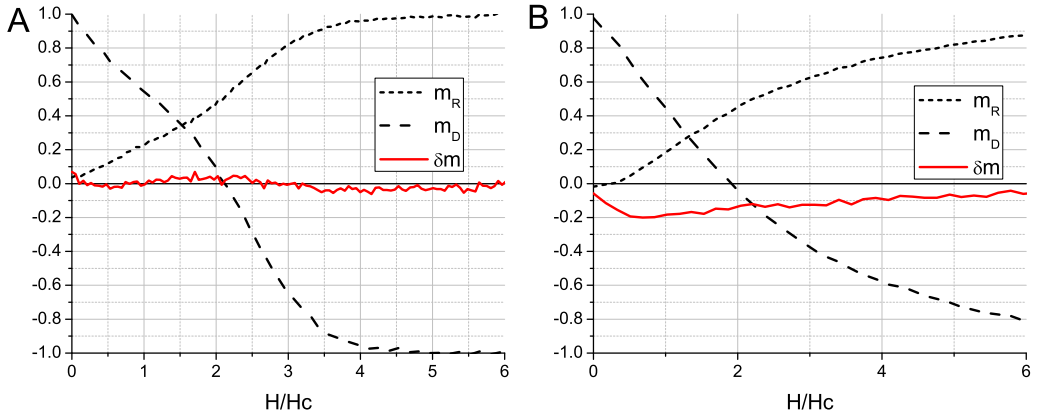


FIGURE 4.9: Henkel plots for varying separation.

Plots of m_R, m_D and δm obtained with applied field directed parallel to the wire direction, for samples having wire width of 30 nm and separation 60 nm (sample A) and 15 nm (sample B).

negative peak with amplitude of approximately 0.85 [117]. While the amplitude of the peak shown here is small by comparison, this is not altogether unexpected, since the wires in the present study have a thickness of only 4.4 nm and therefore have a much smaller cross-sectional area. Furthermore, for each of the wires in this study there are two nearest neighbours whereas in a vertical array there are six.

In conclusion it has been shown that Henkel analysis can be used to differentiate between interacting and non-interacting arrays of magnetic nanowires caused by dipolar coupling, and this is the first such finding for a self-assembled planar array of nanowires. This finding paves the way for a full investigation of intermediate separations. It would also be interesting to examine the temperature dependence of this effect, which was not available to us at the time of writing. By removing thermal effects all measured remanences should be greater, and while this might not necessarily correspond to larger peaks in δm vs H plots, it should at least reduce the noise level in the data.

4.2.4 FMR

A preliminary FMR examination of Fe nanowire arrays was carried out using the Bruker EMX device at the University of Notre Dame, Indiana, USA. FMR spectra were measured as the sample was rotated about various axes. The labelling of the axes and angles between them are shown in figure 4.10. The first sample measured was an Fe nanowire array deposited onto a step-bunched vicinal Si template which had a step periodicity of 140 nm. The Fe was deposited in the uphill direction yielding wires with a width of 30 nm and a thickness of 6.3 nm. In-plane FMR spectra were measured with the angle

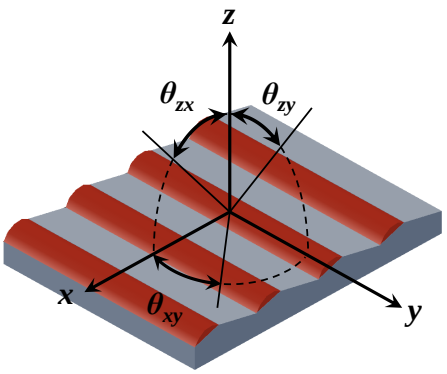


FIGURE 4.10: Axis and angle labels for FMR.

θ_{xy} varied in increments of 5 °. The results are shown in figure 4.11. Also shown in red in this figure is the background signal for this sample which is angle invariant and has been subtracted from the other spectra. As can be seen, there is unfortunately no observable angular variation in these spectra. The spectra measured under variation of θ_{zy} produced similar results. These findings were unexpected since the greatest variation in the anisotropy was expected to involve the axis parallel to the wires (see table 4.1). It may have been the case that the resonance peaks were not observed because of a large distribution in the continuous length of the nanowires along the y-axis. This may cause very wide resonance peaks whose amplitude are too wide to be measured.

However, the FMR spectra did exhibit angular variation for sample rotation about the y-axis. Figure 4.12(a) shows the spectra as θ_{zx} is rotated through 360 ° in steps of 5 °. In this study the sample was almost identical to that which provided the data in figure 4.11, but with a wire thickness of 4 nm rather than 6.3 nm. There are two features which do not vary with angle, a peak at approximately 0.25 T and a slope from 0 to 0.2 T. These are part of the background signal and are ignored in further discussion. More interestingly, there is a dip in the plot which can be seen moving from one spectrum to the next, with a period of 180 °. Usually a resonance on an FMR spectrum has a peak and a trough, but here only the position of the trough can be seen. Thus one cannot reliably make calculated fittings to the resonance position. A qualitative discussion on the position of the trough as a function of angle is possible, however. By comparing the behaviour of the trough with the the schematic in figure 4.12(b), one can see that the angles where the trough is close to 1.0 T correspond to the out-of plane direction, while the angles when the trough is lowest ($\approx$ 0.5 T) correspond to the in-plane direction perpendicular to the wires. Thus it seems that the anisotropy measured in this case is due to the fact that the thickness is less than the width of the nanowires (thickness = 6.3 nm, while width $\approx$ 30 nm). The value of the applied field corresponding to the position of the trough seen in the spectra (figure 4.12(a)) is plotted as a function of angle in figure 4.12(c). It can be seen that maximum and minimum positions of the trough are offset from 0 ° and 180 °

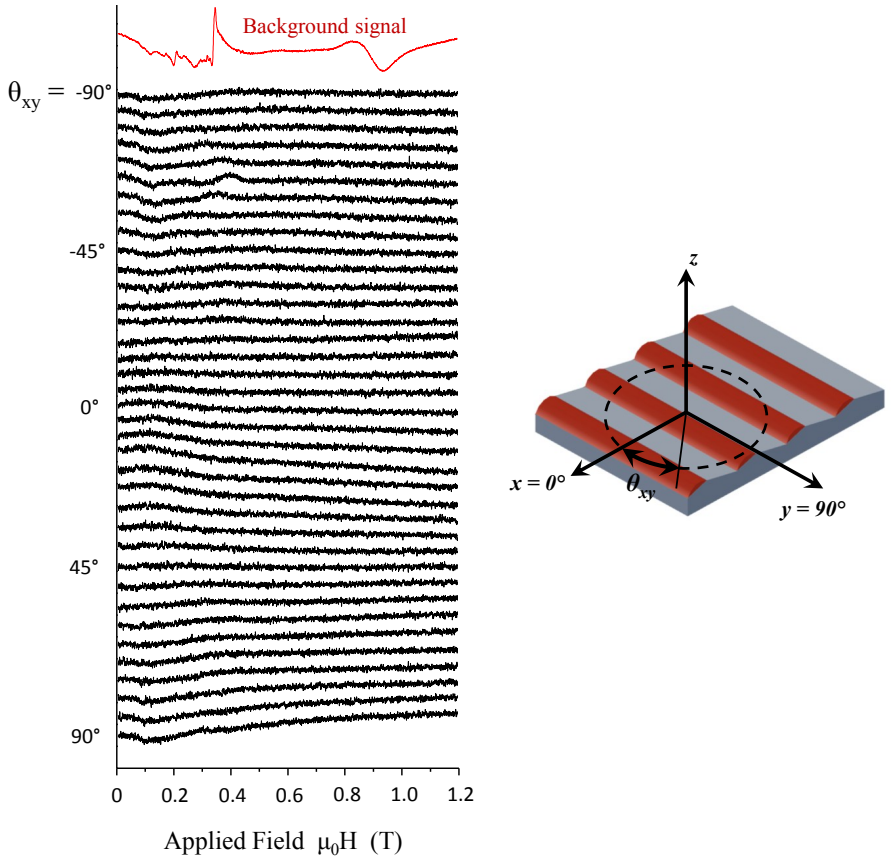


FIGURE 4.11: In-plane FMR spectra for Fe nanowire array.

In-plane FMR spectra of a Fe nanowire array with the angle θ_{xy} varied in steps of 5 °. The background signal, which has been subtracted from the raw data to produce the spectra plotted here, is shown at the top in red.

by approximately 15 °. This is close to the value of 18.5 ° made by the step-bunches and the macroscopic sample surface (see figure 3.11). Thus the hard axis of the sample is not precisely the out-of-plane direction, but the direction normal to the surface of the step bunches.

For a more in-depth investigation, FMR was carried out at the Institute of Magnetism at the National Academy of Sciences in Kiev, Ukraine [139]. Four Fe nanowire array samples were measured using FMR, shall be referred to as samples 1A, 1B, 2A and 2B. Each of the arrays were fabricated on step-bunched vicinal Si templates which were prepared in an identical manner. The miscut angle of the templates was 3.5 °, and the periodicity following the annealing sequence was ≈ 130 nm. Fe was deposited in the uphill direction at an angle equal to the miscut angle, with the deposition time chosen to achieve a wire thickness of 4.2 nm for samples 1A and 2A and 7 nm for samples 1B and 2B. Samples 1A and 1B were then coated in 10 nm of Ag, while samples 2A and 2B were coated in a similar thickness of MgO. The sample preparation description is

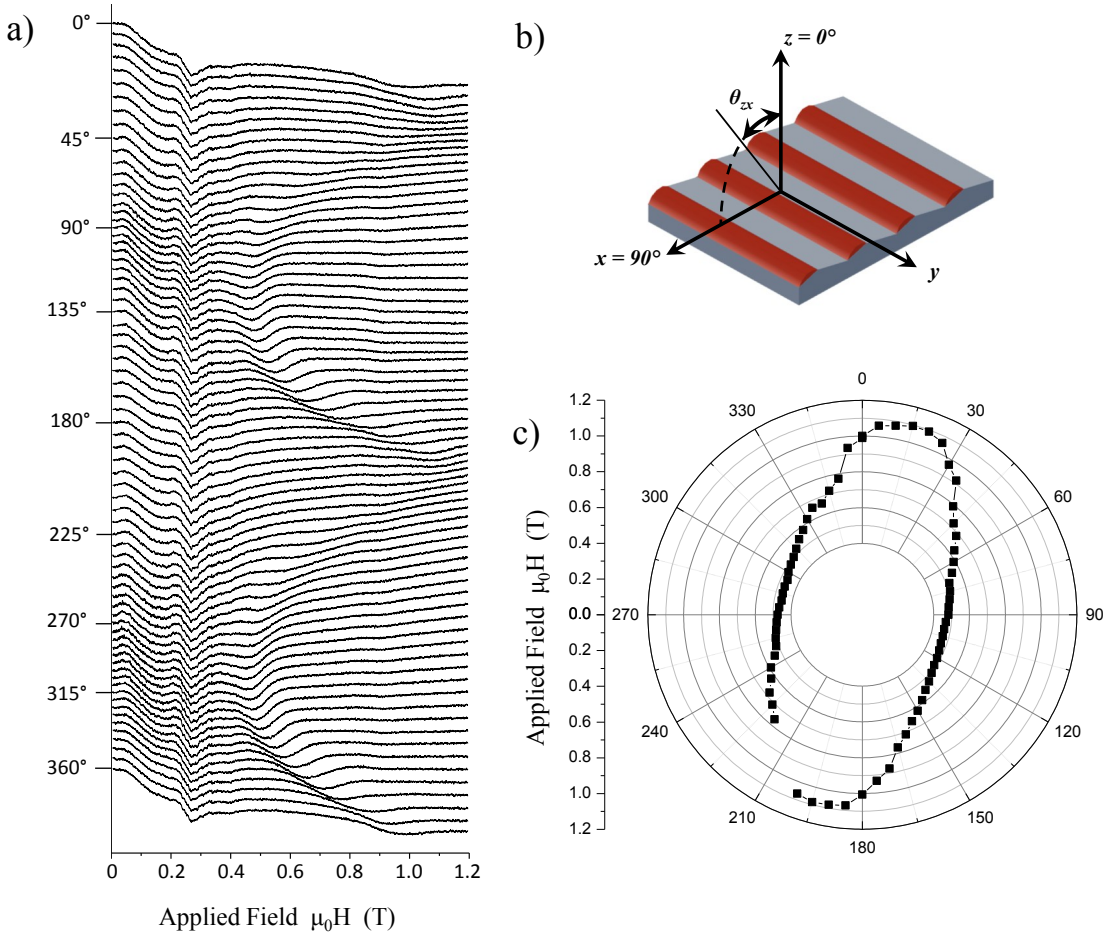


FIGURE 4.12: Out of plane FMR spectra for Fe nanowire array.

a) FMR spectra of an Fe nanowire array with the angle θ_{zx} varied in steps of 5 °.
b) Schematic of sample with relevant axes and angle of rotation (θ_{zx}) labelled.
c) Polar plot of position of trough seen in (a) as a function of angle.

TABLE 4.4: Summary of Fe nanowire array samples analysed with FMR.

Sample name	**1A**	**1B**	**2A**	**2B**
Wire thickness (nm)	4.5	7	4.5	7
Capping Material	Ag	Ag	MgO	MgO

summarised in table 4.4. This device was also unable to detect or track a resonance peak while rotating the sample in plane (x-axis to y-axis as described by figure 4.10) or from the in-plane parallel (y-axis) to the out of plane direction (z-axis). Like the previous experiments, angular variation was measurable while rotating about the y-axis, and in this case it was possible to determine both peaks and troughs. As an example, 6 spectra measured using sample 1B which were taken while varying θ_{zx} in 15 ° steps are shown in figure 4.13. The 'X's in this image indicate the centre of the resonance point for each spectrum. The value of the resonance field was measured as the sample was rotated

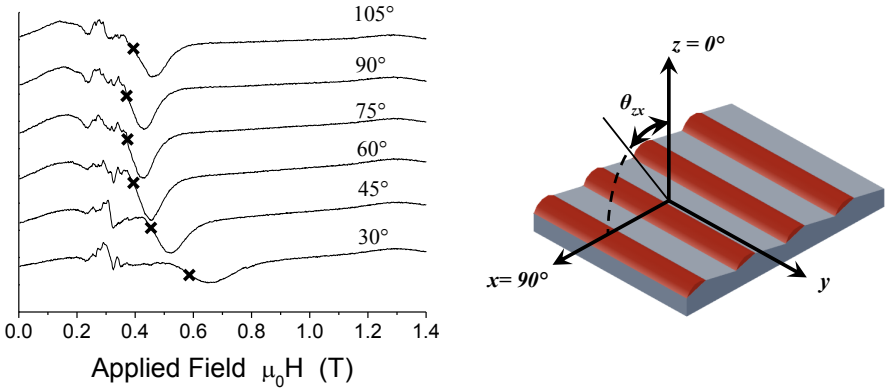


FIGURE 4.13: Sample of FMR spectra.

FMR spectra measured for sample 1B while rotating θ_{zx} between 30 ° and 105 °. The position of the resonance peak for each spectrum is marked by an 'X'. The schematic on the right illustrates the plane in which the sample is being rotated.

through the zx plane for each of the four samples listed in table 4.4. The results for samples 1A and 2A are shown in figure 4.14(a). As can be seen there is a clear anisotropy caused by the difference in wire dimension in the z and x directions. It should be noted that the offset of $\approx 15\,^\circ$ between the surface normal and the direction corresponding to the largest value of the resonance field (hard axis) was also found using this measurement setup. In the following graphs this offset has been subtracted with 0 ° corresponding to the direction of maximum resonance field. The fit to the data was calculated using equation 4.11. As can be seen, the theory matches the data very well. It is noticed that there is a greater anisotropy for sample 1A, which was coated with MgO, compared to sample 2A, which was coated with the same quantity of Ag. This could be due to the formation of an Fe-oxide interface between the MgO capping layer and the underlying Fe nanowires, which may reduce the effective thickness of the Fe nanowires. A similar increase in anisotropy was noticed in samples 1B and 2B (see figure 4.14(b)).

FMR measurements were also carried out on samples 2A and 2B (MgO coated samples) after a duration of two months and five months after the initial measurement to study the effect of ageing on the anisotropy. The results for 2A and sample 2B are shown in figure 4.15(a) and (b) respectively. As can be seen, in the initial measurements the results are much like those seen in figure 4.14, with symmetry about 90 ° which is well explained by the shape anisotropy of the nanowire cross-section. However, for the later measurements (2 months and 5 months following sample fabrication indicated by the red circles and blue triangles respectively), there is an asymmetry about 90 °, with a noticeably lower resonance field H_R for 180 ° compared to 0 °. The appearance of this asymmetry indicates the introduction of unidirectional anisotropy with ageing. This is modelled by adding an additional term 'U_{UD}' to the expression for free energy in

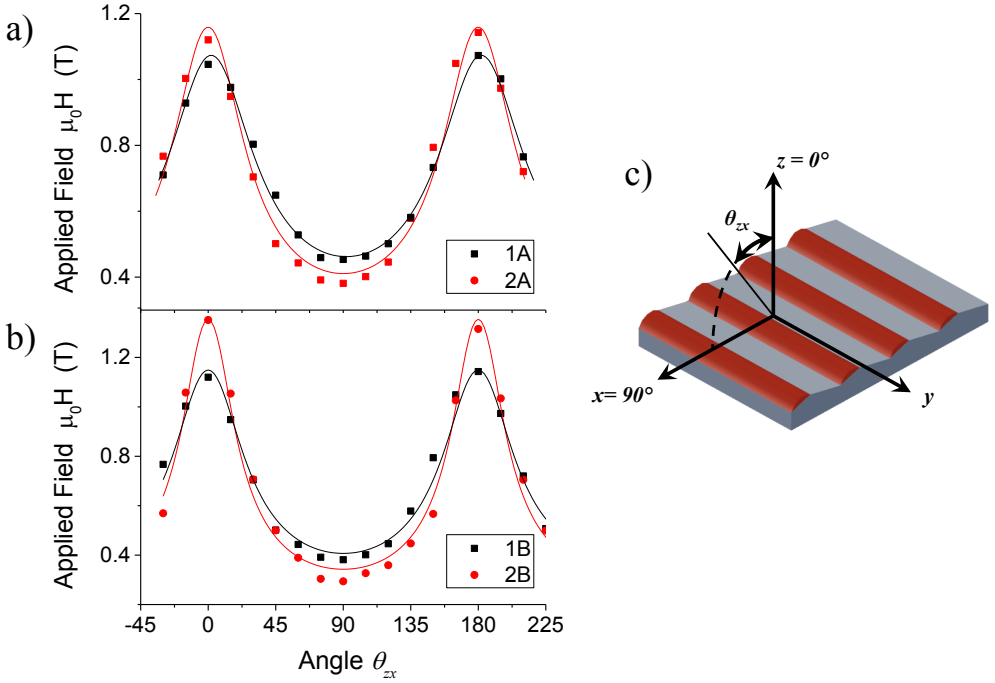


FIGURE 4.14: Resonance Field as a function of angle.

a) H_R as a function of angle for sample 1A (black squares) and sample 2A (red circles) as described in table 4.4. The fits are calculated using equation 4.11.
b) H_R versus angle for samples 1B (black squares) and sample 2B (red circles). Again, the fits are calculated using equation 4.11.
c) Schematic of the sample, axes and angle being varied (θ_{zx}).

equation A.26, which now is given by

$$U = U_Z + U_{SH} + U_{UD} \tag{4.27}$$

where U_{UD} is given by

$$U_{UD} = M\, H_{UD} \cos\,(\theta - \theta_{UD}) \tag{4.28}$$

where H_{UD} is the unidirectional anisotropy field, and θ_{UD} is the direction of the hard axis, which in the present case is equal to 0. The condition for resonance given in equation 4.11 must be modified to include the unidirectional anisotropy as follows:

$$H_R \sin\,(\theta_H - \theta) - \tfrac{1}{2}\,(1 - 2\mathcal{N}_z)\, M \sin\,(2\theta) - H_{UD} \sin\theta = 0$$

$$\left(\tfrac{\omega}{\gamma}\right)^2 = \left[H_R \cos\,(\theta - \theta_H) + (1 - 2\mathcal{N}_z)\, M \cos\,(2\theta) - H_{UD} \cos\theta\right] \times \left[H_R \frac{\sin\theta_H}{\sin\theta} - M\,(1 - \mathcal{N}_z)\right]. \tag{4.29}$$

These equations were used to provide the fitted curves shown in figure 4.15. The parameters derived from the fitting are given in table 4.5. In this table, it is interesting to note

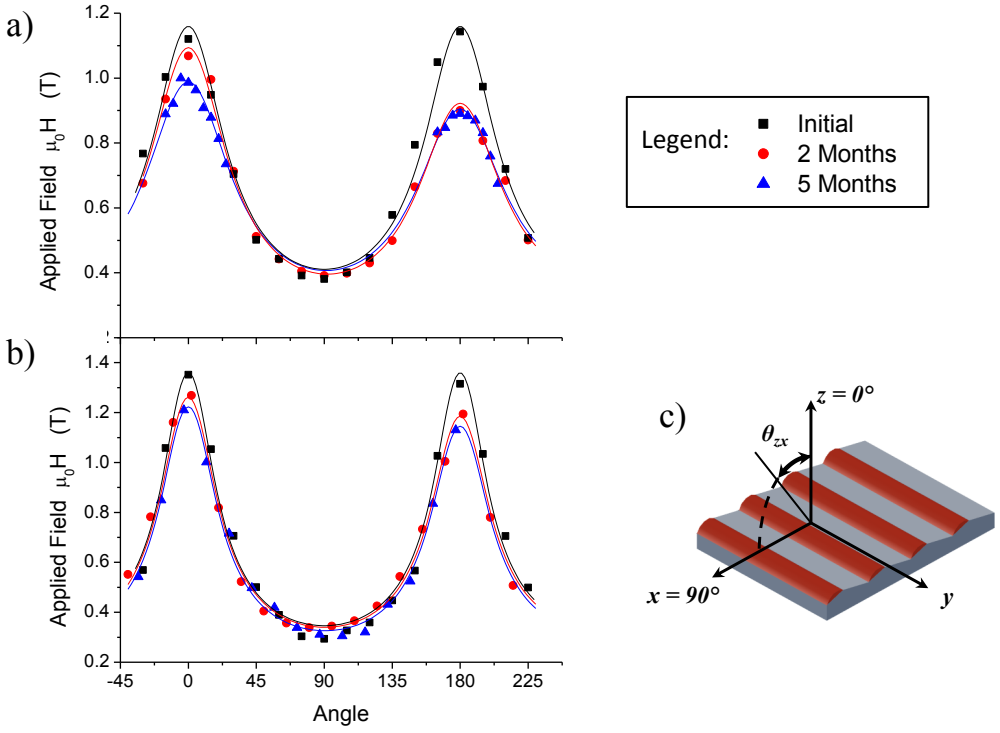


FIGURE 4.15: Resonance Field as a function of angle for sample with ageing effects.

H_R as a function of angle for sample 2A (a) and 2B (b). The black symbols correspond to the measurements taken initially following sample fabrication, while the red and blue symbols correspond to measurements taken after a period of 2 months and 5 months following the initial measurements. The schematic in (c) shows the angle being varied (θ_{zx}) in relation to the axes and the sample layout.

the effect of ageing the demagnetising factor $\mathcal{N}_z$ for the two samples. For the thicker nanowires, the value of $\mathcal{N}_z$ is almost constant, which indicates that the reduction in wire thickness associated with oxidation is small relative to the nanowire thickness. For sample 2A, which had thinner wires, $\mathcal{N}_z$ decreases rather than increases as the sample ages. This suggests that the oxidation not only reduces wire thickness but also affects wire width or the continuity of the wires across their width. The observation of unidirectional anisotropy is unusual. It is clear from the above that it is related to the ageing of the sample, and therefore related to the partial oxidation of the Fe nanowires. The appearance of unidirectional anisotropy was not noticed in the case of the Ag capped Fe nanowire arrays. This would seem to indicate that, over time, MgO does not perform as well as Ag in protecting the Fe from oxidation. Exchange bias is the usual cause of unidirectional anisotropy in nanoparticle systems that include an interface between Fe and FeO [140–144]. The most likely source of the unidirectional anisotropy seems to be that following the initial measurement, the sample was left in a magnetised state with a certain remanence. As the Fe oxidised, this directionality may have become 'stored' in the oxide layer, and pins the underlying unoxidised Fe to a degree for subsequent series of

TABLE 4.5: Parameters determined from fitting to samples with unidirectional anisotropy.

Parameters determined from fitting equation 4.29 to the experimental data shown in figure 4.15.

Sample	Age (Months)	$\mathcal{N}_z$	μ_0 M (mT)	μ_0 H_{UD} (mT)
2A	0	0.76	99	…
	2	0.74	84	86
	5	0.72	79	42
2B	0	0.82	110	…
	2	0.81	97	38
	5	0.8	92	40

measurements. Further magnetic measurements, including $M - H$ measurements taken at a range of temperature as a sample ages, may be necessary to confirm this interesting finding.

4.3 Conclusions and Further Work

It has been shown that the one-dimensional structures fabricated using the glancing angle deposition technique described in the previous chapter has successfully given rise to an in-plane magnetic shape anisotropy due to the large aspect ratio of the nanowires. An attempt was made to ascertain the reversal mechanism in these structures through analysis of the coercivity as temperature is reduced from 300 K down to 10 K, with theoretical fittings corresponding to both coherent reversal and nucleation-propagation reversal modes fitted to the experimental data. It was expected that the nucleation-propagation reversal mode would become more dominant as thickness was increased over several samples. Unfortunately neither model fitted the data precisely, with the coherent reversal mode being statistically closer to the data points over the entire sample range. This is thought to be due to either a systematic error in the measurement, or possibly due the presence of superparamagnetic nanoparticles as well as the one-dimensional nanowire structures. Nonetheless, the fitting parameters provided meaningful results, with an increase in the effective volume of magnetisation reversal (V_{eff}) and the energy barrier for magnetisation reversal at 0 K (E_{00}) as thickness was increased. This trend was continuous, with the exception of the thickest sample, which is thought to be have had its coercivity reduced due to the influence of magnetic nanoparticles on the step terraces between the wires. In the future, the reversal mechanisms in the arrays may be more accurately investigated by conducting coercivity measurements at a greater number of temperatures, particularly in the range from 0-100 K.

The effect of interwire interactions was investigated by fabricating two Fe nanowire array samples which were identical except for the interwire separation. It was noted that this caused a marked reduction in $H_C^{\parallel}$ as well as an increase in $H_C^{\perp}$, as the nanowire array gradually approaches the limit of a uniform Fe layer. A Henkel plot was also used to show that the array with reduced separation preferred anti-parallel alignment of magnetisations in neighbouring nanowires. This type of measurement has not been carried out for self-assembled planar arrays of nanowires before. There is great scope for further studies in this area, such as conducting remanence measurements on wire arrays of incremental interwire separation, and investigating the effect of varying wire thickness.

The findings from the FMR analysis were surprising, in the sense that no identifiable resonance was noticed for sample rotation in planes which include the direction parallel to the axis of the wires. However, the anisotropy between the in-plane perpendicular and out-of-plane perpendicular directions was successfully probed. It was found that the hard axis corresponded not exactly to the surface normal direction, but to the direction which is normal to the surface of the step-bunches onto which the nanowires were deposited. The effect of capping with Ag compared to MgO was investigated with FMR. It was found that the anisotropy (in-plane perpendicular vs. out-of-plane perpendicular) was more pronounced for MgO capped samples, which may be due to the reduced effective thickness of the nanowires due to the formation of an oxide layer at the Fe-MgO interface. Furthermore, it was noticed that a unidirectional anisotropy appeared over the course of several months for the MgO capped nanowire samples. The cause must be related to the ageing of the sample, and therefore is likely due to the formation of an oxide layer at the top of the nanowires. The remanent magnetisation of the wires following measurements may influence the magnetisation of the oxide layer as it grows with time, which in turn partially pins the Fe nanowires during subsequent measurements. Further magnetisation measurements may be carried out to investigate this interesting finding in further detail. It would be interesting to see if the direction of anisotropy can be manipulated to point in other directions. The study could be corroborated by measuring $M(H)$ loops as a function of angle using either VSM or AGFM. A small number of such studies have been carried out on nanowire arrays and have shown the potential of this technique to provide insight into reversal mechanism as well as the parameters relating to anisotropy [145, 146].

Another technique for analysis of magnetic nanowire arrays is the use of FORC distributions. First order reversal curves (FORCs) are measured as described in section 2.3.2.1. To produce a FORC distribution, the partial derivative of the magnetisation with respect to the reversal field H_a and the applied field H_b is calculated. The distribution is

denoted by ρ, so

$$\rho\left(H_a, H_b\right) = -\frac{\partial^2 M}{\partial H_a \partial H_b} \tag{4.30}$$

where, by definition, H_b is always greater than or equal to H_a. FORC distributions are usually plotted via a change of co-ordinates from $\{H_a, H_b\}$ to $\{H_{cr}, H_u\}$ where H_{cr} and H_u are the 'critical axis' and the 'interaction axis' respectively, and are given by:

$$\begin{aligned} H_{cr} &= \tfrac{1}{2}\left(H_b - H_a\right) \\ H_u &= \tfrac{1}{2}\left(H_b + H_a\right) \end{aligned} \tag{4.31}$$

where $H_{cr} > 0$. Other studies which do not carry out this change of co-ordinates usually include a factor of $1/2$ in the definition for ρ given in equation 4.30, but here we follow Pike *et al.* in which the $1/2$ is omitted [147–150]. The distinction is not critical since, in this study, features on the FORC diagram will be discussed in relative terms.

The FORC distribution plot $\rho\left(H_{cr}, H_u\right)$ may contain a variety of different peaks and ridges. The nature of these features in terms of their position and symmetry allows us to identify the magnetic phenomena that caused them. Roberts *et al.* carried out a useful summary on the signature features on a FORC distribution plot caused by magnetic components such as superparamagnetic particles, single domain particles and one-dimensional structures [151]. A schematic representation of the different features described by Roberts *et al.* is shown in figure 4.16. It is undoubtable that there will be some discrepancies between the experimental data and this simplistic interpretation, but this will serve as a starting point in deciphering the results. The irreversible reversal of magnetisation gives rise to a peak along the H_{cr} axis, as illustrated by the green ellipse in figure 4.16. The width of this peak indicates the distribution of the coercivities of the constituent elements of the system. The average coercivity of the system can be interpreted as being equal to the maximum point of this peak or a weighted average of the values along the H_{cr}-axis. Discrepancies between coercivity measured in this way and the 'conventional' coercivity (measured at the point where the hysteresis loop crosses the H-axis) has been the focus of previous studies [152]. The spread of this peak in the H_u direction is related to the magnetostatic and exchange interactions within the system. The width of this peak has previously been analysed to investigate dipolar coupling between nanowires in regular arrays [153]. The main peak (green ellipse) may be offset from the H_{cr}-axis for several reasons. A stabilising mean interaction field may cause the peak to have a negative H_u value, while the presence of multidomain structures may cause the peak to be shifted to positive H_u [151].

Superparamagnetic particles, having zero or near-zero coercivity, appear as a concentrated peak about the origin. This peak may include a ridge which runs parallel to the

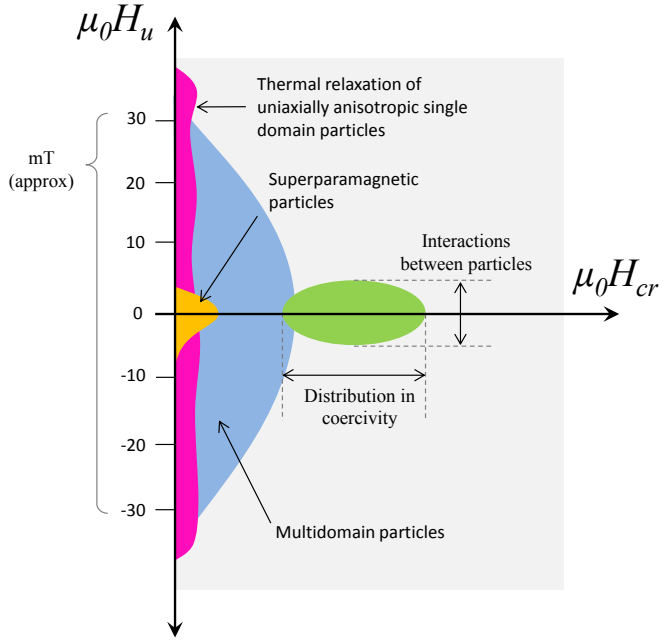


FIGURE 4.16: Signatures of magnetic features on a FORC distribution plot.

Different peaks and ridges that may be expected on a FORC distribution plot and the magnetic components that may give rise to them.

H_u-axis, though usually this only appears predominantly in the $-H_u$ direction and does not extend much further than $-10\,\mathrm{mT}$. Thermal relaxation of multidomain particles or uniaxial particles can produce a longer ridge along the H_u-axis which typically extends beyond $\pm 30\,\mathrm{mT}$ (pink and blue regions in figure 4.16 respectively). In the case of a ridge due to multidomain particles this often is connected to the main peak at the H_{cr}-axis.

For an example, a FORC plot for an Fe nanowire array with applied field directed along the axis of the nanowires is shown in figure 4.17. There are 113 individual FORCs in this plot, with $\mu_0 H_a$ increasing in increments of $5\,\mathrm{mT}$. The FORC distribution plot for this Fe nanowire array calculated using equation 4.30 is shown in figure 4.18(a). [1] This array was formed of 30 nm wide wires on a step-bunched template with 100 nm periodicity ($\Rightarrow$ 70 nm interwire separation). The wire thickness is 5.4 nm. As can be seen, some of the features in the schematic in figure 4.16 are present. There is a slightly elliptical peak along the H_{cr}-axis which represents the coercivity of the wires in the array. The peak of this ellipse shape matches closely with the actual coercivity measured separately via hysteresis measurement ($H_C^{\parallel}\,\mu_0 = 63\,\mathrm{mT}$). There is pronounced peak near the origin, indicating that the sample includes a certain amount of paramagnetic material, or particles with low coercivity. This may be due to small particles on the

[1] These FORC distribution plots were generated from the raw data using an algorithm called FORCinel which was developed by the NanoPaleoMag project lead by Dr. Richard Harrison at the Department of Earth Sciences, University of Cambridge [154]

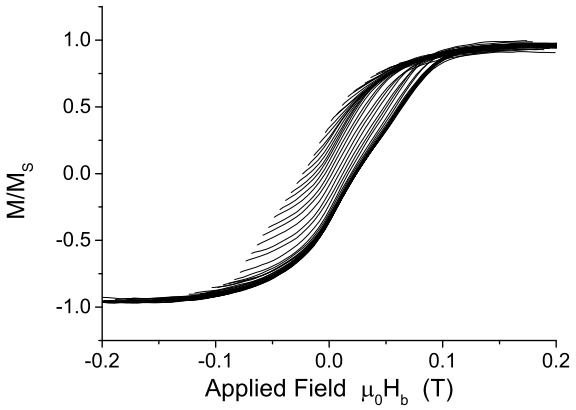


FIGURE 4.17: FORC plot for Fe nanowire array.

FORC plot for Fe nanowire array comprising 113 individual FORCs with H_a increasing in 5 mT increments. The substrate is oxidised, step-bunched vicinal Si. Nanowire width, thickness and separation are 30 nm, 5.4 nm and 70 nm respectively. Deposition was carried out at room temperature.

terraces between the wires, or parts of the wires themselves which are poorly coupled. There is also a long ridge which extends along the $mu_0\, H_u$-axis as far as $\pm\, 100$ mT. This is likely due to thermal relaxation of magnetisation in one-dimensional structures. For comparison, a FORC distribution plot was also produced for a Co nanodot array which was deposited on faceted Al_2O_3, similar to those shown in figure 3.26. For this sample the step-edge periodicity was 75 nm and the Co was deposited in the uphill direction to produce nanoparticle rows approximately 10 nm wide. The substrate temperature during deposition was 200 °C, and the sample was capped with 20 nm of MgO. The FORC distribution plot for this sample is shown in figure 4.18(b). In this plot it can be seen that, like in figure 4.18(a), there is an elongated ellipse which is centred around the coercivity of the sample, which was found via separate hysteresis measurements ($H_C^{\parallel}\, \mu_0 = 38$ mT). Here is it noticeable that the ridge present in (a) which corresponds to multidomain structures or one-dimensional anisotropic structures is much less pronounced. This is expected since the aspect ratio of the ellipses is likely to be significantly less than that of the Fe nanowires, and as shown in table 4.2, the expected width of a domain wall in bulk Co is approximately 24 nm, which is greater than the size of the particles themselves.

Another Co nanodot sample was produced in an identical manner to that described above, but with a substrate temperature during deposition of 500 °C rather than 200 °C. As shown in section 3.4.2.3, this is known to result in nanodots that have a lower ellipticity (and therefore lower magnetic shape anisotropy) as well as a greater interparticle separation at fixed volume, which is expected to reduce coupling between nanodots and thereby further reduce the anisotropy of the system. The FORC distribution plot for

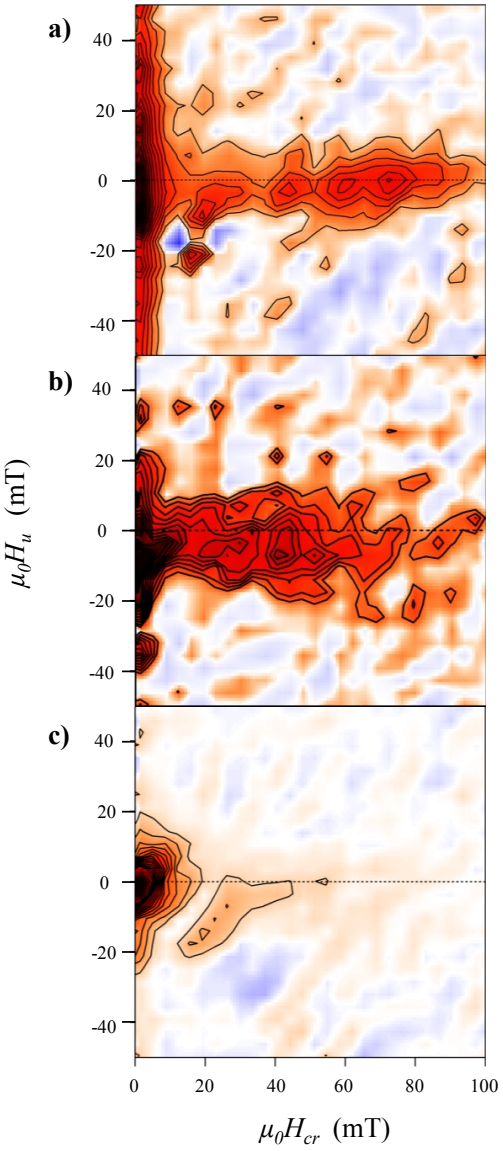


FIGURE 4.18: FORC distribution plots for different nanowire and nanodot arrays.

a) FORC distribution plot for Fe nanowire array on oxidised, step-bunched vicinal Si. Nanowire width, thickness and separation are 30 nm, 5.4 nm and 70 nm respectively. Deposition was carried out at room temperature.
b) FORC distribution plot for Co nanodot array deposited onto a faceted Al_2O_3 template. Deposition was carried out at 200 °C to produce elliptical Co nanodots.
c) FORC distribution plot for Co nanodot array produced as for (b) but with a substrate temperature of 500 °C during deposition.

this sample is shown in figure 4.18(c). As can be seen, the ellipse representing irreversible magnetisation change is barely visible, while the main feature is the peak near the origin representing the contribution coming from superparamagnetic nanodots or nanodots with very low coercivity. The ridge corresponding to multidomain particles or one-dimensional structure is also no longer visible, suggesting that the anisotropy and magnetostatic coupling of the nanodots has been significantly reduced compared to figure 4.18(b).

These preliminary results show that FORC distribution analysis may be a very useful tool for probing the behaviour of arrays of magnetic nanostructures. FORC analysis may be used to clarify unusual behaviour seen in other studies, such as in figure 4.3 where it was suspected that the influence of superparamagnetic particles caused a reduction in coercivity. It would also be interesting to carry out these measurements as a function of temperature, to see if the ridge along the H_u-axis and the peak at the origin reduce as $T \rightarrow 0$. Pike *et al.* used FORC distribution plots to analyse arrays of Co ellipses similar to those shown here, but an order of magnitude greater in size [149]. The study found a range of features on the FORC plots related to the geometry and the extent of magnetostatic coupling between the ellipses. The fabrication of Co nanodots via glancing angle deposition onto faceted surfaces provides a great opportunity for further exploration of these effects.

Another type of measurement that can be carried out using the AGFM is the time relaxation of magnetisation. In these measurements, the sample is first saturated with a large applied field in one direction. Then the applied field is reduced to a smaller value in the opposite direction, and the magnetisation is measured as a function of time, often for periods of an hour or more. The behaviour of this plot will depend on the magnetic viscosity of the system, which depends on the magnetisation reversal mechanism [155]. This method has been used in the past to complement an investigation of reversal mechanism via measurements of coercivity versus temperature as was attempted in section 4.2.2. This mode of analysis has also been used to investigate 'exchange-spring magnets', which are nanostructured materials consisting of a layer with very high anisotropy (such as $Nd_2Fe_{14}B$) exchange coupled with a soft ferromagnet which has high saturation magnetisation (such as Fe) [156]. Time-dependent measurements have also been used to investigate the asymmetry in reversal mechanisms in exchange-biased bilayers [157].

Chapter 5

GaAs Nanowires

5.1 GaAs

GaAs is a III-V semiconductor with a bandgap of 1.424 eV at 300 K. While Si is ubiquitous owing to its abundance [1] and the ability to produce near perfect boules with very high yield [158], there are several characteristics of GaAs that give it an advantage over Si in certain niche applications. For example, the bandgap of GaAs is direct and higher than that of Si, meaning that it can emit light efficiently and is useful for applications such as lasers and LEDs [159]. Its electron mobility is also higher, making it useful for high frequency transistors in communication devices [160, 161]. Another benefit of the wider bandgap is that GaAs is more resistant to radiation damage, allowing opportunities for use in space electronics and other high intensity environments [162]. The crystal structure of GaAs is normally zincblende in the bulk, but for nanostructures it may be wurtzite. These structures will be described in more detail in section 5.4.

5.2 Motivation for Ordered Arrays of GaAs nanowires

The bulk of studies into the growth processes of GaAs nanowires have a starting point consisting of a random dispersal of Au droplets for nanowire growth. The most common method of producing these droplets is to deposit a thin (≈ 1 nm) layer of Au which, when heated, results in a layer of droplets which have no pre-determined position and varying diameter. Since wire length is related to diameter there is little control over wire dimensions. Nanowire arrays produced in this method are typically quite dense, and the effect of shadowing caused by neighbouring nanowires is usually unavoidable for lengths exceeding 1 μm. Nanowire arrays are also commonly grown from Au droplets synthesised in solution and drop-cast onto GaAs substrates. While significant advances in droplet

synthesis mean that diameter can be tightly controlled in this method, locations of nanowires are still random.

Attempts are often made to conduct a study by analysing a subset of wires in a random array. This is prone to errors, however, since certain wire sizes may be affected by nearby neighbours with different properties. A number of parameters may be shifted in a non-uniform way across the sample-space. For example, droplets could become slightly enlarged due to dissolved Ga increasing their volume, or the ability of initial droplets to successfully produce wires (as opposed to becoming buried under the flux of Ga and As) may be size-dependent. As an example, a work by Plante and Pierre found a broad distribution of tapering ratios for a specific droplet diameter [163], and this was proposed to have originated from the effect of having non-uniform neighbouring nanowires. For reasons such as this it is preferable to have a well-defined pattern of Au droplets to begin with so that subsequent data can be correctly interpreted.

From an applications point of view it is highly desirable to be able to specify precisely the locations of individual nanowires. Proposed Field-Emission Display (FED) devices require specific sites for either individual nanowires or groups of nanowires [7, 164]. Solar cell applications for vertical nanowires are also likely to require ordered rather than random arrays [2, 5, 165–167]. Another proposed application is the use of a nanowire as an AFM tip [168]. Again, this would require nanowire growth in a precise location.

5.3 VLS Method

There are a number of methods for fabrication of vertical GaAs nanowires. Here will be a brief description of a few of the main approaches, followed by a more in-depth discussion of the VLS process with atomistic deposition in UHV.

One of most studied mechanisms for GaAs nanowire growth is metal-organic vapour phase epitaxy (MOVPE). Some of these approaches use Au catalysts for the growth sites [169–171] while others use a selective-area growth (SAG) process by defining the growth sites using EBL and a wet etching technique [172–176]. MOVPE is usually carried out in a partially evaporated, tube-like reaction chamber with the precursor molecules flowing across the heated substrate. The vast majority of these studies found zincblende structure with twinning defects, which are common for zincblende nanowire growth in the [111] direction. The production of wurtzite type nanowires using MOVPE was not achieved until recently; in 2008 Moewe *et al.* recorded needle-like wurtzite nanowires which were grown without catalysts or selective-area growth [177]. In 2010, Bauer *et al.* presented findings of wurtzite nanowires grown using Au catalysts [172]. The change

from zincblende to wurtzite seems to have been brought about by increasing the V/III partial pressure ratio to 40 (values of 1.5 to 20 are common). One of the drawbacks of the MOVPE process is the potential for inclusion of contaminants into the nanowires, arising from the precursor gases (usually trimethylgallium (TMG) and AsH_3 (arsine)) [178].

Another approach is Laser-Assisted Catalytic Growth (LCG) wherein a laser ablation is carried out using a GaAs target containing small quantities of Au [159, 179]. This approach produces disordered networks of nanowires and so far has only produced zincblende GaAs nanowires (although wurtzite wires have been grown for CdS and CdSe). Similar results are achieved using the slightly different approach known as oxide-assisted growth (OAG) wherein GaO_3 replaces the Au in the target [180, 181]. These two techniques, which are still somewhat in their infancy, are useful for high-throughput of disordered nanowires but so far have not been shown capable of producing ordered arrays of nanowires.

Chemical Beam Epitaxy (CBE) has also been used to grow GaAs nanowires [182]. This method uses precursors similar to those in MOVPE while carried out in a chamber more closely resembling an MBE setup, although with higher pressures. The As precursor is cracked as it enters the growth chamber while the Ga precursor decomposes on the substrate. Fine examples of an InAs nanowire arrays produced using EBL in tandem with CBE have been shown in studies by Jensen *et al.* and Persson *et al.* [183, 184].

The above-mentioned approaches may be described as VLS, or vapour-liquid-solid, processes, if all three phases are present and growth occurs preferentially at the triple-phase line. Here we now refer to VLS growth under UHV conditions with pure deposition sources (atomistic Ga and dimer or tetramer As). The substrate in this procedure is usually GaAs (111)B. Au nanodots are first formed on the substrate usually via one of the following methods

- Annealing a continuous, thin ($\approx 1\,\mathrm{nm}$) film of Au. Upon heating this forms a disordered array of Au nanodroplets. This can be done in the same chamber as is used for the nanowire growth if it includes a heated stage and Au source.
- Au nanoparticles are produced via colloidal chemistry and drop-cast onto the substrate.
- The aerosol method described by Magnusson *et al.* [185]. Au nanoparticles are produced by heating a crucible of Au, and together with a carrier gas these nanoparticles form an aerosol. The desired diameter of Au particles is specified by first charging the particles and then passing the aerosol through a differential mobility

analyser (DMA). Here the application of an electric field allows only a specific mass:charge ratio to emerge from the DMA. The aerosol is passed through a furnace to sinter the particles and finally introduced to the deposition chamber.

- Au nanodiscs are defined precisely using EBL. This is the focus of the present study.

With the Au catalysts on the substrate, the sample is loaded into a UHV chamber with Ga and As evaporation sources. Prior to entry into the deposition chamber, the As undergoes a 'cracking' procedure which determines whether As_2 or As_4 molecules reach the substrate. After a usual deoxidation anneal (which may also produce Au droplets if the sample is covered in a thin layer of Au) the sample is then exposed to the Ga and As fluxes. The Au nanodots form a Au-Ga liquid alloy droplet. These droplets act as preferential sites for adsorption for the incoming As. When a supersaturation is reached, the Ga and As atoms condense at the solid-liquid interface, driving the droplet upwards as each new layer is formed. The result is a free-standing GaAs nanowire with a Au-Ga droplet left at its top.

VLS growth without the use of a catalyst material is also possible. In this mode the droplet is composed entirely of Ga and the As concentration must be very carefully maintained so there is steady state growth. Otherwise the droplet can become consumed and nanowire growth will stop. Catalyst-free VLS growth of nanowires is usually carried out on Si or GaAs substrates covered in a thin (5-40 nm) layer of SiO_2. The Ga makes its way to the underlying substrate through pores in the SiO_2 and nanowire growth then begins. Recent examples of wires grown in this way can be seen in the work of Colombo *et al.* [186], Rieger *et al.* [187] and Gibson and LaPierre who formed ordered arrays of GaAs nanowires by using EBL to define a grid of holes in the SiO_2[188]. Ga is very mobile on SiO_2, and can migrate several microns to the nearest nanowire. For large nanowire separations, excess Ga may form crystallite lumps between the nanowires. Catalyst-free VLS growth of nanowires can also be achieved without the SiO_2 layer, although growth rates are poor and, so far, positions cannot be defined [189].

The remainder of the discussion shall focus on GaAs nanowire growth which is catalysed by Au droplets, although many of the principles discussed are also relevant to catalyst-free growth.

There are a number of pathways for adatoms to find their way to the Au-Ga droplet, but first it is worth discussing precisely which adatoms are doing the migrating. While some papers discuss the importance of considering the ability of As migrating along surfaces towards the droplet [190], most publications focus on the migration of Ga in particular [182, 191–193]. This is because Ga is assumed to have a significantly longer

lifetime and diffusion length on the surface involved, whereas As may quickly desorb [193, 194]. One study by Ramdani *et al.* [195] found that As diffusion to the catalyst is negligible, and furthermore that direct impingement on the catalyst was insufficient to explain the growth rate. They concluded that the necessary supply of As was maintained by a contribution from As desorbing from the nearby surfaces such as the substrate and nanowire sidewalls. Due to its poorer ability to migrate, As partial pressures are typically higher than those for Ga, i.e. growth is carried out in an As-rich regime. This is not to say that As pressure is arbitrary, since it can affect Ga diffusion [194], growth rate [195, 196] and crystal structure [172]. In MOVPE growth, increased As pressure may also suppress TMG decomposition [182]. Thus, the following discussion will describe the pathways of Ga from the source to the point of incorporation, while it is acknowledged that there is an outside possibility of As behaving in a similar manner.

The possible routes of incident Ga to the growth interface are shown in figure 5.1. As can be seen, the Ga adatoms may land directly on the Au-Ga catalyst droplet on top of the wire. This droplet can act as a reservoir, storing Ga before it diffuses through the droplet to the growth interface. Ga may also land on the wire sidewalls if the angle of incidence is not normal to the substrate plane. Once on the sidewalls they may migrate to the droplet, or, particularly if the length of the wire has exceeded the diffusion length of Ga on the sidewalls, may nucleate on the sidewall and contribute to radial growth. Finally Ga adatoms may also migrate onto the wire sidewalls from the substrate 'floor'. This is probably an important mechanism in the early stages of growth and may become negligible when the wire height and density has increased to the point where the floor is

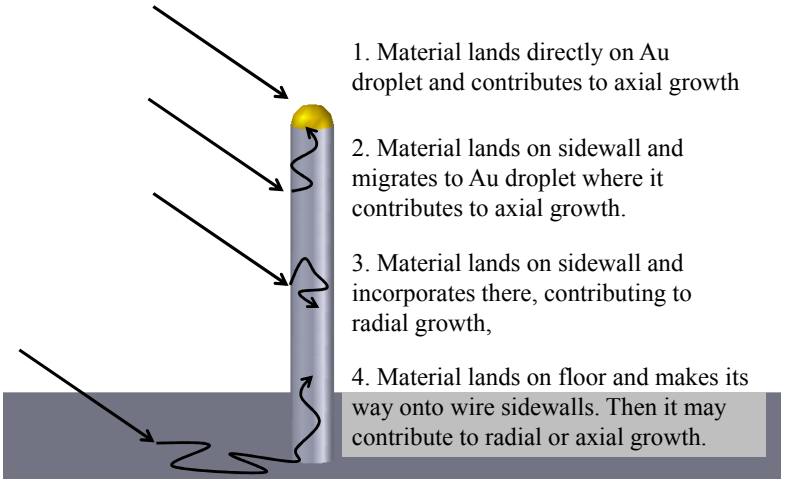


FIGURE 5.1: Routes of Ga to growth interface

Four possible routes that Ga adatoms may take before incorporating into the solid crystal. Not shown is the migration of As adatoms, which is assumed to be negligible, or desorption of adatoms, which may occur at any stage during migration with varying rate.

no longer 'visible' to the Ga source. There is a question surrounding the energy barrier confronting the adatoms as they transition from the floor to the sidewalls, and this effect may lead to mounds or pyramids of growth at the base of the wires [163, 192]. These four routes will be discussed regularly when analysing the results of nanowire growths. Desorption is not shown in this image, but is possible during any of these four routes, although some findings suggest that Ga desorption is not significant below temperatures of around 650 °C [197], which is at the upper end of temperatures used during nanowire growth in the present study.

The ability of adatoms to migrate from the sidewalls to the growth interface leads to a well-known relationship between nanowire height and diameter. The rate of arrival of adatoms, dV/dt (where V is volume), onto nanowire sidewalls depends on the sidewall area. This is proportional to the circumference of the nanowire which varies as d, where d is the diameter of the Au-Ga droplet. When this material incorporates into the nanowire crystal it contributes to the volume which, assuming constant radius, is given by $\pi(d/2)^2 H$, where H is the height. Thus we have

$$\begin{aligned} d \propto \frac{dV}{dt} &= \pi \left(\frac{d}{2}\right)^2 \frac{dH}{dt} \\ \Rightarrow d \propto d^2 \frac{dH}{dt} & \\ \Rightarrow \frac{dH}{dt} &\propto \frac{1}{d}. \end{aligned} \tag{5.1}$$

This $(1/d)$ dependence is very commonly observed in VLS growth when the angle of incidence for Ga flux is not normal to the substrate surface. Discrepancies from this dependence have been studied in the past and, depending on the circumstances, have been linked to the nucleation mechanism within the Au-Ga droplet [190, 198], competition between radial and axial growth [199] and the rate of Ga consumption by the Au-Ga droplet at its perimeter [191]. Most studies find that the the $(1/d)$ dependence fits the data well up to a critical diameter, with typical values between 100-400 nm, depending on the mechanism causing the divergence.

The species of As plays an important role in the VLS process. The As is introduced into the chamber using an effusion cell in series with an intermediate high-temperature chamber called a 'cracker'. When the cracker is operated above ≈ 750 °C, As_2 dimers are produced, but below this temperature As_4 emerges [200]. For the experiments described here, the cracker temperature was kept at either 600 °C for As_4 or 1000 °C for As_2. A detailed study into the effect of As species on the kinetics of GaAs nanowire growth was carried out by Sartel *et al.* [197]. They found axial growth rates for As_4 of approximately double that for As_2 gas. They found significant radial growth resulting in tapered nanowires when As_2 was used, while with As_4 the nanowires had near-uniform width

along their entire length. The findings were put down to the higher reactivity of Ga with As_2 than As_4, causing a shorter diffusion length and leading to radial growth [201, 202]. The exception is on the (111)B surface, where As_2 can cause a reconstruction that impedes Ga incorporation [197, 202].

During growth, it is possible that the length of the nanowires exceeds the diffusion length of Ga on the sidewalls. If so, material landing on the sidewalls may not able to migrate to the Au-Ga droplet for incorporation at the growth plane. Instead it may desorb or also may become incorporated at the sidewall, thereby increasing the wire radius beyond the droplet radius. Near the droplet, however, the adatoms are able to migrate to the growth interface and so in this area the diameter is equal to the droplet diameter. The result is a tapering near the tip of the wire yielding a 'pencil-shape' overall. This has been noticed in separate studies by Plante and Pierre [163] and Sibirev *et al.* [203]. Plante and Pierre state that the the straight sidewalls of pencil-shaped nanowires are due to the preference of adatoms to incorporate at step-edges, thereby preventing tapering away from the droplet region (provided there are no stacking faults), whereas Sibirev *et al.* state that the sidewalls are straight only due to the effect of shadowing from neighbouring wires, and that otherwise the wires would be conical. By using EBL to define the wire sites and thereby control the effect of shadowing, it is hoped to determine which of these explanations is responsible.

With regard to crystal structure and radial growth, an interesting paper by Shtrikman *et al.* [204] found that near-perfect wurtzite nanowires with a minimum of zincblende defects could be grown by using small droplet diameter, in their case $\approx 10\,\text{nm}$. They propose that these wurtzite wires be used as a sort of shell from which to grow thicker wurtzite structures via radial growth, which, as mentioned above, occurs when the nanowire length exceeds the diffusion length of Ga on the wire sidewalls. They suggest that lateral growth may occur epitaxially with the crystal structure being defined by the sidewall facets, and predict a minimum of stacking faults for this lateral growth mode. While limited radial growth has been shown in the studies of Plante and Pierre [163] and Sibirev *et al.* [203], and epitaxial growth has been demonstrated for core-shell nanowires (for example in the work of Tambe *et al.* [205]), here the focus is on the fabrication of perfect wurtzite structures having a width on the order of hundreds of nanometres, which has not yet been demonstrated. EBL defined catalyst sites present an attractive starting point since the effect of shadowing, which limits nanowire diameter for high density arrays, can be avoided.

5.4 Crystal Structure of GaAs Nanowires Grown in [111] Direction

The crystal structure of bulk GaAs is zincblende[1]. It has a cubic unit cell similar to Si as shown in figure 5.2(a) (cf. unit cell of Si in figure 3.1). The (111) surface of zincblende GaAs is shown in figure 5.2(c). Like Si, this surface appears to be hexagonal when viewed from above but is in fact three-fold symmetric, with one element slightly above the other. For GaAs, this means that the two $\langle 111 \rangle$ directions are distinct, with the Ga-terminated face known as (111)A and the As-terminated surface known as (111)B. The full structure of zincblende GaAs can be considered a stacking of these (111) layers with a spacing of 3.26 Å in an ABCABC ordering as shown in figure 5.2(d).

In certain cases, particularly in smaller structures such as nanowires, studies have found that the crystal structure may take the wurtzite form [172, 196, 197, 204, 206–210]. Wurtzite is simply the same (111) layer as shown in figure 5.2(c) stacked in an ABABAB ordering as shown in figure 5.2(e), with the same interlayer spacing (3.26 Å). From the perspective of an individual atom in the crystal, the structure is the same until the third nearest neighbour is reached, and as a result the cohesive energies of the structures differs by a relatively small amount, just 24 meV per pair ([207, 211]). More importantly, the band structure may also depend on the specific crystal structure [212]. The crystal structure of wurtzite is not cubic like zincblende but hexagonal, with the unit cell shown in figure 5.2(b). As a result, the Miller indices for the common planes are different, with the (111) plane of zincblende corresponding to the (0001) plane of wurtzite, for example.

The fact that the difference between wurtzite and zincblende GaAs structures can be reduced to a different stacking order of (111) planes means that the two structures can coexist, especially when the growth direction is along the [111]. The ability of a crystal to change structure by changing the stacking sequence is called 'polytypism'. It is this polytypism that also allows the growth of wurtzite nanowires on zincblende substrates. A 'twinning defect' can be formed when the stacking order of zincblende GaAs reverses via a single layer defect, called the twin plane. In addition, the structure is mirrored at the twin plane. The stacking order therefore proceeds: ABC ABC AB**C**ḂÀ ĊḂÀ ĊḂÀ, where **C** is the twin plane and the dot indicates a reflection of the original layer. Examples will be given later.

The exact reasons for the preference of wurtzite over zincblende for small structures is an interesting question. One would assume that this is due to a lower surface or edge

[1] Zincblende is also known as sphallerite. GaAs with wurtzite crystal structure will also be discussed. Although in mineralogy 'zincblende' and 'wurtzite' refer to compounds of Fe, S and Zn, here these expressions will refer solely to GaAs crystal structures having the architecture of those compounds.

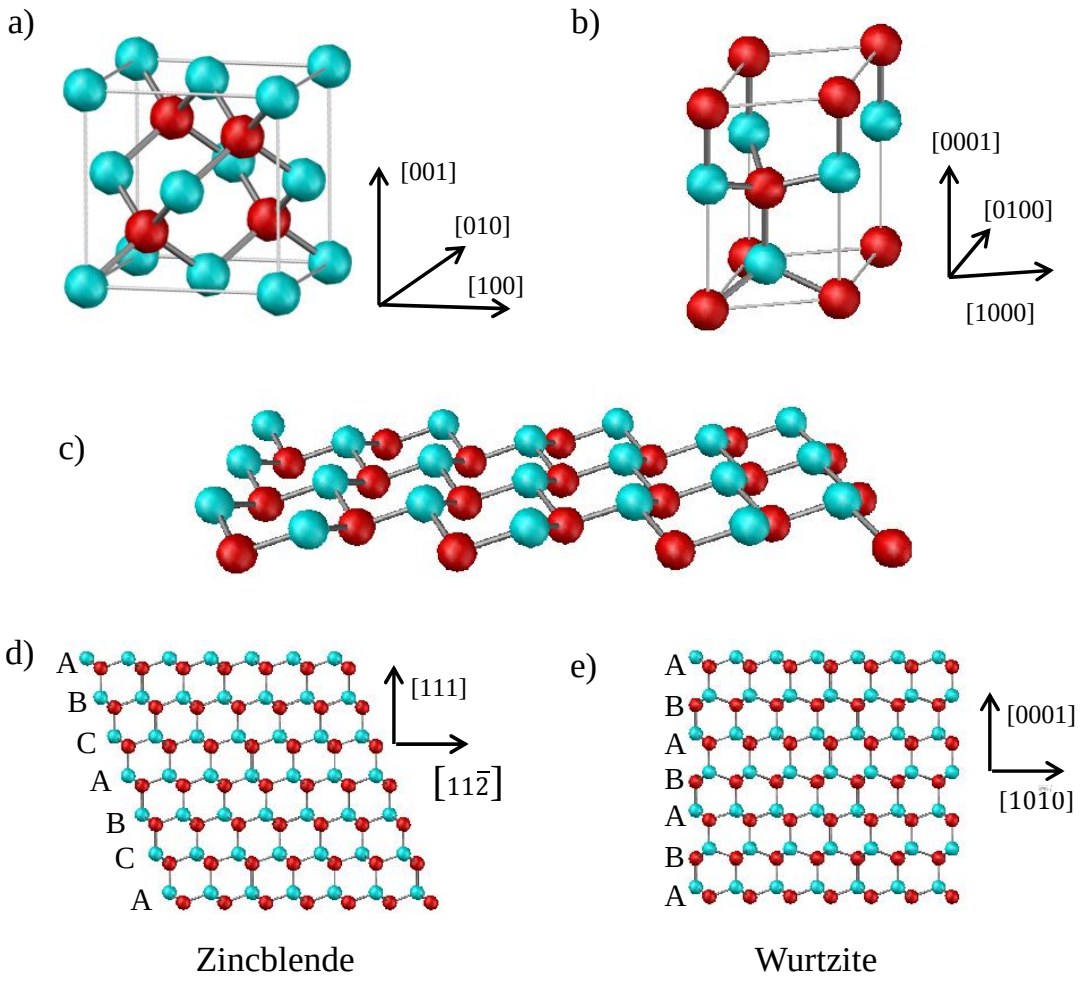


FIGURE 5.2: Unit cell of zincblende GaAs.

a) and b): The unit cells of GaAs zincblende and wurtzite crystal structures respectively.
c): The (111) plane of zincblende GaAs, or alternatively, the (0001) plane of wurtzite GaAs. If the cyan and red spheres represent the Ga and As atoms respectively, then this plane would be the (111)A face of zincblende GaAs, and vice versa for (111)B.
d) and e): Views of zincblende and wurtzite GaAs crystals, looking along the [110] and $[11\bar{2}0]$ directions respectively. The letters indicate layers that are identical by vertical translation only. It takes three layers for zincblende GaAs to repeat and only two for wurtzite GaAs.

energy for wurtzite which outweighs the bulk energy difference at high surface to volume ratios, and that there exists a critical diameter, d_c, below which wurtzite growth is more energetically favourable. However, a few studies have followed this argument only to find d_c values much lower than those seen in experiments (e.g. 11.2 nm [161], 5 nm [213]).

An in-depth nucleation-based study into some more subtle reasons for the occurrence of wurtzite structure for GaAs nanostructures was carried out by Glas *et al.* [207]. Their examination is specific to the Vapour-Liquid-Solid (VLS) growth mechanism of GaAs nanowires as was used in the present study. They looked in detail at the various energy

densities at play in the vicinity of the nucleus. They concluded that there were two conditions necessary for the preferential growth of wurtzite structure over zincblende. One was that the supersaturation of Ga needed to be higher than a critical value, which they showed was the case for their experimental values. The second conclusion relates to the areal energy density of the nucleus-vapour interface $\tilde{\gamma}_j$, where $j = W$ for wurtzite and $j = ZB$ for zincblende. For wurtzite growth to dominate, one requires $\tilde{\gamma}_W < \tilde{\gamma}_{ZB}$. Importantly, the value of $\tilde{\gamma}_{ZB}$ is dependent on the contact angle between the nanowire sidewall and the droplet which is on top of the nanowire during its growth. This contact angle is dependent on the diameter of the droplet relative to the diameter of the nanowire. Since the inequality between $\tilde{\gamma}_W$ and $\tilde{\gamma}_{ZB}$ is, according to the authors, quite closely matched, it is conceivable that the crystal structure might depend on the ratio of the size of the droplet at the top of the GaAs nanowire to the width of the body of the wire itself.

As mentioned, GaAs is zincblende in the bulk, while the nanowires can have zincblende or wurtzite crystal structure. Both of these structures are composed of stacked (111) planes (or (0001) planes in the case of wurtzite), and so there are, in principle, two possible hexagonal sets of facets for each structure which can make up the sidewalls of GaAs nanowires. These two facet families, which here are referred to as "Type 1" and "Type 2", are symbolised by the two blue hexagons superimposed on the (111) plane shown in figure 5.3. Whether nanowires have Type 1 or Type 2 facets can be determined by comparing the nanowire sidewalls to the cleavage edges of the substrate, which are the $\{1\bar{1}0\}$ facets. Type 1 facets correspond to $\{11\bar{2}\}$ for zincblende and $\{10\bar{1}0\}$for wurtzite, while Type 2 facets are $\{1\bar{1}0\}$ in the case of zincblende and $\{11\bar{2}0\}$ in the case of wurtzite. For wurtzite structures there is only a marginal difference in the surface energies for Type 1 and Type 2 facets, so the outcome will depend on phenomenological growth processes. For zincblende structures, however, it has been shown that the Type I or $\{11\bar{2}\}$ surface has approximately 15% more dangling bonds per unit area, and a surface energy approximately 33% greater, when compared to Type II surfaces [214, 215]. They are therefore more likely to reconstruct, but it has also been shown that the resulting microfacets, due to their larger surface area, are still energetically less favourable than Type 2 or $\{1\bar{1}0\}$ facets [216]. Therefore, if a particular growth results in nanowires with Type 1 facets then one would expect the crystal structure to be wurtzite rather than zincblende. Note that the edges (corners of hexagons) in figure 5.3 were chosen at random and are not representative of the lowest energy options, which in any case play a very minor role for wire diameters greater than 5 nm [215].

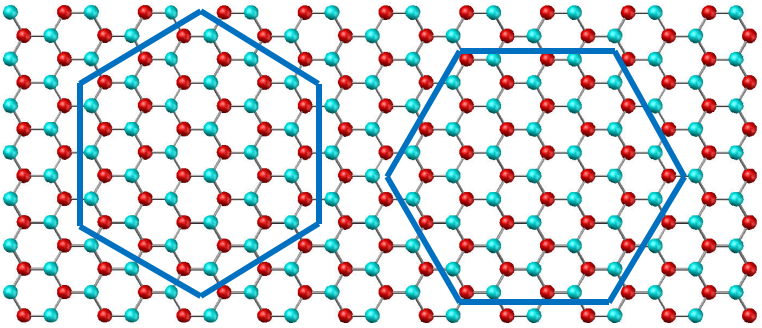


FIGURE 5.3: Different Hexagonal Facet Groups for Zincblende and Wurtzite Structures.

This figure shows a ball and stick model of the (111) zincblende plane, or equivalently the (0001) wurtzite plane, with blue hexagons indicating the possible facet groups for terminating the sidewalls of nanowires grown in the (111)B direction.

In fluid mechanics the contact angle for a droplet lying on a flat surface, θ_{ca}, is given by Young's equation [217, 218]:

$$\gamma_{LV} \cos\,(\theta_{ca}) = \gamma_{SV} - \gamma_{SL} \tag{5.2}$$

where γ is the interfacial energy, and the suffixes S, L and V denote that the interface is between solid, liquid and vapour, respectively. Two modifications can be made to this equation to more accurately represent the circumstances for a droplet on top of a nanowire [219–221]. Firstly, an effect known as line tension, represented by τ, becomes relevant on the nanoscale. This tension acts along the solid-liquid interface and can be directed inwards or outwards on the circumference of the droplet base, thereby altering the contact angle. It varies as $1/r_0$, where r_0 is the contact area radius that the droplet would have if it were on a perfectly flat surface (see figure 5.4(a)). Thus for macroscopic droplets ($r_0 \to \infty$) the term can be neglected. The second modification takes into account the fact that the surface on which the droplet rests is not entirely flat, but the droplet is essentially pinned by the boundaries of the solid-liquid interface. This term depends on the inclination angle of the wire sidewalls, α, as shown in figure 5.4(b). Including these terms gives us the modified Young's equation:

$$\gamma_{LV} \cos\,(\theta_{ca}) = \gamma_{SV} \cos\,(\alpha) - \gamma_{SL} - \frac{\tau}{r}. \tag{5.3}$$

A full theoretical modelling of the contact angle as a function of height and droplet radius will not be pursued here, but there are some findings from other studies and general comments based on equation 5.3 that will be relevant for later findings here.

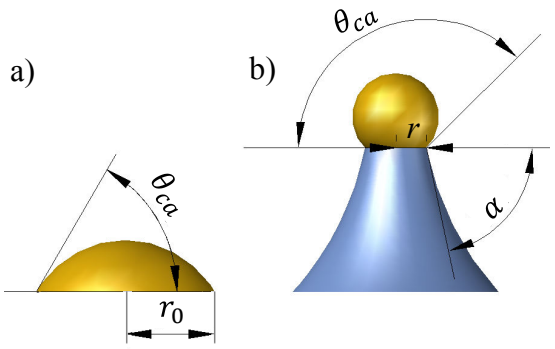


FIGURE 5.4: Schematic of contact angle and angle of inclination of sidewalls.

a) Droplet on a flat surface. Labelled are its contact angle, θ_{ca}, and the radius of the contact area r_0, where the 0 suffix denotes the value of r specifically for the case of the flat surface. b) Nanowire with contact angle, θ_{ca}, and the radius of the contact area r, labelled as shown. Also labelled is the angle of inclination between the nanowire sidewall and the solid-liquid interface, α.

Firstly, the introduction of the line tension term introduces a size dependency of contact angle on the the droplet volume. If τ is positive then the contact angle is increased for very small droplets. However, except for values close to zero, a positive τ will result in a termination of growth at a certain height, and so for steady state growth τ is usually assumed to be negative [217, 220, 222, 223].

A study by Schmidt, Senz and Gösele used equation 5.3 to describe the appearance of a wider base at the foot of nanowires [220]. As mentioned above, the mounds at the base of nanowires are sometimes thought to be caused by adatoms arriving at the wires via migration across the surface (pathway 4 in figure 5.1). However, Schmidt *et al.* pointed out that this effect is not temperature dependent, as would be expected for a diffusion activated process. Furthermore they show that since the base diameter scales approximately with the diameter of the droplet, it cannot be caused exclusively by overgrowth on the sidewalls. Under the assumption that the wide base has a contact angle related origin, they go on to calculate the radius of the wire as a function of height (i.e. tapering) and show how it matches well with experimental measurements of wires which are at an early stage of their growth.

The cross-sectional shape of GaAs nanowires grown in the [111] direction varies from cylindrical to hexagonal, although some studies reporting cylindrical nanowires were carried out without the means to examine whether or not the nanowire sidewalls were faceted [224, 225]. For growth of crystalline nanowires in which there is some element of radial growth, it is generally the case that it is the slowest growing facet group that ends up dominating the resulting structure. The reason for this is shown in figure 5.5. This series of images shows a cross-sectional view of part of a nanowire in its early stages

of growth. There are two families of facets, red and blue, which have high and low

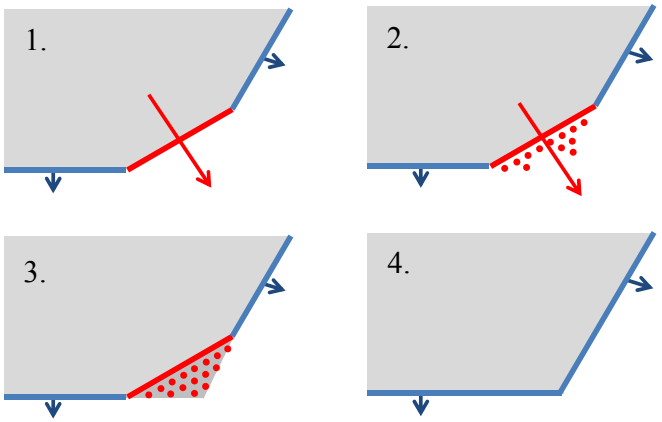


FIGURE 5.5: Schematic of competing facet groups during growth.

Cross section of part of a nanowire during early stages of its growth. There are two competing families of facets with faster and slower radial growth rates (red and blue respectively, with relative growth rates symbolised by the arrows). Because the red facet has a higher growth rate, it grows outwards (2) until it is flush with the slower-growing facets (3), leaving only the blue facets remaining (4).

growth rates respectively, as symbolised by the arrows (5.5(1)). Since more material is incorporated at the red facet, it grows outwards fastest (5.5(2)) until eventually the region grown is flush with the slower-growing facets (5.5(3)). Then the red facet has extinguished itself leaving only the blue facets remaining (5.5(4)).

Identification of sidewall facets is important, since it determines the atomic morphology and hence the mobility of adatoms on these surfaces. The atomic surfaces of the wurtzite $\{10\bar{1}0\}$ and $\{11\bar{2}0\}$ surfaces are shown in figure 5.6. An in-depth density functional theory study of these facets was carried out by Pankoke *et al.* to determine the potential energy surfaces experienced by Ga, As and GaAs molecules on these surfaces [193]. Of particular interest from this study was the energy barriers for adatoms to move upwards along the wire walls. To move up or down in the [0001] direction to an identical position to the starting point requires hopping the height of two layers, or 6.528 Å. For a Ga adatom, the energy barrier involved is 0.60 eV for the $\{10\bar{1}0\}$ facet and 0.32 eV for the $\{11\bar{2}0\}$ facet. Interestingly, the combination of a Ga adatom with As does not prevent further migration, since the critical nucleus for radial growth is larger than a single GaAs molecule. Pankoke *et al.* go on to calculate the hopping barriers for GaAs along [0001], which are 0.51 eV and 0.81 eV for the $\{11\bar{2}0\}$ and $\{10\bar{1}0\}$ facets respectively. The diffusivity of As adatoms on sidewalls is lower that of Ga for both facets, and for the researchers this supports their contention that As arrives at the Au-Ga droplet mainly by direct impingement. They did not conduct a full study into As_2 diffusion since its lifetime is so short. Also included in this study is the local minimum energy for adatoms

on the two facets, which informs us of the energy needed to evaporate the atoms from the sidewalls. For $\{10\bar{1}0\}$ the energy minimum for a Ga adatom is -2.34 eV while for $\{11\bar{2}0\}$ it is -2.56 eV. For GaAs molecules the energy minima are -2.91 eV and -3.26 eV for $\{10\bar{1}0\}$ and $\{11\bar{2}0\}$ facets respectively. This may have important consequences for the temperature dependence of radial growth.

5.5 GaAs Nanowire Fabrication Procedure

Ordered arrays of Pd-Au nanodiscs on GaAs (111)B substrates were created using EBL (see section 2.2.2.1) at the Polish Academy of Sciences, Warsaw. The Pd layer is 5 nm thick and the Au layer varied from 10 to 30 nm. The inclusion of the Pd layer is an unfortunate necessity to ensure adhesion of the Au during the EBL process. Although no sign of Pd could be found following the growth, and the droplet size following growth corresponded to Au rather than Pd, it cannot be ruled out that it affected the growth in some way. The liquid-solid phase boundaries extracted from phase diagrams for the Au-Ga and Pd-Ga systems are shown in figure 5.7. As can be seen, the proportion of Ga required to form a liquid at typical growth temperatures is substantially greater for a PdGa alloy compared to a AuGa alloy. Since it is the presence of the extra metal (Au or Pd) that promotes nanowire growth, it seems less likely that Pd would be a suitable metal to carry out this role. For this reason and since there are no reports of Pd being used to catalyse GaAs nanowire growth, the likelihood of Pd being responsible for nanowire growth appears remote.

Each sample had 100×100 µm patterned regions with four different separations (0.5 µm, 1 µm, 1.5 µm and 2 µm) and three different dot diameters (30, 60 and 100 nm). These

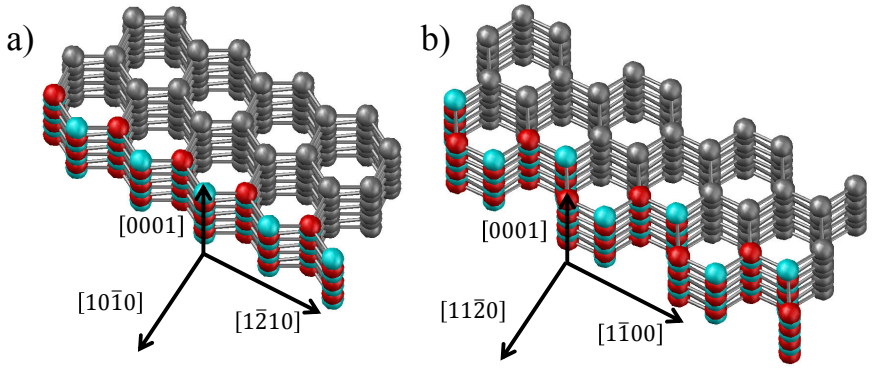


FIGURE 5.6: Two possible facets of wurtzite GaAs nanowire sidewalls.

Wurtzite GaAs facets are shown by the coloured spheres, with the grey spheres representing the bulk structure. a) is $\{10\bar{1}0\}$ and b) is $\{11\bar{2}0\}$.

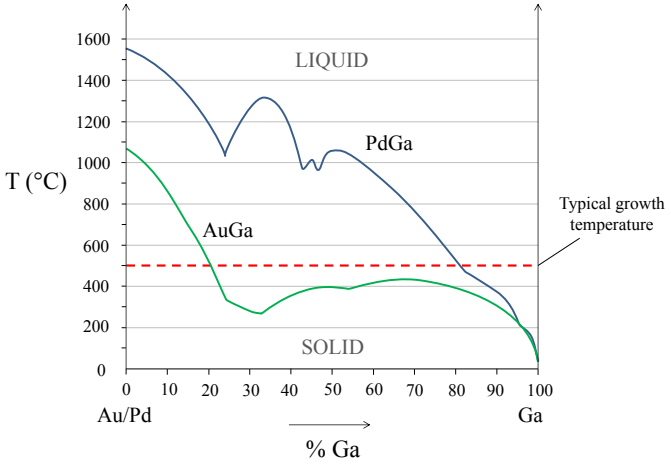


FIGURE 5.7: Liquid-solid phase boundaries for AuGa and PdGa alloys.

Liquid-solid phase boundaries extracted from phase diagrams of AuGa (green) and PdGa (blue) systems. The dashed red line indicates a typical temperature used during nanowire growth (500 °C).

were attached to the sample stage (cylindrical molybdenum blocks) by melting In onto their surface and then applying the sample wafer. Even though the substrate temperature is above the melting point of In ($\approx 157\,^{\circ}$C), the surface tension of the liquid metal is sufficient to adhere the wafer to the molybdenum stage. Alongside each patterned wafer was loaded another (111)B GaAs wafer with a 1 nm thick layer of Au. This uniform layer of Au will, upon heating, form a layer of Au nano-droplets which will catalyse the growth of a random array of GaAs nanowires. This procedure represents the conventional approach for VLS growth of GaAs nanowires. These wafers, which are referred to as "witness samples", are included to check for any differences between patterned and non-patterned methods, and also to provide samples for TEM analysis.

The samples are deoxidised by heating the molybdenum stage to 600 °C in the presence of As_4 (As pressure during deoxidation is approximately 1×10^{-3} Pa). This step also causes the Au layer of the witness sample to form a random array of Au-Ga liquid alloy droplets. Temperature was monitored using an infra-red pyrometer, although uncertainties exist since the emissivity of the sample changes as growth continues, and increases as much as 30 °C when both Ga and As source shutters are opened. Quoted temperatures for growth are those at the beginning of growth with both shutters opened, and have an uncertainty of $\pm 10\,^{\circ}$. Following the deoxidation process, the As and Ga fluxes are set and shutters are opened for the duration of the growth (30 mins - 4 hrs). The sample stage is rotated at approximately 0.2 Hz to ensure uniformity and the Ga flux angle is inclined at 40 ° to the surface normal.

5.6 Results

5.6.1 Ordered Arrays of Nanowires

A regular array (square grid) of GaAs nanowires grown from EBL-defined Au nanodots is shown in figure 5.8(a). The separation of droplets for this pattern is 2µm and initial Au discs had a diameter of 60 nm and a height of 10 nm. Here the array is well ordered with only a small number of wires which have moved from their ideal sites, possibly due to motion of the Au droplet at high temperature. Other grid sites have missing wires, perhaps because the Au droplet failed to generate nanowire growth and became buried under the arriving flux. Another common fault in arrays was double or triple wires growing in the vicinity of an array site. This is most likely due to the initial EBL-defined Au discs splitting into more than one droplet upon heating. Nonetheless this result shows significant promise for the ability to grow ordered arrays of GaAs nanowires. Figure 5.8(b) shows the 'witness sample' for this growth, i.e. the random

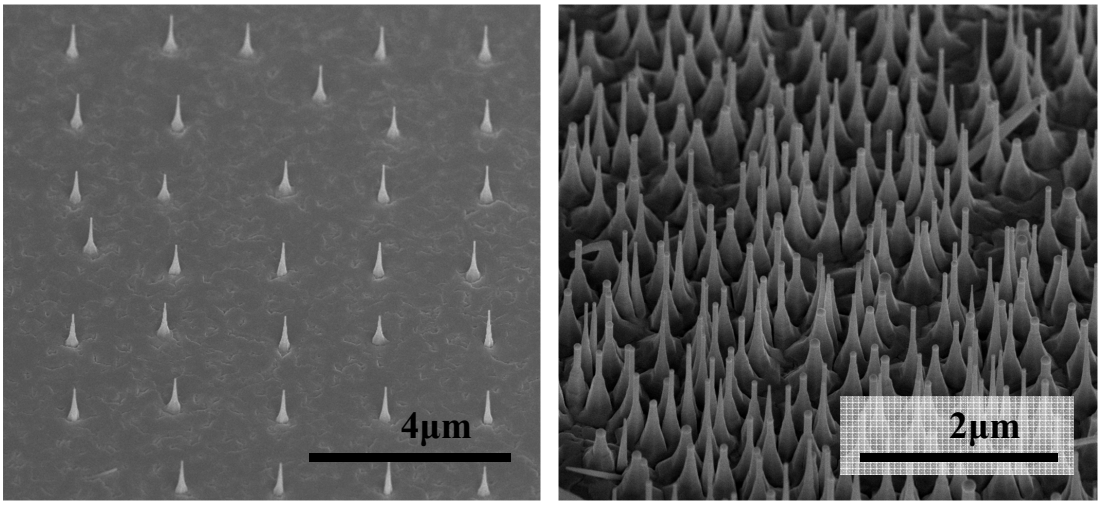


FIGURE 5.8: Ordered and Random Array of GaAs Nanowires.

a) Ordered array of GaAs nanowires viewed at 45 °.
b) 'Witness Sample' of (a). This is the disordered array of nanowires grown alongside the patterned sample, also viewed at 45 °.

nanowire array grown from a distribution of Au droplets produced by heating a uniform 1 nm thick Au layer. One can see that the nanowire shape on the witness sample is similar to the patterned sample, indicating that the growth is not significantly affected by the EBL process. One also notices that there is a wide distribution of wire diameters and heights for the witness sample compared to the ordered array. This is clearly shown in the height distribution analysis as shown in figure 5.9. Measurements from the SEM images were carried out using AutoCAD software as described in section 2.2.5. In this

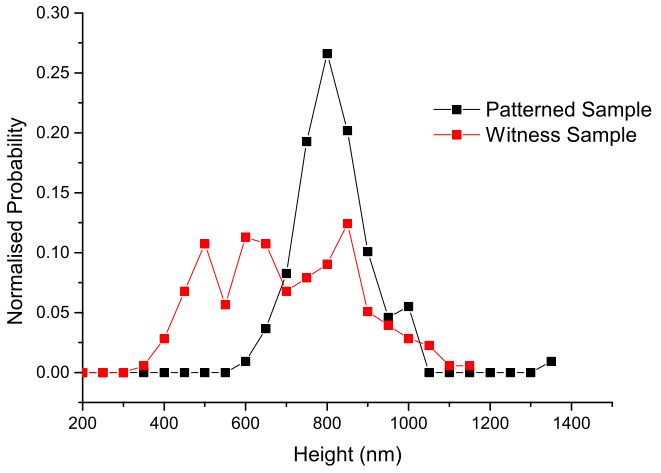


FIGURE 5.9: Height Distributions for Ordered and Random Nanowire Arrays.

Height distribution profiles for the pattered nanowire array shown in figure 5.8(a) (black) and the random array of the witness sample shown in figure 5.8(b) (red). There is a much broader distribution for the random array and lower mean height (724 nm vs. 844 nm).

graph it is clear that there is a much greater distribution of wire heights for the witness sample compared to the patterned sample, and also a reduction of the average height from 844 nm for the patterned sample to 724 nm for the witness sample. These effects have two causes: 1) There is a greater distribution of Au droplet diameters for the witness sample, and since height is related to diameter this incurs a distribution also. 2) Shadowing of neighbouring nanowires allows tall nanowires to grow taller at the expense of their neighbours, and also reduces the average amount of incident flux per nanowire. The effect of shadowing shall be examined in a more quantitative manner in coming sections.

A close-up SEM image of a wire from the sample shown in 5.9 and TEM images of a wire grown in a similar manner are shown in figure 5.10. Figure 5.10(a) is taken by looking in a direction inclined at 45 ° to the $[1\bar{1}0]$ direction, meaning that the facets that make up the pyramidal base (outlined by dashed red lines in 5.10(a)) are Type 1 according to figure 5.3. Therefore the facets are either $\{11\bar{2}\}$ if the structure is zincblende, or $\{10\bar{1}0\}$ if the structure is wurtzite. As mentioned previously however, the $\{11\bar{2}\}$ facets of zincblende are very unstable, so it is expected that the crystal structure of these nanowires to be wurtzite on the basis of the facets that can be seen.

Figure 5.10(b) shows a broad TEM view of the nanowire. Already stacking faults can be seen as dark lines crossing the wire perpendicularly to the growth direction. There is no evidence as yet for a core-shell structure. Also visible in this image is the darker Au

droplet at the top of the wire. A close-up view of the wire 'neck' is shown in figure 5.10(c). The crystal structure in this region is wurtzite with a very low density of stacking faults. A close-up view of the tapered base region is shown in figure 5.10(d). The zincblende

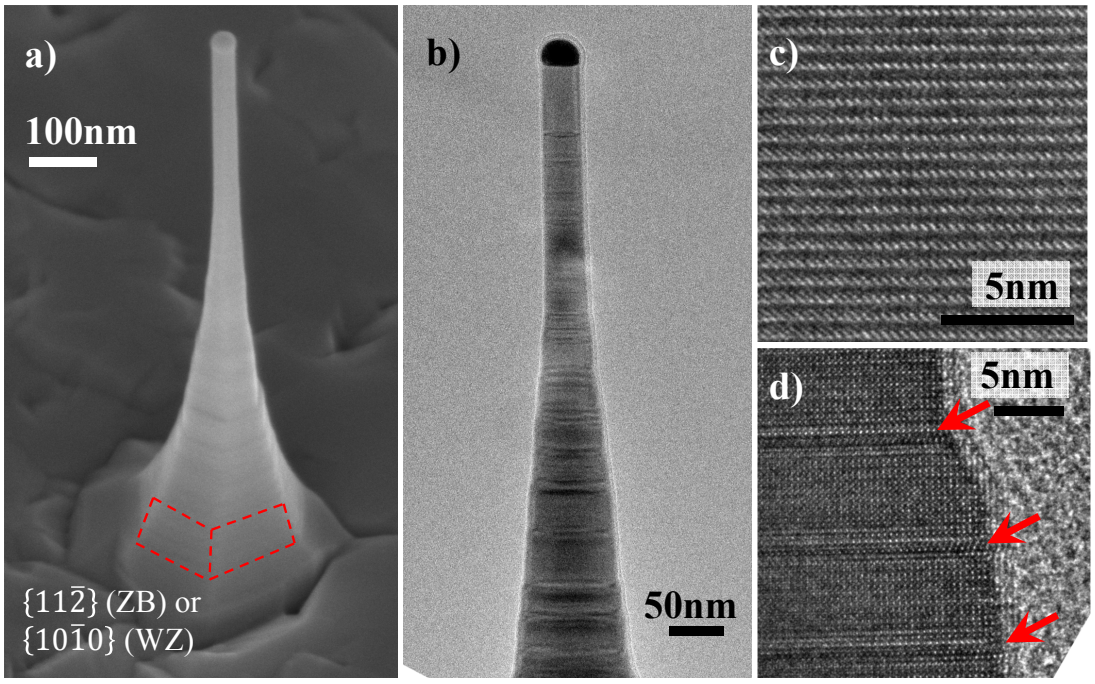


FIGURE 5.10: TEM analysis of wires in patterned array.

a) SEM image taken at 45 °of GaAs nanowire from the sample shown in figure 5.8. The image is taken looking along the $[1\bar{1}0]$ direction, so the facets of the tapered base which are highlighted with a dashed red line are most likely $\{10\bar{1}0\}$ (wurtzite structure).
b) TEM image of a nanowire grown using a similar recipe to that shown in (a). Stacking faults are visible as dark lines crossing the wire perpendicularly to the growth direction.
c) Close-up view of 'neck' region of nanowire which exhibits near-perfect wurtzite crystal structure.
d) Close-up view of tapered base region of the nanowires. Zincblende stacking faults crossing the predominantly wurtzite structure are indicated by the red arrows.

stacking faults crossing the wire diameter are indicated by red arrows, and these seem to coincide with locations where the wire diameter changes. The juxtaposition of tapering and stacking faults is interesting. It points to the theory of Schmidt *et al.* whereby the tapering originates from the decreasing area of the solid-liquid interface as growth continues [220]. The contact angle is likely to be quite low and fluctuate frequently as the wire diameter decreases, leading to the stacking faults that we see. The facets that are visible are likely to be the result of a certain amount of radial growth, which may have been favoured in the tapered region since the stacking faults can act as a preferential site for adhesion. Due to this radial growth an attempt to fit the sidewall profile to theory will be ineffective, or at least the complexity of the problem will be increased significantly.

5.6.2 Pencil-Shaped Nanowires

As mentioned at the end of section 5.3, Shtrikman *et al.* showed how near-perfect wurtzite nanowires could be grown by using Au catalyst droplets with small diameter [204], and recommended using these as a 'core' around which to grow a wider wurtzite structure via radial growth, whose growth rate increases rather drastically when the wire length exceeds the diffusion length of Ga on the wire sidewalls. It was decided to examine this theory by carrying out nanowire growth on a patterned sample as described in section 5.5. The growth was carried out at 520 °C, which is close to that used in the work of Shtrikman, and kept a high V/III ratio of ≈15. Growth was carried out on the patterned sample and a witness sample for 4 hours. SEM images from some of the resulting 12 patterned nanowire arrays are shown in figure 5.11. A portion of one of the 12 wire arrays is shown in figure 5.11(a). In this case the separation is 2μm and the droplet diameter is approximately 60 nm. The grid array is somewhat disordered by wires which have moved slightly from the sites defined by EBL, and by droplets which have divided and caused the growth of 2 wires at one site. Both of these effects are likely to have occurred during the deoxidation anneal, and further experiments may find some way of reducing these problems. The tapering near the wire tip is more evident

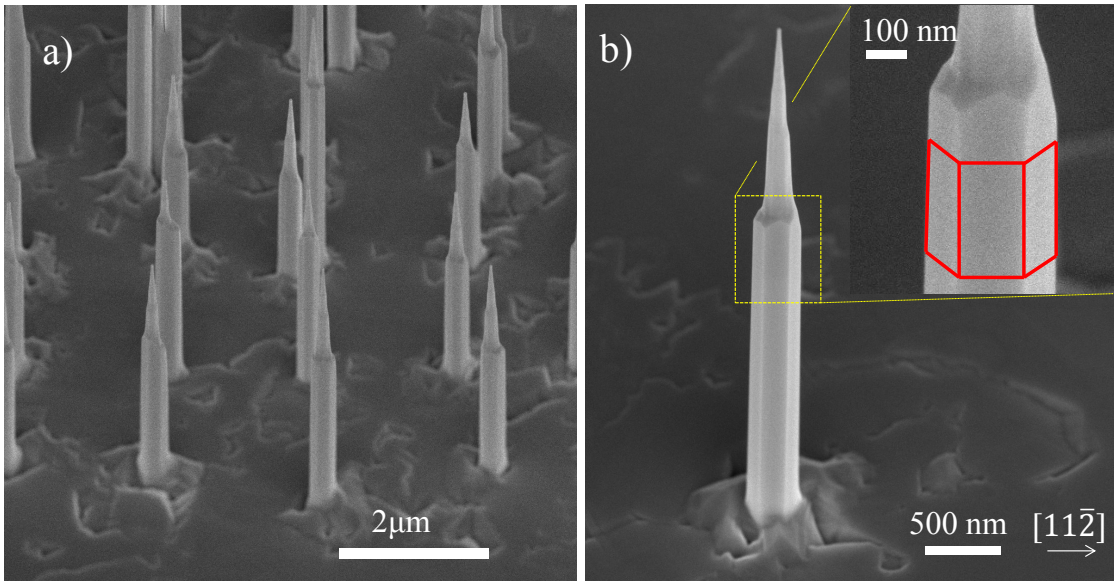


FIGURE 5.11: SEM images of pencil-shaped nanowire array.

a) SEM image taken at 45 °of GaAs nanowire array. The wires have a pencil-shape and the square-grid array pattern is visible (separation for the region shown is 2μm).
b) The tapering of the nanowire is more clearly visible in this image. The wire in this case is ≈300 nm wide, much wider than the diameter of the droplet, which is approximately 30 nm. Also visible are the facets which make up the wire sidewalls, which are enlarged in the inset and highlighted by red lines. As shown, the $[11\bar{2}]$ direction is to the right, while the direction facing the viewer (in the plane of the substrate) is the $[1\bar{1}0]$ direction.

in figure 5.11(b). This image shows the clear pencil-shape produced by the separate regions dominated by tapering and radial growth, as seen previously by Plante and Pierre [163] and Sibirev *et al.* [203]. However, in the present case the low density achieved by using EBL-defined catalyst sites has enabled us to attain much greater width. One also notices that the width is uniform from the base up, with none of the 'reverse tapering' near the base caused by shadowing as seen in previous studies. The finding also confirms that the sidewalls are not vertical due to the effect of shadowing which would prevent the base region from outgrowing the remainder of the wire, but is more likely due to radial growth occurring in a layer-by-layer manner, where adatoms preferentially attach at an unfinished layer. From the inset of 5.11(b) it can be seen that the sidewalls are Type 2 according to figure 5.3, i.e. the nanowire sidewalls are parallel to the $\left[1\bar{1}0\right]$ edges of the bulk (zincblende) substrate. Therefore the facets may be $\left\{1\bar{1}0\right\}$ if it is zincblende or $\left\{11\bar{2}0\right\}$ if it is wurtzite, and TEM must be used to confirm which is correct.

TEM was carried out using wires from the witness sample with the results shown in figure 5.12, beginning with a broad TEM view in 5.12(a). The tapering of the nanowire near the tip is evident in this image as was seen in the SEM images. A high-resolution image of part of the right hand side of this wire is shown in figure 5.12(b). The structure has no stacking faults over the 100 or so layers shown. In fact, no stacking faults were visible anywhere in the wire in the region shown in figure 5.12(a). This represents a remarkable level of control over the crystal structure and a promising fabrication method for applications where pure wurtzite structures are required, with a capability of achieving dimensions in the region of hundreds of nm. It should be noted that the dark and light bands running along the length of the wire to the right-hand side of this image are simply contrast effects related to the varying depth of the wire along the direction of viewing, and are not structural in origin. The rows of dots in figure 5.12(b) which presumably represent atomic layers appear to come grouped in pairs. This hints at wurtzite structure which has a periodicity of two layers. The average distance between the pairs of layers in the region shown was measured at 6.46 Å, which is close to the actual distance between two planes in wurtzite GaAs (6.52 Å). Figure 5.12(c) shows the Au-Ga cap of the nanowire, which is hemispherical in shape. As mentioned in section 5.4, the contact angle can play a role in determining the crystal structure of the resulting wire, and so the fact that the droplet is almost perfectly hemispherical, and that the contact angle is therefore almost exactly 90 ° may provide the explanation for the perfect wurtzite structure seen in these wires. Energy Dispersive X-Ray Spectroscopy (EDX, as described in section 2.2.2.1) was carried out on the wire cap, and found an Au to Ga ratio in the droplet of 3:1. This suggests that the Au droplets opt to consume as much Ga as is required to remain a liquid at a given temperature, until the eutectic point at the local minimum of the liquid phase of the Au-Ga phase diagram is reached. The

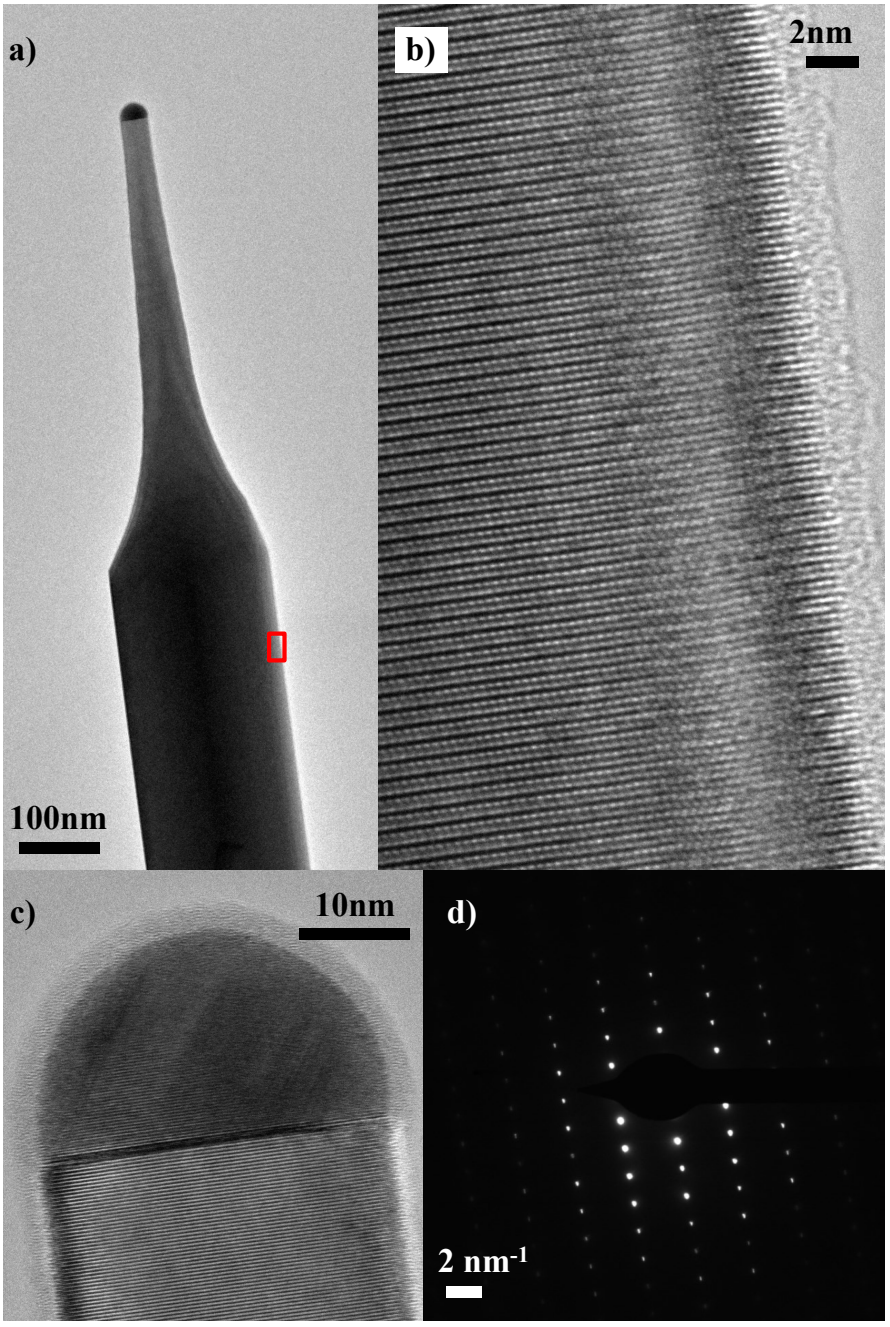


FIGURE 5.12: TEM images of pencil-shaped nanowire.

a) Low resolution TEM image showing general nanowire shape. Features visible include the Au-Ga cap and the tapering near the tip.
b) Atomic resolution image of the area in the red rectangle in (a), showing the stacked layers making up the wire structure. The separation between the layers is 3.26 Å, and the distance between identical points along the growth axis is twice this value, indicating that the stacking is ABABAB, or wurtzite.
c) TEM image of the Au-Ga cap. The crystal planes are also visible in the wire neck.
d) Selected area diffraction pattern of the wire body. The pattern corresponds to the $[11\bar{2}0]$ direction of wurtzite GaAs.

crystal planes of the wire can also be seen. The structure in this region is the same as the body of the wire, with no sign of a switch to zincblende as was noticed in the work of Plante and Pierre and other studies [172, 199, 207, 226]. The switch to zincblende is normally associated with excess Ga being consumed after the flux has been turned off due to sufficient heat and As in the chamber, but condensing with zincblende structure due to lower supersaturation. For the sample described here, the implications are either (a) there is no excess Ga during growth, (b) excess Ga is present but is condenses in wurtzite structure despite lower Ga saturation, (c) excess Ga desorbs following growth or (d) excess Ga forms a thin layer around the Au droplet and was not detected by us for some reason. Further examinations should be carried out to confirm which option is responsible. Figure 5.12(d) shows a Selected Area Electron Diffraction (SAED) pattern measured at the centre of the wire body. The separation between bright points along the growth axis is $1.56\,\mathrm{nm}^{-1}$, corresponding to a distance of 6.34 Å, which is close to the actual separation of two (0001) wurtzite planes (6.52 Å). The separation of bright points across the growth axis is $2.96\,\mathrm{nm}^{-1}$, corresponding to a separation of 3.37 Å. This is close to the periodicity of the $\{11\bar{2}0\}$ facet of GaAs (3.46 Å). It is not unexpected that the $\{11\bar{2}0\}$ facet is facing upwards, since this means that the wire is lying with its downward facing facet flat on the TEM grid, rather than lying on its edge.

5.6.3 Examination of Effect of Shadowing for Pencil-Shaped Nanowires

Wire volumes were measured for each of the twelve patterned regions of the sample described in section 5.6.2. Each wire was approximated as a cylinder (the faceted lower portion with uniform width) with a cone on top (representing the tapered region). The 'cylinder' diameter, and heights of the two individual portions were manually measured using AutoCAD for a total of 1372 nanowires, from which averages were found for each of the 12 patterned regions. Since there was a tendency for some Au droplets to become buried rather than produce nanowires or to split into 2 or more droplets resulting in multiple nanowires per EBL site, the 'true' nanowire density was also measured by finding the area occupied by ≈ 200 wires for each site. As shown in figure 5.13, there is an increase in nanowire volume with separation, asymptotically reaching a maximum volume for the case of wires which are effectively isolated. For nanodot arrays with similar separation but varying diameter, the resulting wire volume was found to increase slightly for decreasing diameter of the nanodot/droplet. This is probably due to the fact that if two cylinders have differing radii and height but the same volume, then the taller one will have a greater surface area with which to gather Ga adatoms and will therefore grow at a faster rate. This is examined in greater detail in the model described below.

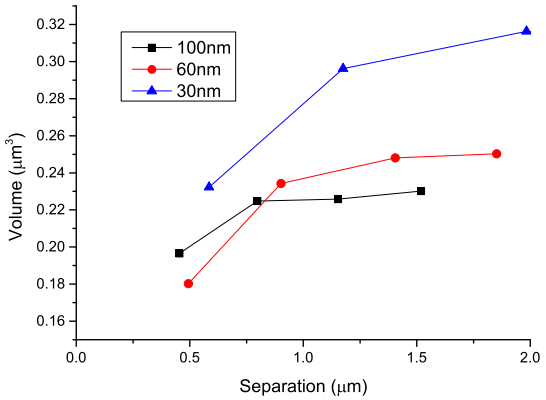


FIGURE 5.13: Dependency of Nanowire Volume with Separation.

Plot of nanowire volume versus inter-wire separation. There is an increase in volume with separation until it saturates for large separations, where the nanowires are effectively isolated. The symbols are coloured according to the diameter of the initial diameter of the Au disc created by EBL.

Shadowing causes tall wires to grow at a faster rate at the expense of shorter wires. One would therefore expect to see a greater distribution of wire volume at higher wire densities (i.e. lower separation). To examine this for the pencil-shaped nanowire sample, the standard deviation in volume was calculated for each of the 12 patterned regions. The results were normalised by dividing by the average volume for each of the 12 regions. This normalised distribution was then plotted as a function of separation. The results are shown in figure 5.14. As expected there is a decrease in the normalised distribution with increasing separation. This is further evidence of shadowing, and illustrates the need for isolated nanowire growth in order to achieve uniform results. There was no clear influence of the droplet size on this relationship, although the noise in the data prevents any concrete assertions.

A simple numerical model of the influence of shadowing on nanowire growth was carried out in an effort to reproduce some of the phenomena observed here. The model is described in appendix A. Briefly, it assumes that the nanowires have cylindrical shape and experience an increase in volume per unit time which is proportional to their exposed cross-sectional area. Wires are shadowed by their nearest neighbours when the neighbours are tall enough to do so and when they are aligned with the flux direction. The model also assumes that adatoms landing within a distance D of the wire top contribute to the axial growth, where D represents the diffusion length of adatoms on the nanowire sidewalls. The remainder of the adatoms contribute to radial growth. It was found that increasing the diffusion length does not affect the resulting diameter a great deal, but increases the height quite significantly. The model was also found to depend

on the initial diameter φ_0. Smaller diameter wires had a greater rate of axial growth in the initial stages, resulting in greater cross-sectional area and consequently greater final volume.

The results of the numerical model are plotted along with the experimental data in figure 5.15. For these simulations the initial diameter of the cylinders (φ_0) was equal to the diameter of the nanodots patterned using EBL, and the diffusion length D was fixed at 225 nm. As can be seen the fit is quite good, especially for the wires grown from nanodots having diameters of 30 nm and 60 nm. The fit is not so accurate for the case of wires grown from nanodots having 100 nm diameter. The discrepancy is not likely to be due to the value of the diffusion length, but probably related to these larger Au nanodots breaking up into smaller droplets, which would reduce their average diameter and result in wires with greater volume. This reasoning is supported by the fact that there is a greater discrepancy between the wire density and nanodot density (determined by EBL) for larger droplets. This is explored qualitatively in the coming section. As shown in appendix A, the volume depends very strongly on the diffusion length and within the assumptions of the model the value of D is certainly not out by more than 10%, although the actual value may be quite different due to the simplicity of the model. Nonetheless, the value of the diffusion length used in these simulations, 225 nm, is not unreasonable. It matches very closely to the value of 300 nm found by Sugaya *et al.* at this growth temperature [202]. In figure 5.12(a) it can be seen that the tapered region at the top of a nanowire is ≈ 500 nm, so it is reasonable that the diffusion

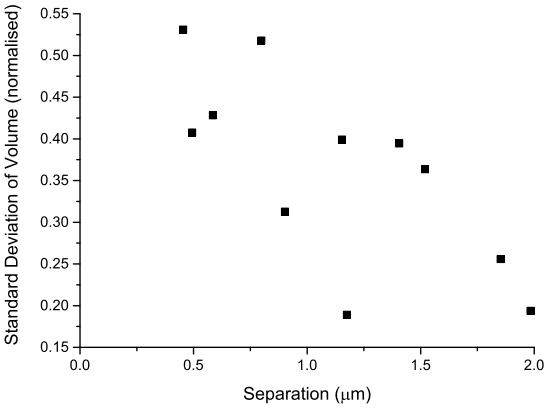


FIGURE 5.14: Dependency of nanowire volume distribution with separation.

Plot of the standard deviation of wire volume, divided by the average volume for that region as a function of separation. There is a decrease with separation, indicating more uniform volumes at greater separation.

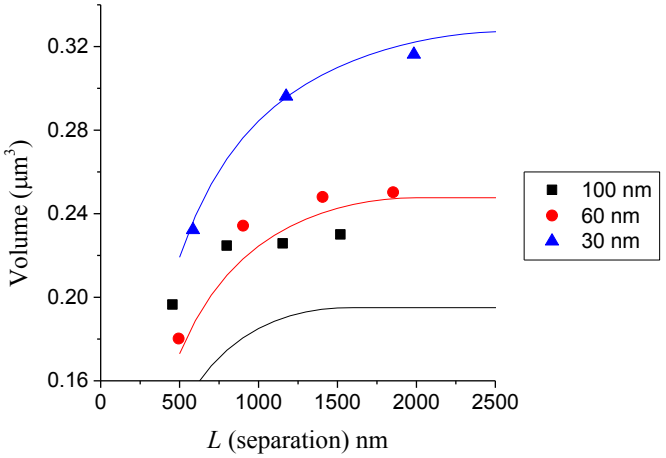


FIGURE 5.15: Nanowire volume vs. separation with numerical model

Plot of nanowire volume versus inter-wire separation as shown in figure 5.13. Also shown are the results of a numerical simulation for nanowire growth which includes the effect of shadowing (solid curves). The only parameter varied for each of the curves was the initial wire diameter which was set equal to the diameter of the nanodots as defined by EBL. The value of the diffusion length D was kept fixed for these datasets at 225 nm.

length is approximately half of this length, though further study should be carried out to examine exactly how the diffusion length is related to this exact shape.

5.6.4 Critical Dot Diameter for Nanowire Growth

Most studies of a 'critical diameter' in III-V nanowire growth refer to the transition diameter between zincblende and wurtzite growth, or the diameter above which the $1/d$ dependence of height breaks down. Very little consideration is given to the possibility of a minimum size of Au catalyst, below which nanowire growth is no longer possible, or below which the probability of generating wire growth falls below 50%. The reason for this blind spot is related to the traditional VLS growth mode, where nanowire growth directly follows the Au droplet formation via annealing, and the distribution of droplet sizes following nanowire growth is assumed to be representative of the distribution prior to growth.

One early study by Givargizov described a critical diameter for growth of Si nanowires catalysed by Au droplets on Si (111) [227]. In this study it was noticed that the growth rate was lower for smaller Au droplets, and this was related to lower supersaturation with decreasing diameter. At a certain diameter the supersaturation falls to zero and VLS growth is no longer possible. However, this may not be relevant for the present study since there seem to be key differences in the growth process; for example in the work of Givargizov, smaller droplets have lower growth rates, which is at odds with the

findings seen above. A later study of Ge nanowires on Si (111) by Dailey *et al.* was the most thorough examination that could be found on the subject of minimum catalyst sizes for initiating nanowire growth [228]. While they used catalyst droplets as small as 4 nm in diameter, they found a minimum nanowire diameter of 12 nm. They favour the explanation of nucleation-limited growth, whereby the nucleation rate in smaller particles was too small to generate wire growth. They also found evidence for delayed nucleation in small catalysts, which supports this argument. In contrast, another study of Si nanowires catalysed by Au droplets by Hofmann *et al.* found faster nucleation for smaller droplet diameters [229]. This was explained as being due to the rate of Si inclusion in the catalyst scaling with surface area ($\propto d^2$, where d is diameter), while the rate of Si concentration scales with volume ($\propto d^3$), resulting in a $1/d$ threshold saturation rate. This range of different findings in the area of size-limited nucleation of nanowires exemplifies the need for further examination, particularly if ordered nanowire arrays of narrow (order of tens of nm) are required for application purposes, where high failure rates of nucleation would be highly problematic.

For the patterned GaAs nanowire arrays presented here, F is defined as the nanowire areal density divided by the areal density of nanodots fabricated using EBL, and is expressed as a percentage. In the ideal case where every nanodot generates wire growth F should always equal 100%. When the initial nanodot diameter was greater than 60 nm, F was commonly found to be greater than 100%. This is most likely caused by the nanodots splitting into two or more droplets upon annealing. Most interestingly F was found to decrease with increasing separation. Provided F remains greater than 100%, this can be explained by neighbouring dots coalescing during the anneal, a process whose probability will decrease with increasing separation. However, for the smallest nanodot sizes ($\approx$30 nm) F was noticed to decrease well below 100%. While greater separation may imply a greater quantity of Ga which can migrate to the sample across the surface, this is not thought to impede nanowire development. Upon closer inspection it was noticed that the nanodot arrays of varying separation, which were supposed to be of equal diameter, in fact had shrinking diameter with separation. It was also noticed that dots at the edge of arrays were slightly smaller than average. The origin of these features is most likely that nanodots in higher density arrays are overexposed by the electron beam during the EBL procedure and therefore have a larger diameter following development. For the small ($\approx$30 nm) dots, the diameter increased by approximately 30% as the separation decreased from 2 µm to 0.5 µm. Although this was an unwanted feature in the nanodot arrays, once quantified it can be used to examine the diameter dependence of F. The nanodots were assumed to form hemispheres upon annealing. The radius of such hemispheres were calculated given the diameter and thickness of the deposited nanodots, and F was measured for a total of 16 arrays whose droplets had

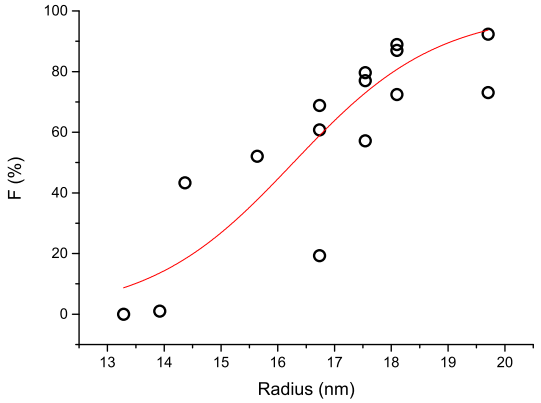


FIGURE 5.16: Probability of Nanodot initiating Wire Growth vs. Radius of Nanodot.

Probability of Au nanodot in an array initiating growth of a nanowire F, plotted against average radius of Au droplet within that array. The radius is that for an Au hemispherical droplet having equal volume to the nanodot fabricated using EBL, and F is found by dividing the nanowire areal density by the areal density of Au nanodots which initially formed the array. The red line shows a sigmoidal fit to the data.

a diameter in the region of 30 nm. The resulting plot of the values of F for varying hemisphere radius is shown in figure 5.16. As can be seen from the graph the data is quite noisy and does not fit exactly to the sigmoidal curve which has been fitted to the data. A sigmoidal curve is chosen simply because it is one which drops from 1 to 0 over a certain region, and is not believed to represent any underlying physical model. Despite the poor fit, it illustrates that there is a size dependence of the catalysing droplets on the probability of initiating nanowire growth. In the case of these samples grown at close to 500 °C with As_4, one can see that the probability drops below 50% for catalyst radii below approximately 16 nm. This implies that resulting nanowire width and density distributions should not be taken as indicative of the initial distributions of the catalysts. This finding points to the need for optimisation of growth conditions not only for a specific wire shape and structure, but also to ensure 100% nucleation rates, since reliability of nucleation will be a necessary feature for application purposes. For example, values of F close to or above 100% for radii down to 16 nm were achieved when As_2 was used instead of As_4 (this data is not included in figure 5.16 which deals only with nanowires grown in As_4). This is likely related to the higher reactivity of Ga with As_2 molecules. Other dependencies such as temperature, As pressure and choice of catalyst material should also be investigated.

5.6.5 Growth in As-limited Regime

The study of nanowire growth in an As-limited regime is most common in the area of catalyst-free growth. The reason for this is that in the catalyst-free growth mode the Ga and As fluxes have to be perfectly matched to ensure uniform diameter along the wires, since excess As will consume the droplet, putting an end to axial growth. Because the growth is so sensitive to the III-V ratio, experiments invariably stray into the As-limited regime where there is a build-up of Ga. This regime has a number of peculiarities not seen in Ga-limited growth. One effect is 'inverse tapering', where the diameter of the wire increases further from its base. This is due to the Ga droplet at the top of the wire increasing in size as the growth progresses due to a marginally insufficient supply of As. Also noticeable in this mode is the build-up of 'blobs' or crystallites of Ga between wires. The use of Au catalysts in an As-limited regime has been largely ignored, and it is desirable to examine whether or not these features noticed in catalyst-free growth can be reproduced when Au catalysts are used.

Several samples, both patterned and random, were grown with a V/III ratio of approximately 2 as was used for the sample shown in 5.8. To achieve As-limited growth an elevated temperature was used (520 °C), thus reducing the *effective* As flux through increased As desorption. Increasing temperature also extends the diffusion length of Ga, allowing it to travel more effectively to the droplet. Examples of growth from the random sample are shown in figure 5.17. Immediately one notices vast differences between these images and those shown in figure 5.8. The nanowires, which have a rather uniform height of approximately 2.3 µm, show inverse tapering with a large droplet on top (average diameter approximately 270 nm). Radial growth is likely to be very low judging from the narrowness of the wire bases. The average contact angle between the nanowire sidewall and the droplet was measured to be 138 °, ±2 °. The droplet is assumed to be excess Ga, but more conclusive proof shall be shown later. The reverse tapering is very similar in style to that seen in the studies of wires grown without the use of catalysts, so it is very likely due to the same effect, i.e. growing droplet diameter during the growth. Shadowing is not thought to be responsible for the inverse tapering in this case, since the wire density is quite low and tapering is not dependent on variation in density. Results from the patterned samples will be more telling in relation to the possibility of shadowing, since interwire separation can hopefully be specified.

Another very obvious feature in figure 5.17(a) are the large droplets on the surface between the nanowires. These are likely to be pools of excess Ga. Some of these, particularly the smaller droplets to the left of 5.17(a), have formed nanowire-like bases, and may be evidence of Ga-catalysed nanowire growth.

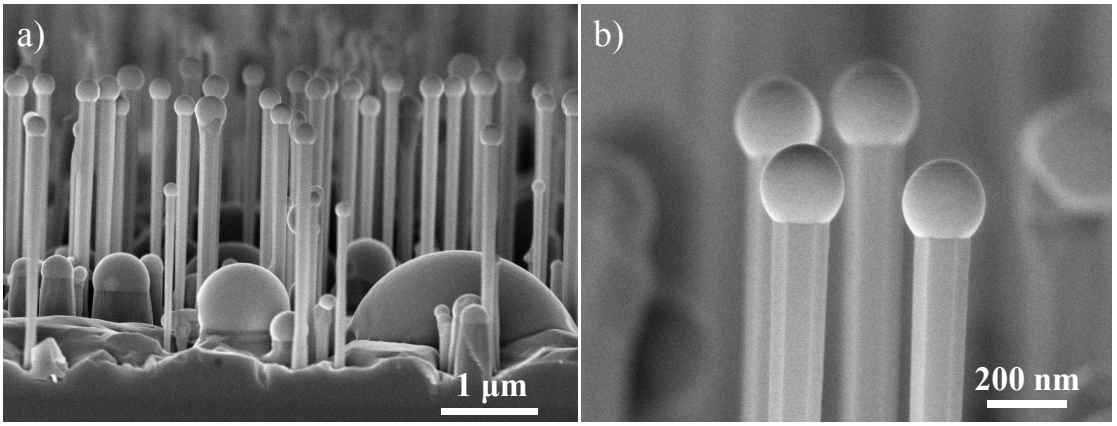


FIGURE 5.17: Nanowires grown in As-limited regime

SEM images of the nanowires grown in As-limited condition on the witness sample (random array covering entirety of substrate). These images were taken at a very shallow angle ($\approx 5\,^{\circ}$) to the substrate surface. As we can see in (a) the nanowires each have a large droplet at their tip. The nanowires seem to have a regular length and exhibit inverse tapering, with a larger diameter at their top than their base. There are also a large number of large droplets on the surface, which are most likely excess Ga droplets. Some of these, particularly the smaller ones to the left of (a), seem to be have grown a nanowire-like base. Figure (b) shows a close-up of the droplets on top of the nanowires.

To demonstrate the uniformity of the wire length, the lengths of 350 wires were measured from the witness sample. The histogram showing the results is shown in figure 5.18. Height was measured from base to top of the droplet. All visible wires and even short pillars, whether misshapen or not, were included in the examination. Just over 54% of

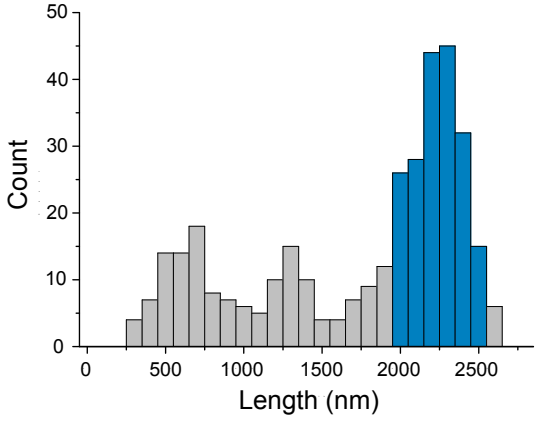


FIGURE 5.18: Histogram of heights of nanowires grown in As-limited regime

Histogram showing the numbers of wires having a particular height for 350 wires measured from the sample shown in figure 5.17. The blue bars denote wires with height in the region of 2 - 2.6 µm, which comprise 54% of all wires measured.

the wires have a height in the narrow region between 2.0 and 2.6 μm, as indicated by the blue bars in figure 5.18. This is despite the random dimensions of the gold droplets and the wide variations in wire density across the sample. This indicates that the outcome depends weakly on droplet arrangement. It also shows that arrival of As to the growth interface, which is process limiting wire growth, is not affected by shadowing, which is consistent with the findings of Ramdani *et al.* [195]. The apparent independence on separation suggests that migration of adatoms from the substrate floor constitutes only a minor contribution to the wire volume.

A patterned sample was grown alongside the witness sample shown above. SEM images from the patterned sample are shown in figure 5.19. Figure 5.19(a) shows a corner of one of the patterned arrays in the top right. The remainder of the image was once a bare (111)B substrate but is now covered in large droplets ranging in diameter from 1 to 10 μm, similar to those seen between wires on the witness sample (figure 5.17). Since there was no Au in these areas, it is concluded that the droplets are composed of excess Ga adatoms, which, aided by the high temperature (high mobility) and low As pressure (lower reactivity) were able to nucleate as droplets rather than become incorporated into the crystal substrate. Some of these Ga droplets also have nanowire-like bases similar to those seen in figure 5.17. The facets of these 'nano-pillars' are Type 1 according to figure 5.3, suggesting that the crystal structure is wurtzite. There is also a row of these large droplets along the perimeter of the patterned area, implying that the Au grid as a whole acts as a preferential sink for migrating Ga adatoms. This image shown in 5.19(a) also confirms that Au is necessary for growth of the tall (> 1 μm) nanowires, since up to this point the possibility that all structures were Ga-nucleated could not be ruled out. It also suggests that a significant proportion of the large droplets seen on the witness sample, and of the shorter nanowires in the height histogram in figure 5.18, are actually Ga-nucleated. Therefore if only Au-catalysed nanowires are considered, the percentage of nanowires having a height between 2.0 and 2.6 μm is likely to be greater than the 54% measured for all nanowires. A closer look at the interior of the patterned area is shown in figure 5.19(c). This area originally was covered in Au nanodots with a separation of 1 μm, but unfortunately no sign of the pattern is visible, and this was the case for all arrays. This is perhaps due to the increased mobility of the Au due to the elevated temperatures and also due to the highly mobile liquid Ga on the surface which may act as a medium for the Au to migrate. However, like the witness sample, the height and droplet diameter of the wires above 1 μm in length is surprisingly uniform.

A close-up image taken at 45 ° of an individual nanowire is shown in figure 5.19(b). The tapering of the nanowire and roundness of the droplet can be more clearly seen. It is also evident that the wires have hexagonal cross-section. Since the image is taken along the

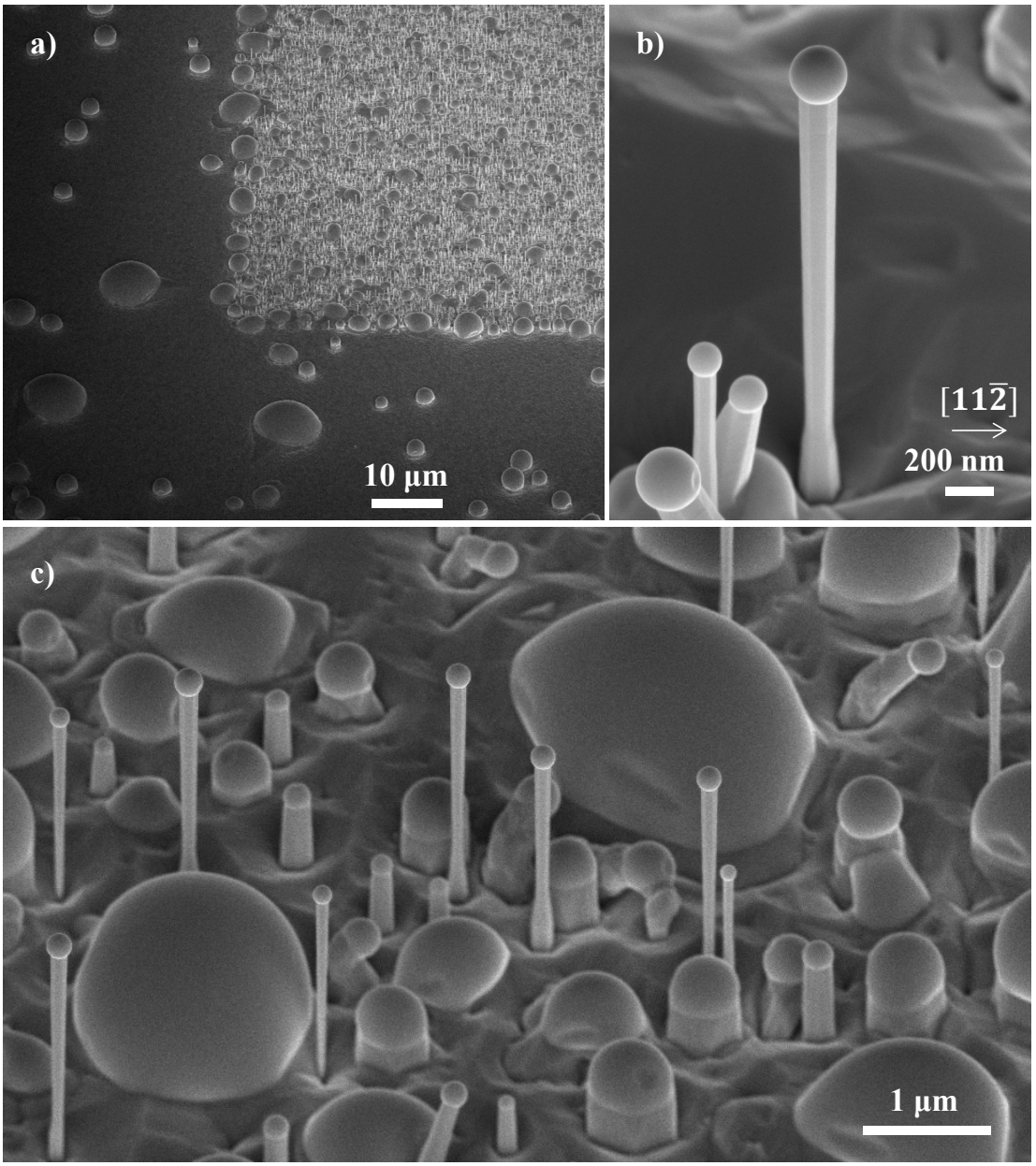


FIGURE 5.19: Nanowires grown from patterned arrays in As-limited regime

SEM images taken at 45 ° of the nanowires grown on a patterned array in As-limited conditions.
a) Corner of patterned area is visible, as well as droplets beyond the patterned region.
b) Individual nanowire with clear reverse-tapering. The direction indicated here also applies to (a) and (c).
c) Part of a patterned region with tall nanowires as well as large Ga droplets.

$\{1\bar{1}0\}$ direction we can tell that the facets are Type 2 according to figure 5.3, meaning that the crystal structure may be either wurtzite or zincblende.

In order to identify the material comprising the droplets at the top of the nanowires, STEM, TEM and EDX were carried out. STEM results of the droplets at the top of

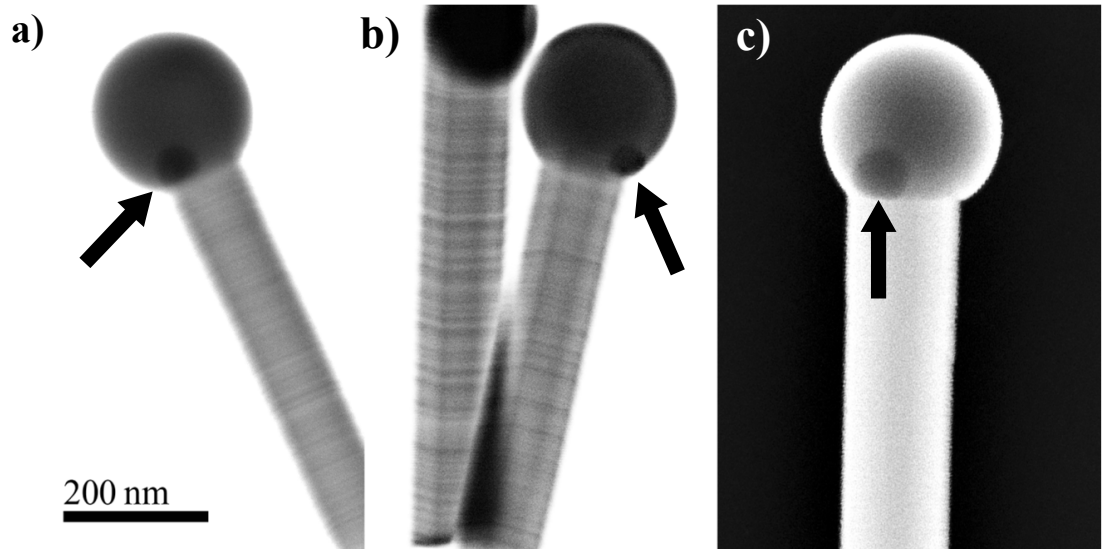


FIGURE 5.20: STEM of Nanowires grown in As-limited regime

STEM images of nanowires grown in As-limited conditions taken in bright field mode (a and b) and dark field mode (c). Au-Ga droplets within the Ga sphere are indicated by the black arrows.

three representative nanowires are shown in figure 5.20. Images (a) and (b) are taken in bright-field mode while (c) is taken in dark-field mode. A high density of stacking faults can be seen as dark lines across the diameter of the wires, particularly in (a) and (b). The Ga droplet is almost spherical, and the Au-Ga droplet within can be seen as a dark spot (due to the higher atomic mass of Au) within the droplet.

Figure 5.21 shows an SEM image of part of a nanowire as well as the accompanying EDX plot measured along its length. We see equal fractions of Ga and As along the wire body, and then a large increase in Ga at the droplet, concurrent with a falloff of As. There is a small increase in Au concentration at the droplet (blue line). The Au peak at the droplet is not as large as we expected, but it is quite possible that the line being analysed by EDX crossed a portion of the Ga sphere not containing the Au-Ga droplet.

A TEM image taken near the top of one nanowire is shown in figure 5.22. Overlaid on this image is a ball and stick model of the zincblende crystal structure. The image and model were scaled independently, confirming the accuracy of the match between the two. The twinning defects, where the ordering of the stacking sequence reverses, can be clearly seen. All twinning defects crossed the wire horizontally, suggesting that they came about during layer-by-layer growth at the solid-liquid interface. There were no defects running vertically through the wire, suggesting that if there was any appreciable radial growth, then it occurred epitaxially, following the crystal structure of the underlying sidewall.

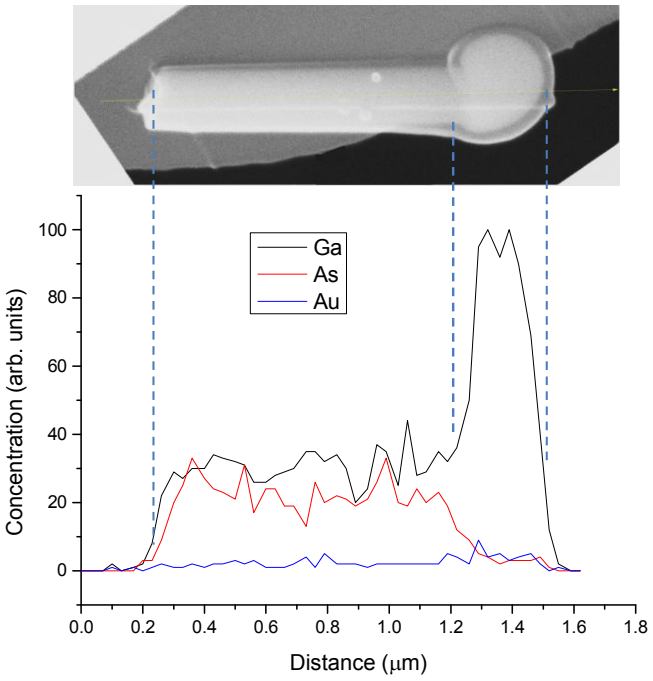


FIGURE 5.21: EDX examination of Nanowires grown in As-limited regime

SEM image of a nanowire grown in As-limited conditions, with the EDX plot underneath which was taken along its length. This confirms that the droplets atop the wires grown in this regime are mainly excess Ga.

The density of these defects in this approximately once every 7 atomic layers, or 0.4 defects nm^{-1}.

In figure 5.23(a) we see a broader view of this region, including the edge of the wire. We can see that due to the regular twinning defects the edge of the wire has a zig-zag profile of {111} microfacets. Thus the seemingly perfect $\{1\bar{1}0\}$ facets seen in the SEM images of figure 5.19 may in fact be a series of closely spaced microfacets giving the impression of $\{1\bar{1}0\}$. The FFT produced for this area (inset) is streaked in the direction of growth due to the high density of stacking faults. Figure 5.23(b) shows another TEM image taken near the base of the wire. Here the density of defects is approximately an order of magnitude lower than near the top, and the wire sidewalls appear to be 'true' $\{1\bar{1}0\}$ facets. The inset of this image shows a selected area FFT taken in this region. This FFT is seen more clearly in 5.19(c), where the distance between bright points have been converted to Å and angles have also been measured. These results can be compared to the actual distance between the planes shown in figure 5.19(d). As can be seen, the match between (c) and (d) is very close.

The presence of {111} microfacets is unusual but not without precedent. Highly ordered GaP nanowires with {111} microfacets were grown by Johansson *et al.* [230], and later

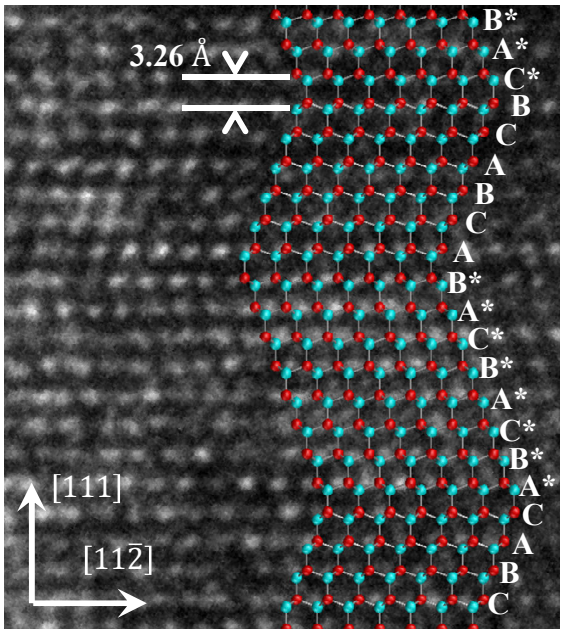


FIGURE 5.22: High resolution TEM images with crystal structure overlay.

TEM image taken near the top of a wire grown in As-limited conditions. Overlaid is a crystal structure model for zincblende, which highlights the twinning defects in the wire.

the same team showed excellent regularity of the {111} microfacets on InAs wires [226]. Both of these studies showed how the microfacets can be viewed as slices of octahedral crystals stacked on top of each other as shown in figure 5.24. Another group showed the existence of {111} microfacets on GaAs nanowires using glancing angle x-ray diffraction [231].

The lower portion of the wire, as mentioned before, has a low density of stacking faults, and the sidewalls in this region do not zig-zag at 19.5 °as is the case for {111} microfacets, meaning that the sidewalls near the base are simply $\{1\bar{1}0\}$ facets. In order to more closely examine the transition between the lower faceted and upper microfaceted regions of the nanowires, it was decided to carry out a similar growth but with shorter duration (60 minutes vs. 90 minutes). The results were broadly similar to those seen for the 90 minutes growth (figure 5.19) although average wire length was shorter, as expected. One feature which was new for the shorter growth was the occurrence of wires having different facets along its length. The transition, when observed, was always Type 1 near the base to Type 2 near the top (as defined in figure 5.3), and the transition was rather abrupt, changing within a few tens of nanometres. Five examples of wires with facets transitions are shown in figure 5.25. Since we know that the structure near the base is zincblende with a relatively low density of defects, we can say that the crystal structure of the lower portions of these wires is zincblende with $\{11\bar{2}\}$ facets. This facet is unstable and is likely to have reconstructed on an atomic scale.

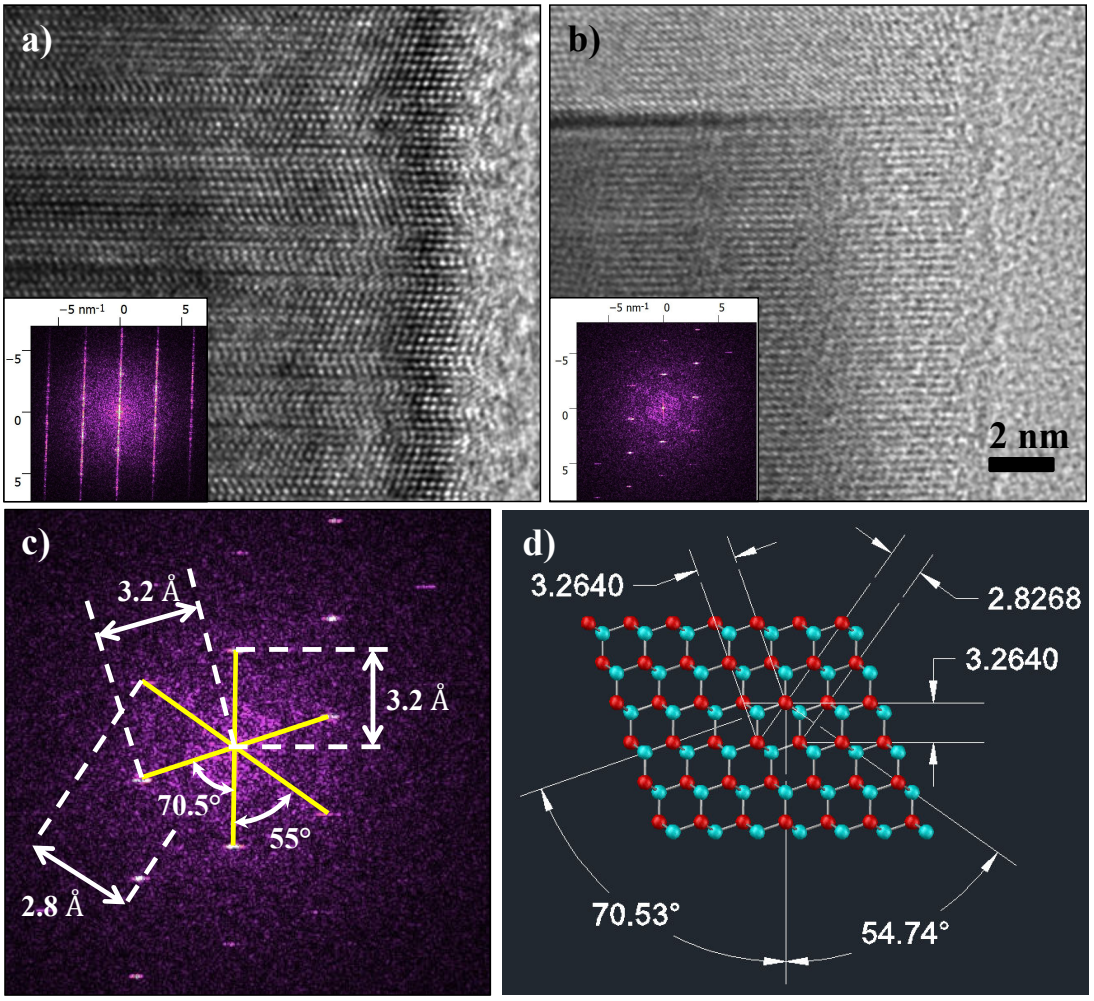


FIGURE 5.23: High resolution TEM images taken of a nanowire grown in As-limited conditions.

a) Image taken near top of wire showing the twinning defects and zig-zag profile of the sidewalls, which is likely to consist of {111} microfacets. The inset shows the FFT produced from this region.
b) Image taken near the base of the wire showing a much lower density of twinning defects. The sidewalls appear to be conventional $\{1\bar{1}0\}$ facets. The inset shows an FFT taken of a region between stacking faults.
c) Closer view of the FFT shown in the inset of (b). Distances shown refer to distances between diffraction points inverted to give units of length.
d) 3D model of zincblende GaAs structure with measurements and angles highlighted which correspond to diffraction pattern in (c).

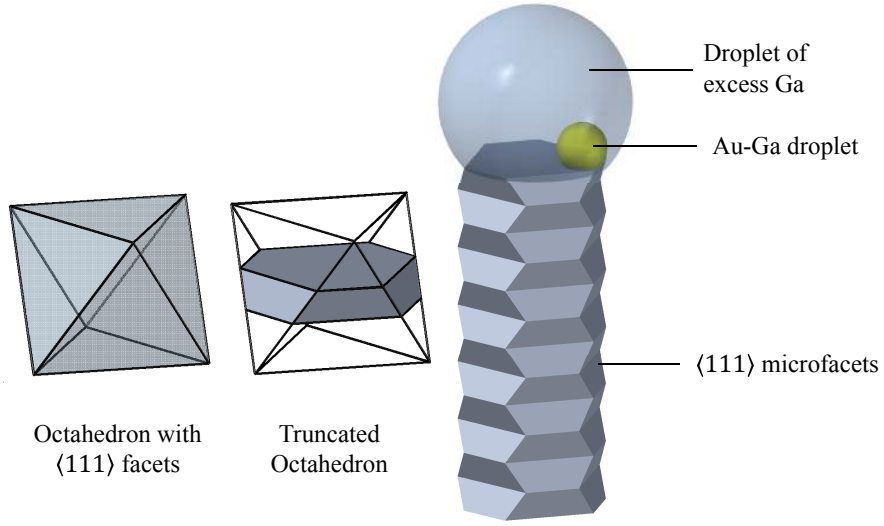


FIGURE 5.24: Schematic of nanowire with microfacets

Schematic presentation of nanowire with {111} microfacets. Each 'slice' of the nanowire can be considered as a truncated octahedron with {111} facets.

Throughout their length, these nanowires grown in As-limited conditions exhibited zincblende crystal structure. As mentioned in section 5.4 to Glas *et al.* found that wurtzite forms due to a high supersaturation and a contact angle between the droplet and the wire of close to 90 ° [207]. Due to the larger droplet at the top of the wire, the contact angle seen in these wires is much greater than 90 ° (≈ 132 °). It is possible that this is the reason for the preference for zincblende growth in these conditions.

Again, all defects are planar, crossing the wire radially rather than axially. This suggests that zincblende (111) island nucleation occurs at one edge of the solid-liquid interface, with each new layer growing until it covers the entire interface. Any radial growth on

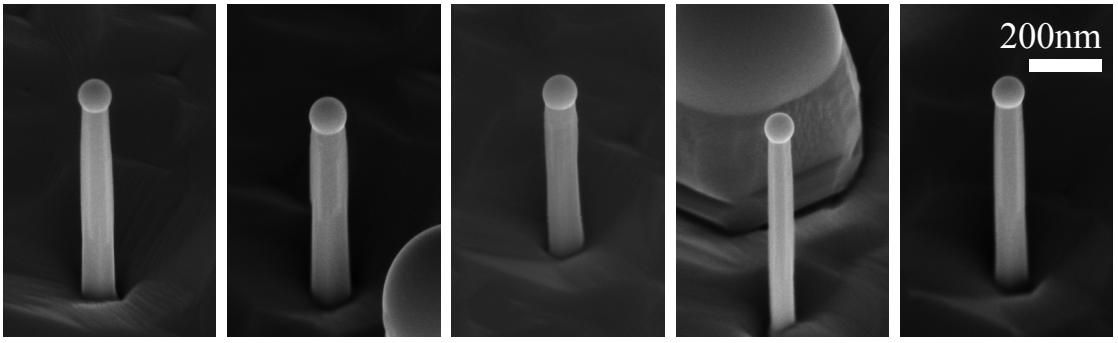


FIGURE 5.25: As-limited growth of shorter duration

Wires grown in an identical manner to those seen in figure 5.19 but with a growth duration of 60 minutes rather than 90 minutes. These particular 5 wires all exhibit facet transitions along their length from Type 1 near the base to Type 2 near the top (as defined in figure 5.3).

the nanowire sidewalls is epitaxial, following the underlying crystal structure without inducing defects. However, radial growth appears to be minimal, as evidenced by the reverse tapering seen for tall nanowires (e.g. figure 5.19).

The combined evidence from the TEM data and the observations of the nanowires grown for shorter duration suggest that there are at least two stages to the growth of these nanowires. Initially, the wire grown has zincblende crystal structure with a low density of twinning defects and $\{11\bar{2}\}$ facets. At some point, the density of twinning defects increases and the wire adopts $\{111\}$ microfacets, which at lower resolution appear to be smooth $\{1\bar{1}0\}$ facets. By the end of the 90 minute growth, there is no sign of the initial $\{11\bar{2}\}$ facets in the lower portion, implying that radial growth on the sidewalls has overgrown these previous facets and left the lower region with $\{1\bar{1}0\}$ facets, which have a smoother boundary with the $\{111\}$ microfaceted upper portion. It is quite likely that the border between the $\{11\bar{2}\}$ and $\{1\bar{1}0\}$ regions as seen in figure 5.25 acted as preferential attachment points for adatoms. Thus the border between these two regions moves downwards as adatoms attach there, until all sidewalls are $\{1\bar{1}0\}$ or $\{111\}$ microfacets.

It remains to be proven why the wires initially preferred the $\{11\bar{2}\}$ facets and what caused the increase of twinning defects that led to the onset of $\{111\}$ microfacets. With regard to the former problem, it is notable that all of the squat nanopillars have Type 1 facets, i.e. $\{11\bar{2}\}$ if zincblende. It is possible therefore that this is the preferred facet arrangement in As-limited conditions, and that the $\{1\bar{1}0\}$ facets seen on the tall nanowires are the exception rather than the rule, brought on by the microfacetting behaviour at greater heights. Although this appears to be the case it is difficult to explain why the system has opted for these high energy surfaces. The study by Dick *et al.* [226] cites the earlier theoretical work of Leitsmann and Bechstedt [214] which described how under highly passivated conditions, surface energies can be negative, and zincblende $\{11\bar{2}\}$ facets may be preferred. Furthermore, higher surface areas will then be preferred, which would explain the microfacetting seen near the top of the wire. Johansson *et al.* who also grew nanowires with $\{111\}$ microfacets, mention how the energy barrier for formation of twin planes is very low and can easily be caused by fluctuation in mass transport [230]. Thus a transition in the rate of arrival of Ga as the wire grows taller may be the cause. Another possible cause, as mentioned earlier, is the growing contact angle between the liquid droplet and the solid wire as growth continues. Further study should be carried out to confirm whether or not Ga flux can be varied to control crystal structure, or whether there is a dependency of contact angle on sidewall facets.

An important finding of this study was the difficulty in conversion of ordered arrays of Au nanodots defined by EBL to ordered arrays of nanowires. As stated above, no

patterned region resembled the original grid. Those wishing to make use of nanowires grown in Ga-rich environments for application purposes will need to examine ways of preventing the migration of entire droplets over large distances.

A positive finding from this study was that structures very similar to those seen in Ga-catalysed conditions were achieved, but at a temperature of only 520 °C, which is lower than that of Rieger *et al.* (590 °C), Bauer *et al.* (600-850 °C), Cirlin *et al.* (560-630 °C, with poor growth below 600 °C), Colombo *et al.* (630 °C), Kim, Park and Lee (600 °C) and Gibson and LaPierre (630 °C) [172, 186–188, 211, 232]. It is clear that while the addition of Au is perhaps not necessary for nanowire growth, it reduces significantly the temperature needed for wire growth to occur.

5.6.6 Nanowire Growth using As Dimers

The effect of using As_2 molecules was examined by carrying out nanowire growth with an As cracker temperature of 1000 °C. The substrate temperature was 480 °C and the growth was conducted in conventional Ga-limited mode, with a V/III ratio of approximately 15, as was used for the pencil-shaped nanowires described above. SEM results of the growth taken at 45 ° are shown in figure 5.26. In 5.26(a) we can see a part of the sample which includes the edge of a patterned region. The nanowires are arranged in rows 1 µm apart with some defects in the array such as missing and extra wires. A close-up of one wire is shown in figure 5.26(b). Here the tapering of the wires can be clearly seen. The ratio of altitude to diameter indicates that the average axial growth is 25 times that of the radial growth rate. A closer view taken near the base of the wire is shown in figure 5.26(c). Here we can see that the wire is Type 2, according to figure 5.3, meaning that the facets are $\{11\bar{2}\}$ (or some reconstruction thereof) if the crystal structure is zincblende, or $\{10\bar{1}0\}$ if the structure is wurtzite.

The uninterrupted cone-shape is likely due to the existence of radial growth throughout the entire growth of the nanowires, rather than the case of pencil-shaped wires where radial growth appears only when the height exceeds the diffusion length of Ga on the sidewalls. Sartel *et al.*, who compared nanowire growth under As_2 and As_4, also found greater radial growth when As_2 was used [197]. The results here support their suggestion that due to the increased reactivity of the Ga adatoms with As_2 compared to As_4, Ga incorporation into the crystal has an increased probability of occurring at the sidewalls, and Ga adatoms are less likely to migrate to the droplet at the top of the nanowire before reacting with As.

A detailed examination was carried out measuring the height, tapering angle and droplet diameter for nanowires in each of the 12 patterned regions of the sample. A total of

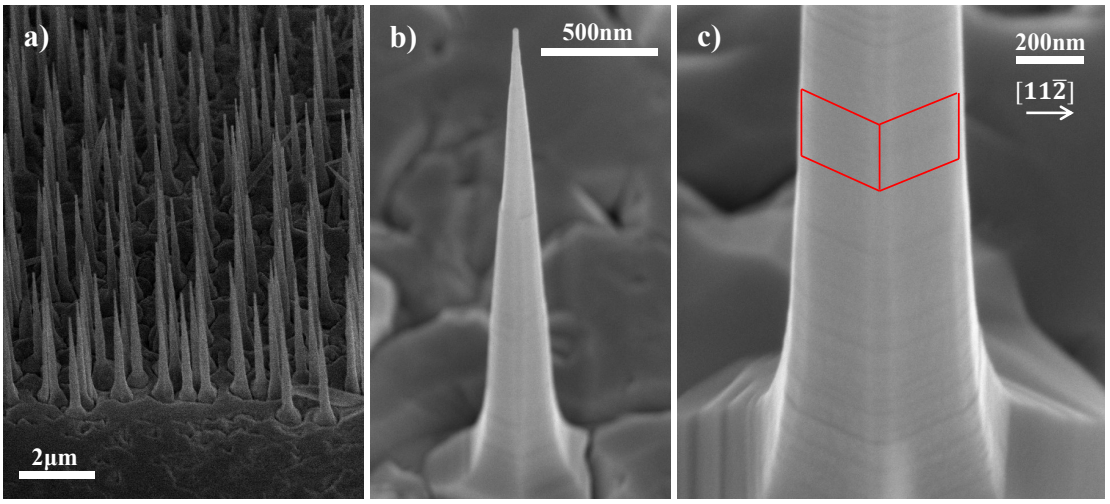


FIGURE 5.26: Nanowires grown using As_2

a) SEM image taken at 45 ° showing boundary of patterned nanodot area resulting in nanowire array after growth in fluxes of Ga and As_2. The rows of nanowires 1 µm apart can be seen.
b) A higher magnification image of a single nanowire in the array. We can see that the sidewalls are tapered, with an average height to radius ratio of 25.
c) Close up view showing the facets of the nanowire. We can see that they are Type 1 facets as described in figure 5.3, meaning that they are either $\{11\bar{2}\}$ or $\{10\bar{1}0\}$. The direction indicated also applies to (a) and (b).

987 nanowires were measured in this way. Using the tapering angle and the height, the volume of each wire could be measured by approximating its shape as a cone. Again, the number of wires per unit area was also measured using AutoCAD to find an accurate description of the inter-wire separation, rather than relying on the separation defined by EBL. The results of the volume dependency on separation for each of the 12 patterned regions are shown in figure 5.27. As can be seen, the volume varies very little with separation. This may be an indication that shadowing had little effect during the growth. This, in turn, may be due to the wires having a triangular cross-section, resulting in a lower area being shadowed by neighbouring wires. One also notices that the average volume of the 12 regions (approximately 0.085 μm^3) is lower than any of the volumes measured for the pencil-shaped nanowires (see figure 5.13 for comparison), despite similar quantities of material being deposited on both samples. In fact, the heights and base diameters are broadly similar, but it is their cone-like shape that gives them a volume approximately one third that of the pencil-shaped wires. This volume dependency on As species has never been examined in such detail before. As mentioned above, a study by Sartel *et al.* looked at the different heights and shapes of nanowires grown using As_4 and As_2. They noticed lower heights for nanowires grown under As_2, but greater rates of radial growth. They concluded that the greater radial growth "more or less" corresponded to the excess axial growth under As_4, but since radii were not examined

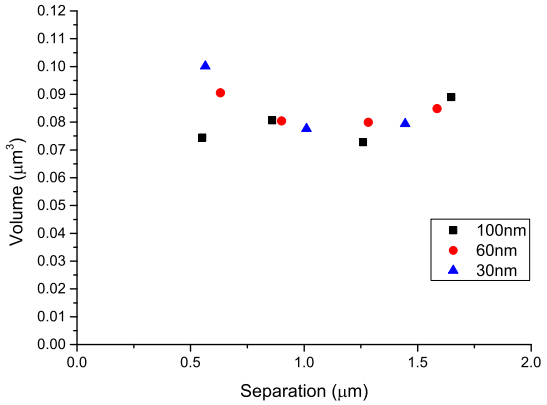


FIGURE 5.27: Volume of cone-shaped nanowires as a function of separation

Plot of nanowire volume versus inter-wire separation. Wire volume was calculated by measuring the height and angle of tapering for each wire and approximating its shape as a cone, and the separation was calculated from the measured wire density.

qualitatively this statement is not certain. One possible reason for the lower volume of the cone-shaped wires in the present study is the effect of the growth mode on the surface to volume ratio of the nanowires. Larger surface area corresponds to a greater quantity of material falling on the wire surface and contributing to the wire volume. Axial growth, which is more prevalent in As_4 growth, is more effective at increasing the surface to volume ratio than radial growth, and would therefore lead to a higher rate of increase in volume. A comprehensive theoretical model should be conducted to confirm whether or not this mechanism alone is sufficient to account for a three-fold increase in volume, as reported here.

The relationship between the height and the tapering angle was also investigated. Using the data from all 987 wires, a 2D density plot was produced which illustrates the number of wires falling within particular values for height and angle (the 'bin' size for height and angle was 250 nm and 0.5 ° respectively). The results are shown in figure 5.28. As can be seen, the nanowires seem to be grouped into one of two regions. One, towards the top left of the plot, is centred around a nanowire height of 4200 nm and a tapering angle of 4 °. The other, towards the bottom right, is centred around a height of 3000 nm and an angle of approximately 6.5 °.

Following further analysis, it was noticed that wires with larger droplet diameters were more likely to belong to the first region, and those with smaller diameters were more likely to belong to the second region. To illustrate this, the density plot of all 987 wires shown in figure 5.28 was broken down into subsets based on the diameter of the droplet

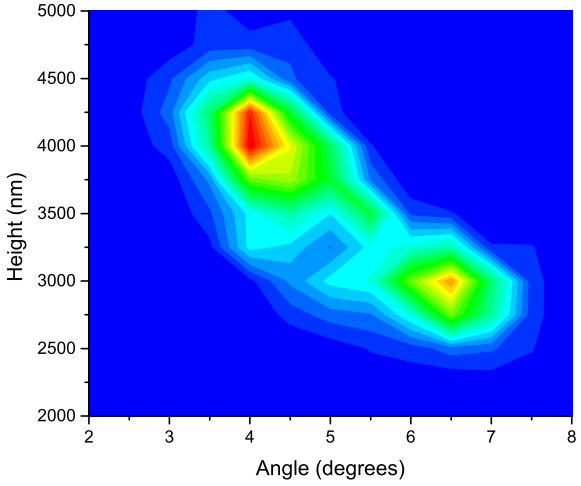


FIGURE 5.28: 2D density plot of wire heights and angles

2D density plot illustrating the relationship between height and angle for 987 nanowires grown under As_2. The bin sizes used were 250 nm for height and 0.5 ° for angle. The red colour corresponds to the maximum 64 nanowires having those particular properties.

at the top of the wire. The subsets were chosen as 60-80 nm, 40-60 nm, 30-40 nm, 20-30 nm and 0-20 nm. The results are shown in figure 5.29. As can be seen, for large droplet diameters the wire is most likely to have a height of approximately 4 µm and a tapering angle of approximately 4 °. At around 30 nm there is a transition, below which the wires are more likely to have a length of 3 µm and a tapering angle of 6.5 °. It is interesting that the transition is not via a gradual shift in values of height and angle but rather a shift in the population densities of the two regions. This suggests that there are two distinct preferred shapes of wire depending on the size of the droplet. We refer to the wires with small droplet diameter, larger tapering angle and height of approximately 3 µm as Category 1 wires, and those which have a droplet diameter greater than 40 nm, lower tapering angle and height of approximately 4 µm as category 2 wires.

As with previous growths, a 'witness' sample was placed alongside the patterned sample during the growth. Wires from this witness sample were examined using TEM to determine the crystal structure of the wires and thus identify the facets seen in the SEM images (figure 5.26(c)). The results from two different wires shall be shown, firstly one with a small diameter of 17.5 nm which should make it a 'category 1' wire as described above. Figure 5.30(a) shows a TEM image taken near the top of this wire. The hemispherical cap can be seen as a dark semicircle. The crystal structure can be clearly seen, and there are a low density of defects (<1 defect for 8 nm of wire length). As with previous wires, the defects always run across the wire diameter and never parallel to the axis. This indicates that defects are introduced as layers are nucleated at the solid-liquid

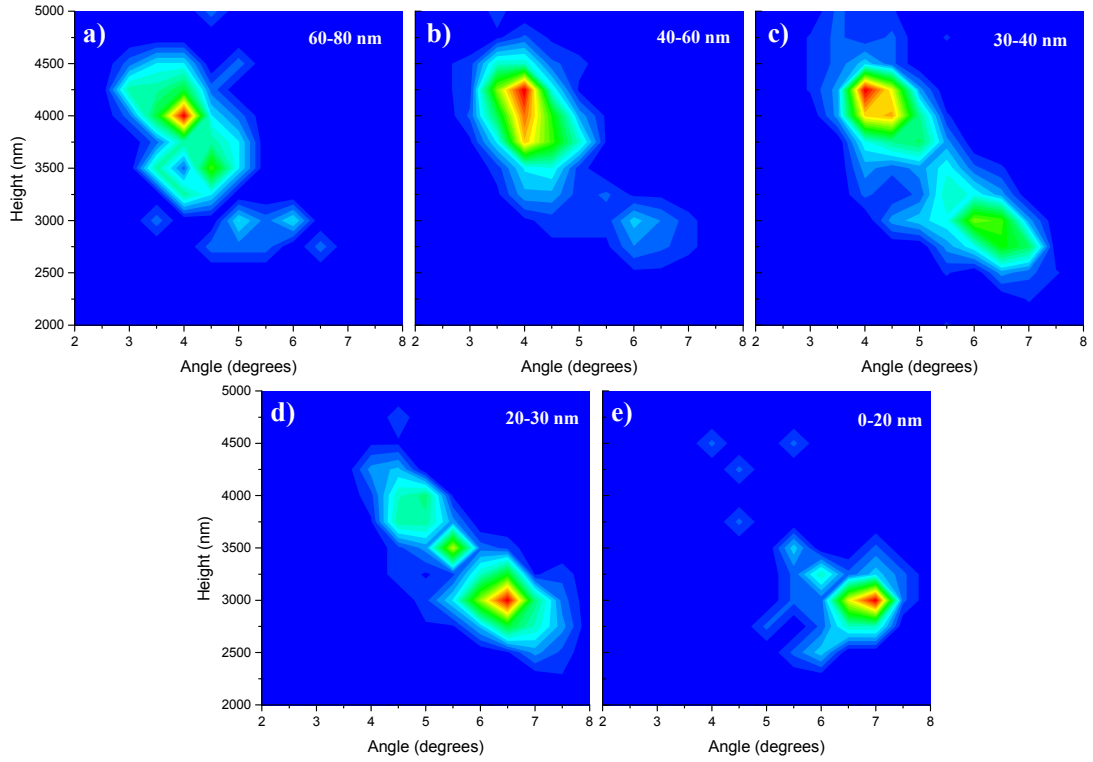


FIGURE 5.29: 2D density plots of wire heights and angles for wires with varying droplet diameter

2D density plots of height and angle for wires with droplet diameters in the regions (a) 60-80 nm, (b) 40-60 nm, (c) 30-40 nm, (d) 20-30 nm and (e) 0-20 nm. The red colour indicating maximum density for each plot corresponds to 9, 31, 20, 27 and 10 wires for images (a), (b), (c), (d) and (e) respectively.

interface, and that all radial growth is perfectly epitaxial. The inset of this image shows the FFT produced from a region of this wire. The clear 4-fold pattern and the spacing of the bright dots (6.4 Å in the growth direction and 2.3 Å across the diameter) indicates that the crystal structure is wurtzite.

Figure 5.30(b) is a close-up view of the region shown in the dashed yellow rectangle of 5.30(a). A 3D ball and stick model, which was scaled independently of the TEM image, is overlaid to illustrate the crystal structure of the wire. Most of the wire is wurtzite (denoted 'WZ' in figure 5.30(b)) while the defects running perpendicular to the growth direction are zincblende (marked ZB). The stacking fault can be considered a single layer defect between two wurtzite regions, which effectively results in three consecutive zincblende layers, i.e. ABABA**B**ĊB̊ĊB̊. All stacking faults seen in this wire were of this variety.

Now that it has been ascertained that the structure is mostly wurtzite, we can identify the facets seen in the SEM images (figure 5.26(c)) as being $\{10\bar{1}0\}$. Following the

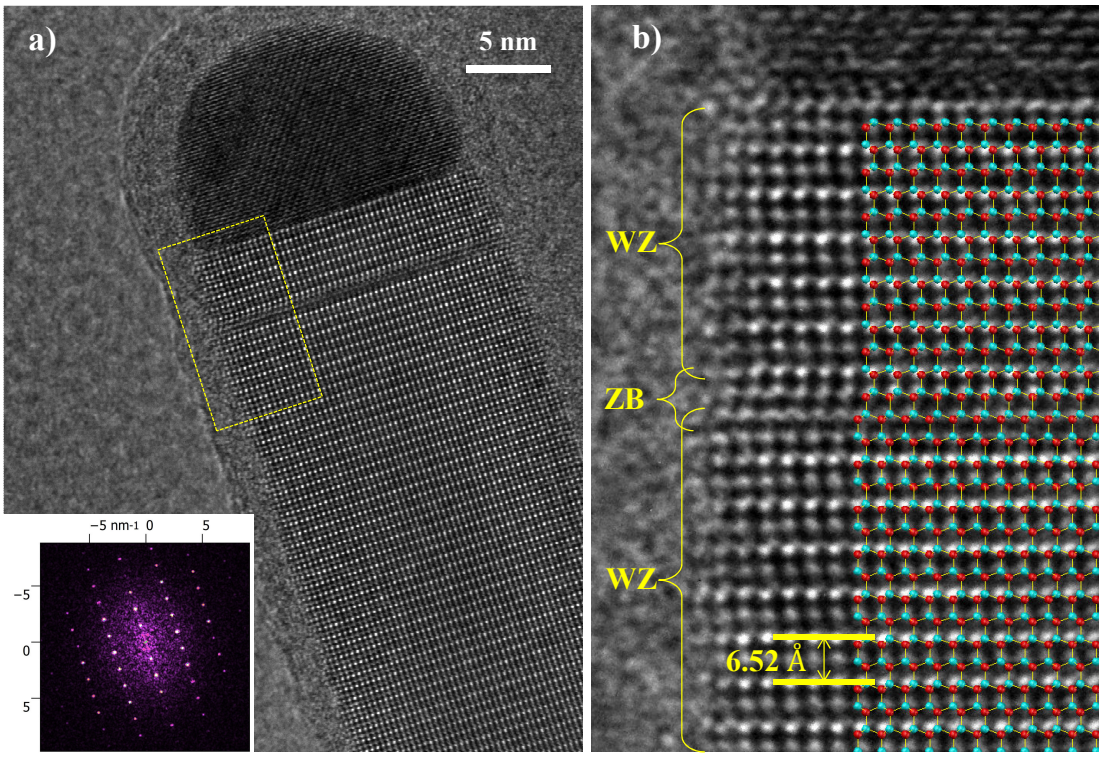


FIGURE 5.30: TEM analysis of wire with small droplet grown in As_2.

a) TEM image of top of wire which has a small droplet (diameter 17.5 nm). A zincblende defect can be seen as a band about 1 nm thick 4 nm from the top. The inset shows the FFT produced for a region near the centre of the wire in this image.
b) Close-up TEM image of the area in the dashed yellow rectangle in (a). A 3D model, which was scaled independently of the image, has been overlaid to clarify the crystal structure. 'WZ' and 'ZB' denote regions of the wire which have wurtzite and zincblende crystal structure respectively.

argument described in section 5.4 and illustrated in figure 5.5, we assume that the visible facets are those which had the lowest radial growth rate. This may be due to the fact that since Ga is more reactive with As_2 than As_4, and as a result there is a significant population of GaAs molecule on the sidewalls of the cone-shaped nanowires. These have a very low potential well on $\{11\bar{2}0\}$ facets (-3.26 eV). Thus GaAs molecules easily become embedded on the $\{11\bar{2}0\}$ facets giving them the higher growth rate of the two families of facets. On the other hand for the pencil-shaped nanowire which were grown under As_4, the facets were $\{11\bar{2}0\}$, meaning that the $\{10\bar{1}0\}$ facets had a higher radial growth rate. This is possibly due to the higher barrier for Ga adatoms migration on $\{10\bar{1}0\}$ (0.6 eV compared to 0.32 eV on $\{11\bar{2}0\}$). Thus Ga adatoms on $\{11\bar{2}0\}$ facets can easily migrate to the top of the wire, whereas those on $\{10\bar{1}0\}$ facets have difficulty migrating, leading to a higher surface density and eventual incorporation and radial growth.

A category 2 type wire (those grown in As_2 which have a droplet diameter of greater than 40 nm) was also examined using TEM. The results are shown in figure 5.31. The first of these images in figure 5.31(a) shows the top of the wire including its cap. Stacking faults can be seen crossing the diameter of the wire. The density of these stacking faults is much higher than was the case for the category 1 wire, with an average spacing between faults of 1-2 nm. Figure 5.31(b) shows a close up of a typical region of the wire, including its edge. The main features seen throughout this nanowire can be seen in this image.

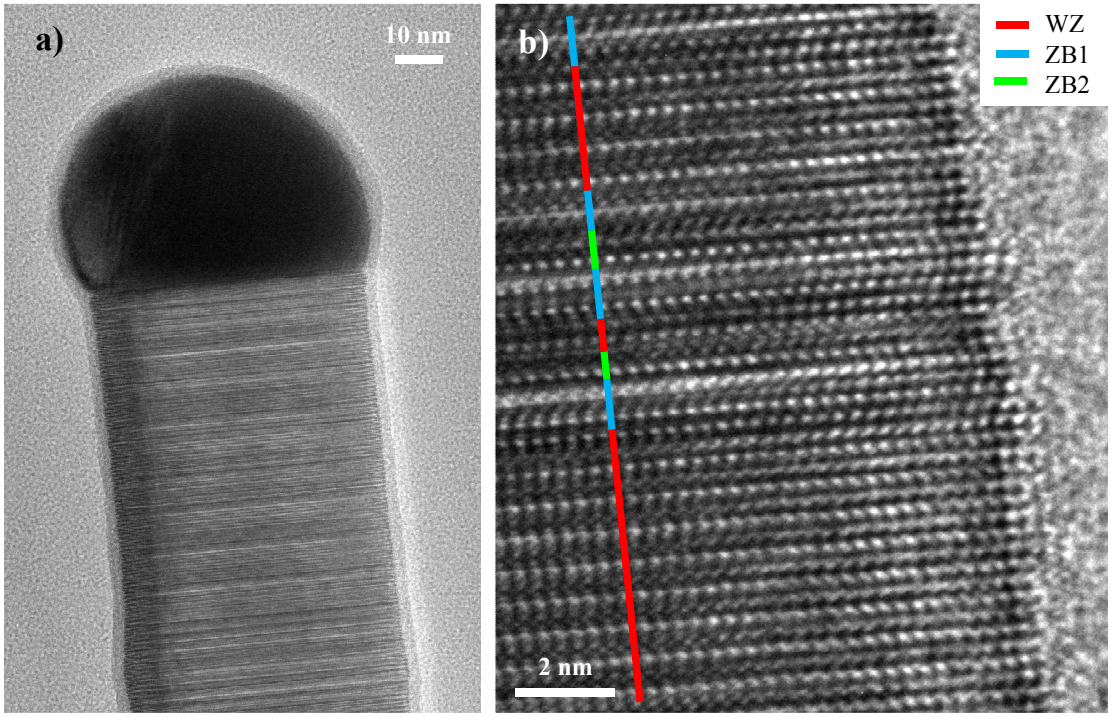


FIGURE 5.31: TEM analysis of wire with large droplet grown in As_2.

a) TEM image of top of wire which has a large droplet (diameter 60 nm). Stacking faults can be seen running across the wire diameter with quite a high density ($\approx$0.5-1 stacking fault per nm). b) Close-up TEM image of the edge of the wire. The coloured lines represent the different crystal structures along the wire length, with 'WZ' representing wurtzite and ZB1 and ZB2 representing the two stacking possibilities for zincblende when viewed along the $[1\bar{1}0]$ direction.

There are regions with wurtzite structure on the order of a few nm thick (indicated with red lines in figure 5.31(b), here thickness refers to distance along the growth direction), and regions of zincblende structure (blue and green lines in figure 5.31(b)) which are usually not more than 5 atomic layers thick before encountering a stacking fault which is either a twinning defect or a switch to wurtzite. One other feature noticed is that the sidewalls are not nearly as smooth as was the case with the category 1 wire, which had atomically flat sidewalls except for near the occasional zincblende stacking faults, which had an average spacing of more than 8 nm apart. Furthermore, whereas for the category 1 wire the diameter decreased monotonically towards the top, for the category

2 wire it was occasionally noticed that the diameter increased. An example of this can be seen at very bottom of figure 5.31(a).

These differences in crystal structure are likely related to the existence of the two categories of nanowire that came about during this growth. There appears to be some mechanism whereby larger droplets instigate a much greater density of zincblende defects, which in turn abets the smaller tapering angle and greater height. These final two effects may be related, since a narrower angle of tapering would necessarily require a greater height if the volume is to remain the same (the volume varies very little as a function of droplet diameter over the range shown). The instigation of zincblende defects may have been brought about in the same manner as was seen for the nanowires grown in As-limited conditions (5.6.5), i.e. the greater the droplet diameter, the more energetically favourable it is to have zincblende growth. Indeed, for the two samples examined by TEM shown here, the contact angle was 127 ° for the wire with the large droplet and 106 ° for the wire with the small one, as shown in figure 5.32. Thus it is possible that the

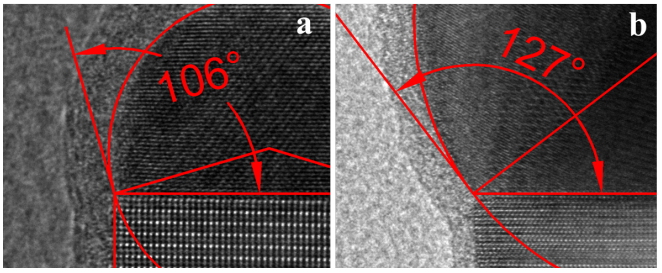


FIGURE 5.32: Contact angles for wires with varying droplet size

TEM images showing the contact angle between the wire sidewall and the droplet for (a) a category 1 wire (droplet diameter 17.5 nm) and (b) a category 2 wire (droplet diameter 60 nm)

greater droplet diameter has given rise to the zincblende defects. In fact, the angle made by the sidewall at the edge of a zincblende defect and the (111)/(0001) plane is 109.5 °, which is between the two contact angles measured. Thus the contact angle may be the parameter that actuates the transition from category 1 wires to category 2. The cause of the increase in contact angle with droplet volume may be related to the line tension at the solid-liquid interface, as mentioned in section 5.4. The effect of line tension on the contact angle is represented by τ in equation 5.3. As mentioned previously, it is quite plausible that τ would have a negative value which would indeed cause contact angle to decrease with droplet volume.

The differing in shape between category 1 and 2 wires is likely a result of the variation in growth process associated with the droplet diameter. For the large droplets (category 2) the droplets have a diameter significantly wider than that of the wire (for category 1

wires the diameters are almost equal). Therefore, it is possible during the growth that a new GaAs layer will nucleate at a point slightly beyond the width of the wire itself, resulting in an increase in wire diameter (reverse tapering). This is seen on occasion in the TEM analysis, as evident towards the bottom of the wire shown in figure 5.31. Hence the tapering angle of category 2 wires is lower than that of category 1. The difference in height between the two categories of wires may be related to the fact that there is little variation in volume from one category to the other. If volume is constant for both types (which may be a condition of the arrival mechanism of the Ga adatoms), then the height must be greater in category 1 to compensate for the lower tapering angle.

5.7 Conclusions and Further Work

The ability to produce ordered arrays of GaAs nanowires via EBL defined Au catalysts was demonstrated. Through the use of 'witness' samples the results were compared to the more conventional approach of annealing a film of Au to produce a disordered array of catalyst nanodots. For all growths, the general structural features were well replicated, while dimensions such as height and diameter were well-controlled.

The idea of Shtrikman *et al.* [204] whereby narrow, defect-free nanowires grown using a small nanodroplet were used as a core about which much wider defect-free wurtzite nanowires could be grown was achieved. The ability to define the droplet sites using EBL was key to allowing a uniformly wide diameter down to the base, avoiding the reverse-tapering caused by shadowing. In terms of volume, these wires are among the largest continuous wurtzite GaAs structures that have been grown, with volumes as great as $0.3\,\mu m^3$. The technique demonstrates the potential for the fabrication of wurtzite GaAs structures with volumes on the order of μm^3. A reduction in volume due to closer spacing was noticed, and a simple model based on experimental parameters was derived which correlated well with the experimental data points.

Due to the fact that the most common VLS procedure involves nanowire growth directly after the formation of the catalyst droplets, the question of the droplets' probability of successfully instigating nanowire growth has received very little attention. Here the dependency of wire density on droplet diameter was examined, and revealed that hemispherical Au nanodroplets with a diameter of approximately 16 nm have a less than 50% chance of resulting in nanowire growth. Although the data for this section of the study is noisy, it demonstrates that one cannot expect the distribution of nanodroplets at the end of a growth to be an accurate representation of the droplets that were present before growth commenced. It also raises the issue of finding ways of guaranteeing, or at least maximising the probability of droplets of all sizes being able to promote wire growth.

This will be a very important consideration for application purposes, since a failure of, for example, 5% of wires in a device could be catastrophic for its proper functionality. The study of wires grown under As_2 successfully produced wires from almost 100% of catalyst sites. An interesting approach may be to initiate wire growth using As_2 for a short period, and then continuing the remainder of the growth under As_4 (if particular features of As_4-grown wires were desired).

Growth in an As-limited regime was carried out, which is very unusual for VLS-grown GaAs nanowires with Au catalysts. The procedure is very promising since even without using patterned grids, the distribution of wire widths and heights is quite narrow. This is because the growth is limited by the arrival of As, which is not affected by shadowing or the size of the Au catalyst droplet. Several features of As-limited growth seen in catalyst-free studies were successfully replicated, including reverse-tapering, which has not been seen in Au-catalysed VLS growth of GaAs nanowires when it was not due to shadowing. Moreover, these effects were replicated at a significantly lower temperature than those used in catalyst-free studies. The crystal structure of these wires was examined in great detail, and it was found that as growth progressed and the droplet diameter increased, the density of twinning defects increased to approximately once every 7 atomic planes. This change resulted in sidewalls made up of $\{111\}$ microfacets, which when the entire wire is viewed appear to be $\left\{1\bar{1}0\right\}$ facets. A number of wires grown at an intermediate duration had $\left\{11\bar{2}\right\}$ facets near their bases, suggesting that the microfaceting in the upper portion causes the remainder of the wire to adopt $\left\{1\bar{1}0\right\}$ facets. One goal which was not achieved in the As-limited regime was the growth of a regular grid of nanowires as defined by the EBL-fabricated Au nanodots. The mobility of Au droplets in this regime seems to be a hurdle that prevents well-defined arrangements of nanowires. If these wires are desirable for application purposes then methods for limiting droplet mobility should be explored. This might take the form of a slight change in growth conditions at the very beginning of the growth to ensure nanowire nucleation occurs precisely at the points specified lithographically or otherwise.

The effect of using As_2 rather than As_4 was examined. The main finding was that wires adopted a conical shape rather than the pencil shape seen earlier. This was attributed to the higher reactivity of Ga adatoms with As_2 compared to As_4, which caused a higher growth rate on the nanowire sidewalls. Through extensive statistical analysis of wires from each of the 12 patterned regions on this sample, a relationship between nanodroplet diameter and structural properties was noticed. The relationship's dependency on droplet diameter had a sharp transition for diameters of approximately 30 nm. This effect was linked to the size of the contact angle as a function of the droplet diameter. This argument is consistent if the line tension, which can affect contact angle as described in equation 5.3, is negative. This seems likely since the range of possible

values for line tension considered in other studies is mostly negative, and positive values have been linked to the wire terminating at a certain height, rather than continuous steady growth.

The relationship between contact angle and wire structure just mentioned was noticed in almost all samples grown. In every case where zincblende structure dominated or became prevalent, it was associated with a droplet diameter noticeably greater than the wire diameter, and thus a contact angle well in excess of 90 °. Zincblende structure was also noticed in the pyramidal bases of nanowires grown with short growth times (see figure 5.10). Here the contact angle was well below 90 °, due to the influence of the angle of inclination of the wire sidewalls (equation 5.3). These results show that the contact angle plays a very important role in determining the crystal structure of the resulting nanowires. Generally it was found that wires with smaller droplet diameters were more likely to have a smaller contact angles, and this was related to negative values of the droplet line tension across the solid-liquid interface.

In general, this work exhibits the benefits of using Au catalyst sites which are pre-defined by EBL, in terms of control over shadowing, droplet diameter, and distribution of wire dimensions. Growth conditions were varied to produce a variety of wire shapes, which can be correlated to the growth process on an atomic level. The crystal structure and defect density was examined in great detail, and was also related to the growth process, in particular the contact angle of the droplet with the solid-liquid interface.

Chapter 6

GaAs Nanowires Coated with Fe

6.1 Introduction

The previous chapter outlined the variety of morphologies possible when growing GaAs nanowires via the VLS mechanism. Such wires are commonly used as a core about which to grow a shell of a second material. GaAs is an attractive candidate for the nanowire core in a core-shell structure, since other III-V materials may be grown epitaxially on the wire sidewalls. Examples for shell materials on GaAs nanowires include AlGaAs [172, 175, 205, 233], AlInP [234] and InGaP [2]. These structures are attractive for the formation of novel LED devices [234], p-n junctions [235] and photovoltaic applications [236].

An area that has received much less attention is vertical GaAs nanowires coated in magnetic material. One reason is that it is difficult to grow magnetic material epitaxially on the wire sidewalls. Another issue is related to the method of examining the magnetic properties of the resulting wires. If the entire sample (wires + substrate) is examined, then the contribution from the substrate may be difficult to discern from that of the wires themselves. If the wires are removed in some way, then one can either examine a large number of randomly oriented wires, which will tell us little about the effect of wire shape and magnetic direction, or we can examine single wires, which is very difficult and prone to errors and uncertainties.

FMR is an attractive method for the examination of subsets of magnetic shapes in larger magnetic samples. This is because there will be a resonance peak associated with each set of magnetic entities provided that they are well aligned and sufficiently uniform. FMR also lends itself well to angle-by-angle measurements with a high level of precision, allowing the user to track the changes of the resonant peaks associated with the different

features of the sample about their high-symmetry axes. In a previous study of Fe-coated GaAs nanowires by Tivakornsasithorn *et al.* the different resonant peaks were measured as a function of angle as the sample was rotated, but since the wires were grown on (111)B GaAs substrates and therefore grew normally to the substrate, it was almost impossible to discern the contribution from Fe on the nanowire sidewalls from the Fe on the substrate floor between the nanowire bases [237]. The present study aims to isolate the behaviour of the resonant peak of the Fe shells by growing GaAs nanowires in a direction that is not perpendicular to the substrate.

Should one achieve the growth of an Fe shell around a GaAs nanowire, the result would effectively be a tube of magnetic material. The implications for domain structure are interesting. On the one hand, due to the long shape of the tube, one might expect the magnetisation to lie along its length due to the shape anisotropy. However, it is also possible that the magnetisation would prefer to lie in closed loops around the GaAs interior. This would greatly reduce the magnetostatic energy since the stray field would be almost zero (see equation 4.10). There would be an exchange energy cost associated with this arrangement since the direction of magnetisation would vary slightly from one atom to the next around the tube. The reality is more complex than this ideal design since the Fe deposition will result in the top of the wire being coated with a hemispherical shell of Fe, and the tapered base and substrate floor will also be coated in Fe. These effects must be taken into consideration, especially when making arguments about the influence of domain structure on stray fields.

In the previous chapter it was shown how GaAs nanowires grown on (111)B GaAs substrates grow vertically in a layer-by-layer fashion. It can also be shown that if wires are grown on a substrate other than (111)B they will most likely still choose to grow in the [111] direction, since they grow by adding (111) planes at the solid-liquid interface [204, 238]. There are some reports of nanowires that chose to grow in other directions, and a very good review of the different directions that III-V type wires may grow in was carried out by Fortuna and Li [238]. They cover the range of effects that can govern the direction of growth, including choice of materials for wire and substrate, growth temperature, droplet diameter etc. In their own work they show excellent control of the growth direction of Si nanowires by varying the total and partial pressures of precursor gases. In relation to free-standing GaAs wires grown in directions other than $\langle 111 \rangle$B on GaAs substrates, they cite the work of Wu *et al.* [239] and Givargizov [227]. In the study by Wu *et al.* they found approximately 8% of the wires growing in $\langle 110 \rangle$ directions with the remainder along $\langle 111 \rangle$. Givargizov is said to have found a small number of wires growing in the $\langle 112 \rangle$ direction, but these are not confirmed by TEM and therefore could possibly be $\langle 111 \rangle$ growth misaligned due to a defect at the wire base. In summary, there is little evidence for GaAs nanowires on GaAs substrates with a majority growth

direction other than ⟨111⟩. Therefore the best approach to achieve wire growth at angles that are not normal to the substrate is to grow on (100) or (110) substrates. Figure 6.1 shows the directions of growth relative to the substrate for wires growing in the ⟨111⟩B and ⟨111⟩A crystallographic directions on (111)B, (100) and (110) GaAs substrates. The image is modelled on a schematic in the review by Fortuna and Li [238]. It should

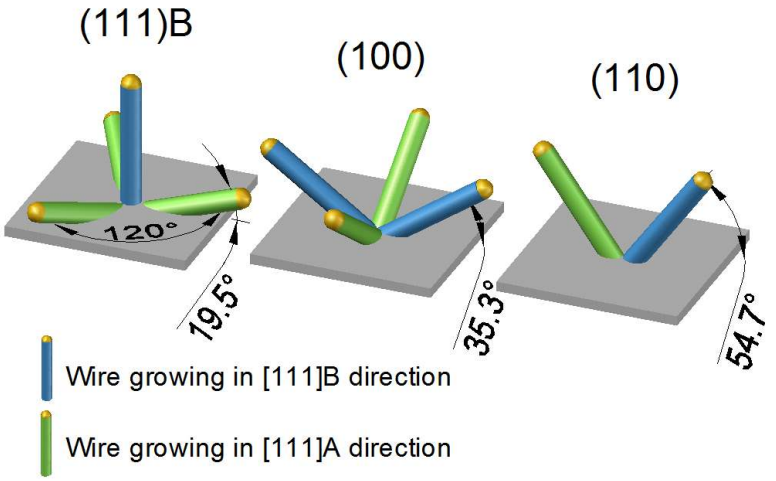


FIGURE 6.1: Growth directions of GaAs nanowires on various GaAs substrates

3D schematic images of the possible directions of growth for wires growing in the ⟨111⟩B (blue) and ⟨111⟩A (green) crystallographic directions on three different GaAs surfaces.

be noted that growth in the ⟨111⟩B directions is more likely than ⟨111⟩A due to the lower surface energy of (111)B. Of the two substrate options, (100) and (110), the (110) substrate is more attractive since there is only one possible direction for ⟨111⟩B growth, in principle making it easier to identify in FMR.

6.2 Experimental Procedure

The procedure for fabrication of Fe-coated GaAs nanowires was as described in chapter 5, with some exceptions. The first was that (110) GaAs substrates were occasionally used so that nanowires would grow in a direction that was not normal to the substrate, thereby making it easier to identify their magnetic signal with FMR. The second change is that the thin Au film is deposited shortly before nanowire growth in the same chamber. The sample is then annealed at 640 °C for 60 minutes to produce a random array of Au droplets. The final difference is, of course, the deposition of Fe onto the sidewalls, followed by a capping layer of Au. These depositions are carried out at 20 °C in the same chamber as the GaAs nanowire growth, reducing the possibility of atmospheric

contamination and oxidation. The samples are rotated about an axis normal to the plane of the substrate during deposition as is the case during nanowire growth.

Following the growth, small segments ($\approx 2\times2$ mm) were cut from the larger pieces (which were on the order of cm^2). These were fixed to Si strips and inserted into high-purity quartz tubes. The tubes were then filled with He gas and sealed, at which point they were ready for FMR examination. FMR measurements were carried out at increments of 5° about the in-plane and out-of-plane axes of the sample with the applied field varied from 0 to 1.2 T.

The morphology of the samples was investigated by SEM (FEI Magellan 400 FESEM) and the Fe-coating was investigated with STEM and EDX on the FEI Titan 80-300.

6.3 Results

6.3.1 SEM

SEM images from two Fe/Au coated arrays are shown in figure 6.2. The wires in figure 6.2(a) are grown on a (111)B template and the growth direction is therefore normal to the surface [240]. The growth time in this case was 3 hours and the average length of the resulting nanowires is 1.1 μm (±0.3 μm), while the average diameter at the midpoint along the wire length is 125 nm (±16 nm). The substrate in figure 6.2(b) is (110), and so the growth direction (i.e. the [111]B direction) is inclined at 54.7° to the substrate surface. The wires have an average length of 4.8 μm (±0.5) and a width of 148 nm

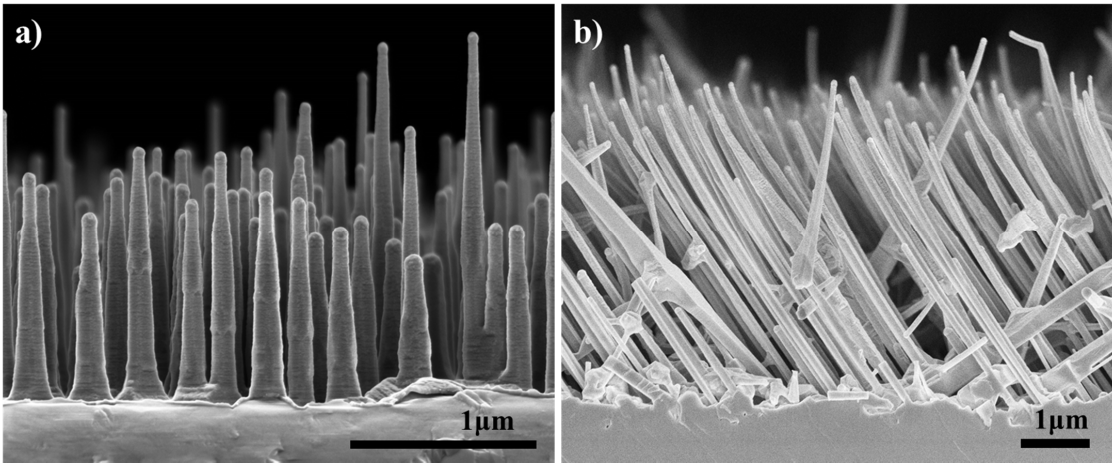


FIGURE 6.2: GaAs Nanowire arrays coated in Fe and Au

SEM images of GaAs nanowires which have been coated with Fe and Au. The substrate in (a) is (111)B GaAs while that in (b) is (110) GaAs.

(±32 nm). While the wires and also the substrate floor are covered in a shell of Fe/Au, it is likely that due to shadowing and the angle of the wires to the substrate (in the case of wires grown on the (110) substrate) that the coating is not rotationally uniform.

6.3.2 STEM and EDX

STEM was carried out on the Fe/Au coated sample shown in figure 6.2(a) with a beam voltage of 300 kV. The imaging mode was High-Angle Annular Dark-Field Imaging (HAADF), in which electrons which are scattered through a large angle are measured, and so empty space appears dark. Some sample images are shown in figure 6.3. Shown in figure 6.3a(i) is the top of one such wire. Here one can see the Au-Ga hemispherical droplet, and also an additional Au cap, whose cross-sectional shape appears to be elliptical. This extra cap is caused by the Au capping process. The Au content of these features is confirmed by the EDX linescan shown in figure 6.3a(ii) which was taken along

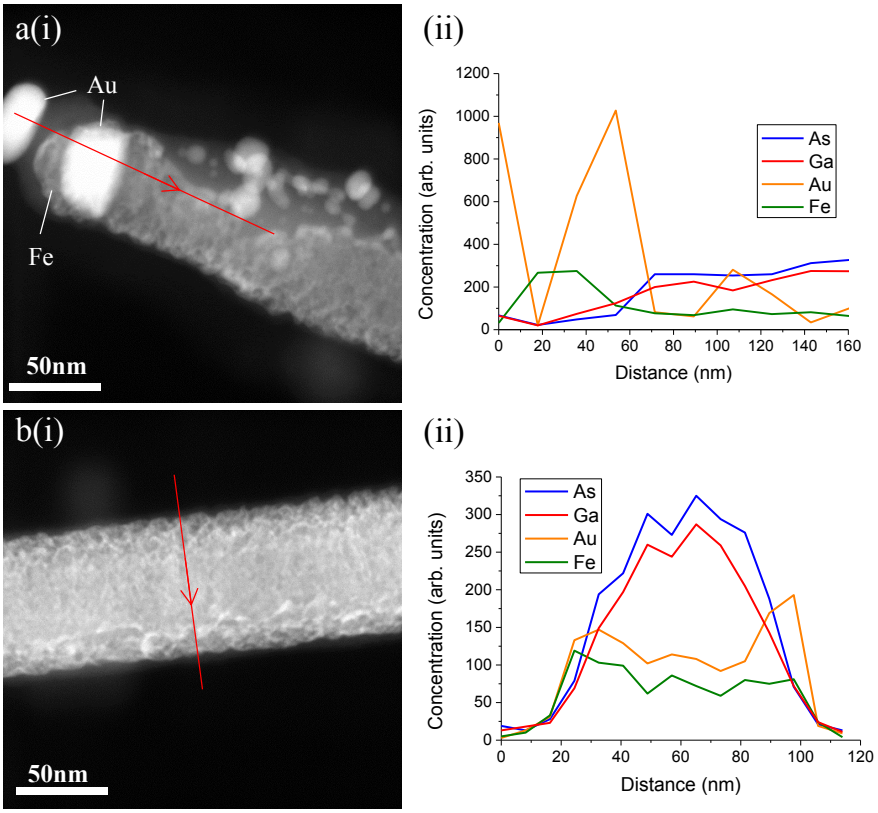


FIGURE 6.3: STEM and EDX linescans of Fe/Au coated GaAs nanowires

a(i) STEM image of top of Fe/Au coated GaAs nanowire. a(ii) EDX linescan taken along the red arrow in a)i.
b(i) STEM image of middle of an Fe/Au coated GaAs nanowire. b(ii) EDX linescan taken along the red arrow in b)i.

the red arrow shown in a(i). We can also see that the region between the Au hemispherical droplet and the extra Au cap is occupied by Fe. As regards the body of the wire itself, one can see that while one side appears to be evenly covered in an amorphous or polycrystalline coating, the other side seems to be partially covered by droplets with a diameter in the region of 5-20 nm. These features are undesirable, since they suggest a non-uniform coating, and were noticed on more than half of all nanowires surveyed. Figure 6.3b(i) shows a STEM image taken across a nanowire where the coating appears to be more uniform. An EDX linescan taken along the red arrow in this image is shown in figure 6.3b(ii). Here we can see broad peaks for Ga and As, as expected, while the profiles for Fe and Au have small peaks at the edges of the wires. This is due to the greater effective thickness (the thickness along the beam direction) of the Fe and Au coatings in these regions.

It was decided to examine the droplets which decorated some sidewalls (as shown in figure 6.3a(i)) and the edge profile in more detail. Figure 6.4a(i) shows a STEM image of one such droplet and the accompanying EDX linescan across its diameter is shown in figure 6.4a(ii). One can see that the Ga, As and Fe concentrations vary very little while there is a large Au peak. This suggests that for some reason (and only in some areas) the Au is forming droplet-like structures instead of a uniform cap layer. Figure 6.4b(i) shows another STEM image taken near the top of a Fe-Au coated nanowire, and shown in 6.4b)ii is the EDX linescan taken along the red arrow in b)i. Here we can see the increase in Ga and As associated with the edge of the line, as well as the small peaks of Au and Fe due to the greater effective thickness of these materials at the edge. What is concerning about this plot in particular is that the Au peak seems to be on top of the Fe peak, or perhaps closer to the wire body than it. The strategy of the deposition was that the Au would form a protective capping layer around the Fe to prevent it from oxidising, and yet here there is little evidence of the sequence of the depositions of the coating layers (Fe and Au).

The results from the STEM examination of these Fe/Au coated nanowires are mixed in terms of the success of the strategy. It is obvious that the Au has not formed a uniform capping layer in all regions. In figures 6.3a(i) and 6.4b(i) it is clear a large Au cap is formed at the very top of the wire. This is not altogether unexpected since the top of the wire is always exposed to the Au flux. However, the Au droplets visible on the sidewalls in figures 6.3a(i) and 6.4b(i) are unexpected and suggest that the Fe is exposed in these areas. Furthermore the high-resolution linescan across the edge shown in figure 6.4b(ii) suggests that the Au may have diffused through the Fe layer. It may be the case that the surface energy of a Au/GaAs interface is lower than an Fe/GaAs one, or that the Au seeks to form Au-Ga alloy nanodroplets. The latter explanation would seem unlikely at room temperature for bulk Au and Ga, but for nanoparticles/droplets the phase diagram

is unknown and may allow such alloying. The results indicate that further examinations should be carried out to confirm precisely whether or not Au is a suitable candidate for the coating material, and if not, then what other materials (such as MgO or Ag) may be better suited for this role. For the remainder of the study, however, Au was the only capping material available, and since the majority of the nanowire sidewalls seem to be uniformly coated there should be a sufficient volume of unoxidised Fe to perform some preliminary magnetic analysis.

6.3.3 FMR

FMR was carried out for the Fe/Au coated GaAs nanowire sample shown in figure 6.5(b), i.e. grown on a (110) substrate with the [111]B growth direction inclined at 35.3 ° to the substrate normal. The sample arrangement with respect to the applied field H is illustrated schematically in figure 6.5(a). In this figure the green disc indicates

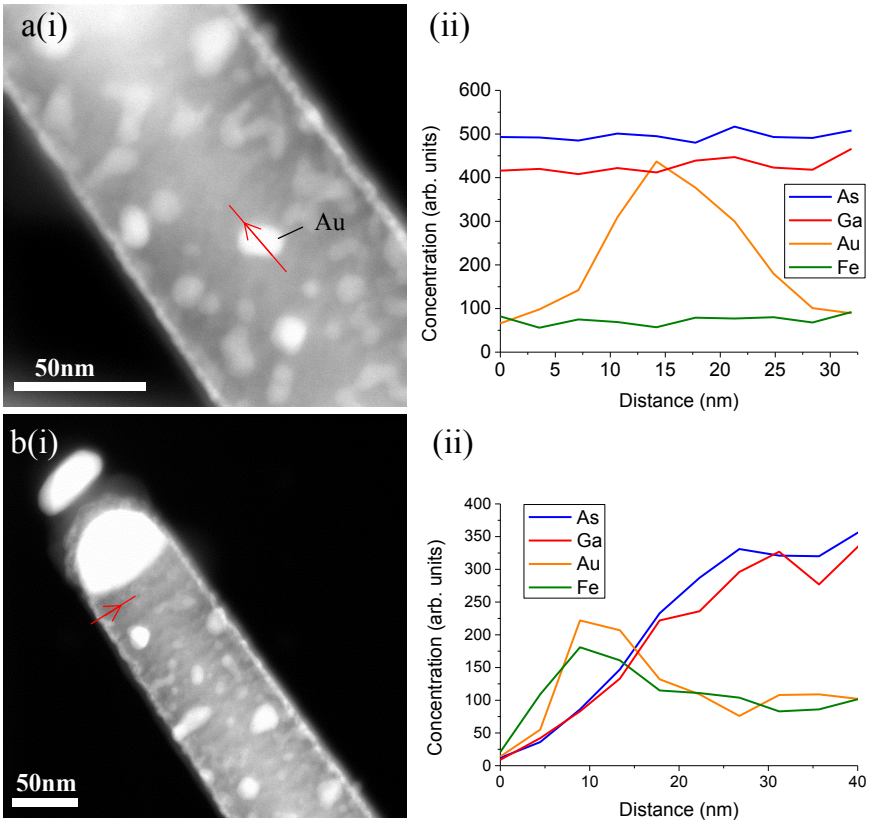


FIGURE 6.4: STEM and EDX linescans of particular features on Fe/Au coated GaAs nanowires

a(i) STEM image of a droplet on the sidewall of an Fe/Au coated GaAs nanowire. a(ii) EDX linescan taken along the red arrow in a)i.
b(i) STEM image of an Fe/Au coated GaAs nanowires. b(ii) EDX linescan taken along the red arrow in b(i).

the plane in which H was applied. It was varied through 360 ° from out-of-plane (0 ° and 180 °) to in-plane (90 ° and 270 °). Sample FMR scans taken close to 0 ° are shown

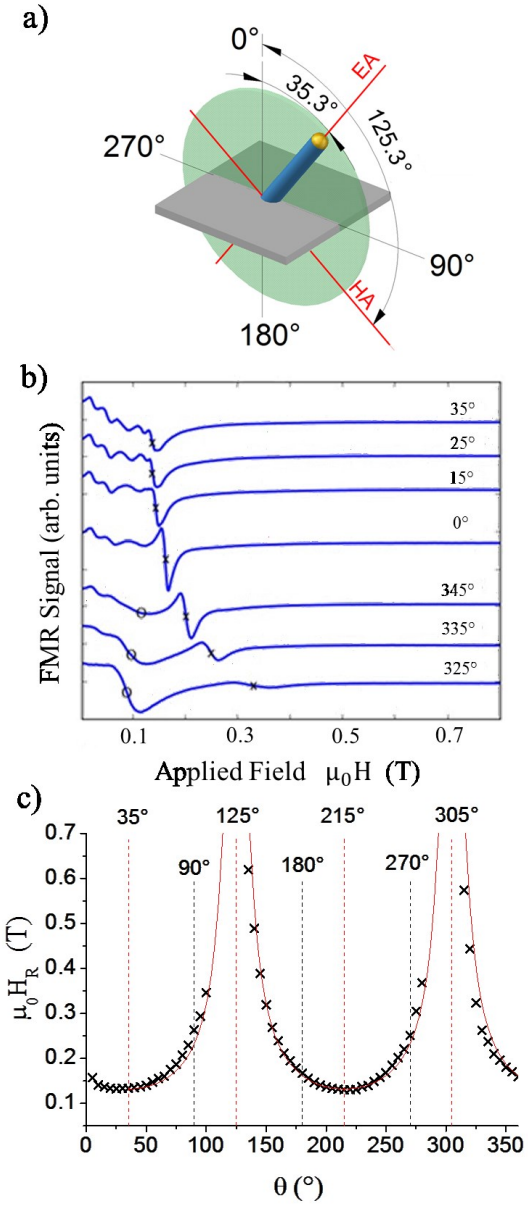


FIGURE 6.5: FMR of Fe-coated GaAs nanowires

a) Schematic of FMR measurement arrangement. The green disc indicates the plane in which the applied magnetic field was directed. EA and HA refer to the easy and hard axes respectively of the Fe coating the nanowire.
b) Sample FMR scans taken with the applied field close to 0 ° as indicated in (a)
c) Angular dependence of the resonance peaks marked "×" in (b). The minima and maxima of the plot for the × peaks correspond to the easy and hard axes (respectively) shown in (a). The red line is a fit to the data using equation A.29.

in figure 6.5(b). As can be seen there are two main resonances. One, which is marked by "○", has a resonance field (H_R) which moves slightly between 60 and 110 mT. The

other, marked by "×", starts close to 130 mT and moves to higher fields e.g. in the scan for 325 °. The behaviour of these two peaks as a function of angle is plotted in figure 6.5(c). For some angles the position of the × resonance peak could not be determined either because it moved to a field beyond that which could be produced by the device or because it became too wide to locate accurately. One can see that the × resonance has maxima at 125 ° and 305 °, and minima at 35 ° and 215 °. By comparing to the schematic in figure 6.5(a) one can see that the maxima and minima correspond to the magnetic field being applied perpendicular and parallel (respectively) to the wire direction. This suggests that there is a shape anisotropy effect acting in the Fe-coated nanowires which preferentially keeps the magnetisation directed along the wire length. The labels "EA" and "HA" in figure 6.5(a) refer to Hard and Easy axes of the wire respectively.

The red curve in figure 6.5(c) is a fit to the data using equation A.29. This equation assumes that the demagnetisation factors for the two radial directions, $\mathcal{N}_x$ and $\mathcal{N}_z$, are equivalent, which implies that $\mathcal{N}_y$ (where y is the axis parallel to the wire length) is equal to $1-2\mathcal{N}_x$. The correction of 35 ° between the y-axis and the actual wire direction is corrected manually. From the fitting parameters we find that $\mu_0 M_s$ =106 mT, and $\mathcal{N}_x = 0.49$. This implies that $\mathcal{N}_x \approx 0$ as would be expected for the elongated length of such a magnetic nanostructure.

It is possible that the feature marked by "∘" in figure 6.5(b) originates from Fe on the substrate floor. However, it is unlikely that this Fe is a uniformly thick layer due to shadowing by the nanowires. It is difficult, therefore, to make interpretations of the angular variation of this feature.

6.4 Conclusions and Further Work

It has been shown that Fe-coated nanowires can be fabricated, and that the angle between the nanowire and the substrate can be chosen from a small set of values through choice of the orientation of the GaAs substrate. It may be possible to have a wider range of angles by choosing different substrate orientations or a vicinal substrate. The effectiveness of the Au layer in capping the Fe-GaAs structure is drawn into question by the STEM results shown in section 6.3.2. Here, it was shown that the Au had a tendency to occasionally form droplets rather than a uniform coating, which may allow partial oxidation of the Fe. It is recommended that this is studied in more detail and that other capping materials are considered instead of Au. A small number of studies have also indicated a possibility for Fe to alloy with GaAs, resulting in an interfacial layer several monolayers thick with magnetic behaviour different to that of pure Fe.

Therefore it is recommended that other magnetic materials with a lower tendency for alloying with GaAs are considered for future studies.

In spite of this, the FMR results in figure 6.5 show that there is a resonance peak whose angular dependence matches very well with the actual orientation of the wires. It is therefore concluded that the wires are coated in ferromagnetic material. The FMR results do not directly imply that the wires were uniformly coated; in fact it is likely not the case due to the geometry of the deposition and the fact that it was carried out at room temperature. The effect of the deposition temperature on the crystallinity of the Fe layer should be investigated if epitaxial growth is desired. If achieved, this may give rise to magnetocrystalline anisotropy in addition to the existing shape anisotropy. Further study should also be carried out to determine if the magnetisation can be caused to form closed loops around the GaAs core. It is not clear how one would go about defining the chirality of the magnetic loops, or perhaps more importantly, how one would confirm that the magnetisation is in closed loops at all. Ordinary hysteretic magnetic measurements would have difficulty detecting such an arrangement, and MFM (Magnetic Force Microscopy) may not be suitable since in principle there would be no stray fields. The chiral magnetic pattern may have some effect on a spin-polarised current or light source, but setting up such an experiment would present both practical and theoretical challenges. It may be possible to investigate the existence of closed magnetic loops indirectly by searching for evidence of reversal mechanisms specific to hollow magnetic cylinders [241]. This is left for future work.

Chapter 7

Conclusions and Outlook

Ordered arrays of morphological patterns were successfully produced on two semiconductor surfaces. Specifically, aligned rows of step bunches or facets were produced on vicinal Si (111) templates via DC annealing of the Si in UHV, and vertical GaAs nanowires were produced from EBL-defined Au seed particles on GaAs (111)B substrates using the VLS mechanism. These structures then became templates for the deposition of magnetic material, resulting in arrays of magnetic nanowires. Magnetic phenomena related to their geometries were investigated in detail.

In the case of the step-bunches on Si, it was shown that very well ordered step arrays could be produced, and that the dimensions of the steps could be reproducibly controlled through choice of the miscut angle of the Si template and the annealing parameters. It was shown that by annealing at 920 °C (Regime I), small steps (periodicity <150 nm) could be achieved with a current in the ascending step direction, and large steps (periodicity >800 nm) could be produced with the current in the descending step direction. Even larger step arrays with a periodicity of approximately 3 μm were produced by annealing at 1120 °C (Regime II) with a step-up current. These findings are in line with the various temperature regimes found in other studies, and in some cases present a significant improvement in terms of the regularity of the step arrays. In addition, for the first time a systematic investigation into the effect of the cooling rate on the resulting step periodicity was carried out for step arrays produced in Regime I with step-up current. Cooling rate is an attractive tuning parameter, since large changes in the cooling rate produce very fine adjustments in the periodicity (for example, increasing the cooling rate by two orders of magnitude was shown to reduce the periodicity by half). It was observed that faster cooling rates corresponded to smaller periodicities. This is a revealing finding in terms of the mechanism of step-bunching, since it implies that the

formation of the steps is a process that occurs during cooling, and that at high temperatures the structure is simply an array of single atomic-height steps. The appearance of the steps during cooling is explained as the co-stabilisation of two facet groups (the 7×7 reconstruction of the (111) facets and the (331) facets which make up the step bunch) as the temperature is reduced across the 1×1→7×7 transition temperature.

A glancing angle deposition technique was then used to produce ordered arrays of magnetic nanowires on these step-bunched templates. It was shown that the wires produced using this technique are highly regular, with good control over their thickness, width and separation through appropriate choice of the template annealing conditions and the deposition parameters. The arrays exhibited in-plane shape anisotropy, which was investigated as a function of wire thickness. Measurements of the magnetisation as a function of decreasing temperature down to as low as 10 K revealed important parameters relating to the energy barrier for magnetisation reversal, which was found to increase with wire thickness as expected. In the future, conducting such measurements with a smaller increment of temperature may allow the analysis of reversal mechanism as wire thickness is varied. Additional phenomena that were investigated in these wire arrays include the effect of interwire separation on dipolar coupling, which was investigated using Henkel plots. This mode of analysis may be used in the future to examine dipolar coupling and other interwire interactions in greater detail, for example by studying the Henkel plots for nanodot arrays or analysing dipolar coupling as a function of wire thickness. A preliminary investigation into FORC measurements and their analysis is also presented. This type of study has the potential to produce useful results, such as the distribution of coercivities of particles within the system and the effects of superparamagnetic particles which may be lying on the terraces between the wires. In the future this is likely to be a very important tool in our investigations.

In the future, it would be interesting to attempt the growth of epitaxial nanowires using glancing angle deposition. To achieve this, a material for use as a substrate will need found which satisfies two conditions: it must be possible to form an ordered array of step-bunches or facets on its surface, and it must be lattice-matched with a material used for the nanowires. One avenue is to grow Fe_3O_4 on faceted Al_2O_3 or MgO. This would require the addition of an oxygen plasma source to the system. The magnetite structure would need to be confirmed using XPS (x-ray photoelectron spectroscopy) and TEM. The magnetic behaviour of these wires, if grown, should exhibit an interesting mixture of shape and magnetocrystalline anisotropies.

FMR measurements of the wire arrays as they were rotated about their principle axes were also carried out. The results were surprising in the sense that no identifiable signal was observed for rotation in planes which included direction parallel to the axis

of the wires. This may be due to a distribution in the continuous length of wires in this direction. Further studies including low temperature measurements may be able to shed some light on this result. Signals were observed, however, for rotation from the out-of-plane direction to the in-plane perpendicular direction, and it was possible to extract the demagnetising factors from the plots of resonance field as a function of angle. The effect of using MgO as a capping material compared to Ag was investigated, with the finding that an oxide layer seems to form when MgO is used, resulting in a lower effective thickness of the nanowires. A unidirectional anisotropy developed in the MgO capped samples as they aged over a time frame of months. This unexpected finding seems to be related to the formation and growth over time of an oxide layer at the MgO/Fe interface. The cause seems to be an exchange coupling at at the interface between the oxide layer and the underlying Fe nanowires, where the direction of the anisotropy is brought about by the remanence of the system following measurements, which becomes 'fixed' in the oxide layer as it grows in thickness. Further measurements will be carried out to investigate if this phenomenon can be used to manipulate the direction of the anisotropy. If ageing-induced exchange anisotropy is the cause of the unidirectional anisotropy, and if the direction is defined by sample remanence, then the effect may be more pronounced if the direction of anisotropy is along the wire axis.

With regard to the vertical GaAs nanowires, an attempt was made to produce ordered arrays of nanowires through the use of EBL-defined seed particles, which is in contrast to the more common approach of using seed particles of random size and location. This is an important topic to investigate, since it is likely to be more representative of the fabrication process for application purposes. The resulting ordered arrays of nanowires had a far greater uniformity in shape and size compared to the random arrays. This uniformity facilitates a discussion on the effects of growth procedure on the resulting wire shape and crystal structure. For example, the effect of shadowing of the deposition flux due to neighbouring nanowires was investigated as a function of interwire separation, and a simple model was constructed to explain the phenomenon. The ability to control shadowing also allows the fabrication of nanowires which have a width that is much greater than the droplet diameter because of radial growth, while still preserving the wurtzite crystal structure of the "core" nanowire. There are very few example of continuous, defect-free wurtzite GaAs structures on this scale. The effects of growing in As-limited conditions was investigated, which is usually only done in catalyst-free growths. It was found that similar wire structures were possible at much lower growth temperatures (approximately 100 °C lower) compared to previous studies. These wires exhibited notable reverse tapering due to the increasing size of the alloy droplet as growth continued, which is very rarely reported. The nanowires grown on the sample with a random distribution of seed particles had a narrow height distribution in this

growth mode, which illustrates that the effect of shadowing has little or no effect on the arrival of As at the growth interface. Growth was also carried out under As_2 rather As_4. The shape of the resulting nanowires was dramatically different, with $\{10\bar{1}0\}$ facets rather than the $\{11\bar{2}0\}$ facets seen in the case of growth under As_4, and an overall conical shape, as well a volume of approximately one third that for wires grown in As_4. These findings were explained in terms of the different reactivity of and mobility on the nanowire sidewalls of As_2 compared to As_4.

The crystal structure of the GaAs nanowires was investigated in each case using high resolution TEM. The structure was wurtzite in the majority of cases, with the density of zincblende defects varying depending on the growth conditions. A common finding was that the density of these defects seemed to be closely related to the contact angle between the alloy droplet and the nanowire sidewall. In cases where this angle was close to 90 °, the density of defects was exceptionally low, and in cases where it was significantly greater or less than 90 °, such as at the beginning of growth and when the droplet diameter was greater than the diameter of the nanowire itself, the defect density was much higher. This finding was related to a previous study which looked at the how the energy cost of nucleating a new layer at the growth interface depends on the different stacking patterns of zincblende and wurtzite structures.

A simple numerical model was composed to describe the growth of the nanowires under the influence of shadowing as a function of time. The effect of different diffusion lengths and initial wire diameters was examined as a function of interwire separation. Although simple in nature, the model was able to reproduce observations in the experimental data, such as the fact that nanowires grown from smaller nanodots had a greater average volume post-growth than those from larger nanodots. Assuming a diffusion length of 225 nm, the model was a reasonably good fit to the experimental data. It would be interesting in future to refine this model and investigate its accuracy as a function of deposition time.

Finally, some GaAs nanowire samples were coated with Fe and Au to produce core-shell structures. STEM was used to show that the coating was not quite uniform over the entire nanowire surface, with the Au appearing as droplets in some instances rather than a uniform thin film. In further work, either the deposition conditions or the choice of capping material should be varied to ensure complete coating of the Fe. With regard to the magnetic properties of these core-shell structure, FMR revealed a resonance peak whose value as a function of angle correlated with the angle made by the nanowires with the substrate surface. No evidence as yet was seen of closed magnetic loops which have the potential to form in such hollow cylindrical structures, which would theoretically may be very stable due to the near absence of stray field. It is this same property which

would make such a phenomenon difficult to detect. In the future, efforts should be made to design an experiment which could reveal the existence of such closed magnetic loops.

Appendix A

Derivation of Magnetic Resonance Expression

Here shall be given the derivation of the Smit-Beljers formalism for the resonance condition of a ferromagnetic system. The results shall be used in section 4.2.4 to extract parameters relating to the magnetic anisotropy from the data.

First a co-ordinate system must be described, which is done with the aid of figure A.1. The unit vectors of the spherical co-ordinate system, $\hat{\mathbf{r}}$, $\hat{\boldsymbol{\theta}}$ and $\hat{\boldsymbol{\varphi}}$ can be given by

$$\hat{\mathbf{r}} = \begin{bmatrix} \sin\theta\cos\varphi \\ \sin\theta\sin\varphi \\ \cos\theta \end{bmatrix} \qquad \hat{\theta} = \begin{bmatrix} \cos\theta\cos\varphi \\ \cos\theta\sin\varphi \\ -\sin\theta \end{bmatrix} \qquad \hat{\varphi} = \begin{bmatrix} -\sin\varphi \\ \cos\varphi \\ 0 \end{bmatrix} \tag{A.1}$$

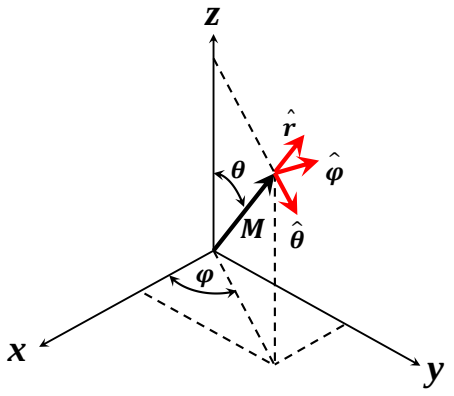


FIGURE A.1: Spherical co-ordinate system used in FMR

Thus the magnetisation $\mathbf{M}$ can be written

$$M = M_s\hat{\mathbf{m}} = M_s\left(m_x\hat{\mathbf{x}} + m_y\hat{\mathbf{y}} + m_z\hat{\mathbf{z}}\right) \tag{A.2}$$

$$= M_s\left(\sin\theta\cos\varphi\hat{\mathbf{x}} + \sin\theta\sin\varphi\hat{\mathbf{y}} + \cos\theta\hat{\mathbf{z}}\right) \tag{A.3}$$

$$= M_s\hat{\mathbf{r}} + 0\hat{\theta} + 0\hat{\varphi} \tag{A.4}$$

where $\hat{\mathbf{m}}$ is the unit vector whose direction is equal to $\mathbf{M}$, and the m_i ($i = x,y,z$) are the projections of $\hat{\mathbf{m}}$ along the respective axes. The magnetic field $\mathbf{H}$ may be given by

$$\mathbf{H} = H_r\hat{\mathbf{r}} + H_\theta\hat{\boldsymbol{\theta}} + H_\varphi\hat{\boldsymbol{\varphi}}. \tag{A.5}$$

A magnetic moment in the presence of a magnetic field experiences a torque given by

$$\frac{d\mathbf{M}}{dt} = \gamma\mathbf{M}\times\mathbf{H} \tag{A.6}$$

which can be written in ($\hat{\mathbf{r}}$, $\hat{\boldsymbol{\theta}}$, $\hat{\boldsymbol{\varphi}}$) form as

$$\frac{d\mathbf{M}}{dt} = \gamma\mu_0\begin{pmatrix} 0 \\ -H_\varphi M_s \\ H_\theta M_s \end{pmatrix} \tag{A.7}$$

This can also be expressed in terms of the time derivatives of the unit vectors, which are as follows:

$$\frac{\partial\hat{\mathbf{r}}}{\partial t} = \sin\theta\frac{\partial\varphi}{\partial t}\hat{\boldsymbol{\varphi}} + \frac{\partial\theta}{\partial t}\hat{\boldsymbol{\theta}} \tag{A.8}$$

$$\frac{\partial\hat{\boldsymbol{\theta}}}{\partial t} = -\frac{\partial\theta}{\partial t}\hat{\mathbf{r}} + \cos\theta\frac{\partial\varphi}{\partial t}\hat{\boldsymbol{\varphi}} \tag{A.9}$$

$$\frac{\partial\hat{\boldsymbol{\varphi}}}{\partial\varphi} = -\frac{\partial\varphi}{\partial t}\left(\sin\theta\hat{\mathbf{r}} + \cos\theta\hat{\boldsymbol{\theta}}\right) \tag{A.10}$$

Since $\mathbf{M} = \left(M_s\hat{\mathbf{r}} + 0\hat{\boldsymbol{\theta}} + 0\hat{\boldsymbol{\varphi}}\right)$, only the first of these three expressions is needed to give another expression for $d\mathbf{M}/dt$:

$$\frac{d\mathbf{M}}{dt} = \begin{pmatrix} 0 \\ -\dot{\theta}M_s \\ \dot{\varphi}\sin\theta M_s \end{pmatrix}. \tag{A.11}$$

In thermal equilibrium the free energy U is minimised with the angles corresponding to the orientation at equilibrium given by θ_0 and φ_0, i.e.

$$\left.\frac{\partial U}{\partial \theta}\right|_{\theta=\theta_0} = 0 \tag{A.12}$$

$$\left.\frac{\partial U}{\partial \varphi}\right|_{\varphi=\varphi 0} = 0 \tag{A.13}$$

We consider small perturbations of the angles θ and φ away from the equilibrium values θ_0, φ_0:

$$\begin{aligned} \theta &= \theta_0 + \Delta\theta \\ \varphi &= \varphi_0 + \Delta\varphi \end{aligned} \tag{A.14}$$

where $\Delta\theta \ll \theta_0$ and $\Delta\varphi \ll \varphi_0$. Since we are very close to being in equilibrium, we can carry out a first order expansion of the free energy terms:

$$\frac{\partial U}{\partial \theta} = \frac{\partial^2 U}{\partial \theta^2}\Delta\theta + \frac{\partial^2 U}{\partial \theta \partial \varphi}\Delta\varphi \tag{A.15}$$

$$\frac{\partial U}{\partial \varphi} = \frac{\partial^2 U}{\partial \varphi \partial \theta}\Delta\theta + \frac{\partial^2 U}{\partial \varphi^2}\Delta\varphi \tag{A.16}$$

We make use of the fact that the magnetic field is related to the functional derivative of the free energy with respect to the magnetisation:

$$H = -\frac{1}{\mu_0}\nabla_{\mathbf{M}} U \tag{A.17}$$

In spherical co-ordinates the operator ∇ is given by

$$\nabla = \frac{\partial}{\partial r}\hat{\mathbf{r}} + \frac{1}{r}\frac{\partial}{\partial \theta}\hat{\theta} + \frac{1}{r\sin\theta}\frac{\partial}{\partial \varphi}\hat{\varphi}. \tag{A.18}$$

Therefore the components of H along $\hat{\theta}$ and $\hat{\varphi}$ can be given as follows

$$H_\theta = -\frac{1}{\mu_0 M_s}\frac{\partial U}{\partial \theta} \qquad H_\varphi = -\frac{1}{\mu_0 M_s \sin\theta}\frac{\partial U}{\partial \varphi} \tag{A.19}$$

Substituting these values into equation A.7 and setting the result equal to A.11 gives us

$$\dot{\theta} M_s = \gamma\mu_0 M_s H_\varphi = \gamma\mu_0 M_s \left(\frac{-1}{\mu_0 M_s \sin\theta}\right)\frac{\partial U}{\partial \varphi} \tag{A.20}$$

$$\dot{\varphi}\sin\theta\, M_s = \gamma\mu_0 M_s H_\theta = \gamma\mu_0 M_s \left(\frac{-1}{\mu_0 M_s}\right)\frac{\partial U}{\partial \theta} \tag{A.21}$$

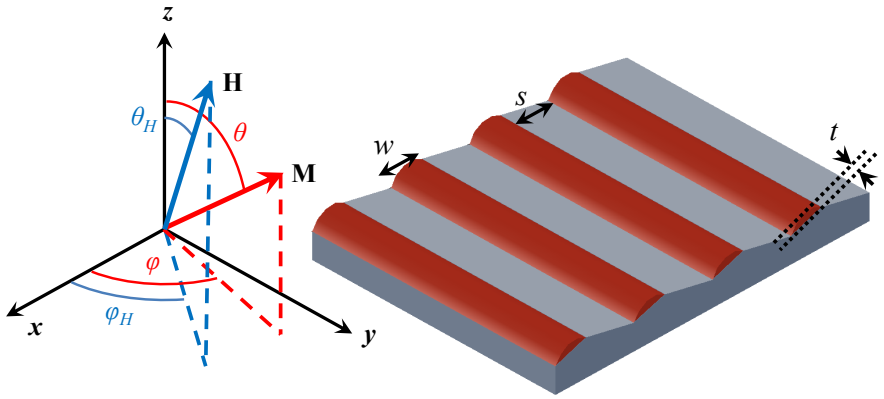


FIGURE A.2: Labels and axes of wire array parameters.

Simplifying the above, and making use of the expansions of the partial derivatives of U in equation A.16 we have:

$$-\sin\theta_0 \frac{M_s}{\gamma}\frac{d\theta}{dt} = \frac{\partial U}{\partial \varphi} = \frac{\partial^2 U}{\partial \varphi \partial \theta}\Delta\theta + \frac{\partial^2 U}{\partial \varphi^2}\Delta\varphi \tag{A.22}$$

$$\sin\theta_0 \frac{M_s}{\gamma}\frac{d\varphi}{dt} = \frac{\partial U}{\partial \theta} = \frac{\partial^2 U}{\partial \theta^2}\Delta\theta + \frac{\partial^2 U}{\partial \theta \partial \varphi}\Delta\varphi \tag{A.23}$$

It is assumed that θ and φ are varying as $e^{i\omega t}$, and so the above pair of equations can be expressed in matrix form as

$$\begin{bmatrix} \dfrac{\partial^2 U}{\partial \varphi \partial \theta} - i\omega\sin\theta_0 \dfrac{M_s}{\gamma} & \dfrac{\partial^2 U}{\partial \varphi^2} \\ \dfrac{\partial^2 U}{\partial \theta^2} & \dfrac{\partial^2 U}{\partial \theta \partial \varphi} + i\omega\sin\theta_0 \dfrac{M_s}{\gamma} \end{bmatrix} \begin{pmatrix} \Delta\theta \\ \Delta\varphi \end{pmatrix} = 0. \tag{A.24}$$

Non-trivial solutions are found by setting the determinant equal to 0, which gives us

$$\left(\frac{\omega}{\gamma}\right)^2 = \frac{1}{M_s^2 \sin^2\theta_0}\left[\frac{\partial^2 U}{\partial \varphi^2}\frac{\partial^2 U}{\partial \theta^2} - \left(\frac{\partial^2 U}{\partial \varphi \partial \theta}\right)^2\right] \tag{A.25}$$

This is a very important equation which will be used to find the resonance condition for a given free energy U. First, the axes of the magnetic field and the magnetisation in relation to the sample are defined, as shown in figure A.2. As can be seen the definition of **M** has not changed (see figure A.1), while **H** is defined as making an angle θ_H with the z-axis and its projection on the xy plane makes an angle of φ_H with the x-axis.

The total free energy U is made up of the Zeeman energy U_Z plus terms for any anisotropies that may be present in the system, as described in section 4.1.1. Initially just the shape anisotropy shall be considered. Therefore:

$$U = U_Z + U_{SH}. \tag{A.26}$$

Using the axis labels described in figure A.2, and the general form of the energy due to shape anisotropy given in equation 4.5, we have:

$$\begin{aligned} U = &- \mu_0 MH \left[\sin\theta \sin\theta_H \cos\left(\varphi - \varphi_H\right) + \cos\theta\cos\theta_H\right] \\ &+ \tfrac{1}{2}\mu_0 M^2 \left(\mathcal{N}_x \sin^2\theta\cos^2\varphi + \mathcal{N}_y \sin^2\theta\sin^2\varphi + \mathcal{N}_z \cos^2\theta\right) \end{aligned} \tag{A.27}$$

For the case of elongated nanowires in a planar array, we allow $\mathcal{N}_y = 0$, meaning that $\mathcal{N}_x = 1 - \mathcal{N}_z$. In addition, all fitting in the present study was carried out for data taken with the applied field in the xz plane, meaning that $\varphi_H = 0$. Inserting the somewhat simplified value of U into A.25 allows us to solve for $H = H_R$, where H_R is the value of the applied field at resonance:

$$H_R \sin\left(\theta_H - \theta\right) - \tfrac{1}{2}\left(1 - 2\mathcal{N}_z\right) M \sin\left(2\theta\right) = 0$$

$$\left(\frac{\omega}{\gamma}\right)^2 = \left[H_R \cos\left(\theta - \theta_H\right) + \left(1 - 2\mathcal{N}_z\right) M \cos\left(2\theta\right)\right] \times \left[H_R \frac{\sin\theta_H}{\sin\theta} - M\left(1 - \mathcal{N}_z\right)\right]. \tag{A.28}$$

This result will be fitted to the experimental data for H_R as the sample is rotated about the y-axis (as shown in figure A.2).

For the case of the core-shell GaAs-Fe nanowires, we define the y-axis to be parallel to the length of the nanowires. It is assumed that the two radial directions are equivalent, i.e. $\mathcal{N}_z = \mathcal{N}_x$, and therefore $\mathcal{N}_y = 1 - 2\mathcal{N}_x$. Again it is assumed that $\varphi_H = 0$. Using these assumptions we obtain

$$\begin{gathered} H_R \sin\left(\theta - \theta_H\right) + \tfrac{1}{2}\left(1 - 3\mathcal{N}_x\right) M \sin\left(2\theta\right) = 0 \\ \left(\frac{\omega}{\gamma}\right)^2 = \left[H_R \cos\left(\theta - \theta_H\right) + \left(1 - 3\mathcal{N}_x\right) M \cos\left(2\theta\right)\right] \times \left[H_R \frac{\sin\theta_H}{\sin\theta}\right]. \end{gathered} \tag{A.29}$$

Since the y-axis is chosen to be parallel to the length of the Fe tubes there is an offset of 35° between this axis and the minima of the plot of the angular dependence of H_R. This is corrected for manually.

Appendix B

Effect of Shadowing on Nanowire Volume

In section 5.6.3 it was found that wire volume increased with separation, but saturated when the interwire separation was greater than $\approx 1.5\,\mu\text{m}$. A numerical model was constructed to describe the observed behaviour. The assumptions of the model are as follows, and are described with the aid of figure B.1:

1. The wires are cylindrical in shape.
2. The effect of shadowing is considered from the point of view of one wire i being shadowed by another j which has identical width $\varphi(t)$ and height $H(t)$ and is separated by a distance L.
3. In reality rotation occurs through 360° and since there is a square grid of wires this includes four nearest neighbours. For simplicity, here rotation is only through one quadrant with one nearest neighbour (i.e. wire j).
4. Shadowing can only occur when wires i, j and the flux are collinear. From figure B.1(a), this proportion of time is considered to be equal to the diameter $\varphi(t)$ divided by the arc length $2\pi L/4$, i.e.

$$\text{Proportion of time that shadowing occurs} = \frac{2\varphi(t)}{\pi L} \tag{B.1}$$

5. Shadowing can only occur when the neighbouring nanowire is tall enough to do so. In figure B.1(b), one can see that this occurs when the height of the wires is h', as shown, which is equal to $L\,\text{Tan}\,\theta$.

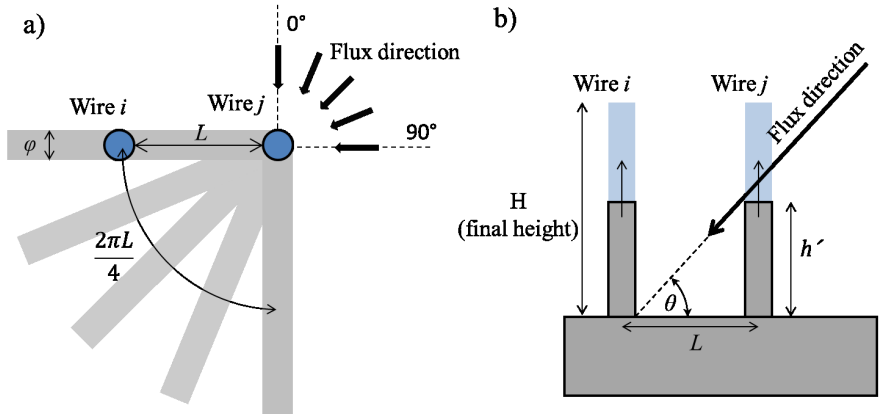


FIGURE B.1: Schematic of shadowing considerations

a) Schematic showing top-down view of two nanowires, i and j, in a square grid array with a separation L. The flux is considered to rotate through 90 ° so that it is equivalent to the effect of four nearest neighbours and a rotation of flux through 360 °. The grey rectangles indicate the regions shaded as the angle of the flux is varied.
b) Schematic showing side view of two nanowires, i and j during their growth. They are at the precise height h' when shadowing will commence. It can be shown that $h' = L \operatorname{Tan} \theta$.

6. When there is no shadowing, the amount of material that arrives in one unit of time (dV) is equal to the flux F multiplied by the cross sectional area of the wire, which is taken as the height multiplied by the width. I.e.

$$dV = F \times \varphi(t) \times H(t) \tag{B.2}$$

When shadowing is occurring, the effective cross sectional area of the wire is now equal to the width multiplied by $L \operatorname{Tan} \theta$, i.e.

$$dV = F \times \varphi(t) \times L \operatorname{Tan} \theta \tag{B.3}$$

7. The volume dV is divided into material that contributes to increasing the height and the diameter of the nanowire. It is assumed that there is a diffusion length D, and that material which lands within a distance D of the top of the nanowire extends the height of the nanowire only, while the remainder of dV produces a thin shell around the entire nanowire, thereby increasing its diameter.

The fact that the flux is deposited at an angle θ and that there are uncertain adhesion and desorption rates are absorbed into the flux F. Thus F is not the 'true' quantity of material impinging directly onto the substrate at normal incidence and cannot reliably be related to experimental parameters. Instead the quantity of material deposited over

the course of the deposition shall be determined from the experimentally measured wire volume of the most isolated wire arrays.

Some of the inaccuracies of this model are:

- The wires are not actually cylinders, but hexagonal prisms with a cone-shaped top.
- Wire dimensions are not constant within an array but have a distribution which becomes wider with smaller separation (see figure 5.14).
- The assumptions relating to the behaviour of adatoms according to the diffusion length are very simplistic. In reality, the probability of where an adatom will eventually end up (finding its way to the droplet, adhering to the sidewall, desorbing, etc.) will vary continuously along the wire length.
- Only nearest neighbours are considered here. A more accurate model will consider second and third nearest neighbours also. 'Line-of-sight' considerations will also need to be made, meaning that certain wires will not be able to shadow others not due to their distance but due to the existence of 'interstitial' wires in the grid.
- The 'shadow' of each wire will not be exactly rectangular but will instead have a triangular shape at its top.
- The model assumes that during shadowing, the same proportion of material can travel to the tip as is the case when there is no shadowing. On the contrary, during shadowing the bulk of the material will land near the tip of the nanowires. However, even if this is corrected for there is still the possibility that the excess density of adatoms near the top of the wire will cause a gradient towards the shadowed portion of the wire.
- The model does not take into account the possibility of material arriving from the substrate.
- The model assumes that the adhesion rate of adatoms is uniform over the entire wire, whereas it is known that adhesion is more likely at the droplet [204].

Despite the deficiencies of the model mentioned above, it is hoped that it will reflect the behaviour of the experimental system and offer insights into the dependencies of the various parameters. In the future, the model may be improved upon by considering some of the drawbacks mentioned above to give more accurate results.

In order to investigate the effect of the diffusion length D, the simulation was run with D varying from 100 nm to 700 nm in steps of 100 nm. The initial nanowire diameter,

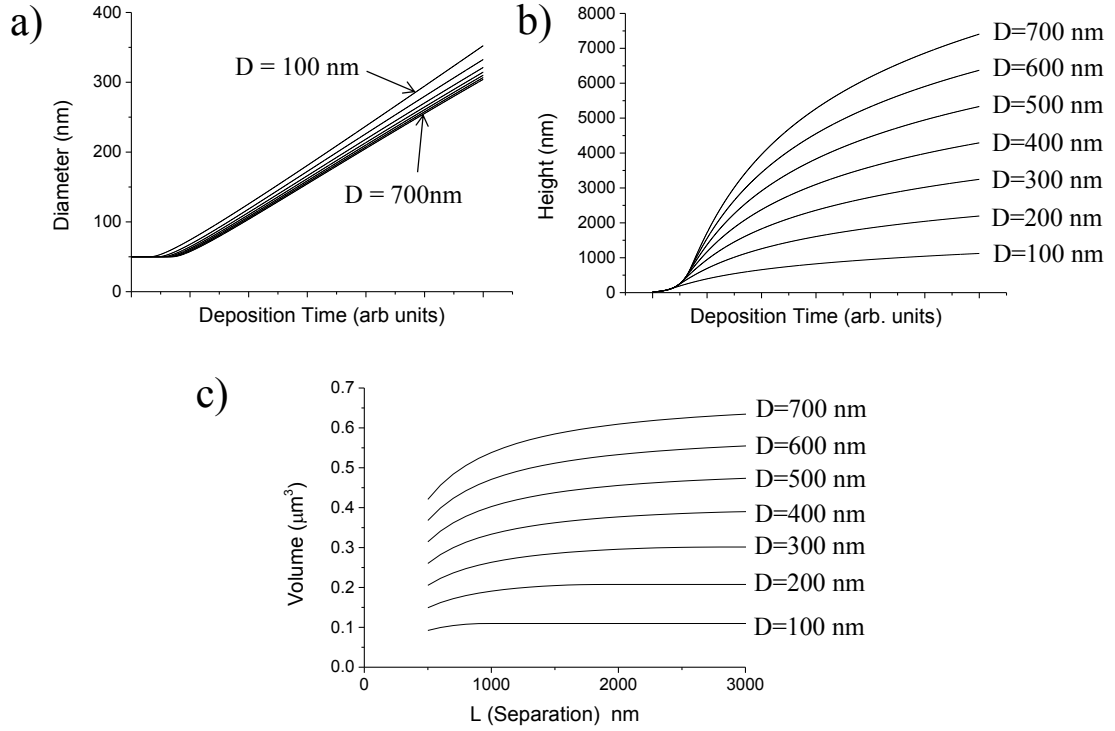


FIGURE B.2: Effect of varying values for the diffusion length (D)

a) Effect of varying the diffusion length, D, on wire diameter as a function of deposition time.
b) Effect of varying D on wire height as a function of deposition time.
c) Effect of varying D on final wire volume as a function of interwire separation.

which shall be called φ_0, was kept fixed at 50 nm, and its initial height was 20 nm. For each value of D, the diameter, height and volume of a wire in the system was calculated as the 'deposition' continued. The results for wire diameter and height as a function of time for wires with a separation of 1 μm are shown in figures B.2(a) and (b) respectively, while the final volumes at the end of the simulation is shown as a function of separation for the 7 values of D are shown in figure B.2(c). It is seen in figure B.2 that increasing the diffusion length has very little effect on the diameter of the nanowires. The diameter stays constant until the wire height has exceeded the diffusion length, and so the point at which the diameter begins to increase becomes more delayed as D is increased, after which it increases in an approximately linear fashion. The height, on the other hand, increases quite dramatically with D. This is due to the fact that more material is making its way to the top of the wire and contributing to its height. Thus there is a significant increase in volume with D (figure B.2) which is almost solely due to the increase in wire height.

The effects of varying the initial diameter φ_0 was studied by running the simulation with values of φ_0 ranging from 20 nm to 100 nm in increments of 20 nm. Again results

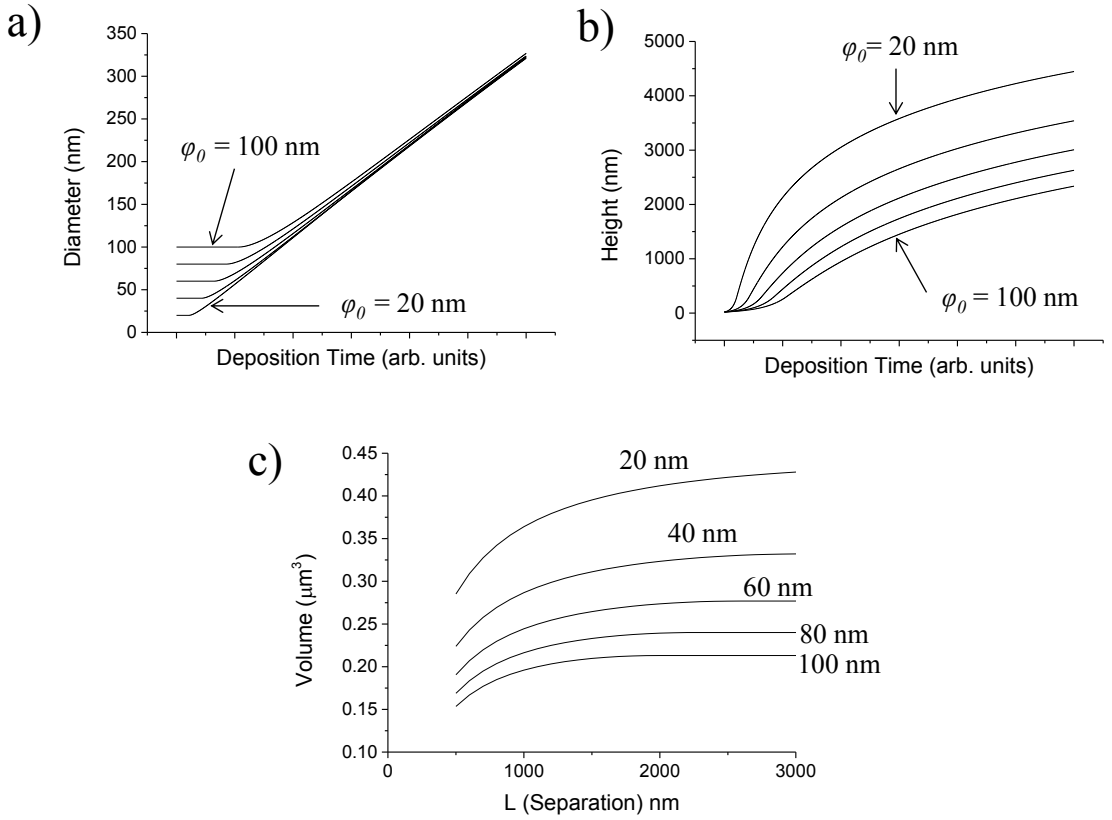


FIGURE B.3: Effect of varying the initial nanowire diameter

a) Effect of varying the initial wire diameter, φ_0, on wire diameter as a function of deposition time.
b) Effect of varying φ_0 on wire height as a function of deposition time.
c) Effect of varying φ_0 on final wire volume as a function of interwire separation.

for wire diameter and height for wires 1 μm apart as the deposition continues are shown in figure B.3. As can be seen in figure B.3(a), the initial nanowire diameter also has little effect on the resulting wire diameter at the end of the deposition. The narrower nanowires begin to increase in height earlier during the deposition than the wider wires, because their height exceeds the diffusion length at an earlier stage. Interestingly, figure B.3(b) shows that the wire height decreases with increasing initial diameter. Due to the reduced height with initial diameter, the volume is also lower for larger φ_0. This is in agreement with the experimental findings shown in figure 5.13, where almost all measured volumes were lower for wires that grew from larger nanodots.

Since both D and φ_0 had little effect on the final nanowire diameter, it was decided to fix the total volume of material deposited (flux × deposition time) for a value which agreed with the experimentally average measured diameter of the most isolated wire array ($\approx 340\,\text{nm}$). The simulation was carried out for values of φ_0 equal to the actual diameters of the Au nanodots which were defined using EBL. The diffusion length D was

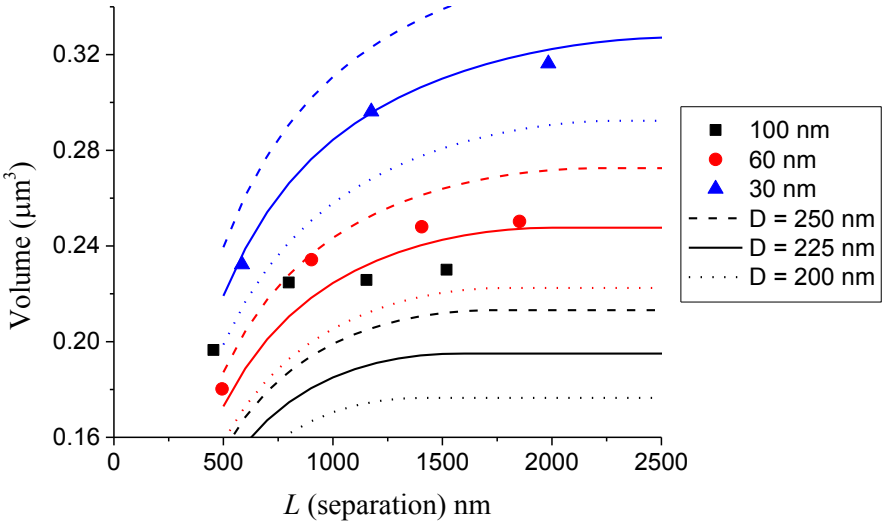


FIGURE B.4: Numerical model with experimental data

This plot shows the experimental data for the average wire volume for each of 12 patterned GaAs nanowire arrays as a function of interwire separation. The blue triangles, red circles and black squares correspond to wires grown from Au nanodots having diameters of 30, 60 and 100 nm respectively.
The curves also plotted here are the results from the numerical model for wire volume as a function of interwire separation which were calculated assuming initial diameters of 30, 60 and 100 nm for the blue, red and black curves respectively. There are three curves per initial diameter; the dashed, solid and dotted lines correspond to diffusion lengths of 250, 225 and 200 nm respectively.

varied manually to find values which matched the experimental data closely. In figure B.4 the experimental data for volume as a function of interwire separation is shown for the three different droplet diameters. Also shown on this graph are the results of the simulation for three different values of the diffusion length for each of the three droplet diameters. The results for D equal to 200 nm, 225 nm and 250 nm are shown as dotted, solid and dashed curves respectively. As can be seen, the shape of the curves replicates the experimental data quite accurately, with the solid line corresponding to a diffusion length of 225 nm fitting very closely to the experimental data for the 30 nm and 60 nm initial nanodot sizes (blue triangles and red circles respectively). The fit is not quite so close for the wires grown from the largest nanodots (black squares). This is not likely to be due to a different diffusion length for these wire, but rather that the nanodots themselves have broken up into smaller nanodots during annealing.

It is interesting that the quality of the fit changes quite dramatically as the diffusion length is varied. Although the current model does not allow incremental adjustments of D to find the optimum value fit for the data, one can quite easily find the value of D (within the assumptions of the model) to within 10% by visual inspection of plotted

curves. Although the model is quite simplistic for the reasons mentioned above, this method may still provide a useful method for estimating the diffusion length.

Bibliography

[1] K. Hans Wedepohl. The composition of the continental crust. *Geochimica et Cosmochimica Acta*, 59(7):1217–1232, 1995.

[2] G. Mariani, A. C. Scofield, C. H. Hung, and D. L. Huffaker. GaAs nanopillar-array solar cells employing in situ surface passivation. *Nature Communications*, 4:1497, 2013.

[3] R. F. Service. Performance of nanowire solar cells on the rise. *Science (New York, N.Y.)*, 339(6117):263, 2013.

[4] H. Xia, Z. Y. Lu, T. X. Li, P. Parkinson, Z. M. Liao, F. H. Liu, W. Lu, W. D. Hu, P. P. Chen, H. Y. Xu, J. Zou, and C. Jagadish. Distinct Photocurrent Response of Individual GaAs Nanowires Induced by n-Type Doping. *ACS Nano*, 6(7):6005–6013, 2012.

[5] J. Wallentin, N. Anttu, D. Asoli, M. Huffman, I. Aberg, M. H. Magnusson, G. Siefer, P. Fuss-Kailuweit, F. Dimroth, B. Witzigmann, H. Q. Xu, L. Samuelson, K. Deppert, and M. T. Borgström. InP nanowire array solar cells achieving 13.8% efficiency by exceeding the ray optics limit. *Science*, 339(6123):1057–60, 2013.

[6] E. Halpern, G. Elias, A. V. Kretinin, H. Shtrikman, and Y. Rosenwaks. Direct measurement of surface states density and energy distribution in individual InAs nanowires. *Applied Physics Letters*, 100(26):262105, 2012.

[7] J. Chen, Y. Y. Dai, J. Luo, Z. L. Li, S. Z. Deng, J. C. She, and N. S. Xu. Field emission display device structure based on double-gate driving principle for achieving high brightness using a variety of field emission nanoemitters. *Applied Physics Letters*, 90(25):253105, 2007.

[8] A. Talin, K. Dean, and J. Jaskie. Field emission displays: a critical review. *Solid-State Electronics*, 45(6):963–976, 2001.

[9] J. Robertson. Amorphous carbon cathodes for field emission display. *Thin Solid Films*, 296(1):61–65, 1997.

[10] W. B. Choi, D. S. Chung, J. H. Kang, H. Y. Kim, Y. W. Jin, I. T. Han, Y. H. Lee, J. E. Jung, N. S. Lee, G. S. Park, and J. M. Kim. Fully sealed, high-brightness carbon-nanotube field-emission display. *Applied Physics Letters*, 75(20):3129, 1999.

[11] T. Coughlin. Declining Growth Projections For Hard Disk Drive Industry In 2013. *Forbes*, 2013.

[12] R. Schaller. Moore's law: past, present and future. *IEEE Spectrum*, 34(6):52–59, 1997.

[13] C. Walter. Kryder's Law. *Scientific American*, 293(2):32–33, 2005.

[14] IBM Archives: 650 RAMAC announcement, 1956.

[15] T. Coughlin. When Will We See Higher Capacity Hard Disk Drives? *Forbes*, 2013.

[16] H. J. Richter, A. Y. Dobin, R. T. Lynch, D. Weller, R. M. Brockie, O. Heinonen, K. Z. Gao, J. Xue, R. J. M. v. d. Veerdonk, P. Asselin, and M. F. Erden. Recording potential of bit-patterned media. *Applied Physics Letters*, 88(22):222512, 2006.

[17] H. Richter, A. Dobin, O. Heinonen, K. Gao, R. v.d. Veerdonk, R. Lynch, J. Xue, D. Weller, P. Asselin, M. Erden, and R. Brockie. Recording on Bit-Patterned Media at Densities of 1 Tb/in¡tex¿$ˆ2$¡/tex¿and Beyond. *IEEE Transactions on Magnetics*, 42(10):2255–2260, 2006.

[18] C. Ross. Patterned Magnetic Recording Media. *Annual Review of Materials Research*, 31:203–35, 2001.

[19] A. Kikitsu. Prospects for bit patterned media for high-density magnetic recording. *Journal of Magnetism and Magnetic Materials*, 321(6):526–530, 2009.

[20] D. A. Allwood, G. Xiong, C. C. Faulkner, D. Atkinson, D. Petit, and R. P. Cowburn. Magnetic domain-wall logic. *Science*, 309(5741):1688–92, 2005.

[21] J. Jaworowicz, N. Vernier, J. Ferré, A. Maziewski, D. Stanescu, D. Ravelosona, A. S. Jacqueline, C. Chappert, B. Rodmacq, and B. Diény. Magnetic logic using nanowires with perpendicular anisotropy. *Nanotechnology*, 20(21):215401, 2009.

[22] D. Kelly, J. E. Wegrowe, T. K. Truong, X. Hoffer, and J. P. Ansermet. Spin-polarized current-induced magnetization reversal in single nanowires. *Physical Review B*, 68(13):134425, 2003.

[23] A. Saib, M. Darques, L. Piraux, D. Vanhoenacker-Janvier, and I. Huynen. An unbiased integrated microstrip circulator based on magnetic nanowired substrate. *IEEE Transactions on Microwave Theory and Techniques*, 53(6):2043–2049, 2005.

[24] M. Lindeberg and K. Hjort. Interconnected nanowire clusters in polyimide for flexible circuits and magnetic sensing applications. *Sensors and Actuators A: Physical*, 105(2):150–161, 2003.

[25] A. Hultgren, M. Tanase, C. S. Chen, G. J. Meyer, and D. H. Reich. Cell manipulation using magnetic nanowires. *Journal of Applied Physics*, 93(10):7554, 2003.

[26] H. Yi and J. Chang. Proximity-effect correction in electron-beam lithography on metal multi-layers. *Journal of Materials Science*, 42(13):5159–5164, 2007.

[27] K. Kanaya and S. Okayama. Penetration and energy-loss theory of electrons in solid targets. *Journal of Physics D: Applied Physics*, 5(1):43–58, 1972.

[28] M. El-Hilo, K. O'Grady, P. I. Mayo, R. W. Chantrell, I. L. Sanders, and J. K. Howard. The effects of different demagnetisation processes on interaction effects in thin film media. *Magnetics, IEEE Transactions on*, 28(5):3282–3284, 1992.

[29] R. Verre, R. Sofin, V. Usov, K. Fleischer, D. Fox, G. Behan, H. Zhang, and I. Shvets. Equilibrium faceting formation in vicinal Al2O3 (0001) surface caused by annealing. *Surface Science*, 606(23-24):1815–1820, 2012.

[30] L. Piraux, J. George, J. Despres, C. Leroy, E. Ferain, R. Legras, K. Ounadjela, and A. Fert. Giant magnetoresistance in magnetic multilayered nanowires. *Applied physics letters*, 65(19):2484–2486, 1994.

[31] O. Fruchart, M. Eleoui, J. Vogel, P. O. Jubert, A. Locatelli, and A. Ballestrazzi. Nanometers-thick self-organized Fe stripes: bridging the gap between surfaces and magnetic materials. *Applied Physics Letters*, 84(8):1335, 2004.

[32] J. Coey. Nanoscale Magnetism. In *Magnetism and Magnetic Materials*, chapter 8, pages 264–304. Cambridge University Press, 2009.

[33] D. Sellmyer, M. Zheng, and R. Skomski. Magnetism of Fe, Co and Ni nanowires in self-assembled arrays. *Journal of Physics: Condensed Matter*, 13:R433–R460, 2001.

[34] G. Heydon, S. Hoon, A. Farley, S. Tomlinson, M. Valera, K. Attenborough, and W. Schwarzacher. Magnetic properties of electrodeposited nanowires. *Journal of Physics D: Applied Physics*, 30:1083, 1997.

[35] K. Nielsch, R. B. Wehrspohn, J. Barthel, J. Kirschner, U. Gosele, S. F. Fischer, and H. Kronmuller. Hexagonally ordered 100 nm period nickel nanowire arrays. *Applied Physics Letters*, 79(9):1360, 2001.

[36] J. H. Gao, Q. F. Zhan, W. He, D. L. Sun, and Z. hua Cheng. Synthesis and magnetic properties of Fe3Pt nanowire arrays fabricated by electrodeposition. *Applied Physics Letters*, 86(23):232506, 2005.

[37] J. Gao, D. Sun, Q. Zhan, W. He, and Z. H. Cheng. Magnetization reversal process and magnetic relaxation of self-assembled Fe3Pt nanowire arrays with different diameters: Experiment and micromagnetic simulations. *Physical Review B*, 75:1–6, 2007.

[38] L. Elbaile, R. D. Crespo, V. Vega, and J. A. García. Magnetostatic Interaction in Fe-Co Nanowires. *Journal of Nanomaterials*, 2012:1–6, 2012.

[39] E. Ferain and R. Legras. Characterisation of nanoporous particle track etched membrane. *Nuclear Instruments and Methods in Physics Research Section B: Beam Interactions with Materials and Atoms*, 131(1):97–102, 1997.

[40] E. Ferain and R. Legras. Pore shape control in nanoporous particle track etched membrane. *Nuclear Instruments and Methods in Physics Research Section B: Beam Interactions with Materials and Atoms*, 174(1):116–122, 2001.

[41] C. Schönenberger, B. M. I. van der Zande, L. G. J. Fokkink, M. Henny, C. Schmid, M. Krüger, A. Bachtold, R. Huber, H. Birk, and U. Staufer. Template Synthesis of Nanowires in Porous Polycarbonate Membranes: Electrochemistry and Morphology. *J. Phys. Chem. B*, 101(28):5497–5505, 1997.

[42] R. L. Fleischer, P. B. Price, and R. M. Walker. *Nuclear Tracks in Solids: Principles and Applications*. University of California Press, 1975.

[43] T. Whitney, P. Searson, J. Jiang, and C. Chien. Fabrication and magnetic properties of arrays of metallic nanowires. *Science*, 261(5126):1316, 1993.

[44] M. M. Hawkeye and M. J. Brett. Glancing angle deposition: Fabrication, properties, and applications of micro- and nanostructured thin films. *Journal of Vacuum Science & Technology A: Vacuum, Surfaces, and Films*, 25(5):1317, 2007.

[45] M. Taschuk, M. Hawkeye, and M. Brett. Glancing angle deposition. In P. M. Martin, editor, *Handbook of Deposition Technologies for Films and Coatings: Science, Applications and Technology*, chapter 13, page 936. Elsevier Ltd., third edit edition, 2010.

[46] H. E. Ruda, J. C. Polanyi, J. S. Y. Yang, Z. Wu, U. Philipose, T. Xu, S. Yang, K. L. Kavanagh, J. Q. Liu, L. Yang, Y. Wang, K. Robbie, J. Yang, K. Kaminska, D. G. Cooke, F. A. Hegmann, A. J. Budz, and H. K. Haugen. Developing

1D nanostructure arrays for future nanophotonics. *Nanoscale Research Letters*, 1(2):99–119, 2006.

[47] P. Gambardella, A. Dallmeyer, K. Maiti, M. C. Malagoli, W. Eberhardt, K. Kern, and C. Carbone. Ferromagnetism in one-dimensional monatomic metal chains. *Nature Letters*, 416:301–304, 2002.

[48] H. Elmers, J. Hauschild, and U. Gradmann. Morphology and magnetism of Fe on vicinal W(110) surfaces with different step orientation. *Journal of Magnetism and Magnetic Materials*, 221(1-2):219–223, 2000.

[49] R. Cheng, K. Guslienko, F. Fradin, J. Pearson, H. Ding, D. Li, and S. Bader. Step-decorated Ferromagnetic Fe Nanostripes on Pt(997). *Physical Review B*, 72(1):1–7, 2005.

[50] B. M. Huth, K. A. K. Ritley, J. Oster, H. Dosch, H. Adrian, and M. Huth. Highly Ordered Fe and Nb Stripe Arrays on Facetted α-Al2O3 (10-10). *Advanced Functional Materials*, 12(5):333, 2002.

[51] J. Lin, D. Y. Petrovykh, A. Kirakosian, H. Rauscher, and F. J. Himpsel. Self-assembled Fe nanowires using organometallic chemical vapor deposition and CaF2 masks on stepped Si (111). *Applied Physics Letters*, 78(6):829–831, 2001.

[52] B. Swartzentruber, Y. Mo, and R. Kariotis. Direct determination of step and kink energies on vicinal Si (001). *Physical Review Letters*, 65(15):1913–1917, 1990.

[53] K. Takayanagi. Structural analysis of Si(111)-77 by UHV-transmission electron diffraction and microscopy. *Journal of Vacuum Science & Technology A: Vacuum, Surfaces, and Films*, 3(3):1502, 1985.

[54] D. Woodruff. Solved and unsolved problems in surface structure determination. *Surface Science*, 500:147–171, 2002.

[55] J. L. Lin, D. Y. Petrovykh, J. Viernow, F. K. Men, D. J. Seo, and F. J. Himpsel. Formation of regular step arrays on Si(111)7x7. *Journal of Applied Physics*, 84(1):255, 1998.

[56] H. Hibino, T. Fukuda, M. Suzuki, and Y. Homma. High-temperature scanning-tunneling-microscopy observation of phase transitions and reconstruction on a vicinal Si (111) surface. *Physical Review B*, 47(19), 1993.

[57] X. Wang, J. Goldberg, and N. Bartelt. Terrace-width distributions on vicinal Si (111). *Physical Review Letters*, 65(19):2430–2433, 1990.

[58] R. Phaneuf and E. Williams. Step-height-tripling transition on vicinal Si (111). *Physical Review B*, 41(5), 1990.

[59] A. Latyshev, A. Aseev, A. Krasilnikov, and S. Stenin. Transformations on clean Si (111) stepped surface during sublimation. *Surface Science*, 213:157–169, 1989.

[60] Y. Homma, R. J. McClelland, and H. Hibino. DC-resistive-heating-induced step bunching on vicinal Si (111). *Japanese Journal of Applied Physics*, 29, 1990.

[61] K. Yagi. Step bunching, step wandering and faceting: self-organization at Si surfaces. *Surface Science Reports*, 43(2-4):45–126, 2001.

[62] D. Kandel and E. Kaxiras. Microscopic theory of electromigration on semiconductor surfaces. *Physical review letters*, 76(7):1114–1117, 1996.

[63] M. Degawa, H. Minoda, Y. Tanishiro, and K. Yagi. Direct-current-induced drift direction of silicon adatoms on Si(111)-(11) surfaces. *Surface Science*, 461(1-3):L528–L536, 2000.

[64] W. K. Burton, N. Cabrera, and F. C. Frank. The Growth of Crystals and the Equilibrium Structure of their Surfaces. *Philosophical Transactions of the Royal Society A: Mathematical, Physical and Engineering Sciences*, 243(866):299–358, 1951.

[65] S. Stoyanov. Electromigration Induced Step Bunching on Si Surfaces- How Does it Depend on the Temperature and Heating Current Direction? *Japanese Journal of Applied Physics*, 30(part 1):1–6, 1991.

[66] S. Stoyanov. Heating current induced conversion between 2 1 and 1 2 domains at vicinal (001) Si surfacescan it be explained by electromigration of Si Adatoms. *Japanese Journal of Applied Physics*, 1990.

[67] Y. Yang, E. Fu, and E. Williams. An STM study of current-induced step bunching on Si (111). *Surface Science*, 356:101–111, 1996.

[68] H. Tanaka, Y. Watanabe, and I. Sumita. Scanning tunneling microscopy of the (331) facets on the vicinal Si (111) surface. *Applied Surface Science*, 6:474–478, 1992.

[69] J. Viernow, J. L. Lin, D. Y. Petrovykh, F. M. Leibsle, F. K. Men, and F. J. Himpsel. Regular step arrays on silicon. *Applied Physics Letters*, 72(8):948, 1998.

[70] F. Men, F. Liu, P. Wang, C. Chen, D. Cheng, J. Lin, and F. Himpsel. Self-Organized Nanoscale Pattern Formation on Vicinal Si(111) Surfaces via a Two-Stage Faceting Transition. *Physical Review Letters*, 88(9):096105, 2002.

[71] D. Petrovykh and F. Himpsel. Self-assembled nanostructures at silicon surfaces. *Encyclopedia of Nanoscience and Nanotechnology*, 9(1):497–528, 2004.

[72] H. Hibino, Y. Shinoda, Y. Kobayashi, and K. Sugii. Reection High-Energy Electron Diffraction Studies of Vicinal Si (111) Surfaces. *Japanese Journal of Applied Physics*, 30(7):1337–1342, 1991.

[73] C. Battaglia, K. Gaál-Nagy, and P. Aebi. Structure and stability of the Si(331)-(121) surface reconstruction investigated with first-principles density functional theory. *Physical Review B*, 80(21):214102, 2009.

[74] V. Usov, C. Coileain, and I. Shvets. Influence of electromigration field on the step bunching process on Si(111). *Physical Review B*, 82(15):1–4, 2010.

[75] R. C. Newman. Defects in silicon. *Reports on Progress in Physics*, 45(10):1163–1210, 1982.

[76] P. Werner, U. Gosele, H.-J. Gossmann, and D. C. Jacobson. Carbon diffusion in silicon. *Applied Physics Letters*, 73(17):2465, 1998.

[77] H. C. Evitts, H. W. Cooper, and S. S. Flaschen. Rates of Formation of Thermal Oxides of Silicon. *Journal of The Electrochemical Society*, 111(6):688, 1964.

[78] C. O Coileain, V. Usov, I. V. Shvets, and S. Stoyanov. Critical field behavior and antiband instability under controlled surface electromigration on Si(111). *Physical Review B*, 84(7):075318, 2011.

[79] V. Usov, C. O. Coileain, and I. V. Shvets. Experimental quantitative study into the effects of electromigration field moderation on step bunching instability development on Si(111). *Physical Review B*, 83(15):155321, 2011.

[80] J. Toofan and P. Watson. The termination of the α-Al2O3 (0001) surface: a LEED crystallography determination. *Surface Science*, 401:162–172, 1998.

[81] J. Heffelfinger, M. Bench, and C. Carter. Steps and the structure of the (0001) α-alumina surface. *Surface Science*, 370(1):L168–L172, 1997.

[82] L. Pham Van, O. Kurnosikov, and J. Cousty. Evolution of steps on vicinal (0001) surfaces of α-alumina. *Surface Science*, 411(3):263–271, 1998.

[83] P. R. Ribič and G. Bratina. Behavior of the (0001) surface of sapphire upon high-temperature annealing. *Surface Science*, 601(1):44–49, 2007.

[84] S. Curiotto and D. Chatain. Surface morphology and composition of c-, a- and m-sapphire surfaces in O2 and H2 environments. *Surface Science*, 603(17):2688–2697, 2009.

[85] E. Thune, A. Boulle, D. Babonneau, F. Pailloux, W. Hamd, and R. Guinebretière. Nanostructured sapphire vicinal surfaces as templates for the growth of self-organized oxide nanostructures. *Applied Surface Science*, 256(3):924–928, 2009.

[86] F. Cuccureddu, S. Murphy, I. Shvets, M. Porcu, H. Zandbergen, N. Sidorov, and S. Bozhko. Surface morphology of c-plane sapphire (α-alumina) produced by high temperature anneal. *Surface Science*, 604(15-16):1294–1299, 2010.

[87] L. Pham Van, J. Cousty, and C. Lubin. Step heights and terrace terminations of a vicinal (0001) α-alumina surface annealed in UHV. *Surface Science*, 549(2):157–164, 2004.

[88] D. Fox, R. Verre, B. J. O'Dowd, S. K. Arora, C. C. Faulkner, I. V. Shvets, and H. Zhang. Investigation of coupled cobaltsilver nanoparticle system by plan view TEM. *Progress in Natural Science: Materials International*, 22(3):186–192, 2012.

[89] R. Verre, K. Fleischer, O. Ualibek, and I. V. Shvets. Self-assembled broadband plasmonic nanoparticle arrays for sensing applications. *Applied Physics Letters*, 100(3):031102, 2012.

[90] R. Verre, K. Fleischer, R. G. S. Sofin, N. McAlinden, J. F. McGilp, and I. V. Shvets. In situ characterization of one-dimensional plasmonic Ag nanocluster arrays. *Physical Review B*, 83(12):125432, 2011.

[91] A. Sugawara and M. Scheinfein. Room-temperature dipole ferromagnetism in linear-self-assembling mesoscopic Fe particle arrays. *Physical Review B*, 56(14):R8499–R8502, 1997.

[92] I. Zutic, J. Fabian, and S. D. Sarma. Spintronics: Fundamentals and applications. *Reviews of Modern Physics*, 76(2):323–410, 2004.

[93] G. Jacoby. Ternary 3PM magnetic recording code and system. *IEEE Transactions on Magnetics*, 17(6):3326–3328, 1981.

[94] Z. G. Vranesic and K. C. Smith. Engineering aspects of multi-valued logic systems. *Computer*, 7(9):34–41, 1974.

[95] S. Lee, D. Y. Shin, S. J. Chung, X. Liu, and J. K. Furdyna. Tunable quaternary states in ferromagnetic semiconductor GaMnAs single layer for memory devices. *Applied Physics Letters*, 90(15):152113, 2007.

[96] T. Blachowicz and A. Ehrmann. Fourfold nanosystems for quaternary storage devices. *Journal of Applied Physics*, 110(7):073911, 2011.

[97] A. Aharoni. *Introduction to the Theory of Ferromagnetism.* Oxford University Press, 2000.

[98] S. Chikazumi. *Physics of Ferromagnetism.* Oxford University Press, 1997.

[99] J. M. D. Coey. *Magnetism and Magnetic Materials.* Cambridge University Press, 2010.

[100] J. Coey. Micromagnetism, domains and hysteresis. In *Magnetism and Magnetic Materials*, chapter 7. Cambridge University Press, 2009.

[101] Z. Frait and D. Fraitová. Ferromagnetic resonance and surface anisotropy in iron single crystals. *Journal of Magnetism and Magnetic Materials*, 15:1081–1082, 1980.

[102] Z. Frait, D. Fraitova, C. Dufour, P. Mangin, and G. Marchal. Magnetic surface anisotropy at the iron-silicon interface. *IEEE Transactions on Magnetics*, 30(2):711–713, 1994.

[103] B. Aktas, B. Heinrich, G. Woltersdorf, R. Urban, L. R. Tagirov, F. Yldz, K. Ozdogan, M. Ozdemir, O. Yalcin, and B. Z. Rameev. Magnetic anisotropies in ultrathin iron films grown on the surface-reconstructed GaAs substrate. *Journal of Applied Physics*, 102(1):013912, 2007.

[104] J. Coey. Spin electronics and magnetic recording. In *Magnetism and Magnetic Materials*, chapter 14, pages 494–541. Cambridge University Press, 2009.

[105] C. H. C. Marrows. Spin-polarised currents and magnetic domain walls. *Advances in Physics*, 54(8):585–713, 2005.

[106] W. Brown. Criterion for Uniform Micromagnetization. *Physical Review*, 105(5):1479–1482, 1957.

[107] R. Skomski. Nanomagnetics. *Journal of Physics: Condensed Matter*, 15(20):R841–R896, 2003.

[108] L. Néel. Théorie du traînage magnétique des ferromagnétiques en grains fins avec applications aux terres cuites. *Annales de Géophysique*, 5:99–136, 1949.

[109] B. Barbara and L. Gunther. The barrier plot as a tool in magnetic relaxation studies. *Journal of Magnetism and Magnetic Materials*, 128(1):35–41, 1993.

[110] P. M. Paulus, F. Luis, M. Kro, G. Schmid, and L. J. D. Jongh. Low-temperature study of the magnetization reversal and magnetic anisotropy of Fe, Ni, and Co nanowires. *Journal of Magnetism and Magnetic Materials*, 224(2):180–196, 2001.

[111] H. Zeng, R. Skomski, L. Menon, Y. Liu, S. Bandyopadhyay, and D. J. Sellmyer. Structure and magnetic properties of ferromagnetic nanowires in self-assembled arrays. *Physical Review B.*, 65(13):1–8, 2002.

[112] P. Schio, F. Vidal, Y. Zheng, J. Milano, E. Fonda, D. Demaille, B. Vodungbo, J. Varalda, a. de Oliveira, and V. Etgens. Magnetic response of cobalt nanowires with diameter below 5 nm. *Physical Review B*, 82(9):1–9, 2010.

[113] J. M. Martinez Huerta, J. De La Torre Medina, L. Piraux, and a. Encinas. Self consistent measurement and removal of the dipolar interaction field in magnetic particle assemblies and the determination of their intrinsic switching field distribution. *Journal of Applied Physics*, 111(8):083914, 2012.

[114] F. Zighem, T. Maurer, F. Ott, and G. Chaboussant. Dipolar interactions in arrays of ferromagnetic nanowires: A micromagnetic study. *Journal of Applied Physics*, 109(1):013910, 2011.

[115] A. Robinson and W. Schwarzacher. Magnetic interactions in Ni -Cu/Cu superlattice nanowire arrays. *Journal of Applied Physics*, 93(10):7250–7251, 2003.

[116] J. Rivas, A. Kazadi Mukenga Bantu, G. Zaragoza, M. C. Blanco, and M. A. López-Quintela. Preparation and magnetic behavior of arrays of electrodeposited Co nanowires. *Journal of Magnetism and Magnetic Materials*, 249(1-2):220–227, 2002.

[117] P. S. Fodor, G. M. Tsoi, and L. E. Wenger. Investigation of magnetic interactions in large arrays of magnetic nanowires. *Journal of Applied Physics*, 103(7):07B713, 2008.

[118] H. Elmers, J. Hauschild, and U. Gradmann. Magnetism of nanowires of Fe(1 1 0) on W(1 1 0). *Journal of Magnetism and Magnetic Materials*, 177-181:827–828, 1998.

[119] J. Hauschild, H. Elmers, and U. Gradmann. Dipolar superferromagnetism in monolayer nanostripes of Fe(110) on vicinal W(110) surfaces. *Physical Review B*, 57(2):R677–R680, 1998.

[120] J. Hauschild, U. Gradmann, and H. J. Elmers. Perpendicular magnetization and dipolar antiferromagnetism in double layer nanostripe arrays of Fe(110) on W(110). *Applied Physics Letters*, 72(24):3211, 1998.

[121] H. J. Elmers. Onset of perpendicular magnetization in nanostripe arrays of Fe on stepped W(110) surfaces. *Physical Review B*, 59(5):3688–3695, 1999.

[122] A. Adeyeye, J. Bland, C. Daboo, and D. Hasko. Magnetostatic interactions and magnetization reversal in ferromagnetic wires. *Physical Review B*, 56(6):3265–3270, 1997.

[123] O. Henkel. Remanenzverhalten und Wechselwirkungen in hartmagnetischen Teilchenkollektiven. *Physica Status Solidi B*, 7(3):919–929, 1964.

[124] S. Thamm and J. Hesse. A simple plot indicating interactions between single-domain particles. *Journal of Magnetism and Magnetic Materials*, 8853(95), 1996.

[125] J. Lyubina and M. Wolf. A two-particle exchange interaction model. *Journal of Magnetism and Magnetic Materials*, 322:2948–2955, 2010.

[126] P. Mayo and A. Bradbury. Interaction effects in the remanence curves of CoTi-doped BaFe systems. *IEEE Transactions on Magnetics*, 26(1):228–230, 1990.

[127] P. Kelly, K. O'Grady, P. Mayo, and R. W. Chantrell. Switching mechanisms in cobalt-phosphorus thin films. *IEEE Transactions on Magnetics*, 25(5):3881–3883, 1989.

[128] S. Thamm and J. Hesse. The remanence of a StonerWohlfarth particle ensemble as a function of the demagnetisation process. *Journal of Magnetism and Magnetic Materials*, 184:245–255, 1998.

[129] S. K. Arora, B. J. O'Dowd, P. Thakur, N. B. Brookes, B. Ballesteros, P. Gambardella, and I. V. Shvets. Magnetization Reversal Behaviour of Planar Nanowire Arrays of Fe. *Current Nanoscience*, 9(5):6, 2013.

[130] D. A. Allwood, N. Vernier, G. Xiong, M. D. Cooke, D. Atkinson, C. C. Faulkner, and R. P. Cowburn. Shifted hysteresis loops from magnetic nanowires. *Applied Physics Letters*, 81(21):4005, 2002.

[131] C. Nam, Y. Jang, K. S. Lee, and B. K. Cho. Characteristics of domain wall pinning and depinning in a three-terminal magnetic Y-junction. *Nanotechnology*, 19(1):015703, 2008.

[132] J. Oster, M. Kallmayer, L. Wiehl, H. J. Elmers, H. Adrian, F. Porrati, and M. Huth. Crystallography, morphology, and magnetic properties of Fe nanostructures on faceted α-Al[sub 2]O[sub 3] m plane. *Journal of Applied Physics*, 97(1):014303, 2005.

[133] J. Sánchez-Barriga, M. Lucas, F. Radu, E. Martin, M. Multigner, P. Marin, A. Hernando, and G. Rivero. Interplay between the magnetic anisotropy contributions of cobalt nanowires. *Physical Review B*, 80(18):1–8, 2009.

[134] H. H. Elmers, J. Hauschild, H. Höche, U. Gradmann, H. Bethge, D. Heuer, and U. Köhler. Submonolayer Magnetism of Fe(110) on W(110): Finite Width Scaling of Stripes and Percolation between Islands. *Physical Review Letters*, 73(6):898–901, 1994.

[135] H.-J. Elmers, J. Hauschild, and U. Gradmann. Critical behavior of the uniaxial ferromagnetic monolayer Fe(110) on W(110). *Physical Review B*, 54(21):15224–15233, 1996.

[136] L. Tauxe, T. A. T. Mullender, and T. Pick. Potbellies, wasp-waists, and superparamagnetism in magnetic hysteresis. *Journal of Geophysical Research*, 101(B1):571, 1996.

[137] S. K. Arora, B. J. O'Dowd, B. Ballesteros, P. Gambardella, and I. V. Shvets. Magnetic properties of planar nanowire arrays of Co fabricated on oxidized step-bunched silicon templates. *Nanotechnology*, 23(23):235702, 2012.

[138] W. Wernsdorfer, E. Orozco, K. Hasselbach, A. Benoit, B. Barbara, N. Demoncy, A. Loiseau, H. Pascard, and D. Mailly. Experimental Evidence of the Néel-Brown Model of Magnetization Reversal. *Physical Review Letters*, 78(9):1791–1794, 1997.

[139] S. K. Arora, B. J. O'Dowd, D. M. Polishchuk, A. I. Tovstolytkin, P. Thakur, N. B. Brookes, B. Ballesteros, P. Gambardella, and I. V. Shvets. Observation of out-of-plane unidirectional anisotropy in MgO-capped planar nanowire arrays of Fe. *Journal of Applied Physics*, 114(13):133903–133903–7, 2013.

[140] C. Baker, S. K. Hasanain, and S. I. Shah. The magnetic behavior of iron oxide passivated iron nanoparticles. *Journal of Applied Physics*, 96(11):6657, 2004.

[141] A. E. Berkowitz and K. Takano. Exchange anisotropy a review. *Journal of Magnetism and Magnetic Materials*, 200(1-3):552–570, 1999.

[142] C. Prados, M. Multigner, A. Hernando, J. C. Sanchez, A. Fernandez, C. F. Conde, and A. Conde. Dependence of exchange anisotropy and coercivity on the Fe-oxide structure in oxygen-passivated Fe nanoparticles. *Journal of Applied Physics*, 85(8):6118, 1999.

[143] A. Shavel, B. Rodríguez-González, M. Spasova, M. Farle, and L. M. Liz-Marzán. Synthesis and Characterization of Iron/Iron Oxide Core/Shell Nanocubes. *Advanced Functional Materials*, 17(18):3870–3876, 2007.

[144] R. L. Stamps. Mechanisms of exchange bias: partial wall pinning, and fluctuations. *Journal of Magnetism and Magnetic Materials*, 242-245(Pt.1):139–145, 2002.

[145] A. Ghaddar, F. Gloaguen, J. Gieraltowski, and C. Tannous. Magnetic crossover effect in nickel nanowire arrays. *Physica B: Condensed Matter*, pages 1–8, 2011.

[146] A. Aharoni. Angular dependence of nucleation by curling in a prolate spheroid. *Journal of Applied Physics*, 82(3):1281–1287, 1997.

[147] C. R. Pike, A. P. Roberts, M. J. Dekkers, and K. L. Verosub. An investigation of multi-domain hysteresis mechanisms using FORC diagrams. *Physics of the Earth and Planetary Interiors*, 126(1):11–25, 2001.

[148] C. R. Pike, A. P. Roberts, and K. L. Verosub. First-order reversal curve diagrams and thermal relaxation effects in magnetic particles. *Geophysical Journal International*, 145(3):721–730, 2001.

[149] C. Pike and A. Fernandez. An investigation of magnetic reversal in submicron-scale Co dots using first order reversal curve diagrams. *Journal of Applied Physics*, 85(9):6668, 1999.

[150] C. R. Pike, A. P. Roberts, and K. L. Verosub. Characterizing interactions in fine magnetic particle systems using first order reversal curves. *Journal of Applied Physics*, 85(9):6660, 1999.

[151] A. A. P. Roberts, C. R. Pike, and K. L. Verosub. First-order reversal curve diagrams: A new tool for characterizing the magnetic properties of natural samples. *Journal of Geophysical Research*, 105(B12):28461, 2000.

[152] S. Alikhanzadeh-Arani, M. Almasi-Kashi, and A. Ramazani. Magnetic characterization of FeCo nanowire arrays by first-order reversal curves. *Current Applied Physics*, 13(4):664–669, 2013.

[153] F. Béron, L. P. Carignan, D. Ménard, and A. Yelon. Extracting Individual Properties from Global Behaviour : First-order Reversal Curve Method Applied to Magnetic Nanowire Arrays. In N. Lupu, editor, *Electrodeposited Nanowires and their Applications*, chapter 7, pages 167–188. InTech, 2010.

[154] R. J. Harrison and J. M. Feinberg. FORCinel: An improved algorithm for calculating first-order reversal curve distributions using locally weighted regression smoothing. *Geochemistry, Geophysics, Geosystems*, 9(5):n/a–n/a, 2008.

[155] D. C. Crew, S. H. Farrant, P. G. Mccormick, and R. Street. Measurement of magnetic viscosity in a Stoner-Wohlfarth material. *Journal of Magnetism and Magnetic Materials*, 163(3):299–312, 1996.

[156] N. H. Hai, N. Chau, D.-T. Ngo, D. T. H. Gam, N. Hoang, D. Thi, and H. Gam. Anomalous magnetic viscosity in exchange-spring magnet. *Journal of Magnetism and Magnetic Materials*, 323(23):3156–3161, 2011.

[157] C. Leighton and I. Schuller. Magnetic viscosity measurements reveal reversal asymmetry in exchange-biased bilayers. *Physical Review B*, 63(17):1–5, 2001.

[158] B. Gollomp. How Market Demands Influence Advances in Technologies [alookback]. *IEEE Instrumentation & Measurement Magazine*, 10(1):42–43, 2007.

[159] M. S. Gudiksen, L. J. Lauhon, J. Wang, D. C. Smith, and C. M. Lieber. Growth of nanowire superlattice structures for nanoscale photonics and electronics. *Nature*, 415(6872):617–20, 2002.

[160] K. A. Dick. A review of nanowire growth promoted by alloys and non-alloying elements with emphasis on Au-assisted IIIV nanowires. *Progress in Crystal Growth and Characterization of Materials*, 54(3):138–173, 2008.

[161] T. Akiyama, K. Sano, K. Nakamura, and T. Ito. An Empirical Potential Approach to Wurtzite-Zinc-Blende Polytypism in Group III-V Semiconductor Nanowires. *Japanese Journal of Applied Physics*, 45(9):L275–L278, 2006.

[162] E. Gaddy. Cost performance of multi-junction, gallium arsenide, and silicon solar cells on spacecraft. In *Conference Record of the Twenty Fifth IEEE Photovoltaic Specialists Conference - 1996*, pages 293–296. IEEE, 1996.

[163] M. Plante and R. LaPierre. Au-assisted growth of GaAs nanowires by gas source molecular beam epitaxy: Tapering, sidewall faceting and crystal structure. *Journal of Crystal Growth*, 310(2):356–363, 2008.

[164] J. C. Johnson, H. Yan, R. D. Schaller, L. H. Haber, R. J. Saykally, and P. Yang. Single Nanowire Lasers. *The Journal of Physical Chemistry B*, 105(46):11387–11390, 2001.

[165] H. Guo, L. Wen, X. Li, Z. Zhao, and Y. Wang. Analysis of optical absorption in GaAs nanowire arrays. *Nanoscale Research Letters*, 6:617, 2011.

[166] J. Jean, S. Chang, P. R. Brown, J. J. Cheng, P. H. Rekemeyer, M. G. Bawendi, S. Gradečak, and V. Bulović. ZnO Nanowire Arrays for Enhanced Photocurrent in PbS Quantum Dot Solar Cells. *Advanced Materials*, 25(20):2790–2796, 2013.

[167] P. Krogstrup, H. I. Jorgensen, M. Heiss, O. Demichel, J. V. Holm, M. Aagesen, J. Nygard, and A. Fontcuberta i Morral. Single-nanowire solar cells beyond the ShockleyQueisser limit. *Nature Photonics*, 7(4):306–310, 2013.

[168] D. P. Burt, N. R. Wilson, J. M. R. Weaver, P. S. Dobson, and J. V. Macpherson. Nanowire probes for high resolution combined scanning electrochemical microscopy - atomic force microscopy. *Nano Letters*, 5(4):639–43, 2005.

[169] Y. N. Guo, J. Zou, M. Paladugu, H. Wang, Q. Gao, H. H. Tan, and C. Jagadish. Structural characteristics of GaSbGaAs nanowire heterostructures grown by metal-organic chemical vapor deposition. *Applied Physics Letters*, 89(23):231917, 2006.

[170] M. Jeppsson, K. A. Dick, J. B. Wagner, P. Caroff, K. Deppert, L. Samuelson, and L.-E. Wernersson. GaAs/GaSb nanowire heterostructures grown by MOVPE. *Journal of Crystal Growth*, 310(18):4115–4121, 2008.

[171] T. Martensson, M. Borgstrom, W. Seifert, B. J. Ohlsson, and L. Samuelson. Fabrication of individually seeded nanowire arrays by vapour-liquid-solid growth. *Nanotechnology*, 14:1255–1258, 2003.

[172] J. Bauer, H. Paetzelt, V. Gottschalch, and G. Wagner. GaAs nanowires grown by MOVPE. *Physica Status Solidi (B)*, 247(6):1294–1309, 2010.

[173] K. Ikejiri, J. Noborisaka, S. Hara, J. Motohisa, and T. Fukui. Mechanism of catalyst-free growth of GaAs nanowires by selective area MOVPE. *Journal of Crystal Growth*, 298:616–619, 2007.

[174] J. Motohisa, J. Noborisaka, J. Takeda, M. Inari, and T. Fukui. Catalyst-free selective-area MOVPE of semiconductor nanowires on (111)B oriented substrates. *Journal of Crystal Growth*, 272(1-4):180–185, 2004.

[175] J. Noborisaka, J. Motohisa, S. Hara, and T. Fukui. Fabrication and characterization of freestanding GaAsAlGaAs core-shell nanowires and AlGaAs nanotubes by using selective-area metalorganic vapor phase epitaxy. *Applied Physics Letters*, 87(9):093109, 2005.

[176] J. Noborisaka, J. Motohisa, and T. Fukui. Catalyst-free growth of GaAs nanowires by selective-area metalorganic vapor-phase epitaxy. *Applied Physics Letters*, 86(21):213102, 2005.

[177] M. Moewe, L. C. Chuang, S. Crankshaw, C. Chase, and C. Chang-Hasnain. Atomically sharp catalyst-free wurtzite GaAsAlGaAs nanoneedles grown on silicon. *Applied Physics Letters*, 93(2):023116, 2008.

[178] K. Mochizuki, M. Ozeki, K. Kodama, and N. Ohtsuka. Carbon incorporation in GaAs layer grown by atomic layer epitaxy. *Journal of Crystal Growth*, 93:557–561, 1988.

[179] X. Duan and C. M. Lieber. General Synthesis of Compound Semiconductor Nanowires. *Advanced Materials*, 12(4):298–302, 2000.

[180] W. S. Shi, Y. F. Zheng, N. Wang, C. S. Lee, and S. T. Lee. Oxide-assisted growth and optical characterization of gallium-arsenide nanowires. *Applied Physics Letters*, 78(21):3304, 2001.

[181] W. Shi, Y. Zheng, N. Wang, C. Lee, and S.-T. Lee. A general synthetic route to III-V compound semiconductor nanowires. *Advanced Materials*, 13(8):591–594, 2001.

[182] A. Persson, B. Ohlsson, S. Jeppesen, and L. Samuelson. Growth mechanisms for GaAs nanowires grown in CBE. *Journal of Crystal Growth*, 272(1-4):167–174, 2004.

[183] L. Jensen, M. Björk, S. Jeppesen, A. Persson, B. Ohlsson, and L. Samuelson. Role of surface diffusion in chemical beam epitaxy of InAs nanowires. *Nano Letters*, 4(10):1961–1964, 2004.

[184] A. I. Persson, L. E. Fröberg, L. Samuelson, and H. Linke. The fabrication of dense and uniform InAs nanowire arrays. *Nanotechnology*, 20(22):225304, 2009.

[185] M. H. Magnusson, K. Deppert, J. O. Malm, J. O. Bovin, and L. Samuelson. Size-Selected Gold Nanoparticles by Aerosol Technology. *Nanostructured Materials*, 12(99):45–48, 1999.

[186] C. Colombo, D. Spirkoska, M. Frimmer, G. Abstreiter, and a. Fontcuberta i Morral. Ga-assisted catalyst-free growth mechanism of GaAs nanowires by molecular beam epitaxy. *Physical Review B*, 77(15):155326, 2008.

[187] T. Rieger, S. Heiderich, S. Lenk, M. I. Lepsa, and D. Grützmacher. Ga-assisted MBE growth of GaAs nanowires using thin HSQ layer. *Journal of Crystal Growth*, 353(1):39–46, 2012.

[188] S. Gibson and R. LaPierre. Study of radial growth in patterned self-catalyzed GaAs nanowire arrays by gas source molecular beam epitaxy. *Physica Status Solidi (RRL) - Rapid Research Letters*, 7(10):845–849, 2013.

[189] S. Plissard, K. A. Dick, G. Larrieu, S. Godey, A. Addad, X. Wallart, and P. Caroff. Gold-free growth of GaAs nanowires on silicon: arrays and polytypism. *Nanotechnology*, 21(38):385602, 2010.

[190] M. Plante and R. LaPierre. Growth mechanisms of GaAs nanowires by gas source molecular beam epitaxy. *Journal of Crystal Growth*, 286(2):394–399, 2006.

[191] V. Dubrovskii, G. Cirlin, I. Soshnikov, A. Tonkikh, N. Sibirev, Y. Samsonenko, and V. Ustinov. Diffusion-induced growth of GaAs nanowhiskers during molecular beam epitaxy: Theory and experiment. *Physical Review B*, 71(20):205325, 2005.

[192] P. Paiano, P. Prete, N. Lovergine, and A. M. Mancini. Size and shape control of GaAs nanowires grown by metalorganic vapor phase epitaxy using tertiarybutylarsine. *Journal of Applied Physics*, 100(9):094305, 2006.

[193] V. Pankoke, S. Sakong, and P. Kratzer. Role of sidewall diffusion in GaAs nanowire growth: A first-principles study. *Physical Review B*, 86(8):085425, 2012.

[194] Y. Nomura and Y. Morishita. Surface diffusion length of Ga adatoms on (1 1 1) B surfaces during molecular beam epitaxy. *Applied Physics Letters*, 64(9):1123–1125, 1994.

[195] M. R. Ramdani, J. C. Harmand, F. Glas, G. Patriarche, and L. Travers. Arsenic Pathways in Self-Catalyzed Growth of GaAs Nanowires. *Crystal Growth & Design*, 13(1):91–96, 2013.

[196] D. Spirkoska, J. Arbiol, A. Gustafsson, S. Conesa-Boj, F. Glas, I. Zardo, M. Heigoldt, M. H. Gass, A. L. Bleloch, S. Estrade, M. Kaniber, J. Rossler, F. Peiro, J. R. Morante, G. Abstreiter, L. Samuelson, and A. Fontcuberta i Morral. Structural and optical properties of high quality zinc-blende/wurtzite GaAs nanowire heterostructures. *Physical Review B*, 80(24):245325, 2009.

[197] C. Sartel, D. Dheeraj, F. Jabeen, and J. Harmand. Effect of arsenic species on the kinetics of GaAs nanowires growth by molecular beam epitaxy. *Journal of Crystal Growth*, 312(14):2073–2077, 2010.

[198] V. Dubrovskii, N. Sibirev, G. Cirlin, J. Harmand, and V. Ustinov. Theoretical analysis of the vapor-liquid-solid mechanism of nanowire growth during molecular beam epitaxy. *Physical Review E*, 73(2):021603, 2006.

[199] M. C. Plante and R. R. Lapierre. Control of GaAs nanowire morphology and crystal structure. *Nanotechnology*, 19(49):495603, 2008.

[200] N. Chand, T. Harris, S. Chu, E. Fitzgerald, J. Lopata, M. Schnoes, and N. Dutta. Performance of a valved arsenic cracker source for MBE growth. *Journal of Crystal Growth*, 126(4):530–538, 1993.

[201] T. Ogura, D. Kishimoto, and T. Nishinaga. Effect of As molecular species on inter-surface diffusion in GaAs MBE for ridge structure fabrication. *Journal of Crystal Growth*, 226(2-3):179–184, 2001.

[202] T. Sugaya, T. Nakagawa, Y. Sugiyama, Y. Tanuma, and K. Yonei. Difference in Diffusion Length of Ga Atoms under As2 and As4 Flux in Molecular Beam Epitaxy. *Japanese Journal of Applied Physics*, 36:5670–5673, 1997.

[203] N. V. Sibirev, M. Tchernycheva, M. A. Timofeeva, J.-C. Harmand, G. E. Cirlin, and V. G. Dubrovskii. Influence of shadow effect on the growth and shape of InAs nanowires. *Journal of Applied Physics*, 111(10):104317, 2012.

[204] H. Shtrikman, R. Popovitz-Biro, A. Kretinin, L. Houben, M. Heiblum, M. Bukaa, M. Galicka, R. Buczko, and P. Kacman. Method for suppression of stacking faults in Wurtzite III-V nanowires. *Nano Letters*, 9(4):1506–10, 2009.

[205] M. J. Tambe, S. K. Lim, M. J. Smith, L. F. Allard, and S. Gradecak. Realization of defect-free epitaxial core-shell GaAs/AlGaAs nanowire heterostructures. *Applied Physics Letters*, 93(15):151917, 2008.

[206] D. L. Dheeraj, G. Patriarche, H. Zhou, T. B. Hoang, A. F. Moses, S. Gronsberg, A. T. J. van Helvoort, B. r.-O. Fimland, and H. Weman. Growth and characterization of wurtzite GaAs nanowires with defect-free zinc blende GaAsSb inserts. *Nano Letters*, 8(12):4459–63, 2008.

[207] F. Glas, J.-C. Harmand, and G. Patriarche. Why Does Wurtzite Form in Nanowires of III-V Zinc Blende Semiconductors? *Physical Review Letters*, 99(14):3–6, 2007.

[208] M. Tchernycheva, J. C. Harmand, G. Patriarche, L. Travers, and G. E. Cirlin. Temperature conditions for GaAs nanowire formation by Au-assisted molecular beam epitaxy. *Nanotechnology*, 17(16):4025–30, 2006.

[209] M. A. Verheijen, R. E. Algra, M. T. Borgström, G. Immink, E. Sourty, W. J. P. V. Enckevort, E. Vlieg, and E. P. A. M. Bakkers. Three-dimensional morphology of GaP-GaAs nanowires revealed by transmission electron microscopy tomography. *Nano Letters*, 7(10):3051–5, 2007.

[210] A. Fontcuberta i Morral. Gold-Free GaAs Nanowire Synthesis and Optical Properties. *IEEE Journal of Selected Topics in Quantum Electronics*, 17(4):819–828, 2011.

[211] G. E. Cirlin, V. G. Dubrovskii, Y. B. Samsonenko, A. D. Bouravleuv, K. Durose, Y. Y. Proskuryakov, B. Mendes, L. Bowen, M. A. Kaliteevski, R. A. Abram, and D. Zeze. Self-catalyzed, pure zincblende GaAs nanowires grown on Si(111) by molecular beam epitaxy. *Physical Review B*, 82(3):035302, 2010.

[212] S. Q. Wang and H. Q. Ye. A plane-wave pseudopotential study on III-V zinc-blende and wurtzite semiconductors under pressure. *Journal of Physics: Condensed Matter*, 14(41):9579–9587, 2002.

[213] M. Galicka, M. Bukaa, R. Buczko, and P. Kacman. Modelling the structure of GaAs and InAs nanowires. *Journal of Physics: Condensed Matter*, 20(45):454226, 2008.

[214] R. Leitsmann and F. Bechstedt. Surface influence on stability and structure of hexagon-shaped III-V semiconductor nanorods. *Journal of Applied Physics*, 102(6):063528, 2007.

[215] V. Pankoke, P. Kratzer, and S. Sakong. Calculation of the diameter-dependent polytypism in GaAs nanowires from an atomic motif expansion of the formation energy. *Physical Review B*, 84(7):075455, 2011.

[216] A. Jenichen and C. Engler. Reconstructions and surface facets of the GaAs(112)A and (112)B surfaces: First-principles DFT supercell calculations. *Surface Science*, 608:204–211, 2013.

[217] H. K. Guo and H. P. Fang. Drop Size Dependence of the Contact Angle of Nanodroplets. *Chinese Physics Letters*, 22(4):787–790, 2005.

[218] L. Schimmele and S. Dietrich. Line tension and the shape of nanodroplets. *The European Physical Journal B*, 30(4):427–30, 2009.

[219] P. Chen, J. Gaydos, and A. W. Neumann. Contact Line Quadrilateral Relation. Generalization of the Neumann Triangle Relation To Include Line Tension. *Langmuir*, 12(24):5956–5962, 1996.

[220] V. Schmidt, S. Senz, and U. Gösele. The shape of epitaxially grown silicon nanowires and the influence of line tension. *Applied Physics A*, 80(3):445–450, 2004.

[221] V. Schmidt, S. Senz, and U. Gösele. Diameter-dependent growth direction of epitaxial silicon nanowires. *Nano Letters*, 5(5):931–5, 2005.

[222] J. Bauer, V. Gottschalch, H. Paetzelt, G. Wagner, B. Fuhrmann, and H. Leipner. MOVPE growth and real structure of vertical-aligned GaAs nanowires. *Journal of Crystal Growth*, 298:625–630, 2007.

[223] J. H. Weijs, A. Marchand, B. Andreotti, D. Lohse, and J. H. Snoeijer. Origin of line tension for a Lennard-Jones nanodroplet. *Physics of Fluids*, 23(2):022001, 2011.

[224] X. Duan, J. Wang, and C. M. Lieber. Synthesis and optical properties of gallium arsenide nanowires. *Applied Physics Letters*, 76(9):1116, 2000.

[225] V. Ruth and J. P. Hirth. Kinetics of Diffusion-Controlled Whisker Growth. *The Journal of Chemical Physics*, 41(10):3139, 1964.

[226] K. A. Dick, P. Caroff, J. Bolinsson, M. E. Messing, J. Johansson, K. Deppert, L. R. Wallenberg, and L. Samuelson. Control of III-V nanowire crystal structure by growth parameter tuning. *Semiconductor Science and Technology*, 25(2):024009, 2010.

[227] E. Givargizov. Fundamental aspects of VLS growth. *Journal of Crystal Growth*, 31:20–30, 1975.

[228] J. W. Dailey, J. Taraci, T. Clement, D. J. Smith, J. Drucker, and S. T. Picraux. Vapor-liquid-solid growth of germanium nanostructures on silicon. *Journal of Applied Physics*, 96(12):7556, 2004.

[229] S. Hofmann, R. Sharma, C. T. Wirth, F. Cervantes-Sodi, C. Ducati, T. Kasama, R. E. Dunin-Borkowski, J. Drucker, P. Bennett, and J. Robertson. Ledge-flow-controlled catalyst interface dynamics during Si nanowire growth. *Nature Materials*, 7(5):372–5, 2008.

[230] J. Johansson, L. S. Karlsson, C. P. T. Svensson, T. Martensson, B. a. Wacaser, K. Deppert, L. Samuelson, and W. Seifert. Structural properties of 111B oriented III-V nanowires. *Nature Materials*, 5(7):574–80, 2006.

[231] S. O. Mariager, C. B. Sorensen, M. Aagesen, J. Nygard, R. Feidenhansl, and P. R. Willmott. Facet structure of GaAs nanowires grown by molecular beam epitaxy. *Applied Physics Letters*, 91(8):083106, 2007.

[232] Y. Heon Kim, D. Woo Park, and S. Jun Lee. Gallium-droplet behaviors of self-catalyzed GaAs nanowires: A transmission electron microscopy study. *Applied Physics Letters*, 100(3):033117, 2012.

[233] F. Glas, G. Patriarche, and J. C. Harmand. Growth, structure and phase transitions of epitaxial nanowires of III-V semiconductors. *Journal of Physics: Conference Series*, 209:012002, 2010.

[234] N. Sköld, J. B. Wagner, G. Karlsson, T. Hernán, W. Seifert, M. E. Pistol, and L. Samuelson. Phase segregation in AlInP shells on GaAs nanowires. *Nano Letters*, 6(12):2743–7, 2006.

[235] J. Caram, C. Sandoval, M. Tirado, D. Comedi, J. Czaban, D. A. Thompson, and R. R. LaPierre. Electrical characteristics of core-shell p-n GaAs nanowire structures with Te as the n-dopant. *Nanotechnology*, 21(13):134007, 2010.

[236] J. A. Czaban, D. A. Thompson, and R. R. Lapierre. GaAs Core-Shell Nanowires for Photovoltaic Applications. *Nano Letters*, 9(1):148–154, 2009.

[237] K. Tivakornsasithorn, R. E. Pimpinella, V. Nguyen, X. Liu, M. Dobrowolska, and J. K. Furdyna. Magnetic anisotropy of GaAs/Fe/Au core-shell nanowires grown by MBE. *Journal of Vacuum Science & Technology B: Microelectronics and Nanometer Structures*, 30(2):02B115, 2012.

[238] S. A. Fortuna and X. Li. Metal-catalyzed semiconductor nanowires: a review on the control of growth directions. *Semiconductor Science and Technology*, 25(2):024005, 2010.

[239] Z. H. Wu, X. Mei, D. Kim, M. Blumin, H. E. Ruda, J. Q. Liu, and K. L. Kavanagh. Growth, branching, and kinking of molecular-beam epitaxial 110 GaAs nanowires. *Applied Physics Letters*, 83(16):3368, 2003.

[240] R. E. Pimpinella, D. Zhang, M. R. McCartney, D. J. Smith, K. L. Krycka, B. J. Kirby, B. J. O'Dowd, L. Sonderhouse, J. Leiner, X. Liu, M. Dobrowolska, and J. K. Furdyna. Magnetic properties of GaAs/Fe core/shell nanowires. *Journal of Applied Physics*, 113(17):17B520, 2013.

[241] C.-R. Chang, C. Lee, and J.-S. Yang. Magnetization curling reversal for an infinite hollow cylinder. *Physical Review B*, 50(9):6461–6464, 1994.